TURBULENCE MEASUREMENTS IN A HIGH REYNOLDS NUMBER TIDAL CHANNEL

by

Justine McMillan

Submitted in partial fulfillment of the requirements
for the degree of Doctor of Philosophy

at

Dalhousie University
Halifax, Nova Scotia
June 2017

for those who have inspired me

TABLE OF CONTENTS

LIST OF TABLES

LIST OF FIGURES

ABSTRACT

Measuring oceanic turbulence in a high Reynolds number flow is a challenge for several reasons: strong flows generate high drag on instrument support structures, turbulent fluctuations are intermittent and irregular, and available instrumentation techniques are limited by the spatial and temporal scales they can accurately resolve. Despite these challenges, field measurements are needed to characterize the dynamics of these energetic flows because Reynolds numbers of $\mathcal{O}(10^8)$ are not yet achievable in either numerical simulations or laboratory experiments.

This thesis presents the analysis and discussion of turbulence measurements that were acquired in Grand Passage, Nova Scotia, which is a tidal channel where the flow speed reaches $2.5\,\mathrm{m\,s^{-1}}$ and the Reynolds number is 8×10^7. The data were collected during three separate field campaigns that included the deployment of four bottom-mounted acoustic Doppler current profilers (ADCPs) and an underwater, streamlined buoy "flown" at mid-depth. The data were used to: (1) assess the capabilities and limitations of both instrumentation techniques and analysis methods for turbulence measurements in high-flow environments, (2) characterize the spatial and temporal variability in turbulence and boundary layer parameters, and (3) investigate the validity of existing theoretical and empirical relationships.

The results indicate that speed-bin averaged dissipation rates, ϵ, computed from ADCP data, agree to within a factor of two with direct estimates obtained from the shear probes. At all sites, the dissipation rate is log-normally distributed, and spectral and second-order structure function (SF2) methods yield estimates of ϵ from the ADCP data that agree to within 16%. Doppler noise levels—estimated using a modified SF2 method—are speed-independent and in agreement with those obtained from the velocity spectra.

Spatial variability and ebb/flood asymmetries in both the velocity profiles and the second-order turbulence statistics are attributed—in part—to the upstream bottom roughness. Imbalances in the local rates of production and dissipation are attributed to streamwise advection, and the degree of anisotropy is shown to vary throughout the water column. A modified form of the Kaimal spectrum is shown to predict the ADCP velocity spectra at large scales.

List of Abbreviations and Symbols Used

Abbreviation	Description
ADCP	acoustic Doppler current profiler (generic)
AD2CP	acoustic Doppler current profiler (Nortek 5-beam ADCP)
ADV	acoustic Doppler velocimeter
BL	boundary layer
CC	cross channel
CICLoPE	Center for International Cooperation in Long Pipe Experiments
CTD	conductivity-temperature-density
DES	detatched eddy simulations
DNS	direct numerical simulations
EC	Environment Canada
FVCOM	Finite Volume Community Ocean Model
IM	integral method
ISR	inertial subrange
LES	large eddy simulations
LS	least squares
MAD	mean absolute deviation
PDF	probability density function
PI	Peter's Island
RANS	Reynolds averaged Navier-Stokes
RDI	RD Instruments
RMS	root-mean-square
RMSE	root-mean-square error
SF	structure function
SF2	second-order structure function
SF3	third-order structure function
SP	shear probes
TKE	turbulent kinetic energy
VMP	vertical microstructure profiler

Notation	Description
$\langle\cdot\rangle$	temporal average
$\langle\cdot\rangle_{\mathrm{ISR}}$	average over ISR
$\cdot'$	fluctuating quantity
$(\cdot)_d$	depth-average
$\overline{(\cdot)}$	mean
$(\cdot)_{rms}$	root-mean-square
$\widehat{(\cdot)}$	measured value or parameter

Roman symbol	Description	Units
a, a_i	regression coefficients	-
a_{K}	scaling coefficient for Kaimal spectra	-
A_i	amplitude of i-th frequency component	m s^{-1}
A, B, C, D	Kaimal spectral constants	-
A_X, A_Y, A_Z	acceleration measured using the MicroRider	m s^{-2}
b_i	regression constant	-
C	spectral constant for IM method	-
C_2	universal constant for SF2	-
C_d	bottom drag coefficient	-
C_q	coefficient in ADCP estimates of TKE	-
C_s	constant for amplitude of synthetic time series	-
C_T	coefficient in ADCP estimates of F_d	-
D_{ii}	second-order longitudinal SF along i-th beam	m^2 s^{-2}
D_{L^n}	n-th order longitudinal structure function	(m/s)$^{\mathrm{n}}$
D_{LL}	second-order longitudinal structure function	m^2 s^{-2}
D_{LLL}	third-order longitudinal structure function	m^2 s^{-2}
D_{uu}	second-order longitudinal SF in u direction	m^2 s^{-2}
D_{ww}	second-order longitudinal SF in w direction	m^2 s^{-2}
e_i	Doppler error in velocity along i-th beam	m s^{-1}
E_v	voltage	V
f	frequency	Hz
f_i	i-th frequency component	Hz

Roman symbol	Description	Units
f_m	maximum frequency in synthetic time series	Hz
f_s	sampling frequency	Hz
f_N	Nyquist frequency	Hz
$\tilde{f}_{\mathrm{vK}}$	non-dimensional von Kármán frequency	-
$\tilde{f}_{\mathrm{K}}$	non-dimensional Kaimal frequency	-
F	longitudinal autocorrelation function	-
F_d	vertical diffusive flux of TKE	$\mathrm{m^3\ s^{-3}}$
$\vec{\mathcal{F}}$	transport vector of TKE	$\mathrm{m^3\ s^{-3}}$
g	acceleration due to gravity	$\mathrm{m\ s^{-2}}$
G	transverse autocorrelation function	-
h'	roughness metric	m
i, j	matrix and vector indices	-
h	height of roughness element	m
H	water depth	m
H_0	water depth at ADCP site	m
H_{sm}	smoothed bathymetric transect depth	m
k	streamwise wavenumber	rad/m
k_0	cutoff wavenumber in von Kármán spectra	rad/m
k_i	wavenumber in resolved range	rad/m
k_i*	summation of folded wavenumber	rad/m
k_m	wavenumber of m-th fold	rad/m
$\hat{k}$	streamwise cyclic wavenumber	cpm
$\tilde{k}$	non-dimensional wavenumber	-
K	correction factor in modified SF2 method	-
L_i	integral length scale for the i-th beam	m
L_{Iw}	vertical integral length scale from ADCP data	m
L_{vK}	length scale in von Kármán spectra	m
L_{K}	length scale in Kaimal spectra	m
$\mathscr{L}$	length scale	m
ℓ_0	length scale associated with large eddies	m
m_i	regression coefficient for SF3 method	-

Roman symbol	Description	Units
M	number of folds in aliased spectrum	-
n	total number	-
n_S	total number of spectra in average	-
n_k	total number of wavenumbers in MAD estimate	-
N_i	spectral noise level for the i-th beam	$m^2\ s^{-2}\ Hz^{-1}$
N_T	summed along-beam Doppler noise level	$m^2\ s^{-2}\ Hz^{-1}$
p	probability density	-
P	pressure	dbar
P_{MR}	pressure measured by MicroRider	dbar
$\mathcal{P}$	production rate of TKE	$W\ kg^{-1}$
$\mathcal{P}_h$	production rate of TKE from horizontal velocity shear	$W\ kg^{-1}$
r	spatial separation distance	m
r_0	reference coordinate	m
r_m	scale of unresolved eddies	m
R_i	autocorrelation of i-th beam velocities	$m\ s^{-1}$
Re	Reynolds number	-
$q^2/2$	turbulent kinetic energy	$m^2\ s^{-2}$
s_{ij}	component of the strain rate tensor	s^{-1}
s_p	sensitivity of the shear pribe	$V\ m^{-2}\ s^2$
S_{ii}	spectral density of i-th beam velocity	$m^3\ s^{-2}$
S_{bb}	pairwise-summed beam velocity spectral density	$m^2\ s^{-2}\ Hz^{-1}$
S_T	summed along beam velocity spectral density	$m^2\ s^{-2}\ Hz^{-1}$
$\mathcal{S}_k$	skewness	-
t	time	s
T	temperature	°C
$\mathcal{T}$	timescale	s
T_d	vertical diffusive transport of TKE	$W\ kg^{-1}$
T_p	pressure transport of TKE	$W\ kg^{-1}$
u_*	friction velocity	$m\ s^{-1}$
u_b	velocity component broadside to shear probe	$m\ s^{-1}$
u_m	velocity scale of unresolved eddies	$m\ s^{-1}$

Roman symbol	Description	Units
u_1, u_2, u_3	velocity components (streamwise, lateral, vertical)	$\mathrm{m\,s^{-1}}$
u, v, w	velocity components (streamwise, lateral, vertical)	$\mathrm{m\,s^{-1}}$
u_E, u_N, u_U	velocity components (frame coordinates)	$\mathrm{m\,s^{-1}}$
u_I, v_I, w_I	velocity components (instrument coordinates)	$\mathrm{m\,s^{-1}}$
u_F, v_F, w_F	velocity components (frame coordinates)	$\mathrm{m\,s^{-1}}$
u_N, v_N, w_N	velocity components (*Nemo* coordinates)	$\mathrm{m\,s^{-1}}$
u_E, u_N, u_U	velocity components (east, north, up)	$\mathrm{m\,s^{-1}}$
$\mathcal{U}$	velocity scale	$\mathrm{m\,s^{-1}}$
U	signed horizontal speed	$\mathrm{m\,s^{-1}}$
U_{1m}	theoretical velocity at 1 m above bottom	$\mathrm{m\,s^{-1}}$
U_A	resultant velocity at shear probe	$\mathrm{m\,s^{-1}}$
U_c	central speed bin value	$\mathrm{m\,s^{-1}}$
U_p	speed of the flow past the shear probe	$\mathrm{m\,s^{-1}}$
U_r	reference signed horizontal speed	$\mathrm{m\,s^{-1}}$
U_w	wind speed	$\mathrm{m\,s^{-1}}$
v_i	velocity along i-th ADCP beam	$\mathrm{m\,s^{-1}}$
x_U	upstream distance	m
x_1, x_2, x_3	Eulerian coordinates	m
x, y, z	Eulerian coordinates	m
x_N, y_N, z_N	coordinates relative to *Nemo* buoy	m
y^+	non-dimensional wall unit	-
z_0	bottom roughness length scale	m

Greek symbol	Description	Units
α_i	Kolmogorov constant for i-th velocity component	-
β	angle between instrument coordinates and streamlines	$^\circ$
γ_2	anisotropy factor of second-order moment	-
γ_3	anisotropy factor of third-order moment	-
Γ	correction ratio for IM method	-
δ	height of zero Reynolds stress	m
δ_L	log-layer thickness	m
ϵ	rate of dissipation of TKE	$\mathrm{W\,kg^{-1}}$

Greek symbol	Description	Units
ϵ_0	rate of dissipation of TKE for synthetic time series	W kg^{-1}
ϵ_i	rate of dissipation along the i-th beam	W kg^{-1}
ϵ_{IM}	rate of dissipation of TKE from integral method	W kg^{-1}
ϵ_{LS}	rate of dissipation of TKE from least squares method	W kg^{-1}
ϵ_{S2}	rate of dissipation of TKE from SF2 method	W kg^{-1}
ϵ_{S3}	rate of dissipation of TKE from SF3 method	W kg^{-1}
ϵ_U	rate of dissipation of TKE from upstream beam	W kg^{-1}
ϵ_D	rate of dissipation of TKE from downstream beam	W kg^{-1}
ζ	deviation of spectrum from -5/3 slope	-
η	Kolmogorov microscale	m
ϑ	ADCP beam angle relative to vertical	$^\circ$
θ_A	angle of attack of resultant flow on shear probe	$^\circ$
θ_H	heading angle	$^\circ$
θ_P	pitch angle	$^\circ$
θ_R	roll angle	$^\circ$
κ	von Kármán's constant	-
$\overline{\kappa}$	triple velocity autocorrelation function	-
μ	intermittency exponent	-
ν	kinematic viscosity	m^2 s^{-1}
ρ	density	kg m^{-3}
σ_{e_i}	standard deviation of Doppler noise	m s^{-1}
$\widetilde{\sigma}_{e_i}$	corrected σ_{e_i} using modified SF2 method	m s^{-1}
σ_i	standard deviation of the i^{th} velocity component	m s^{-1}
σ_{N_i}	normalized Doppler noise	m s^{-1}
τ_b	bed shear stress	N m^{-2}
ϕ_{ii}	wavenumber spectral density of i^{th} velocity component	m^3 s^{-2}
Φ_{ii}	frequency spectral density of i^{th} velocity component	m^2 s^{-2} Hz^{-1}
Φ_{bb}	predicted form of S_{bb}	m^2 s^{-2} Hz^{-1}
ψ	wavenumber spectral density of velocity shear	s^{-2} cpm^{-1}

ACKNOWLEDGEMENTS

One day, nearly six years ago, I was sitting in the Student Union Building when I overheard a conversation between a professor and a grad student. The professor was comparing a PhD to a marathon. His key phrases were "you have to pace yourself", and "there will be many highs and lows". Having just completed the Boston Marathon a couple months earlier, the metaphor resonated with me. I thought it was an interesting analogy, but, at the time, I failed to realize exactly how accurate it was. Running a marathon is a grueling test of physical endurance. Well—it turns out—that a PhD is a grueling test of mental and emotional endurance. And, just like a marathon, I wouldn't have been able to cross the finish line without support and guidance from many people.

First and foremost, thank you to my "coach" and supervisor Alex who has been by my side every step of the way. You witnessed those rare and crucial "eureka" moments. But, more importantly, you guided me during the day-to-day slog. You sent me countless references dating back to 1922, and reminded me that, sometimes, just thinking (in silence) is more productive than beating my head against the wall. So, thank you for the patience, the advice, the laughs, and even the occasional hug.

I would also like to acknowledge my "support team" who were instrumental in establishing a "training plan" and ensuring that I (and Alex) stayed on track. To my committee members, both past and present, thank you for your useful insights and helpful comments which greatly improved the quality of my thesis. Also, thank you for your incredible patience as I missed every self-imposed deadline that I ever made. And to Jackie, Daniel, Lori and Kim, thank you for your help on everything from filling out forms to fixing computers.

I definitely would not have made it to the finish line without my "training partners" and fellow grad students, who helped me push through the tough moments. There were countless times when, just as I was about to give up, you grabbed my hand and encouraged me to put one foot in front of the other. Or as I like to say, "walk me back from the ledge". To Mat, thank you for your optimism, your love of coffee, and your unwavering friendship. To Erica, thank you for the Monday-morning updates and the life-chats which helped me stay sane through all these years. And to everyone else, who are too numerous to name,

thank you for making the LSC an enjoyable place to work.

Every marathon runner needs his or her own “fan club”, which consists of those people who think you are crazy, but still encourage you however they can. To my biggest fans, i.e., my parents, thank you for your unconditional support, and for trying your best to understand what I do. My choice to attend Dal was largely based on a desire to be close to home, and to see you more often. I am so grateful to have finally gotten to know you as an adult, and to see how amazing you are. I am sure life will take me on many adventures that will lead me astray, but I will always come home to visit.

I would also like to acknowledge all the supporters who have been cheering me on from the sidelines. To my sisters, thank you for keeping me grounded and knowing me better than I know myself. To my Hali-family, thank you for all the adventures, the crêpe nights, and for allowing me to be the odd-man out. To Lauren, thank you for being a life-long friend and for always being there with your arms open wide. And to Amy and Andrea, thank you for helping me see my inner strength even when my body was weak.

Finally, I want to express the deepest gratitude to the people who inspired me to run toward the finish line. To Grampie, thank you for spurring my curiosity in the Bay of Fundy so many years ago. I wish I could tell you about my research in person because I know you would beam with pride. And to my source of weekly inspiration, the Start-2-Finish kids, I hope that you get as many breaks and helping hands as I did, so that you can all grow up living to your full potential.

At last, the finish line is in sight and it is time for the final sprint!

CHAPTER 1

INTRODUCTION

Turbulent flows are ubiquitous in both natural systems (e.g., atmospheric and oceanic boundary layers) and engineering applications (e.g., pipe flow, wake generation). Despite its universality, turbulence is difficult to define. Instead, it is described as a *syndrome* characterized by a set of symptoms (*Stewart*, 1969). In this sense, all turbulent flows can be described as (*Tennekes and Lumley*, 1972; *Lesieur*, 1990; *Pope*, 2000):

1) *irregular*: Turbulent flows are disordered, unsteady, and chaotic in that the velocity field varies significantly and irregularly in both position and time. The kinetic energy is concentrated into bursts that are separated by comparatively quiescent regions.

2) *rotational*: Turbulent flows possess three-dimensional vorticity appearing as identifiable structures (e.g., eddies) that exist over a broad range of length scales. Large quasi-two-dimensional structures are generated by gradients in the mean flow (e.g., at boundaries), and evolve into smaller scale three-dimensional features through nonlinear processes.

3) *diffusive*: Turbulent flows cause rapid mixing. Transfer rates of momentum, heat and other scalar properties are much higher than if only molecular diffusion processes are involved.

4) *dissipative*: Turbulent flows lose kinetic energy to heat through the action of viscosity on the smallest scales.

Turbulent flows are further characterized by a high Reynolds number, which is the ratio of inertial and viscous forces acting within a fluid. Mathematically, the Reynolds number is

defined as

$$\mathrm{Re} = \frac{\mathcal{U}\mathscr{L}}{\nu}, \tag{1.1}$$

where $\mathcal{U}$ is a velocity scale, $\mathscr{L}$ is a length scale and ν is the kinematic viscosity of the fluid.

At high Reynolds numbers, the advection terms in the Navier-Stokes equations are significant, resulting in a set of nonlinear equations for which no analytical solution is known. Under the mathematical assumptions of existence and uniqueness, the governing equations describe a deterministic phenomenon; however, the nonlinearity of the system implies that the solutions evolve with time in a complicated way that is—as of yet—impossible to predict theoretically (*Lesieur*, 1990). Recent advances in computing power have enabled fully-resolved numerical solutions to the Navier-Stokes equations in certain conditions. These direct numerical simulations (DNS) have been implemented for flows with moderate Reynolds numbers of $\mathcal{O}(10^4)$ in both boundary layers (*Borrell et al.*, 2013; *Jabbari et al.*, 2015) and channels (*Alfonsi et al.*, 2016). At higher Reynolds numbers, the small scale motion present in the flow cannot be resolved, and thus, the simulation of a deterministic solution is not yet possible. Through the parameterization of the sub-grid scale motions, large eddy simulations (LES) can be used to model flows with Reynolds numbers up to $\mathcal{O}(10^{11})$ (*Cheng and Samtaney*, 2014); however, inaccuracies in the simulations generate errors that are amplified by the nonlinear terms, and thus, the simulated flow quickly deviates from the exact solution (*Lesieur*, 1990). More specifically, LES simulations resolve the general shapes of the large scale patterns, but they do not accurately predict the phase or position of the turbulent structures.

Stochastic approaches to describe turbulent flows are also useful. The first statistical theories of turbulence in high Reynolds number flows were developed over 75 years ago (e.g., *Taylor*, 1935; *Kolmogorov*, 1941b), and were subsequently supported by measurements collected by *Grant et al.* (1962) in a tidal channel where the Reynolds number exceeded 10^8. Additional insight into the small scale properties of highly turbulent flow was gained from the 1968 Kansas Plains Experiment where velocity and temperature measurements were made at three heights within the atmospheric boundary layer (*Wyngaard and Cote*, 1971).

Early attempts to test the statistical theories of turbulence using laboratory experiments within both pipes (*Laufer*, 1954) and boundary layers (*Klebanoff*, 1955) were largely

unsuccessful because sufficiently high Reynolds numbers could not be achieved (*Grant et al.*, 1962). In such experiments, the maximum resolvable scale is limited by the physical size of the experimental domain, and thus, even today the largest pipes and wind tunnels can only generate flows having Reynolds numbers of $\mathcal{O}(10^6)$ (*Talamelli et al.*, 2014; *Örlü et al.*, 2017). In addition, these high experimental Reynolds numbers are typically achieved using pressurized gas, which has lower viscosity than air at standard atmospheric pressure. This reduction in viscosity is associated with a reduction in the size of the smallest eddies in the flow, and hence, the flow conditions do not perfectly model those in natural systems. Recently, the construction of the *Long Pipe Facility* at the Center for International Cooperation in Long Pipe Experiments (CICLoPE) was completed (*Örlü et al.*, 2017). The objective of the facility is to attain higher Reynolds number flows using unpressurized air. The test section has a diameter of 0.9 m and the maximum achievable wind speed is $60\,\mathrm{m\,s^{-1}}$. Thus, the highest attainable experimental Reynolds number (3.6×10^6) is still one to two orders of magnitude smaller than the Reynolds number in many natural flows.

1.1 Importance and Timeliness

Since *Grant et al.*'s benchmark study in 1962, additional measurements of oceanic turbulence in high Reynolds number flows have been sparse (Fig. 1.1). Because stratification inhibits the generation of large eddies, Reynolds numbers of $\mathcal{O}(10^8)$ are typically found in well-mixed regions with strong currents. Data collection in these areas is challenging because strong flows generate significant drag on instrument support structures, and instrumentation techniques are limited by the spatial and temporal scales they can accurately resolve. *Grant et al.* (1962) overcame these challenges in a $1.5\,\mathrm{m\,s^{-1}}$ tidal current using a hot-film anemometer mounted on a 4 m-long paravane that was towed 50 m below the surface. Despite the success of the field campaign, several technical problems were encountered: (1) temperature fluctuations frequently contaminated the velocity measurements, (2) plankton were occasionally caught on the probes, and (3) violent manoeuvres of the ship affected the stability of the towed body. These issues—particularly the latter—are largely responsible for the lack of subsequent ship-towed measurements in high flow regions (*Lueck et al.*, 2002).

In the 1980s, the introduction of acoustic Doppler current profilers (ADCPs) enabled the remote measurement of velocity throughout the water column, thus reducing the need

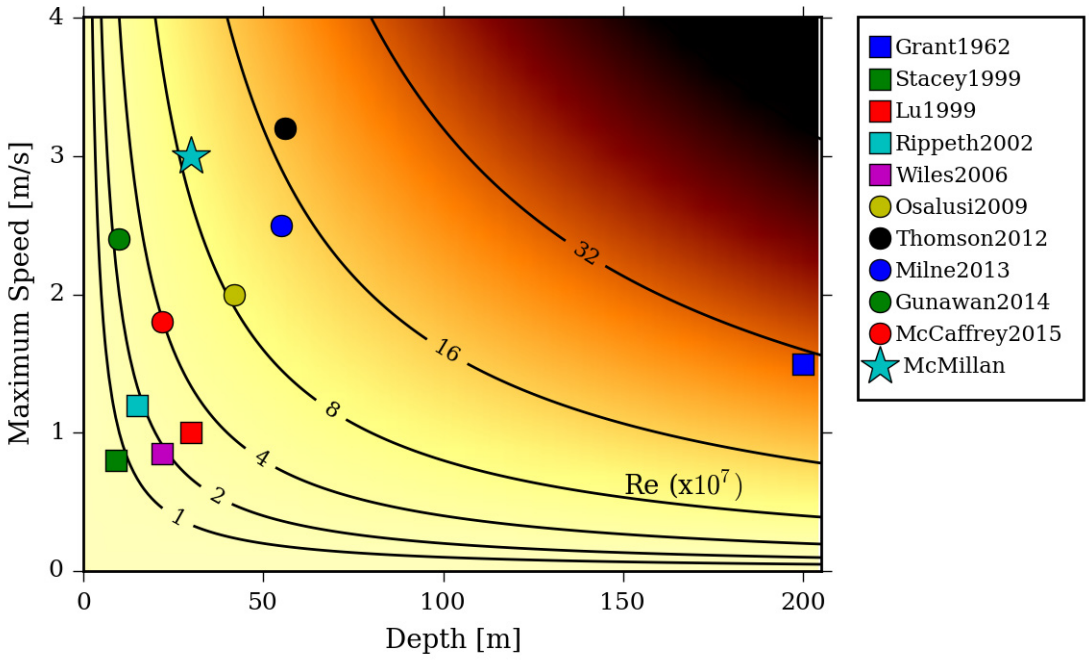

Figure 1.1: Summary of previous measurement campaigns in tidal channels. The markers are used to distinguish between studies that were (circles) and were not (squares) motivated by tidal energy developments. The colours and contours represent the maximum Reynolds number at each site.

for shipboard measurements. The broadband versions of these instruments—which were 100-fold more precise than the narrowband versions (*Gordon*, 1996)—were first used in high flow regions in the late 1990s and early 2000s (*Stacey et al.*, 1999; *Lu and Lueck*, 1999; *Lu et al.*, 2000; *Rippeth et al.*, 2002; *Wiles et al.*, 2006). The measurements were primarily used to estimate turbulence characteristics related to first- and second-order statistical moments (i.e., mean and variance) in tidal channels where the flow speeds reached $1.2\,\mathrm{m\,s^{-1}}$ (Fig. 1.1, squares). More recently, the development and deployment of in-stream tidal turbines has resulted in additional turbulence measurements in tidal channels (*Osalusi et al.*, 2009; *Thomson et al.*, 2012; *Milne et al.*, 2013; *Gunawan et al.*, 2014; *McCaffrey et al.*, 2015). The flow speeds in these latter investigations typically exceeded $2\,\mathrm{m\,s^{-1}}$ (Fig. 1.1, circles).

In-stream tidal turbines harness the kinetic energy in the flow, and operate under the same fundamental principles as wind turbines. Estimates of turbulence quantities at hub-height (i.e., the range of depths swept out by the turbine blades) are needed to address concerns related to the hydrodynamic loading on a turbine, and to assess device survivability

(*Blunden and Bahaj*, 2007). Several studies in the wind industry (e.g., *Moriarty et al.*, 2002; *Wächter et al.*, 2012) have shown that increased turbulence levels, the presence of coherent structures, and intermittency (i.e., gustiness) of the flow can affect both the extreme- and fatigue-loading of a turbine. Turbulent fluctuations can also affect overall power generation (*Chamorro et al.*, 2013; *Mycek et al.*, 2014) and properties of the turbine wake (*Mycek et al.*, 2014; *Blackmore and Batten*, 2014). Because future developments are expected to involve arrays of devices, a better understanding of the impact of turbulence would help reduce cost and financial risk.

In addition to providing necessary information about a proposed development site, accurate turbulence measurements are required to validate and improve the numerical simulations used to estimate turbine performance and hydrodynamic loading (*Wächter et al.*, 2012). To date, tidal turbine models typically implement inflow conditions where turbulent fluctuations are represented simply as a percentage of the mean flow (e.g., *McCann*, 2007). Thus, the distribution of turbulent kinetic energy (TKE) across a range of spatial scales is misrepresented in the simulations. More sophisticated models, which are capable of reproducing measured spectral densities, are frequently used in the wind industry (e.g., *Morales et al.*, 2012); however, the applicability of the same input conditions in tidal flows has yet to be investigated. While flows in tidal channels are expected to have similar dynamics to flows in the atmospheric boundary layer, fundamental differences arise due to the finite water depth in a tidal channel that limits the vertical scale of the turbulent eddies. Furthermore, the bathymetry is highly variable throughout a tidal channel, which may result in turbulence statistics—and hence, input conditions—that are site-specific.

Accurate turbulence measurements are also required to validate and improve regional- and channel-scale numerical models. Such models can provide valuable insight into the dynamics of the flow that cannot be achieved through the use of measurements alone. However, due to computational limitations, the full range of scales present in an $\mathcal{O}(10^8)$ Reynolds number flow cannot be simulated directly. Regional-scale models with a resolution of approximately 1 km to 100 km solve the Reynolds-averaged Navier Stokes (RANS) equations by implementing a closure model to parameterize the small-scale turbulent fluxes. Several closure models of varying complexity and accuracy exist, and the choice of model is highly dependent on the questions being addressed (*Pope*, 2000). Recently, Detached Eddy Simulations (DES) have been used to efficiently simulate tidal flows at

a resolution of $\mathcal{O}(1)$ m by concurrently implementing RANS solutions where very high-spatial resolution is needed (i.e., near the solid boundaries) and LES elsewhere in the domain (*Wilcox et al.*, 2017). This approach allows the turbulent fluctuations in the centre of a channel to be fully resolved to the grid scale, thus capturing variability in the flow on $\mathcal{O}(1)$ m scales. Because these models implement realistic bathymetry, site-specific comparisons to turbulence measurements can be used for validation. The model can then be used to simulate the turbulent flow at other locations in the same channel for which such measurements do not exist.

1.2 Objectives and Thesis Outline

The overall objective of this thesis is to characterize the turbulent properties of the flow in highly energetic tidal channels with a specific focus on assessing the limitations of standard instrumentation techniques, as well as determining the validity of existing theoretical and empirical relationships. The $\mathcal{O}(10^8)$ Reynolds numbers that exist in energetic passages are not attainable in either lab experiments or numerical simulations. Therefore, high-fidelity measurements are required to better describe the dynamics of the turbulent flows. Measurements at multiple locations within a channel are used to address the following questions:

1) Can existing measurement techniques—specifically, acoustic Doppler current profilers and shear probes—be used to obtain turbulence measurements at mid-depth? (Chapter 4)

2) What analysis method best resolves the intermittency in the turbulent fluctuations? (Chapter 5)

3) How do upstream conditions drive the spatial variability in the TKE balance? (Chapter 6)

4) Can the velocity spectra in the production range be better described by von Kármán or Kaimal forms? (Chapter 7)

5) Under what conditions do existing empirical and theoretical relationships governing boundary layer turbulence accurately predict second-order turbulence quantities? (Chapters 4–7)

These questions are addressed using a comprehensive dataset obtained in Grand Passage, Nova Scotia where the Reynolds number is 8×10^7 during strong tidal flow. Turbulence measurements were obtained using shear probes and four acoustic Doppler current profilers positioned along the centreline of the passage. The maximum separation distance of the instruments was 1 km. High resolution bathymetry measurements and numerical simulations were also obtained as part of concurrent studies.

The thesis is organized as follows. In Chapter 2, the relevant background material is presented: key theories pertaining to high Reynolds number turbulence are summarized, and various approaches used to measure oceanic turbulence are discussed. In Chapter 3, the data and mean flow dynamics of the study site are described. The turbulence characteristics of the flow are then presented in Chapters 4–7. The focus—particularly in Chapters 4 and 5—is on the estimation of the rate of dissipation of TKE, ϵ, which is an important second-order parameter used to assess the turbulence level. In Chapter 4, dissipation rates, estimated using both an acoustic Doppler current profiler (ADCP) and horizontally mounted shear probes, are compared. The work is then extended in Chapter 5 where two different analysis methods are applied to the ADCP data to estimate the variability in ϵ on 5-minute time scales at multiple locations. An examination of the TKE energy balance is then presented in Chapter 6 and the influence of the upstream bottom roughness is quantified. In Chapter 7, the ADCP velocity spectra are compared to the von Kármán and Kaimal forms, and modifications to the empirical coefficients are made to incorporate a variable anisotropy ratio. Final conclusions are summarized in Chapter 8.

Parts of this thesis have been published in two conference papers (*McMillan et al.*, 2013, 2015) and two peer-reviewed articles (*McMillan et al.*, 2016; *McMillan and Hay*, 2017). The content of the original papers has been re-organized and expanded upon for the purposes of continuity and completeness. The majority of Chapter 4 is published as *McMillan et al.* (2016)[1], and the bulk of Chapter 5 is published as *McMillan and Hay* (2017)[2]. Both manuscripts are in the *Journal of Atmospheric and Oceanic Technology*. As the lead author on the papers, I was responsible for the development and implementation

[1] **McMillan, J. M.**, A. E. Hay, R. G. Lueck, and F. Wolk, Rates of dissipation of turbulent kinetic energy in a high Reynolds number tidal channel, *J. Atmos. Oceanic Technol.*, 33, 817–837, 2016. ©American Meteorological Society. Used with permission.

[2] **McMillan, J. M.**, and A. E. Hay, Spectral and structure function estimates of turbulence dissipation rates in a high-flow tidal channel using broadband ADCPs, *J. Atmos. Oceanic Technol.*, 34, 5–20, 2017. ©American Meteorological Society. Used with permission.

of the analysis methods, and the interpretation of the results. I also prepared the figures, and wrote and edited the corresponding text. The co-authors provided help and advice on both the research and the manuscript. The contents of Chapters 6 and 7 are currently being prepared for publication.

CHAPTER 2

BACKGROUND

Turbulent flows are highly chaotic and unpredictable; however, standard procedures are used to both describe and measure the properties of the flow. In this chapter, the key ideas and assumptions surrounding existing theoretical and empirical models that pertain specifically to well-mixed, highly energetic flows are presented. Instrumentation techniques used to measure oceanic turbulence are also described.

2.1 Theory

2.1.1 Turbulent Kinetic Energy

In the absence of surface or internal gravity wave motions, Reynolds decomposition can be invoked to write a velocity component, u_i, at a given location as the sum of time-averaged (angle brackets) and fluctuating (prime) components, according to

$$u_i(t) = \langle u_i \rangle + u_i'(t), \tag{2.1}$$

where t is time and i is an index. The separation of timescales is chosen such that, over the averaging interval, the mean flow is statistically stationary and $\langle u_i' \rangle = 0$. For orthogonal coordinates, $i = 1, 2$ or 3. The convention that is used throughout this thesis is that u_1, u_2 and u_3 are equivalent to u, v, and w, corresponding to the streamwise (x_1 or x), lateral (x_2 or y), and vertical (x_3 or z) directions, respectively.

The turbulent kinetic energy (TKE) is related to the total variance of the fluctuating flow

and is defined as

$$\mathrm{TKE} = \frac{q^2}{2} = \frac{1}{2}\left[\left\langle u'^2\right\rangle + \left\langle v'^2\right\rangle + \left\langle w'^2\right\rangle\right] = \frac{1}{2}\left\langle u_i' u_i'\right\rangle, \tag{2.2}$$

where summation over repeated indicies is implied. By taking the dot product of u_i' and the Navier-Stokes equations, it can be shown that the evolution of the TKE in an unstratified fluid is governed by

$$\frac{D}{Dt}\left(\frac{q^2}{2}\right) = -\nabla\cdot\vec{\mathcal{F}} + \mathcal{P} - \epsilon, \tag{2.3}$$

where D/Dt is the mean material derivative, and $\vec{\mathcal{F}}$, $\mathcal{P}$ and ϵ are related to the transport, production and dissipation of TKE, respectively (*Kundu and Cohen*, 2002). The first term on the right hand side of Eq. (2.3) represents the spatial redistribution of TKE by both the turbulence itself and the viscous forces. The j^{th} component of the TKE flux, $\vec{\mathcal{F}}$, is given by

$$\mathcal{F}_j = \frac{1}{2}\left\langle u_i' u_i' u_j'\right\rangle + \frac{1}{\rho}\left\langle P' u_j'\right\rangle - 2\nu\left\langle u_i' s_{ij}\right\rangle, \tag{2.4}$$

where P' is the fluctuating pressure, ρ is the density, and s_{ij} is the strain rate tensor for the fluctuating component defined by

$$s_{ij} \equiv \frac{1}{2}\left(\frac{\partial u_i'}{\partial x_j} + \frac{\partial u_j'}{\partial x_i}\right). \tag{2.5}$$

The rate of shear production is defined as

$$\mathcal{P} = -\left\langle u_i' u_j'\right\rangle \frac{\partial\left\langle u_i\right\rangle}{\partial x_j}, \tag{2.6}$$

and represents the generation of TKE by the interaction of the Reynolds stresses, $-\left\langle u_i' u_j'\right\rangle$, with the mean velocity gradient, $\partial\left\langle u_i\right\rangle/\partial x_j$. The rate of dissipation of TKE is defined as

$$\epsilon = 2\nu\left\langle s_{ij} s_{ij}\right\rangle, \tag{2.7}$$

and represents the removal of TKE by viscosity.

2.1.2 Turbulent Boundary Layers

In a boundary layer, it can be assumed that the horizontal gradients of the turbulent quantities are much smaller than the vertical gradients, and thus, the TKE equation

(Eq. 2.3) can be simplified to

$$\frac{D}{Dt}\left(\frac{q^2}{2}\right) = T_p + T_d + \mathcal{P}_h - \epsilon, \tag{2.8}$$

where the vertical transport has been separated into a pressure transport term, T_p and a diffusive transport term, T_d, which are given by

$$T_p = -\frac{1}{\rho}\frac{\partial}{\partial z}\left\langle w'P'\right\rangle, \tag{2.9}$$

$$T_d = -\frac{1}{2}\frac{\partial}{\partial z}\left\langle w'q^2\right\rangle. \tag{2.10}$$

In the boundary layer, the rate of shear production is dependent on the vertical shear of the horizontal velocity components, i.e., Eq. (2.6) simplifies to

$$\mathcal{P}_h = -\left\langle u'w'\right\rangle \frac{\partial\left\langle u\right\rangle}{\partial z} - \left\langle v'w'\right\rangle \frac{\partial\left\langle v\right\rangle}{\partial z}. \tag{2.11}$$

In a high Reynolds number tidal channel, $\mathcal{P}_h$ is typically highest in the bottom boundary layer where friction at the sea bed generates a large vertical gradient in the mean velocity. If it is assumed both that variations in the streamwise direction of time-averaged quantities are small, and that the channel is relatively straight (i.e., no secondary circulation), then the velocity profile is expected to be self-similar near the bed where there is a constant stress layer (*Yaglom*, 1979; *Pope*, 2000). The mean flow speed in the boundary layer, U_{BL}, can then be described by the universal "law-of-the-wall" given by

$$U_{BL}(z) = \frac{u_*}{\kappa}\ln\left(\frac{z}{z_0}\right), \tag{2.12}$$

where z is the height above the bottom, z_0 is the bottom roughness length scale, u_* is the friction velocity, and $\kappa = 0.4$ is the von Kármán constant. The friction velocity is defined by the bed shear stress, τ_b, as

$$u_* \equiv \sqrt{\frac{\tau_b}{\rho}}. \tag{2.13}$$

For wall-bounded shear flows, Eq. (2.11) can be simplified to

$$\mathcal{P}_h = -\left\langle u'w'\right\rangle \frac{dU_{BL}}{dz}, \tag{2.14}$$

and within the constant stress layer, the Reynolds stress, $-\langle u'w' \rangle$, can be equated to τ_b/ρ to yield

$$-\langle u'w' \rangle = u_*^2. \tag{2.15}$$

Eqns. (2.12), (2.14) and (2.15) can then be combined to obtain an estimate for $\mathcal{P}$ in the boundary layer according to

$$\mathcal{P}_h = \frac{u_*^3}{\kappa z}. \tag{2.16}$$

2.1.3 Turbulent Scales and the Energy Cascade

The production of turbulence occurs at large scales where large eddies, which are characterized by a length scale ℓ_0, extract energy from the mean flow. Spatial gradients within these eddies are weak and, hence, the direct effect of viscosity is negligibly small. In 1922, *Richardson* suggested that there exists an energy cascade in which the TKE is transferred from these large eddies to smaller and smaller scales, until eventually, the smallest eddies are dissipated as heat by viscosity. At the largest scales, the flow is spatially inhomogeneous and is directionally dependent on the gradients in the mean flow (i.e., anisotropic); however, as the eddies interact with each other and pass their energy to the smaller scales, the directional biases are lost and the motions become "locally isotropic": i.e.,

$$\left\langle u'^2 \right\rangle = \left\langle v'^2 \right\rangle = \left\langle w'^2 \right\rangle. \tag{2.17}$$

Kolmogorov was first to hypothesize that for sufficiently high Reynolds number flows, an "inertial subrange" (ISR) exists where the assumption of local isotropy holds over a range of length scales, $\mathscr{L}$. *Pope* (2000) suggests that the ISR is confined to

$$60\eta < \mathscr{L} < \frac{1}{6}\ell_0, \tag{2.18}$$

where η is the Kolmogorov microscale, defined as

$$\eta \equiv \left(\frac{\nu^3}{\epsilon}\right)^{1/4}, \tag{2.19}$$

corresponding to the size of the smallest eddies in the flow.

The energy cascade can be depicted graphically in the form of an energy spectrum where the velocity variance density, ϕ_{ii}, is represented as a function of eddy size, $2\pi k^{-1}$, where k

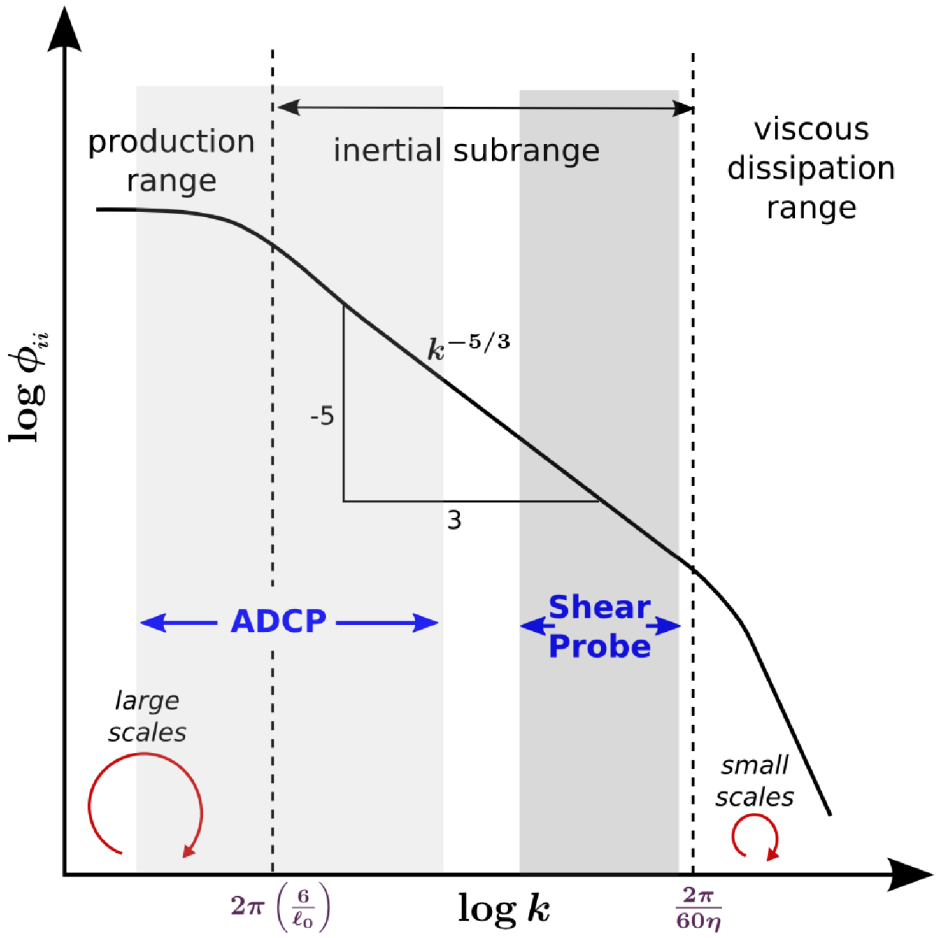

Figure 2.1: Schematic of a turbulence velocity spectrum. The typical regions resolved by each instrumentation technique are highlighted for $\epsilon \sim 10^{-4}$ W kg^{-1}.

is the wavenumber in the direction of the mean flow. A sketch of the typical shape of the spectrum is shown in Fig. 2.1. For high Reynolds number flows, the energy spectrum can be sub-divided into three distinct regions:

1) the *production range* where the spectral maximum occurs, and large eddies contribute significantly to the total velocity variance
2) the *inertial subrange* where ϕ_{ii} falls off at a constant rate proportional to $k^{-5/3}$, and
3) the *dissipation range* where viscosity acts on the smallest eddies, rapidly converting the kinetic energy of the smallest scales to heat.

2.1.4 Inertial Subrange and Local Isotropy

For high Reynolds number turbulence, the ISR is broad with the largest eddies being several orders of magnitude larger than the smallest eddies. Within the ISR, TKE is neither

generated nor destroyed, and the motions are assumed to be locally isotropic. The formal development of the statistical theory of isotropic turbulence arguably began with *Taylor*'s 1935 paper, in which it was shown for the first time that ϵ can be expressed in terms of the mean square value of any component of the velocity gradient, i.e.,

$$\epsilon = 15\nu \left\langle \left(\frac{\partial u_i'}{\partial x_i} \right)^2 \right\rangle = \frac{15}{2} \nu \left\langle \left(\frac{\partial u_i'}{\partial x_j} \right)^2 \right\rangle, \tag{2.20}$$

where the latter relationship holds if $i \neq j$. Taylor based his statistical description on the two-point longitudunal, F, and transverse, G, autocorrelation functions. For two points on the x axis that are separated by a distance r, F and G are defined as

$$F(r,t) = \frac{\langle u'(x+r,t)u'(x,t)\rangle}{\langle u'^2\rangle}, \tag{2.21}$$

$$G(r,t) = \frac{\left\langle u_j'(x+r,t)u_j'(x,t)\right\rangle}{\left\langle u_j'^2\right\rangle}, \tag{2.22}$$

where $j = 2, 3$.

Using the Navier-Stokes equations, *von Kármán and Howarth* (1938) derived an evolution equation for F given by

$$\frac{\partial}{\partial t}\left(\left\langle u'^2\right\rangle F\right) - \frac{\left\langle u'^2\right\rangle^{3/2}}{r^4}\frac{\partial}{\partial r}\left(r^4\overline{\kappa}\right) = \frac{2\nu\left\langle u'^2\right\rangle}{r^4}\frac{\partial}{\partial r}\left(r^4\frac{\partial F}{\partial r}\right), \tag{2.23}$$

where $\overline{\kappa}$ is the triple velocity correlation defined by

$$\overline{\kappa}(r,t) = \frac{\langle u'(x,t)^2 u'(x+r,t)\rangle}{\left\langle u'^2\right\rangle^{3/2}}. \tag{2.24}$$

Structure Functions

The fourth of Taylor's nine conclusions in his 1935 paper states that the Eulerian length scale of turbulence can be estimated from "simultaneous values of velocity obtained along a line". The structure function (SF) description—i.e., velocity differences "along a line"—of isotropic turbulence was then introduced by *Kolmogorov* (1941a, 1941b) in a pair of benchmark studies. In the longitudinal direction, the n-th order structure function at the

position r_0 is defined as

$$D_{L^n}(r,t) \equiv \left\langle [u'(r_0+r,t) - u'(r_0,t)]^n \right\rangle, \tag{2.25}$$

where u' is the fluctuating velocity component in the r direction. It can be shown that the second- and third-order structure functions, D_{LL} and D_{LLL}, are related to the two-point correlations by

$$\left\langle u'^2 \right\rangle F(r,t) = \left\langle u'^2 \right\rangle - \tfrac{1}{2} D_{LL}(r,t), \tag{2.26}$$

$$\left\langle u'^2 \right\rangle^{3/2} \overline{\kappa}(r,t) = \tfrac{1}{6} D_{LLL}(r,t), \tag{2.27}$$

and thus, the Kármán–Howarth equation (2.23) can be re-expressed in terms of structure functions to give the *Kolmogorov* (1941b) result,

$$\frac{\partial D_{LL}}{\partial t} + \frac{1}{3r^4}\frac{\partial}{\partial r}\left(r^4 D_{LLL}\right) = \frac{2\nu}{r^4}\frac{\partial}{\partial r}\left(r^4 \frac{\partial D_{LL}}{\partial r}\right) - \frac{4}{3}\epsilon, \tag{2.28}$$

where it has been assumed that $\partial(u'^2)/\partial t = -(2/3)\,\epsilon$, i.e., both production and transport of turbulence are small. Under the assumption of local isotropy in the inertial subrange, the unsteady and viscous terms in Eq. (2.28) can be neglected. The resulting equation can then be integrated to give the Kolmogorov "four-fifths law", i.e.,

$$D_{LLL}(r,t) = -\frac{4}{5}\epsilon r. \tag{2.29}$$

According to Kolmogorov's second similarity hypothesis, the second-order structure function for r within the inertial subrange must be independent of viscosity. Dimensional analysis can be used to show that D_{LL} must satisfy the "two-thirds law", i.e.,

$$D_{LL}(r,t) = C_2 \epsilon^{2/3} r^{2/3}, \tag{2.30}$$

where C_2 is a universal constant.

Velocity Spectra

The spectral representation of the two-thirds law was obtained independently by *Obukhov* (1941) and gives the now familiar $-5/3$ dependence of the velocity spectral density on k in the inertial subrange: i.e., the range of scales for which the turbulence is locally isotropic.

In one-dimension, the spectra are given by

$$\phi_{ii} = \alpha_i \epsilon^{2/3} k^{-5/3}, \tag{2.31}$$

where the index i corresponds to the longitudinal ($i = 1$) and transverse ($i = 2, 3$) directions. The Kolmogorov constants, α_i, are universal, and satisfy $\alpha_2 = \alpha_3 = 4/3\alpha_1$.

Universal Constants

The structure function and spectral constants, C_2 and α_1, are related. *Kolmogorov* (1941b) argued that the skewness of the velocity differences, given by $\mathcal{S}_k \equiv D_{LLL} D_{LL}^{-3/2}$, is constant in the inertial subrange, allowing C_2 to be expressed as

$$C_2 = \left(-\frac{4}{5\mathcal{S}_k} \right)^{2/3}. \tag{2.32}$$

Pond et al. (1963) showed that $\mathcal{S}_k$ can be written as $\mathcal{S}_k = -0.1\alpha_1^{-3/2}$. Thus Eq. (2.32) yields

$$C_2 = 4\alpha_1. \tag{2.33}$$

The above relationships between the spectral and structure function forms are outlined by *Monin and Yaglom* (1975) [pp. 364, 462–485], who also provide a comprehensive summary of the then-available measurements to suggest $C_2 = 2.0$. More recently, *Sauvageot* (1992) used Doppler radar measurements of turbulence in the atmosphere to conclude that $C_2 = 2.1 \pm 0.1$. A similar range of $C_2 = 2.0 \pm 0.1$ was estimated by *Saddoughi and Veeravalli* (1994) using measurements obtained in a wind tunnel. *Sreenivasan* (1995) compiled the results from experimental studies of both grid turbulence and shear flows to conclude that the best overall agreement with the spectral ISR equation (Eq. 2.31) was obtained with $\alpha_1 = 0.5$, and therefore with $C_2 = 2.0$. Despite this finding, in recent oceanographic studies, a value of $C_2 = 2.1$ is often adopted (e.g., *Wiles et al.*, 2006; *Lorke*, 2007; *Simpson et al.*, 2011; *Thomson et al.*, 2012; *Simpson et al.*, 2015).

Shear Spectra

The variance of a signal is equal to the integral of its spectrum, thus, Eq. (2.20) can be expressed as

$$\epsilon = \frac{15}{2} \nu \int_0^\infty \psi(k) dk, \tag{2.34}$$

where $\psi(k)$ is the spectral density of the velocity shear. An empirical function governing ψ was developed by *Nasmyth* (1970) and an analytical fit was initially obtained by *Wolk et al.* (2002). A slight modification of the mathematical model, which ensures that the integral of the spectrum is equivalent to the variance of the velocity shear, was obtained by *Lueck* (2013) and is given by

$$\psi(\tilde{k}) = \left(\frac{\epsilon^3}{\nu}\right)^{1/4} \frac{8.05\tilde{k}^{1/3}}{1 + (20.6\tilde{k})^{3.715}}, \tag{2.35}$$

where $\tilde{k}$ is a non-dimensional wavenumber defined as $\tilde{k} = 2\pi\eta k$. This form of the shear spectrum spans both the inertial subrange and the dissipation range, i.e., $\eta < \mathscr{L} < \frac{1}{6}\ell_0$.

2.1.5 Intermittency

While "intermittency" is not precisely defined in the turbulence literature, it is generally used to describe localized variations in turbulent fluctuations: i.e., the motion sporadically varies between more and less turbulent, in both space and time. Such variations occur at both large and small scales. At large scales, coherent structures extract energy from the mean flow and contribute to the "external intermittency", whereas, at small scales, eddies are dissipated as heat by viscosity and contribute to the "internal intermittency" (*Pope*, 2000).

The phenomenon of internal intermittency has been an active area of research since the 1960s when adaptations to Kolmogorov's similarity hypothesis were made to account for localized regions of strong dissipation. *Kolmogorov* (1962) and *Obukhov* (1962) hypothesized that the dissipation rate was log-normally distributed, which has since been shown to generally describe measurements made in the atmospheric boundary layer; however, the theoretical model may not accurately predict the probability of the highest and lowest values (*Stewart et al.*, 1970; *Van Atta and Chen*, 1970). Despite this limitation, the log-normal model has been used to predict the higher order moments (skewness and kurtosis) of the velocity derivatives in a turbulent flow (*Van Atta and Antonia*, 1980). The results, which are dependent on the Reynolds number of the flow, are consistent with both laboratory and field measurements (*Van Atta and Antonia*, 1980), and thus, a log-normal distribution is a good approximation for the variability in the dissipation rate.

Intermittency at the largest scales occurs as coherent eddies are swept past the measurement site, causing significant variability in the flow velocity. The variance associated with

these transient structures or "gusts" contributes to the shape of the spectra in the production range. Two of the frequently used semi-empirical spectral models in atmospheric and aeronautical simulations are the von Kármán and Kaimal spectra. The von Kármán spectra are consistent with the analytical equations governing the autocorrelation functions for isotropic turbulence (*von Kármán*, 1948; *Diedrich and Drischler*, 1957). The longitudinal component, Φ_{uu}, is given by

$$\Phi_{uu}(f) = \frac{4\sigma_u^2 L_{\mathrm{vK}}}{|U|} \frac{1}{\left[1 + 70.8\left(\frac{fL_{\mathrm{vK}}}{|U|}\right)^2\right]^{5/6}}, \tag{2.36}$$

where U is the velocity of the mean flow, σ_u^2 is the variance of the longitudinal velocity, and L_{vK} is the longitudinal integral length scale. The Kaimal spectra were obtained using data from the 1968 Kansas Experiment and are applicable to anisotropic turbulence (*Kaimal et al.*, 1972). For neutral atmospheric conditions, the universal form for the longitudinal component is given by

$$\Phi_{uu}(f) = \frac{zu_*^2}{|U|} \frac{102}{\left[1 + 33\left(\frac{fz}{|U|}\right)\right]^{5/3}}. \tag{2.37}$$

At high frequencies, both the von Kármán and the Kaimal spectra converge to $f^{-5/3}$, as expected for the inertial subrange (see Eq. 2.31) since $f = (2\pi)^{-1}|U|k$ by Taylor's Hypothesis (Section 2.2.4). Additional properties of both the von Kármán and Kaimal forms—including the predicted forms for the transverse components—are discussed in Chapter 7.

2.2 Turbulence Measurements

The measurement of turbulent fluctuations is nontrivial due, in part, to the broad range of scales that are present in the flow. Previous studies in tidal channels have primarily used broadband acoustic Doppler current profilers (ADCPs) (*Stacey et al.*, 1999; *Lu et al.*, 2000; *Rippeth et al.*, 2003; *Wiles et al.*, 2006; *Thomson et al.*, 2012; *Osalusi et al.*, 2009; *Hay et al.*, 2013) and acoustic Doppler velocimeters (ADVs) (*Thomson et al.*, 2012; *Milne et al.*, 2013; *Gunawan et al.*, 2014). Despite their widespread use, these acoustic instruments are unable to accurately measure the smallest scale velocity fluctuations due to high

Doppler noise (i.e., errors) that are $\mathcal{O}(0.1)\,\mathrm{m\,s^{-1}}$ for ADCPs and $\mathcal{O}(0.01)\,\mathrm{m\,s^{-1}}$ for ADVs. As an alternative—or perhaps a complementary—approach to acoustic measurements of turbulence, shear probes can be used to measure turbulent fluctuations at dissipation scales.

2.2.1 Acoustic Doppler Velocimeters

While the higher sampling rates (ca. 32 Hz) and improved accuracy of ADVs allow a better resolution of turbulent fluctuations than ADCPs, ADVs measure the flow at only one point in space. Thus, to obtain mid-depth measurements, ADVs must be mounted on either tall frames (*Thomson et al.*, 2012; *McCaffrey et al.*, 2015) or long mooring lines (*Thomson et al.*, 2014). ADV measurements are also sensitive to the concentration of scatterers in the water, which can lead to very low data quality in water with low particulate concentrations (*Hay et al.*, 2013).

2.2.2 Acoustic Doppler Current Profilers

ADCPs can be used to remotely measure the turbulent flow throughout the water column. However, low sampling rates (ca. 2 Hz), high noise levels, and divergent beam geometry of standard ADCPs (Fig. 2.2) place fundamental limitations on the estimation of turbulence parameters. In particular, temporal averages are needed to reduce the influence of noise, and the computation of second-order turbulence statistics (Reynolds stress, dissipation, TKE) requires the assumption that the fluctuations in the flow are statistically homogeneous over the horizontal scale of the beam separation (*Lu and Lueck*, 1999). The estimation of some parameters also relies on empirical anisotropic ratios that are not well constrained. Uncertainties and biases in the ADCP estimates can also be introduced due to instrument tilt angles as low as 2° (*Lu and Lueck*, 1999). To overcome some of these limitations, others (*Mohrholz et al.*, 2008; *Whipple and Luettich*, 2009; *Simpson et al.*, 2011; *Thomson*, 2012; *Lucas et al.*, 2014; *Simpson et al.*, 2015) have used pulse-coherent ADCPs which provide high-accuracy measurements at the cost of a reduced profiling range. Other investigators have implemented modified ADCP configurations (*Vermeulen et al.*, 2011; *Gargett*, 1994). Recent advances in ADCP technology have led to instruments that sample at 8 Hz along a vertical beam that potentially provides more precise estimates of turbulence quantities.

2.2.3 Shear Probes

In the open ocean, in situ turbulence measurements are frequently obtained using airfoil shear probes that consist of an $\mathcal{O}(1)$ cm piezo-ceramic element embedded in a hollow

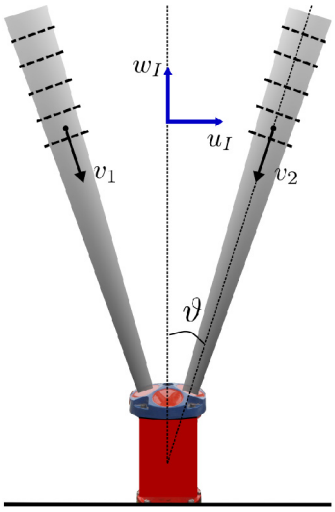

Figure 2.2: Schematic of a diverging-beam acoustic Doppler current profiler where ϑ is the beam angle relative to the vertical axis. Under the assumption of homogeneity, along-beam velocities, v_1 and v_2, can be transformed to instrument coordinates where u_I and w_I are horizontal and vertical components, respectively (Appendix F).

stainless steel support sting (Fig. 2.3a). The probes have a flexible, bullet-shaped, silicone rubber tip that encases the free end of the probe and forms an axially symmetric airfoil. As water flows axially across the probe at speed, U_p, the broadside component of the turbulence velocity, u_b', contributes to the total resultant velocity, U_A. The angle of attack of the flow, θ_A, causes the probe to bend, inducing a voltage, $E_v = s_p U_p u_b'$, that depends on the sensitivity of the probe, s_p. The rate-of-change of the turbulent component is therefore given by

$$\frac{\partial u_b'}{\partial t} = \frac{1}{s_p U_p} \frac{\partial E_v}{\partial t}. \tag{2.38}$$

A measurement of the velocity shear in the axial direction can then be obtained by applying Taylor's Hypothesis (see below).

Shear probes have been used to measure small-scale turbulence in many environments since they were introduced in the 1970s (*Osborn*, 1974; *Lueck et al.*, 2002). They have been mounted on various platforms, including—but not limited to—vertical profilers, mooring lines, gliders, and autonomous underwater vehicles. With low noise levels of $\mathcal{O}(0.001)\,\mathrm{m\,s^{-1}}$ and high sampling rates up to 2048 Hz, shear probes can obtain precise, high resolution measurements. The minimum resolvable length scale is $\mathcal{O}(1)$ mm and is set by the finite size of the probe (*Macoun and Lueck*, 2004). The largest measurable scale is limited by the length of the body upon which the probe is mounted. Larger eddies

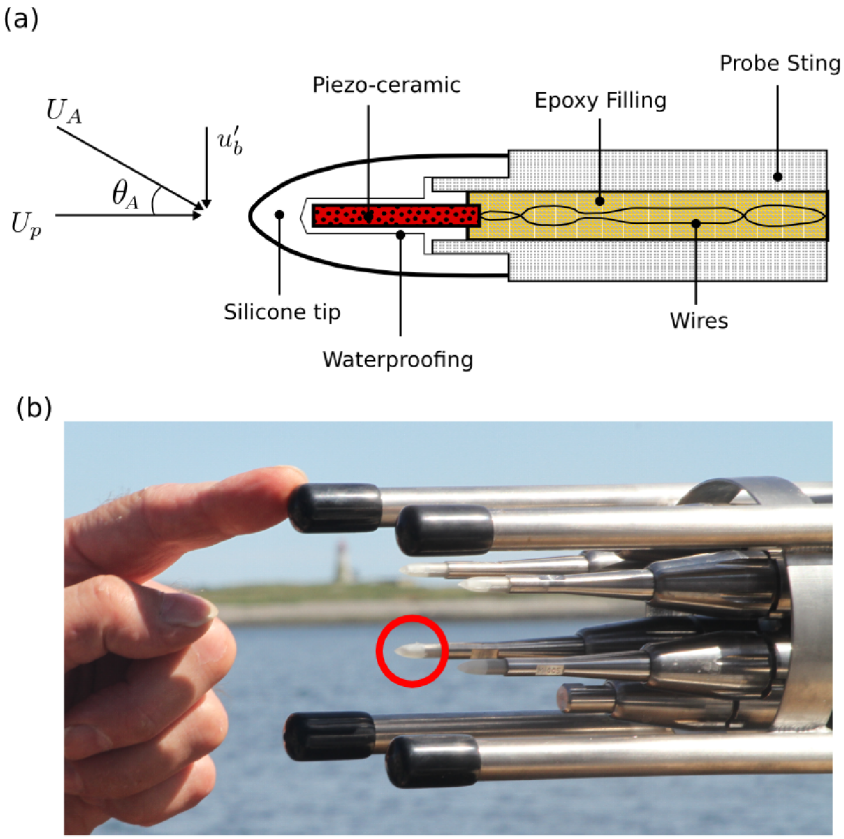

Figure 2.3: (a) Schematic of a shear probe. (b) Picture of a shear probe (red circle) mounted in the nose of a MicroRider.

will simply move the entire body and thus the turbulent fluctuations will not be resolved. These limitations imply that, at high dissipation rates of 10^{-4} W kg^{-1}, the turbulent velocity spectrum can be resolved at the upper end of the inertial subrange as depicted in Fig. 2.1. For lower dissipation rates, the measured spectrum will extend into the viscous dissipation range.

2.2.4 Taylor's Hypothesis

Turbulence properties are often described in terms of spatial scales (i.e., eddy scales); however, the instrumentation used in this study—ADCPs and shear probes—make temporal measurements of fluctuating quantities. Because turbulent eddies evolve slowly in time, the properties of the flow are assumed to be essentially "frozen" as the turbulent field is advected past a sensor by the mean flow. If the measurement interval is short compared to the time-scale of the evolution of the eddies, then Taylor's Frozen Field Hypothesis can be

invoked which allows the time ($\mathcal{T}$) and length scales ($\mathscr{L}$) to be related by

$$\mathscr{L} = |U|\mathcal{T}. \tag{2.39}$$

Taylor's hypothesis is valid provided that $u'^2/|U|^2 \ll 1$, and is thus most applicable for small scale fluctuations.

CHAPTER 3

DATASET

In this chapter, an overview of the study site and the measurement campaigns is provided. The instrument configurations and performance are summarized and the mean flow measurements are discussed. The purpose is to highlight the spatial and temporal variability in the flow because it will aid in the interpretation of the turbulence measurements presented in Chapters 4–7.

3.1 Study Site

Grand Passage, Nova Scotia is located at the mouth of the Bay of Fundy, between Brier Island and Long Island (Fig. 3.1). The passage is about 4 km long and varies in width between 800 m and 2 km. Along the channel centreline, the water depth ranges from ca. 10 to ca. 30 m and there are several bathymetric features that affect the flow. Most notably, a cross-channel ridge ("CC", Fig. 3.1) near the northeast entrance to the passage generates pronounced ebb/flood asymmetry in the turbulence characteristics (*Hay et al.*, 2013). In addition, Peter's Island, which is located at the southern end of the passage ("PI" in Fig. 3.1), generates large eddies that are advected downstream during strong tides.

The tidal range in Grand Passage is approximately 5 m, with the M_2 constituent having the largest amplitude. The flow is highly turbulent with maximum depth-averaged speeds reaching $2.5\,\mathrm{m\,s^{-1}}$ (Fig. 3.2) and Reynolds numbers up to 8×10^7. The current flows northward on the flood tide and southward on the ebb and is nearly rectilinear in the centre of the passage. The water density varies on both seasonal and tidal timescales; however, at any given time, the water column is predominantly unstratified. CTD measurements in July 2012 revealed a maximum density difference of $0.25\,\mathrm{kg\,m^{-3}}$ over the entire water

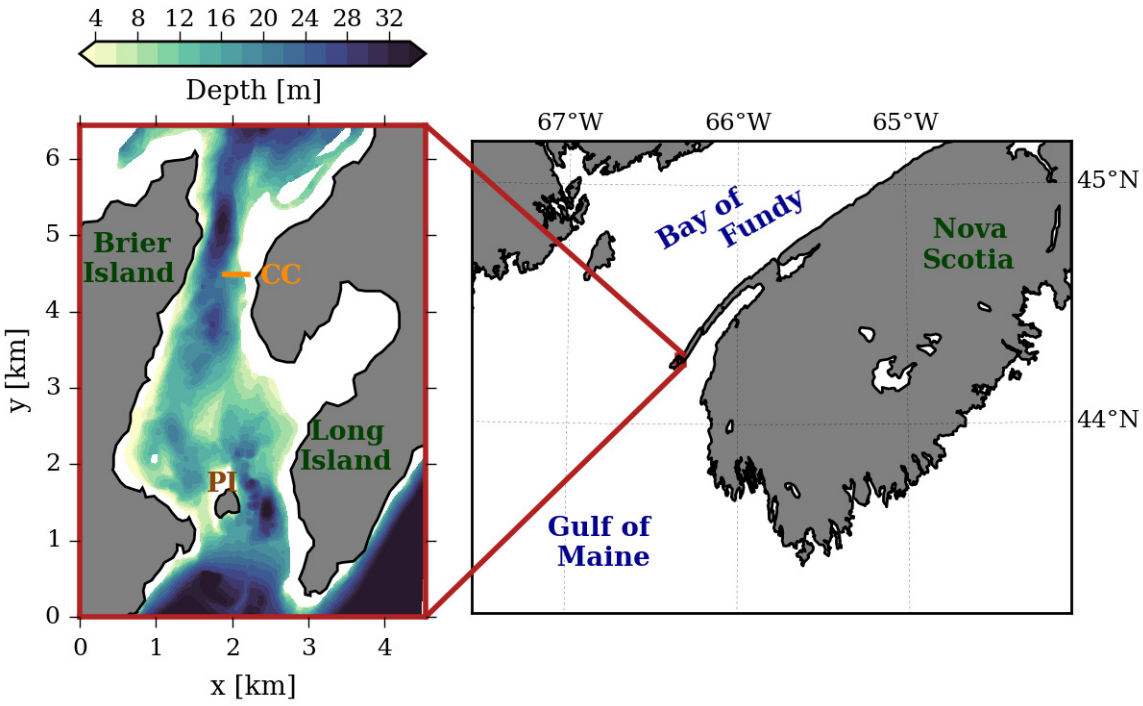

Figure 3.1: Grand Passage location and bathymetry. In the left panel, "PI" is an abbreviation for "Peter's Island" and "CC" highlights the location of a cross channel ridge.

column (*Malinka*, 2013).

The passage is sheltered from easterly and westerly winds, and opens into fetch-limited basins to the north and south, such that surface waves tend to be small, especially during the summer. While waves did not dominate the variability in the flow during the measurement campaigns, they were occasionally observed—typically when the current opposed the wind. The identification of surface waves is summarized in Appendix C. For this thesis, data and results affected by wave motion were either rejected or flagged and the dynamics associated with wave-current interactions were not investigated.

3.2 Turbulence Measurements

3.2.1 Bottom-Mounted ADCP Frames

Four bottom-pods carrying one or more acoustic Doppler profiling instruments and an RBR Ltd. pressure sensor were deployed near the northern extent of Grand Passage (Fig. 3.3) during three distinct measurement campaigns in 2012 and 2013. The duration of the deployments varied between 3 and 18 days (Table 3.1) and the naming convention follows

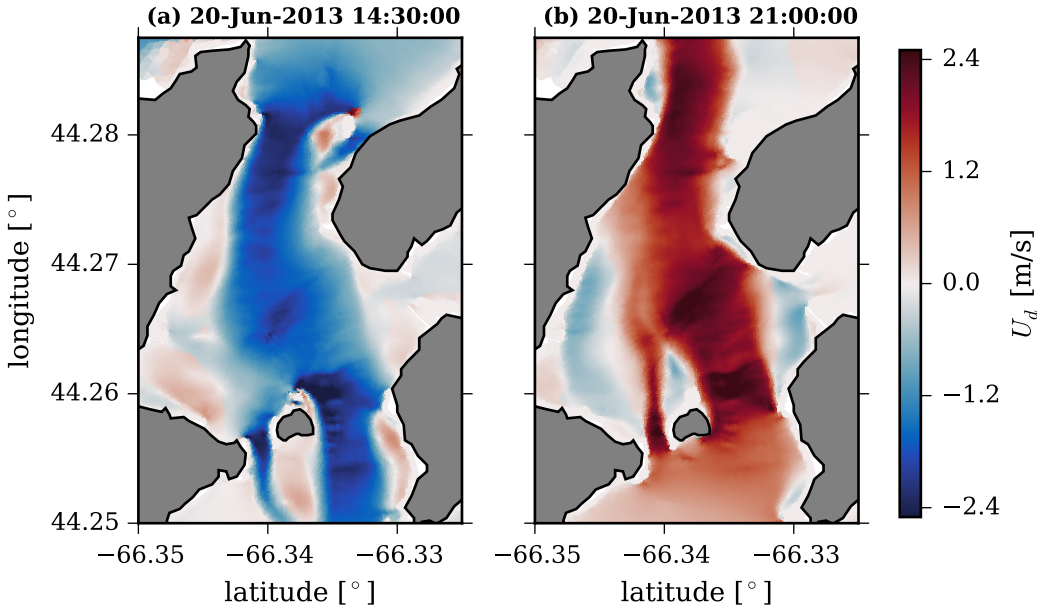

Figure 3.2: Snapshots of the depth-averaged flow speed as simulated by a 2D Finite Volume Coastal Ocean Model during an (a) ebb tide, and (b) flood tide. Positive and negative speeds correspond to northward and southward flows, respectively.

sites labelled sequentially from north to south, with Sites 2a and 2b identifying pods that were deployed concurrently. Each of the low-profile frames were ballasted using three 45-kg lead feet and were constructed from solid fibreglass rods and a fibreglass grating base (Fig. 3.4a). They were retrieved using an acoustic release and float line recovery system.

A 600 kHz RDI Workhorse ADCP was mounted in the centre of each frame. The ADCPs, with four beams oriented at 20° from the vertical (Janus configuration), recorded two-ping averaged along-beam velocities at sampling rates between 1.49 and 1.82 Hz (Table 3.1). The ADCP at Site 1 operated in burst mode to avoid interference with another acoustic instrument mounted on the frame. At this site, approximately 7 minutes of data were collected every 15 minutes. At the other sites, the measurements were acquired continuously. The ADCPs were configured to have 0.5-m range bins with the first bin located 2.1 m above the bottom and the uppermost bin extending beyond the surface at high tide. For these settings (i.e., 0.5-m range bins and 2-ping ensembles), the manufacturer's software specifies an accuracy of $\sigma_U = 9.6$ cm s^{-1} for the horizontal speed, thus the expected accuracy for the along-beam measurements is $\sigma_{v_i} = (\sqrt{2}\sin\vartheta)\sigma_U = 4.7$ cm s^{-1}.

At Site 1, a beta version of the Nortek 1 MHz *Signature 1000* AD2CP (henceforth

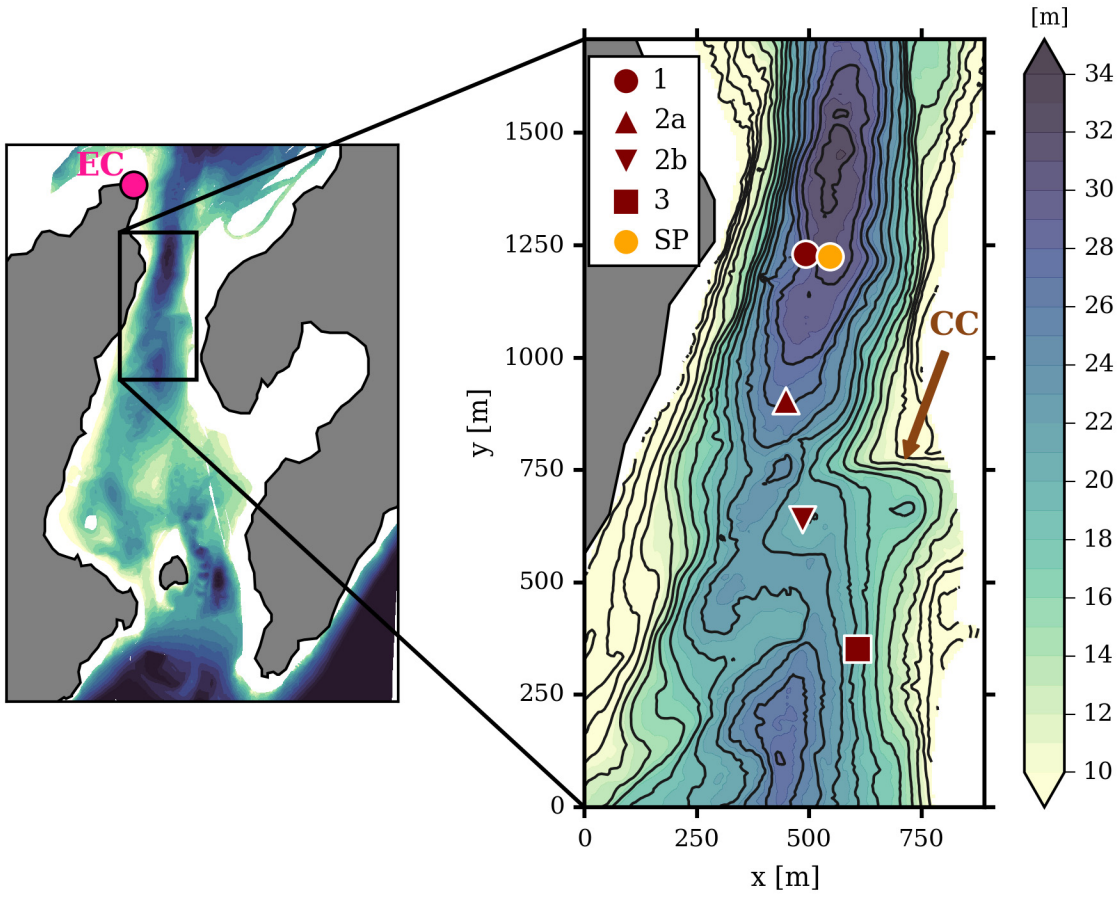

Figure 3.3: Detailed map of the bathymetry in Grand Passage. In the right panel, the cross-channel (CC) ridge is highlighted and the instrument locations are represented by the symbols. Maroon markers correspond to the ADCP deployments and the orange circle is the location where the shear probes (SP) were deployed as part of the *Nemo* turbulence system. Contours (black) are in 2 m intervals. In the left panel, the pink marker shows the position of Environment Canada's (EC) meteorological station.

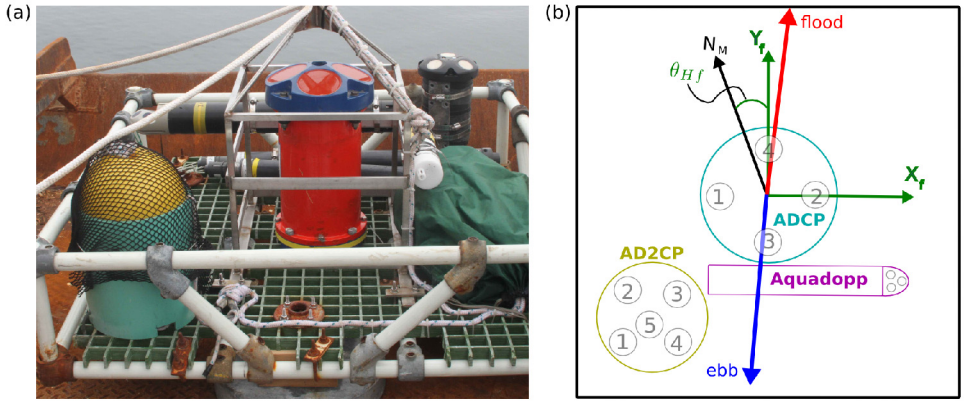

Figure 3.4: (a) Photograph of the bottom-mounted ADCP frame at Site 1 which contains both the ADCP (orange, centre) and the AD2CP (black, back right). (b) The orientation of the frame with respect to magnetic north (N_M) is shown with the frame coordinates denoted by the green arrows. The circled numbers on the instruments correspond to the transducer faces for the diverging beams. The principal direction of the depth-averaged flood and ebb currents are shown by the red and blue arrows, respectively.

referred to as the AD2CP) was also mounted on the bottom pod (Fig. 3.4a) and operated for 3.5 days before its battery died. The AD2CP has five transducers, with four beams diverging at 25° from the vertical and one beam oriented vertically. The four divergent beams recorded along-beam velocities at 1 Hz in forty 0.5-m range bins with the first bin located 0.6 m above bottom. The vertical beam was sampled at 8 Hz in forty 12.5-cm range bins to provide high resolution measurements of vertical velocity over the lowest 5 m of the water column. The AD2CP operated in burst mode with five minutes of data collected every fifteen minutes.

A Nortek Aquadopp was also installed on the frame at Site 1. Its heading measurements were used to determine the orientation of the frame (Fig. 3.4b and Fig. 3.6a) because the compasses on both the ADCP and the AD2CP failed to calibrate properly. At the time of deployment, the AD2CP did not have a battery calibration protocol and the ADCP would not calibrate with its installed battery.

3.2.2 The *Nemo* Moored Turbulence System

Between 06 and 08 August 2013, a streamlined, instrumented underwater buoy (Fig. 3.5a) was deployed about 40 m east of the ADCP frame at Site 1 (Fig. 3.3, orange marker). The entire system, consisting of the buoy and its instrumentation is referred to as *Nemo*. The coordinate system is aligned with the body of the buoy: $+x_N$ points forward into the

Table 3.1: Summary of the fast-sampling RDI 600 kHz ADCP deployments in the northern region of Grand Passage.

Site	Start Date	Long. (deg)	Lat. (deg)	Depth (m)	Duration (days)	Sample Rate (Hz)	Sampling Method
1	2013-07-30	-66.3391	44.2799	28	7[†]	1.49	Burst
2a	2013-06-27[*]	-66.3395	44.2778	29	11.5	1.67	Continuous
2b	2013-06-27[*]	-66.3391	44.2761	23	11.8	1.67	Continuous
3	2012-09-04	-66.3380	44.2743	22	3	1.82	Continuous

[†] The ADCP was deployed for 9 days, but the last two days were omitted from analysis due to low correlations.

[*] The ADCPs were deployed 7 days earlier, but shifted after 1 week. The most stable interval was chosen for analysis.

oncoming flow, $+y_N$ is to port, and $+z_N$ is nominally upward (Fig. 3.5b, inset). A similar system was used by *Fer and Paskyabi* (2014) in the calm waters of a Norwegian fjord and by *Lueck et al.* (2015) in an energetic tidal channel in Scotland.

The buoy is about 4.5 m long and composed mostly of syntactic foam. *Nemo* had a net buoyancy of 1334 N and was "flown", kite-like, at a nominal height of 10 m (Fig. 3.5b). The buoy was free to rotate about both its horizontal and vertical axes allowing it to pivot into the oncoming flow. Due to a design error, it was necessary to add weight to the front of the buoy and flotation to the back. This shifted the centres of mass and buoyancy so that the net torque about the yoke axle was near zero.

Nemo carried three main instrument systems to measure the characteristics of the turbulent flow: a Rockland Scientific MicroRider in the nose (Fig. 3.5a, #1), a Nortek acoustic Doppler velocimeter (ADV) attached to the top (Fig. 3.5a, #2); and a downward-looking Nortek *Signature 1000* AD2CP (beta version) just aft of the yoke axle (Fig. 3.5a, #7). A battery pack, powering both the MicroRider and the ADV, was mounted in the cavity just aft of the ADV. The ADV electronics and pressure sensor were located immediately forward of the lifting ring. A satellite beacon and a JFE Avantech electromagnetic current meter were also installed. The data from the electromagnetic current meter were in general agreement with the ADV data, but they were not used for further analysis.

The MicroRider was the primary turbulence sensor onboard *Nemo*. This self-contained instrument carried a fast-response thermistor probe and four airfoil shear probes that had the "mantle" design described by *Macoun and Lueck* (2004). Two probes sensed the

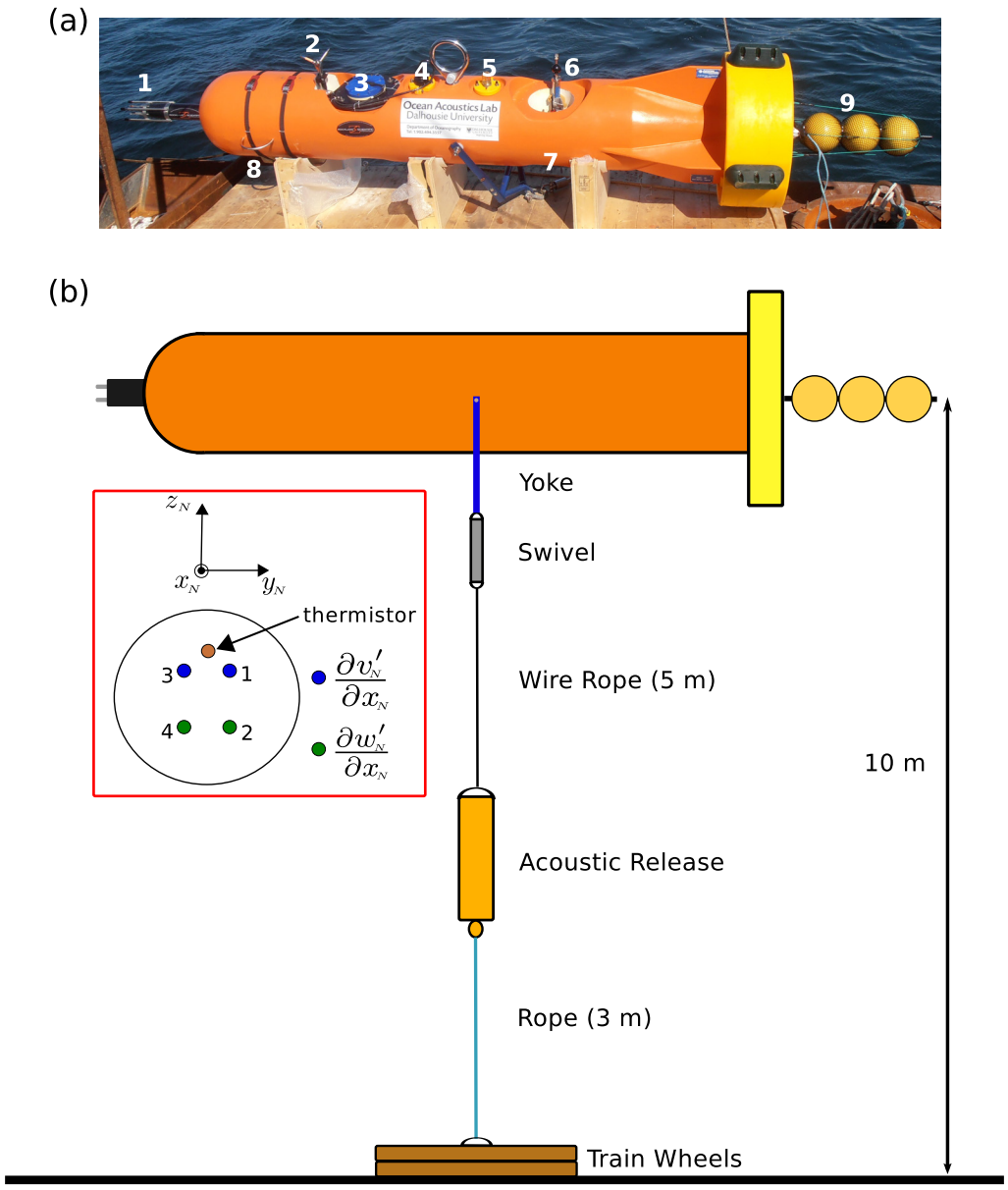

Figure 3.5: (a) A photograph of the *Nemo* turbulence measurement system prior to deployment. The numbers correspond to the on-board instrumentation and components: (1) MicroRider, (2) ADV, (3) battery pack, (4) ADV pressure transducer, (5) satellite beacon, (6) electromagnetic current meter, (7) AD2CP, (8) extra lead weight, and (9) flotation buoys. (b) A schematic of the mooring line used to anchor *Nemo*. The inset in the red box shows the coordinate system as viewed facing the MicroRider and the positions and orientations of the shear probes.

z_N-component of velocity shear fluctuations and two sensed the y_N-component (Fig. 3.5b). Two vibration sensors with their axes of sensitivity aligned with those of the probes were used to measure the inertial accelerations of the shear probes, so that vibration-related contamination could be removed from the shear probe signals. The thermistor, shear probes and the vibration sensors were all sampled at a rate of 2048 Hz.

The MicroRider also contained several other sensors that measured the motion of *Nemo* at a sampling rate of 256 Hz. The mean water depth and heaving motion of the buoy were obtained using a pressure transducer. The system's pitch and roll were measured using a high-accuracy two-axis inclinometer and the yaw was obtained using a magnetometer. A three-axis rotation rate sensor and a three-axis accelerometer were also contained within the MicroRider.

The ADV was used to obtain a measurement of the mean flow speed past *Nemo*. Results from previous experiments in Grand Passage (*Hay et al.*, 2013) indicated that high water clarity and a lack of scatterers resulted in low echo correlation values at high sampling rates, thus the ADV was sampled at the minimum rate of 1 Hz. The ADV was set to use the maximum transmit power, maximum transmit pulse length (8 mm) and maximum sampling volume (22 mm). The ADV was mounted on the buoy such that its velocity components were aligned with the *Nemo*-defined coordinate system (x_N,y_N,z_N).

The downward-looking 1 MHz AD2CP was operated in bottom tracking mode with the vertical beam sampling at 8 Hz and the diverging beams sampling at 1 Hz. The size of the range bins was 0.5 m with the centre of the first bin located 0.1 m from the transducers.

3.3 Instrument Performance and Data Quality

3.3.1 Bottom-Mounted ADCP Frames

The bottom-pods at all four sites remained fairly stable throughout the deployments, however, some movement did occur, particularly during strong spring tides. The analysis interval was therefore chosen to be the longest period over which the pods were stable. The attitude parameters (heading, pitch and roll) as measured by the RDI ADCPs are plotted in Appendix B and the averages for the analysis intervals are summarized in Table 3.2. The orientation of the ADCPs relative to true north (0°) is shown in Fig. 3.6.

Ensemble averages of the correlation and backscatter amplitude of the ADCP measurements were computed for each 7-minute burst (Site 1) and 5-minute interval (Sites

Table 3.2: Summary of the attitude parameters for the ADCP deployments.

Site	θ_H (°)	θ_P (°)	θ_R (°)
1	202.5 ± 0.4	3.87 ± 0.05	-4.40 ± 0.10
2a	342.8 ± 0.3	-3.31 ± 0.10	-7.02 ± 0.05
2b	196.0 ± 0.2	3.80 ± 0.02	2.55 ± 0.01
3	289.5 ± 0.3	-7.88 ± 0.03	0.30 ± 0.03

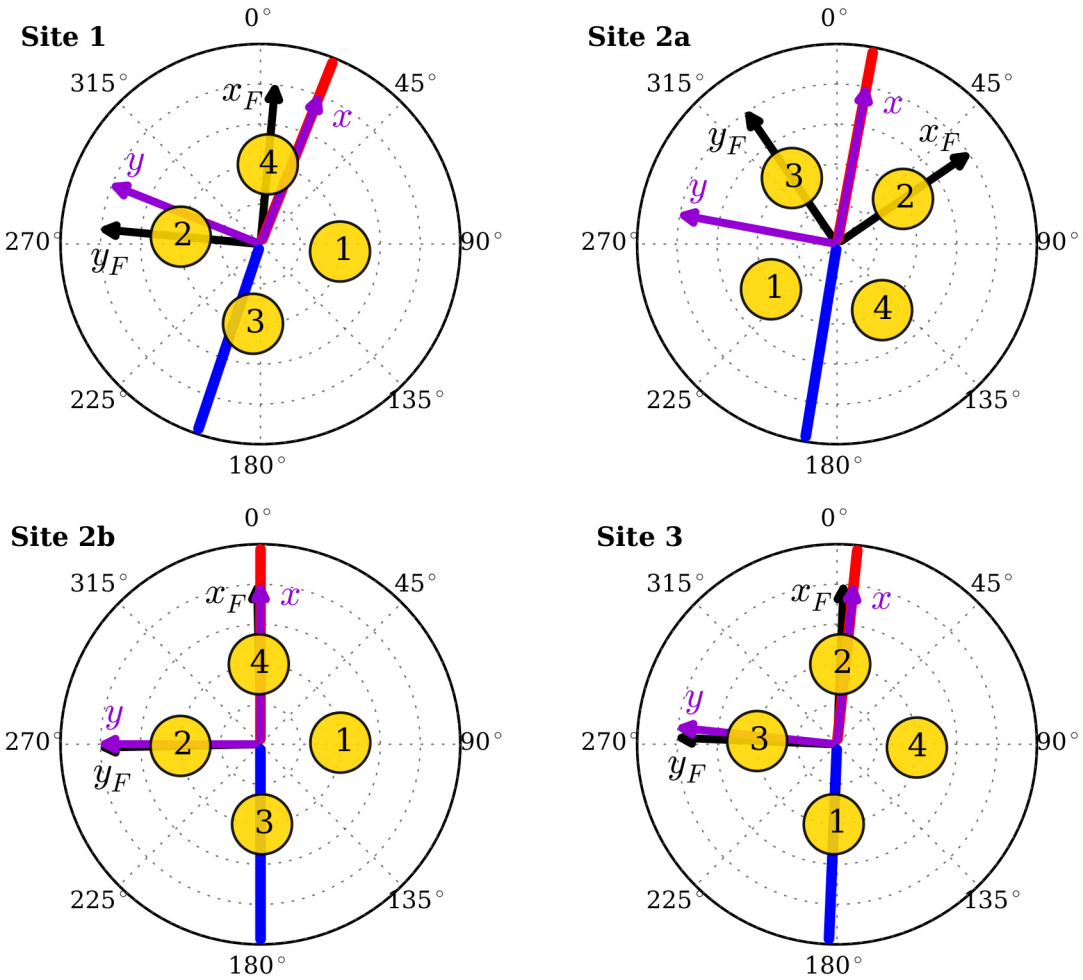

Figure 3.6: Instrument orientation relative to true north (0°). Principal flow directions of the depth-averaged velocity, U_d, are shown in red and blue for the flood and ebb tides, respectively. The site-dependent coordinate system (x, y) is shown in purple and the frame coordinate system (x_F, y_F) is shown in black (Appendix F). The transducer faces are indicated by the yellow circles, and numbered according to the RD Instruments convention.

2a, 2b, 3). The averages were used to qualitatively assess data quality. At all sites, the mean correlations for all four beams were typically within 95% of the level expected (128 counts) for high-quality velocity estimates (*Gordon*, 1996), which indicates that there was sufficient signal-to-noise ratio to generate high-fidelity ADCP data. The backscatter amplitude decreased with height above bed, as expected, due to transmission losses; however, the signal was always strong enough for high fidelity measurements. The variation of the backscatter amplitude and correlation as a function of flow speed at 10 m above bottom is included in Appendix B. Sporadically, there were instances of low correlations within one or more of the beams (not shown) which is likely associated with the presence of seaweed, or some other transitory obstruction, on the transducer face. These measurements were flagged and removed from subsequent analysis.

The AD2CP measurements at Site 1 were also of high quality with 4% of the flow data being rejected due to erroneous measurements (identified by the error flag generated by Nortek's software). However, spectra of the roll angles measured during ebb tides had a significant peak near 0.1 Hz, possibly caused by the vibration of the instrument due to an unstable mounting bracket. The enhanced vibrations on the ebb tide—compared to the flood—were likely generated because, on the ebb tide, the AD2CP was in the wake of the ADCP (Fig. 3.4a). Due to the poor data quality on the ebb tide, only the flood tide measurements were used to estimate turbulence parameters from the AD2CP data.

3.3.2 *Nemo* Buoy

The average flow speed, u_N, past the buoy was computed in two-minute ensembles from the ADV data, discarding measurements with correlations below 70%. The maximum speed on both the flood and ebb tides reached approximately 2.2 m s^{-1} (Fig. 3.7a). Velocity measurements from the second range bin of the downward looking AD2CP were only 5% less than the ADV measurements (not shown), confirming that the ADV measurement volume was positioned outside of the boundary layer of the buoy and therefore provided an accurate measurement of the upstream flow speed.

The bearing computed from the MicroRider magnetometer (Fig. 3.7a) indicates that the buoy spun around quickly at the turn of each tide (approximately 10 minutes for a full 180° rotation). The MicroRider roll angle remained nearly constant throughout the deployment with an average value of $6.4 \pm 0.5°$ (Fig. 3.7b, θ_X). This uniform deviation from zero is an artifact caused by a misalignment in the mounting of the MicroRider, confirmed by the

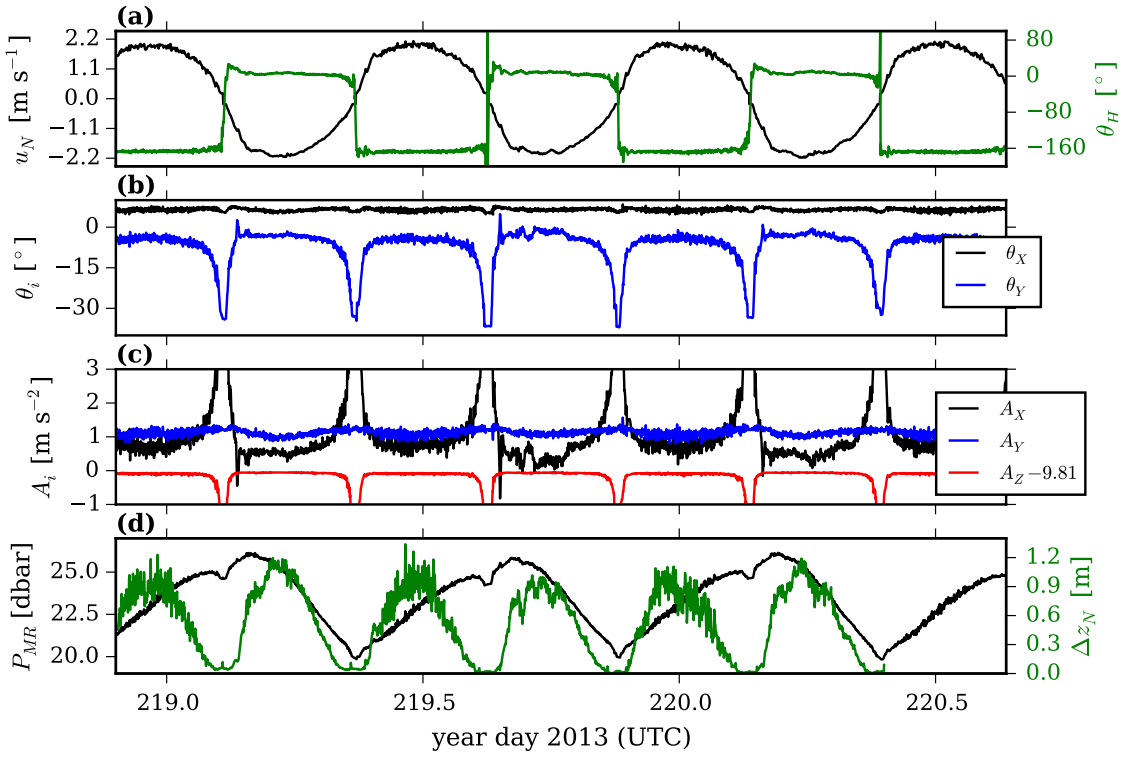

Figure 3.7: Timeseries of the performance of *Nemo* throughout its deployment. (a) The signed flow speed, u_N, registered by the ADV with positive representing flood (northward) flow and negative representing ebb (southward) flow. The bearing angle of the buoy as determined from the MicroRider magnetometer is plotted in green. (b) The pitch, θ_Y, and roll, θ_X, angles from the MicroRider inclinometers. (c) MicroRider accelerometer records. (d) The MicroRider pressure measurements (black) and the estimated blow-down distance of the *Nemo* (green).

mean roll of $0.3 \pm 0.4^\circ$ of the downward looking AD2CP . The MicroRider pitch angle, on the other hand, was strongly correlated with flow speed, varying from ca. -4° during strong flows to ca. -35° at slack water (Fig. 3.7b, θ_Y). During flows stronger than $0.7\,\mathrm{m\,s^{-1}}$, the magnitude of the pitch angle was typically less than 10°. The sense of rotation for the right-handed coordinate system is such that a negative pitch angle corresponds to the nose of the buoy being above the tail.

The MicroRider accelerometer signals, which are composed of the sum of inertial and gravitational acceleration, are small in all three directions and have mean values of 0.7, 1.1 and $-0.08\,\mathrm{m\,s^{-2}}$ for A_X, A_Y and $A_Z - 9.81$, respectively. These means are consistent with the inclinometer signals. There were some short time scale fluctuations, however, these motions did not contaminate the shear probe signals as they were removed from the shear spectra using a cross-correlation technique (*Goodman et al.*, 2006).

The mean water depth above the buoy was estimated from the MicroRider pressure data, P_{MR} (Fig. 3.7d, black line). Near slack water, abrupt pressure drops of approximately 0.5 dbar correspond to the ca. 35° pitching motion of the buoy with the nose (and hence the pressure sensor) being above the tail (Fig. 3.7d). During strong flows, the buoy experienced significant "blow-down" due to flow-induced drag. The associated vertical displacement of the buoy, Δz_N, was estimated by first removing the dominant tidal signal using the pressure measurements obtained at the ADCP frame, and then calculating the mean water depth above the axle location, taking into account the pitch angle of the buoy. The resulting Δz_N estimates (Fig. 3.7d, green line) indicate that, at maximum flow, the vertical displacement was about 1 m, corresponding to a maximum mooring line angle of about 26° from the vertical.

To avoid possible contamination of the measurements by buoy tilt, data for which the absolute pitch, $|\theta_Y|$, of *Nemo* was greater than 10° were rejected. This resulted in the removal of 15% of the measurements. However, the buoy inclination was less than 10° for 99% of the measurements at flow speeds greater than $0.8\,\mathrm{m\,s^{-1}}$.

3.4 Mean Flow

3.4.1 Methods

Depending on the sampling scheme, ensemble averages of the ADCP velocity measurements were computed for each 7-minute burst (Site 1) or 5-minute interval (Sites 2a,

2b, and 3). The along-beam velocities were transformed into earth coordinates (i.e., east-north-up), and a signed horizontal current speed, U, was defined as

$$U = \pm\sqrt{u_E^2 + u_N^2}, \tag{3.1}$$

where u_E and u_N are the eastward and northward velocities, respectively. The sign is used to distinguish between flood (positive) and ebb (negative) tides. The depth-averaged flow speed, U_d, and its variance, $\sigma_{U_d}^2$, were computed by vertically averaging from the lowest range bin to 95% of the total water depth. The principal direction of U_d was determined using empirical orthogonal functions for flow speeds greater than $0.5\,\mathrm{m\,s^{-1}}$.

Vertical profiles of the flow speed were determined by sorting the data into $0.2\,\mathrm{m\,s^{-1}}$ speed bins based on a reference speed U_r measured at $z = 10$ m above bottom. A non-linear least squares best fit to the law-of-the-wall (Eq. 2.12) was performed for $z < 6\,\mathrm{m}$ to determine u_* and z_0. The bottom drag coefficient, C_d, was then estimated from the least-squares regression of

$$u_*^2 = C_d U_{1m}^2, \tag{3.2}$$

where U_{1m} is the speed at 1 m above bottom based on the fitted profile.

Time-variability in the three-dimensional velocity field was examined by introducing a site-specific coordinate system defined such that u was directed along the principal axis of U_d on the flood tide (Fig. 3.6). The transverse, v, and vertical, w, velocities were such that a right-handed coordinate system was obtained with $+w$ opposing the direction of gravity.

3.4.2 Results

The properties of the mean flow are highly site-dependent and occasionally exhibit pronounced ebb/flood asymmetry. The variability can be attributed largely to differences in the upstream bathymetry at each site. High-resolution bathymetric data were used to compute transects of the water depth in the principal flow direction (Fig 3.8).

A discussion of the mean flow dynamics at each site follows. The properties defined in the previous section are illustrated in Figs. 3.9 and 3.10. The time series that are shown span one-day intervals where the subset of data is highlighted by the yellow boxes in Appendix B. The principal directions, speed-bin averaged velocity profiles, and bottom drag coefficients were determined using the entire analysis interval (Table 3.1).

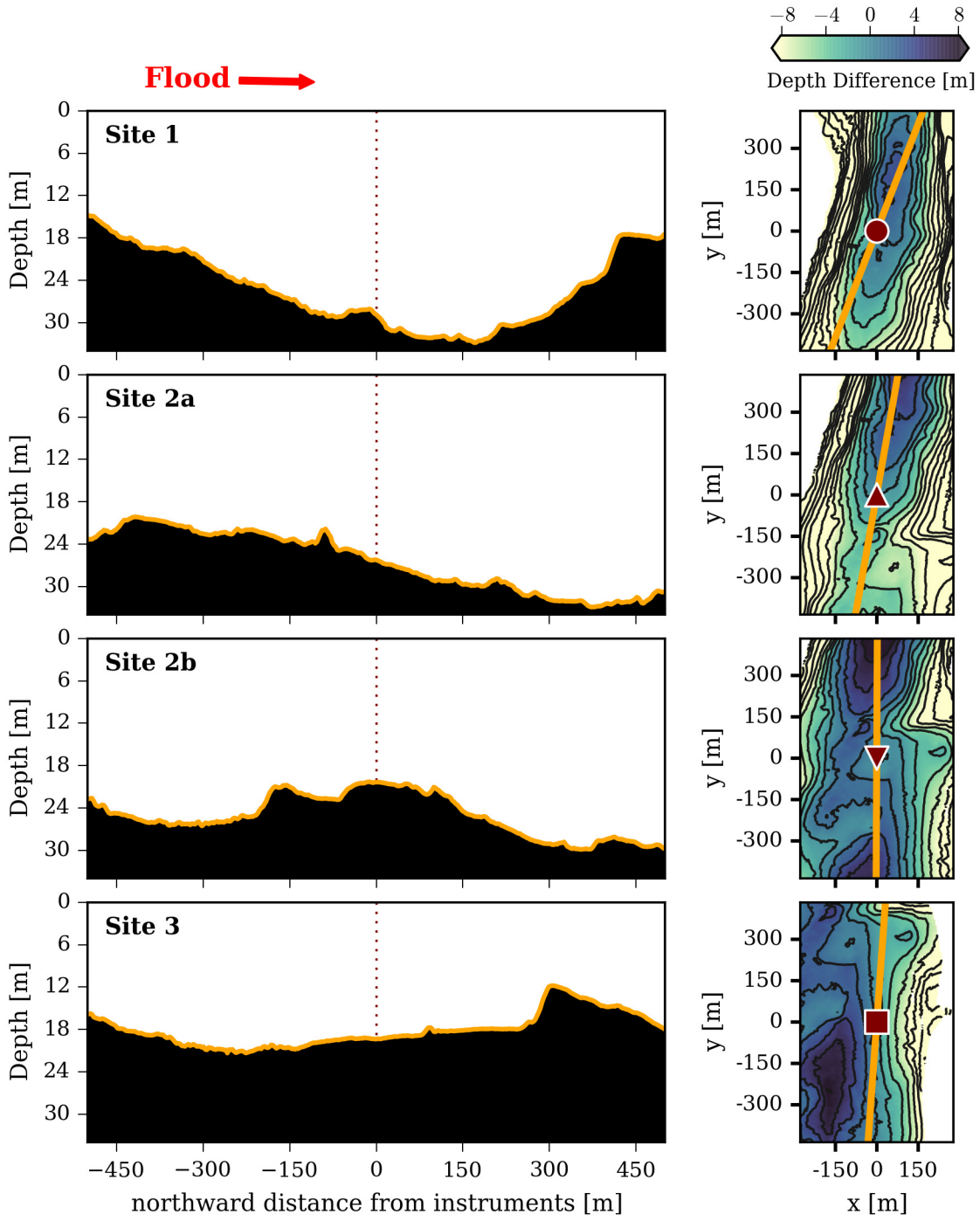

Figure 3.8: (Left panels) Bathymetry transects in the principal flow directions. Flood and ebb tides propagate to the right and left, respectively. (Right panels) Local bathymetry near the instrument sites, where the black contour lines are in 1 m intervals about the low-low-water depth at the ADCP site. The yellow line represents a section of the transect path shown in the corresponding left panel.

Site 1

At Site 1, the ADCP frame was situated toward the western side of the passage where the mean water depth is 28 m. The recorded GPS position indicates that the ADCP was deployed on a downward slope on the flood tide (Fig. 3.8); however, a note in the lab book indicates that the position was logged a few minutes before the instrument frame hit bottom. Because the vessel was drifting during deployment, it is possible that the actual position of the ADCP was different by several tens of metres.

The depth-averaged current speed at Site 1 reaches a maximum of 2.0 m s^{-1} on the flood tide, and 2.1 m s^{-1} on the ebb tide (Fig. 3.9a). There is little variation in the flow direction (Fig. 3.9i) and the principal directions on the ebb and flood tides are within 1° of being perfectly bidirectional (i.e., 180° out of phase). The depth-averaged variance, $\sigma^2_{U_d}$, is almost four-fold larger on the flood tide than on the ebb (Fig. 3.9e), likely due to strong flow passing over the complex bathymetry to the south of the site (Fig. 3.3).

The ebb/flood asymmetry in the flow is also apparent in the speed-bin averaged velocity profiles (Fig. 3.11). On the flood tide, the logarithmic boundary layer extends beyond $z = 18$ m, whereas it is limited to 5–6 m above bottom on the ebb tide. The corresponding drag coefficients are 5.6×10^{-3} and 14.8×10^{-3} on the flood and ebb tides, respectively (Table 6.1).

Time series of the three-dimensional velocities are illustrated in Fig. 3.10. As expected for strong tidal flow, u is near-uniform with depth, with a maximum magnitude of approximately 2.1 m s^{-1} near the surface (Fig. 3.10a). The magnitude of v is small throughout the water column reaching a maximum of 0.25 m s^{-1} (Fig. 3.10e). On the flood tide, v is negative near the bed and positive near the surface, indicating a slight counterclockwise veering of the current with height above bottom; whereas, on the ebb tide, a consistent pattern in v over all tidal cycles was not observed. The vertical velocity, w, is positive on the flood tide and negative on the ebb, and has a typical magnitude of about 0.10 m s^{-1} throughout the water column (Fig. 3.10i). The direction of the vertical flow is inconsistent with the local bathymetric gradient, indicating that the recorded location of the ADCP may be inaccurate.

Site 2a

At Site 2a, the ADCP was situated in the centre of the passage, about 150 m northwest of the cross-channel (CC) ridge. The bathymetry transect (Fig. 3.8) indicates that there is

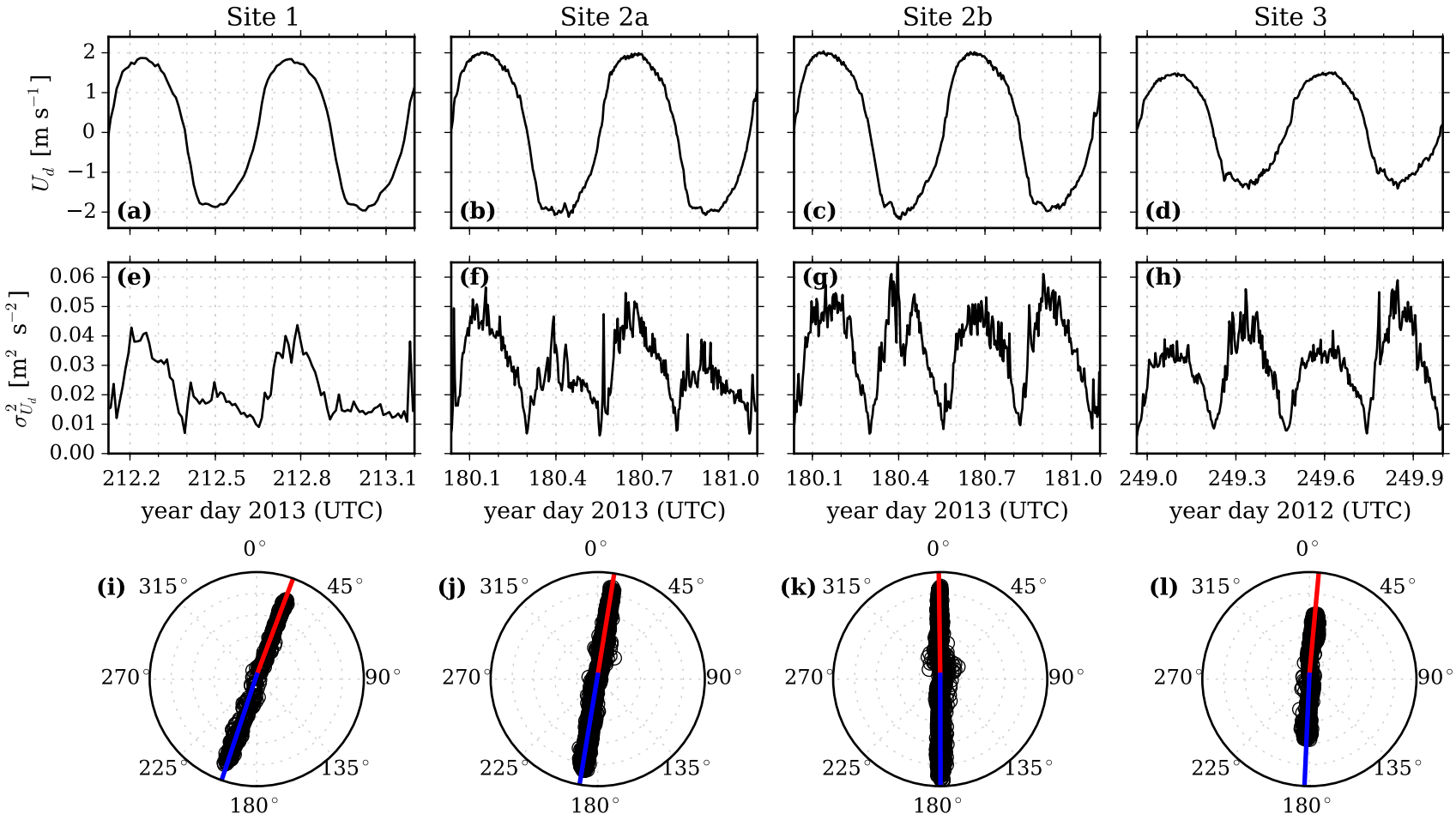

Figure 3.9: Time series of the signed, depth-averaged speed, U_d, and its variance, $\sigma^2_{U_d}$, are shown in the top and middle rows, respectively. Compass plots of the eastward and northward velocities are shown in the bottom row (true north corresponds to 0°). The red and blue lines represent the principal directions for $|U_d| > 0.5$ m s^{-1} on the flood and ebb tides, respectively.

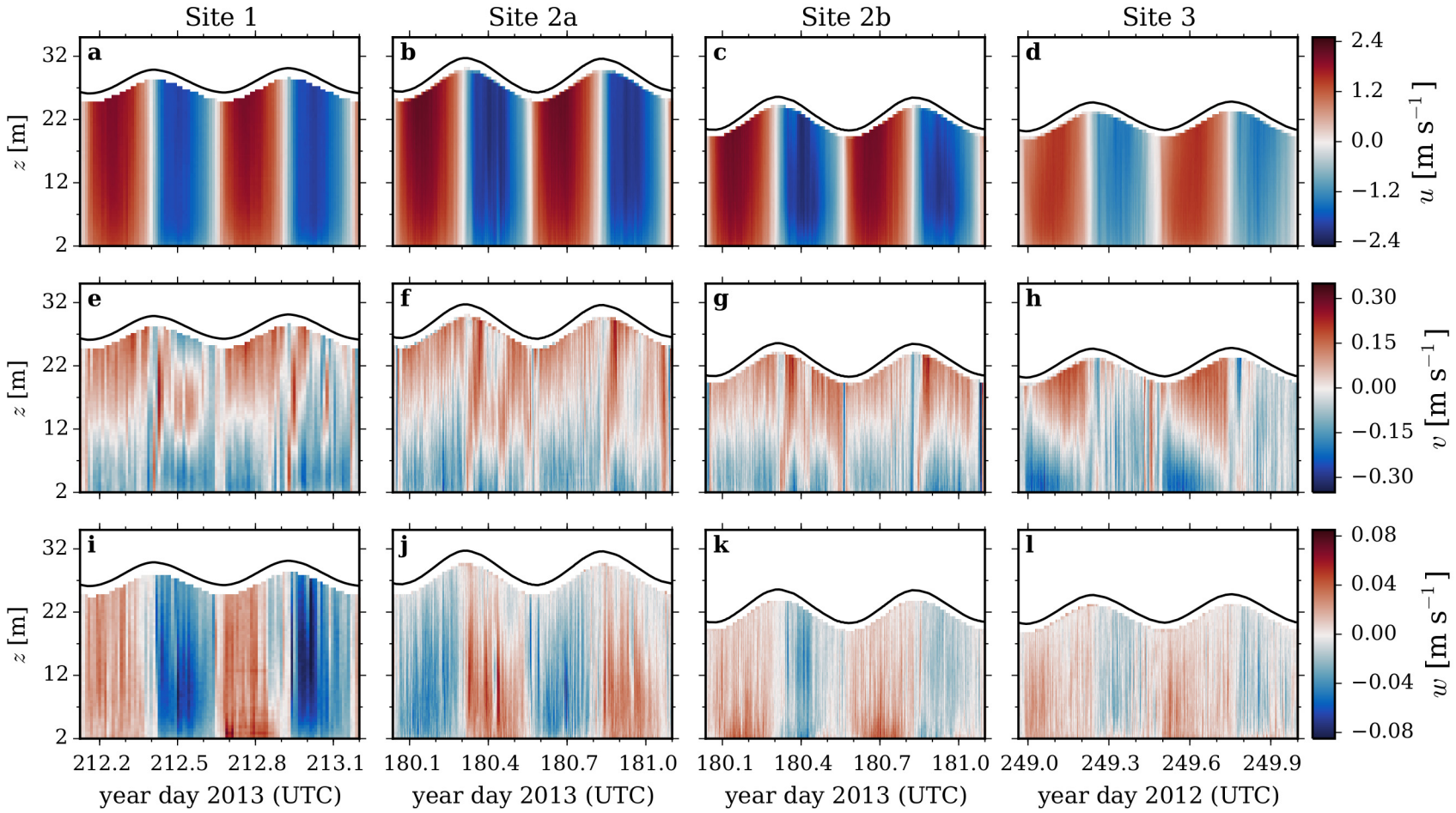

Figure 3.10: Time series of the streamwise (u), lateral (v), and vertical (w) velocities.

also a 2 m ridge located 90 m upstream of the site on the flood tide.

The depth-averaged current speed reaches 2.2 m s^{-1} on both the flood and the ebb tides (Fig. 3.9b), and the principal directions are within 1° of being bidirectional (Fig. 3.9j). The depth-averaged variance is approximately a factor of two higher on the flood tide compared with the ebb (Fig. 3.9f), which is consistent with the asymmetry at Site 1, but of smaller magnitude.

The speed-bin averaged velocity profiles are logarithmic to about 8 m on the ebb and beyond 22 m on the flood (Fig. 3.11). Fits to the law-of-the-wall yield drag coefficients of 8.5×10^{-3} and 9.9×10^{-3} on the flood and ebb tides, respectively (Table 6.1).

Time series of the three-dimensional velocities reveal very strong near surface currents with the maximum in u reaching 2.2 m s^{-1} (Fig. 3.10b). The transverse velocities on the flood tide have a similar tendency as observed for v at Site 1—i.e., the current veers slightly counterclockwise with height above bed (Fig. 3.10f). On the ebb tide, the pattern in v is negative near the bed, positive at mid-depth and then negative again near the surface. During some ebb tides (e.g., day 180.9), v is strongly positive near the surface. Vertical velocities are fairly uniform throughout the water column (Fig. 3.10j). The direction of the flow is predominantly downward on the flood tide and upward on the ebb, consistent with the local bathymetry shown in Fig. 3.8.

Site 2b

Site 2b is situated on a relatively flat region about 60 m southwest of the CC ridge (Fig. 3.8). There is also a prominent feature located approximately 200 m to the south of the site.

The depth-averaged current speed is slightly stronger on the ebb tide reaching a maximum of 2.4 m s^{-1}, compared to 2.2 m s^{-1} the flood (Fig. 3.9c). The variability in the flow direction is very small and the principal axes are directed to true north and true south on the flood and ebb tides, respectively (Fig. 3.9k). The variance in the depth-averaged flow is high on both phases of the tide, reaching 0.05 m^2 s^{-2} (Fig. 3.9g).

Despite the ebb/flood symmetry in $\sigma^2_{U_d}$, the velocity profiles are shaped differently on each phase of the tide. During the flood tide, the logarithmic region extends toward the surface, whereas the log-layer is terminated near $z = 5 - 6$ m on the ebb. The drag coefficients are 4.4×10^{-3} and 15.4×10^{-3} on the flood and ebb tides, respectively (Table 6.1). Interestingly, on the ebb tide, the flow speed near the surface is slower than that at mid-depth due to the entrainment of slower surface water to the northeast of the site

(see Chapter 6).

The three-dimensional velocity measurements indicate streamwise velocities that reach 2.3 m s^{-1} (Fig. 3.10c), and transverse velocities that are slightly westward near the surface and eastward at depth (Fig. 3.10g). Consistent with Sites 1 and 2a, the cross-channel currents are more irregular on the ebb tide. As expected based on the bathymetry, the vertical velocities are weak (Fig. 3.10k). Upwards flow is observed on the flood tide, and downward on the ebb, consistent with the local bathymetric gradient.

Site 3

Site 3 is located about 300 m due south of the CC ridge on a flat region where the bathymetric contours are nearly parallel with the principal flow direction. The water depth is approximately 20 m and the bathymetry slopes downward toward the west.

The depth-averaged speed reaches a maximum of 1.5 m s^{-1} on the flood tide and 1.4 m s^{-1} on the ebb tide (Fig. 3.9c), making Site 3 the least energetic of the ADCP deployment locations. There is very little variation in the flow direction and the principal axes are approximately 2.5° from being perfectly bidirectional (Fig. 3.9l). The variance in the depth-averaged flow is typically 0.03 m^2 s^{-2} on the flood tide and 0.05 m^2 s^{-2} on the ebb (Fig. 3.9h). The increased variability on the ebb tide is generated because the flow passes over the CC ridge, which is located upstream of the site.

The velocity profiles have the opposite asymmetry relative to the other sites. On the ebb tide, the logarithmic layer extends beyond $z = 18$ m for all speed-bins except for $U_r = 1.4$ m s^{-1}, where the log-layer terminates around $z = 12$ m. On the flood tide, the logarithmic layer is present only in the lowest 5-6 m, whereas there is very little shear elsewhere in the water column. The drag coefficients are 8.0×10^{-3} and 6.7×10^{-3} on the flood and ebb tides, respectively (Table 6.1).

The three-dimensional velocity measurements indicate streamwise velocities that reach 1.6 m s^{-1} (Fig. 3.10d). On the flood tide, the flow veers slightly westward toward the surface and eastward toward the bed (Fig. 3.10h). On the ebb tide, v is typically negative throughout the water column, however, there are occasional intervals where the flow direction changes. The vertical velocity is low on both the flood and the ebb tides (Fig. 3.10l), reaching a maximum magnitude of 0.05 m s^{-1}. The slight upward flow on the flood tide and downward on the ebb is consistent with the local bathymetric gradient.

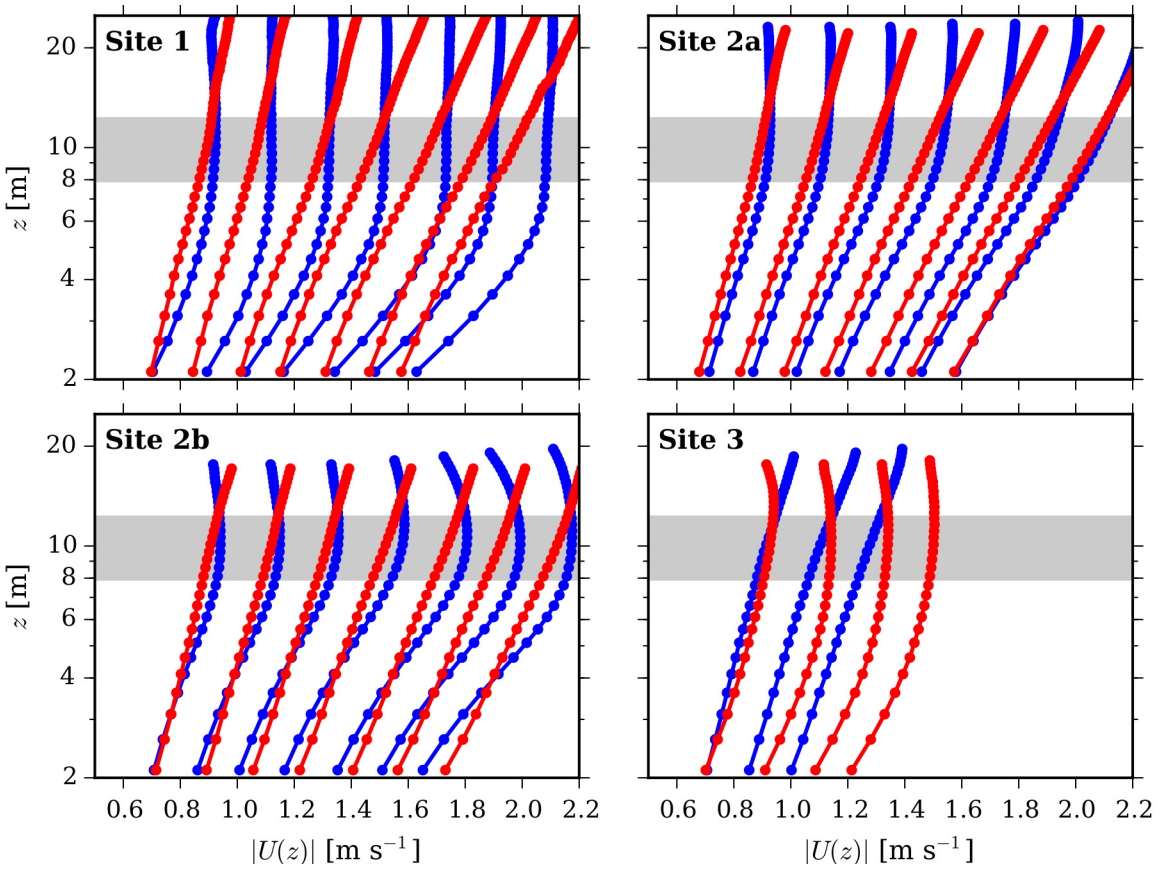

Figure 3.11: Speed-bin averaged velocity profiles during flood (red) and ebb (blue) at each site. The light grey region identifies the depth range over which the dissipation rates are calculated for the results presented in Chapter 5.

Table 3.3: Drag coefficients, C_d, at each of the ADCP sites determined using Eq. (3.2).

Site	**Flood** ($\times 10^{-3}$)	**Ebb** ($\times 10^{-3}$)
1	5.6	14.8
2a	8.5	9.9
2b	4.4	15.4
3	8.0	6.7

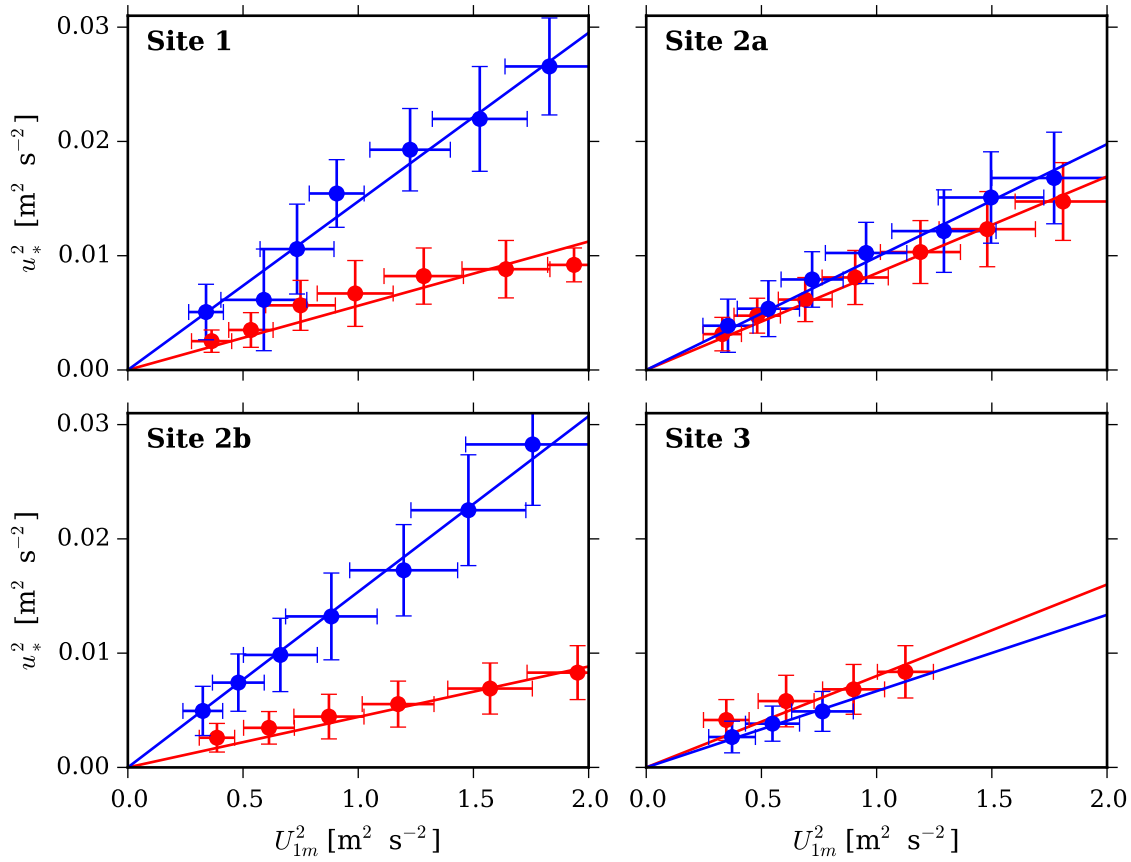

Figure 3.12: Bottom drag coefficients at the ADCP sites. Values determined from the lines of best fit are summarized in Table 6.1.

3.5 Summary

In this chapter, the measurements collected in Grand Passage were summarized. The strong flow speeds caused three of the bottom frames to shift significantly during spring tides, limiting the analysis intervals. However, the backscatter amplitude and correlations indicated that the ADCP data were of good quality. The strong flows also caused a 1 m blow-down of the *Nemo* moored turbulence system; however, the buoy remained fairly level for current speeds exceeding 0.8 m s^{-1}.

Using the ADCP data, a description of the mean flow conditions at each site were provided. Several commonalities emerged, including:

1) The depth-averaged flow was essentially bi-directional at all sites, with little variation in the flow direction.

2) The variance of the depth-averaged flow was site-dependent and the highest variability was observed at Site 2b. There was significant ebb/flood asymmetry in $\sigma^2_{U_d}$ at Sites 1, 2a, and 3. Higher variability was observed on the ebb tide at Site 3, and on the flood tide at Sites 1 and 2a. The enhanced variance is attributed to the presence of bathymetric features upstream of the sites which generate macroturbulence that is advected downstream.

3) Speed-bin averaged velocity profiles at all sites were logarithmic for $z < 6$ m. At Sites 1, 2a, and 2b the log-layer extended to the surface on the flood tide, whereas, a thick log-layer was only observed on the ebb tide at Site 3. Reversed shear (i.e., slower flow at the surface than at mid-depth) was observed only at Site 2b.

4) Bottom drag coefficients, C_d, were highly variable. At Sites 1 and 2b, the C_d values on the ebb tide were 14.8×10^{-3} and 15.4×10^{-3}, respectively. The corresponding values on the flood tide were approximately a factor of three smaller. The C_d values at Sites 2a and 3 were comparable on both phases of the tide and ranged between 6.7×10^{-3} to 9.9×10^{-3}. At all sites, the C_d value was higher on the tidal phase (ebb/flood) that was associated with a thinner log-layer.

5) One-day time series of three-dimensional currents showed that the along channel currents were fairly uniform throughout the water column, consistent with the speed-bin averaged profiles. At all sites, the transverse currents are typically less than 30 cm s^{-1}. On the flood tide, $v > 0$ near the surface and $v < 0$ near the

bed, indicating a slight counterclockwise veering of the current with height above bed. The same directional variation was observed on the ebb at Sites 1, 2a, and 2b, however, the transverse currents were more variable in comparison with the flood. On the ebb tide at Site 3, v was slightly negative throughout the water column. Vertical velocities at all sites were fairly uniform throughout the water column and consistent with the bathymetric gradients, except at Site 1 where the GPS location may have been inaccurate. The vertical velocities were the largest at Site 1, where they exceeded $10\,\mathrm{cm\,s^{-1}}$.

CHAPTER 4

RATE OF DISSIPATION OF TKE FROM SHEAR PROBES AND BROADBAND ADCPS

In this chapter[1], the ability of both shear probes and ADCPs to measure turbulence in a high Reynolds number tidal channel is assessed. Speed-bin averaged estimates of ϵ at mid-depth, obtained directly using the shear probes mounted in the nose of the *Nemo* turbulence system (Fig. 3.5 and Sec. 3.2.2), are compared to estimates of ϵ made remotely using the ADCP and AD2CP at Site 1 (Fig. 3.4 and Sec. 3.2.1). The instruments were deployed concurrently and separated by about 40 m (Fig. 3.1, Site 1 and Site SP) in the cross-channel direction.

Diverging-beam ADCPs are limited in their ability to measure turbulence because they require the assumption of statistical homogeneity across the beam spread (Section 2.2.2). In addition, high Doppler noise places a fundamental constraint on the accuracy of the instantaneous velocity estimates. Despite these limitations, ADCPs are often the instrument of choice for several reasons, particularly for tidal energy resource assessments. The ability to measure the flow remotely enables the characterization of the undisturbed flow throughout the water column. In addition, they can be deployed for long intervals (months to years), allowing an assessment of variability over a wide range of time scales.

Several previous studies have used ADCP data to estimate ϵ by implementing a variety of methods. Using a customized ADCP with a vertical beam, *Gargett* (1994) implemented

[1]The majority of this chapter was first published in:
McMillan, J. M., A. E. Hay, R. G. Lueck, and F. Wolk, Rates of dissipation of turbulent kinetic energy in a high Reynolds number tidal channel, *J. Atmos. Oceanic Technol.*, 33, 817–837, 2016.

a large eddy method to estimate ϵ from the energy containing scales. A similar approach was recently applied to ship-board data by *Greene et al.* (2015). Other studies have relied on the assumption that turbulent production and dissipation are appoximately equal in well-mixed conditions. Thus, by applying a variance method (*Lohrmann et al.*, 1990), an estimate of $\mathcal{P}_h$ can be made, which is assumed to be comparable to ϵ (*Rippeth et al.*, 2003). Structure function approaches—discussed in more detail in Chapter 5—have been implemented in most other studies (*Wiles et al.*, 2006; *Lorke*, 2007; *Whipple and Luettich*, 2009; *Simpson et al.*, 2011; *Collignon and Stacey*, 2013; *Thomson et al.*, 2012; *Simpson et al.*, 2015; *Lucas et al.*, 2014; *Thomson*, 2012).

The small size and high sampling rate of shear probes allow for a more accurate measurement of the turbulent fluctuations—particularly at small scales. Previous studies have compared ADCP and shear probe estimates of ϵ (*Rippeth et al.*, 2003; *Wiles et al.*, 2006; *Lucas et al.*, 2014; *McMillan et al.*, 2015); however, the shear probes in the cited studies were mounted on vertical profilers that can only capture the instantaneous dissipation rates at a given depth. Vertical profiles near a deployment site can be averaged together, but care must be taken to obtain meaningful averages due to the strong temporal and spatial variability of the flow. Shear probe measurements obtained using a horizontal profiler were previously compared to ADCP measurements by *Lu et al.* (2000); however, the comparisons were made between estimates of $\mathcal{P}_h$ from the ADCP and ϵ from the shear probes.

In this chapter, a direct comparison of ϵ estimated from the ADCP and shear probe data is made. In doing so, the velocity and shear spectra are shown to agree well with the theoretical forms, thus confirming that the turbulent fluctuations were accurately measured (*Moum and Rippeth*, 2009). The dissipation rate is computed from the ADCP measurements by fitting averaged along-beam velocity spectra to the theoretical forms derived specifically for the orientation of the ADCP relative to the mean flow. This method takes advantage of the broad inertial subrange that is present in a high Reynolds number flow. Adaptations to the spectral method that account for both the pitch and roll of the instrument and the aliasing present in the measured signals are also explored. The dissipation rate is computed from the shear probe measurements by first correcting the spectra to remove the vibrational signals caused by buoy motion. The resulting spectra are then used to estimate ϵ using standard methods (*Lueck*, 2013). The shear probe

measurements are also used to investigate the variability in ϵ on 1-minute timescales by comparing the probability distribution of ϵ to the expected form. Spatial variability and ebb/flood asymmetry in the results are discussed.

4.1 Methods

The velocity registered along the i-th beam of an ADCP is the sum of a mean velocity $\langle \hat{v}_i \rangle$ and a fluctuating velocity $\hat{v}_i'$. The measured fluctuations are composed of both the true turbulent velocity v_i' and an error e_i associated with Doppler noise (i.e., $\hat{v}_i' = v_i' + e_i$). It is assumed that e_i has a Gaussian distribution with variance $\sigma_{e_i}^2$ and that the spectrum of e_i is white with constant spectral density N_i, given by

$$N_i = \frac{\sigma_{e_i}^2}{f_N}, \tag{4.1}$$

where f_N is the Nyquist frequency. It is also assumed that e_i and v_i' are uncorrelated.

Due to the beam geometry, the along-beam velocity variances, $\sigma_{v_i}^2$, at a given range, can be expressed as

$$\sigma_{v_1}^2 = \sigma_{u_I}^2 \sin^2\vartheta + \sigma_{w_I}^2 \cos^2\vartheta + 2\langle u_I' w_I' \rangle \sin 2\vartheta + \sigma_{e_1}^2, \tag{4.2}$$

$$\sigma_{v_2}^2 = \sigma_{u_I}^2 \sin^2\vartheta + \sigma_{w_I}^2 \cos^2\vartheta - 2\langle u_I' w_I' \rangle \sin 2\vartheta + \sigma_{e_2}^2, \tag{4.3}$$

$$\sigma_{v_3}^2 = \sigma_{v_I}^2 \sin^2\vartheta + \sigma_{w_I}^2 \cos^2\vartheta + 2\langle v_I' w_I' \rangle \sin 2\vartheta + \sigma_{e_3}^2, \tag{4.4}$$

$$\sigma_{v_4}^2 = \sigma_{v_I}^2 \sin^2\vartheta + \sigma_{w_I}^2 \cos^2\vartheta - 2\langle v_I' w_I' \rangle \sin 2\vartheta + \sigma_{e_4}^2, \tag{4.5}$$

where ϑ is the beam angle with respect to the vertical (20°), and u_I, v_I and w_I are velocity components in instrument coordinates (x_I, y_I, z_I) as defined in Appendix F. Because the ADCP at Site 1 was oriented with beams 3 and 4 nearly aligned with the along-channel (x) direction (Fig. 3.6), Eqs. (4.4) and (4.5) can be added to yield,

$$\sigma_{v_3}^2 + \sigma_{v_4}^2 = 2\sigma_u^2 \sin^2\vartheta + 2\sigma_w^2 \cos^2\vartheta + \sigma_{e_3}^2 + \sigma_{e_4}^2, \tag{4.6}$$

where the approximations $\sigma_{v_I}^2 \approx \sigma_u^2$ and $\sigma_{w_I}^2 \approx \sigma_w^2$ are used. Following *Hay et al.* (2013), the velocity variances can be replaced by the spectral densities and Eqs. (2.31) and (4.6)

can be combined to give

$$\widehat{S}_T(k) = C\epsilon^{2/3}k^{-5/3} + N_T, \tag{4.7}$$

where $\widehat{S}_T$ and N_T are the summed wavenumber spectral densities and Doppler noise levels, respectively, which are determined using Taylor's hypothesis, i.e.,

$$\widehat{S}_T = \frac{|U|}{2\pi}\left[\widehat{S}_{33}(f) + \widehat{S}_{44}(f)\right], \tag{4.8}$$

$$N_T = \frac{|U|}{2\pi}\left(N_3 + N_4\right), \tag{4.9}$$

where $\widehat{S}_{ii}(f)$ is the spectral density of the measured i^{th} beam velocity ($\hat{v}_i'$) and U is the mean flow speed. The constant C in Eq. (4.7) is dependent on the beam geometry and is given in Table 4.1 ("2 beam" approach). Rearranging Eq. (4.7) yields

$$\epsilon = \left[C^{-1}\left(\widehat{S}_T - N_T\right)k^{5/3}\right]^{3/2}. \tag{4.10}$$

A "4 beam" approach was also implemented where Eqs. (4.2)–(4.5) were summed to give

$$\sum_{i=1}^{4}\sigma_{v_i}^2 = 2(\sigma_u^2 + \sigma_v^2)\sin^2\vartheta + 4\sigma_w^2\cos^2\vartheta + \sum_{i=1}^{4}\sigma_{e_i}^2, \tag{4.11}$$

where $\sigma_{u_I}^2 \approx \sigma_v^2$ represents the variance in the cross-stream direction. By replacing the variances with the spectral densities, Eq. (4.7) can again be obtained with modified forms of $\widehat{S}_T$, N_T and C as given in Table 4.1.

4.2 Results

4.2.1 Dissipation Rates from ADCP data

The along-beam frequency spectral densities, $\widehat{S}_{ii}(f)$, were computed for each 7 minute burst of data (600 points) within each 0.5 m vertical bin. Hanning windowed intervals of 60 points with 50% overlap were used to give 36 equivalent degrees of freedom for each estimate (*Nuttall*, 1971) and a frequency resolution of ca. 0.025 Hz. The resulting spectra were then ensemble-averaged over three adjacent bins in the vertical (corresponding to 1.5 m). Representative frequency spectra for beam 3 velocities are illustrated in Fig. 4.1a, where the spectra have been averaged into 0.4 m s^{-1} speed bins. The 95% confidence

Approach	$\boldsymbol{C}$	$\boldsymbol{2\pi\lvert U\rvert^{-1}\widehat{S}_T(k)}$ [m^2 s^{-2} Hz^{-1}]	$\boldsymbol{2\pi\lvert U\rvert^{-1}N_T}$ [m^2 s^{-2} Hz^{-1}]
2 beam	$2\alpha_1 \sin^2\vartheta + 2\alpha_3 \cos^2\vartheta$	$\widehat{S}_{33} + \widehat{S}_{44}$	$N_3 + N_4$
2 beam (tilt corrected)	$2\alpha_1 \sin^2\vartheta + 2\alpha_3 \cos^2\vartheta$	$\left(\widehat{S}_{33} + \widehat{S}_{44}\right) + \Gamma\left(\widehat{S}_{33} - \widehat{S}_{44}\right)$	$(N_3 + N_4) + \Gamma\,(N_3 - N_4)$
4 beam	$2\alpha_1 \sin^2\vartheta + 2\alpha_3 \sin^2\vartheta + 4\alpha_3 \cos^2\vartheta$	$\widehat{S}_{11} + \widehat{S}_{22} + \widehat{S}_{33} + \widehat{S}_{44}$	$N_1 + N_2 + N_3 + N_4$
vertical beam	α_3	$\widehat{S}_{55}$	N_5

Table 4.1: Expressions of the terms in Eq. (5.5) for each of the methods, where $\widehat{S}_{ii} = \widehat{S}_{ii}(f)$ is the spectral density of the i^{th} beam velocity, $|U|$ is the mean speed, α_1 and α_3 are the streamwise and transverse Kolomogorov constants, and γ is given by Eq. (4.18).

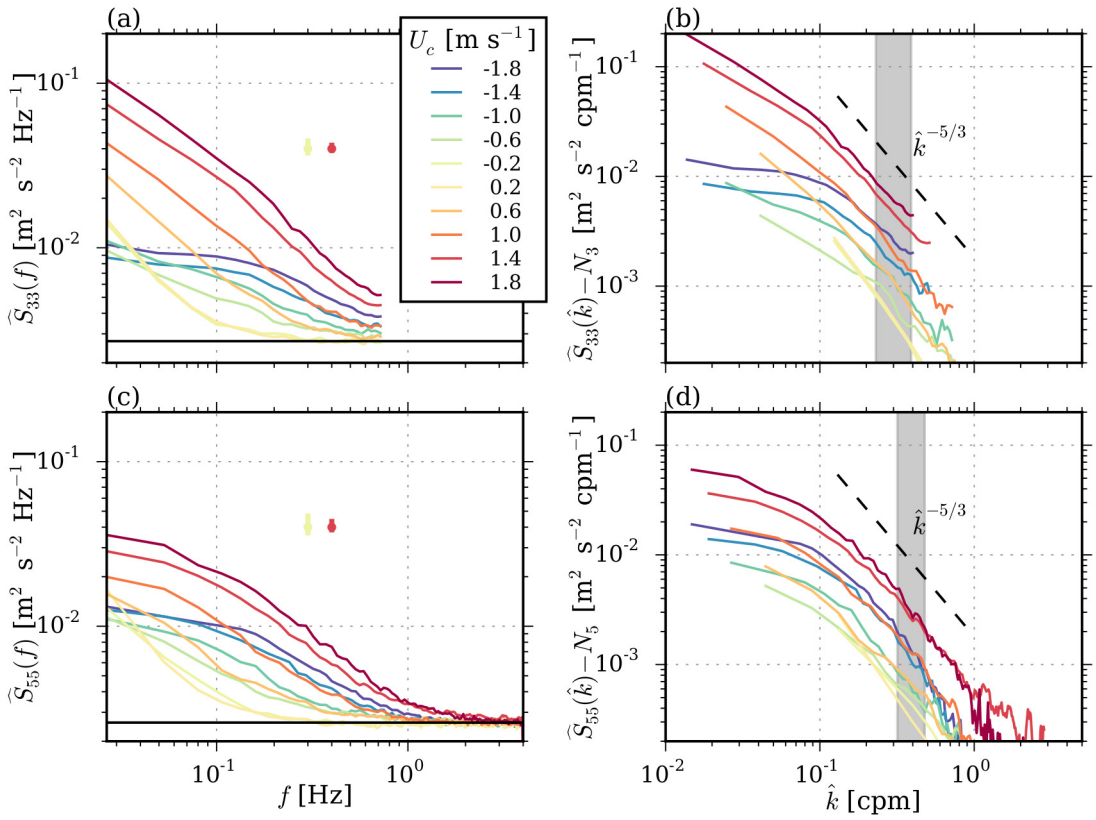

Figure 4.1: Speed-bin averaged frequency and wavenumber spectra from the ADCP (beam 3, a and b) and AD2CP (beam 5, c and d) at z = 4.6 m. The speed bin width is 0.4 m s^{-1} with central values denoted by U_c. The vertical bars in (a) and (c) correspond to the widest (yellow) and narrowest (red) 95% confidence intervals. The grey areas in (b) and (d) correspond to the $(2\pi)^{-1}$ cpm region of the inertial subrange over which the ϵ_{IM} values were determined. The legend applies to all subplots.

intervals were determined using the chi-square distribution with 36 degrees of freedom, taking into account the reduction in error by a factor of $\sqrt{n_s}$, where n_s is the total number of spectra in the speed-bin ensembles. The widest and narrowest confidence intervals are provided as vertical lines in Fig. 4.1a with the yellow and red colours corresponding to speed bins with the smallest and largest n_s values, respectively.

Near the 0.74 Hz Nyquist frequency (f_N), the spectra in Fig. 4.1a level out and approach the noise floor, N_3, represented by the black line. At this particular depth ($z = 4.6$ m) there is evidence of aliasing for the highest flow speeds ($|U_c| > 1.4$ m s^{-1}): i.e., the spectral level remains above the noise floor as f approaches f_N. At distances farther from the sea floor, and hence lower turbulence levels, aliasing was not observed (not shown). For each depth and beam, the noise floor was estimated by computing the average spectral level from

$f \in [0.5 f_N, f_N]$ for the lowest flow speeds ($|U_c| < 0.2$ m s^{-1}). The noise floor was nearly independent of beam and depth with a mean of $(2.9 \pm 0.2) \times 10^{-3}$ m^2 s^{-2} Hz^{-1} amongst all estimates (Appendix D). Given the Nyquist frequency of 0.74 Hz, the measured noise level corresponds to a beam velocity standard deviation of 4.7 cm s^{-1}, which is very close to the manufacturer-specified accuracy of 4.6 cm s^{-1} based on 2-ping averages and 0.5 m range bins. By subtracting the computed noise floor from the frequency spectra and implementing Taylor's hypothesis, the denoised wavenumber spectra (i.e., $\widehat{S}_{ii} - N_i$) can be obtained. The resulting spectra for beam 3 velocities are provided in Fig. 4.1b as a function of the cyclic wavenumber, $\hat{k} = (2\pi)^{-1} k$. It is apparent that the inertial subrange, where $\widehat{S}_{33} \sim \hat{k}^{-5/3}$, is present for a narrow range of wavenumbers, confirming that the expected spectral shape given by Eq. (4.7) was observed with the ADCP data.

From the along-beam velocity spectral densities, $\widehat{S}_T$ and N_T were calculated, and the dissipation rate was estimated from Eq. (4.10) as

$$\epsilon_{IM} = \left[C^{-1} \left\langle \left(\widehat{S}_T - N_T \right) k^{5/3} \right\rangle_{\text{ISR}} \right]^{3/2}, \tag{4.12}$$

where $\langle \cdot \rangle_{\text{ISR}}$ represents a mean over the inertial subrange, i.e., the sum divided by the number of spectral values, and is denoted the "Integral Method" (IM). The $\hat{k}$ limits of the integration region were chosen to be the $(2\pi)^{-1}$ cpm wide region that best conformed to the expected spectral shape.

Speed-bin averaged vertical profiles of ϵ_{IM} were obtained using the "4 beam" approach where the depth-averaged velocity, U_d, was used to sort the data (Fig. 4.2a). Estimates of ϵ_{IM} with high uncertainty (black markers) were flagged based on at least one of the following two criteria:

1) High variability of $Z = \left(\widehat{S}_T - N_T \right) k^{5/3}$ within the inertial subrange, i.e.,

$$\sigma_Z > 0.1 \overline{Z}. \tag{4.13}$$

2) Deviation of the spectral shape of $\widehat{S}_T - N_T$ from the expected -5/3 slope in the inertial subrange, i.e.,

$$\frac{|\zeta|}{5/3} > 0.2, \tag{4.14}$$

where ζ is defined such that $(\widehat{S}_T - N_T) \sim k^{-5/3+\zeta}$.

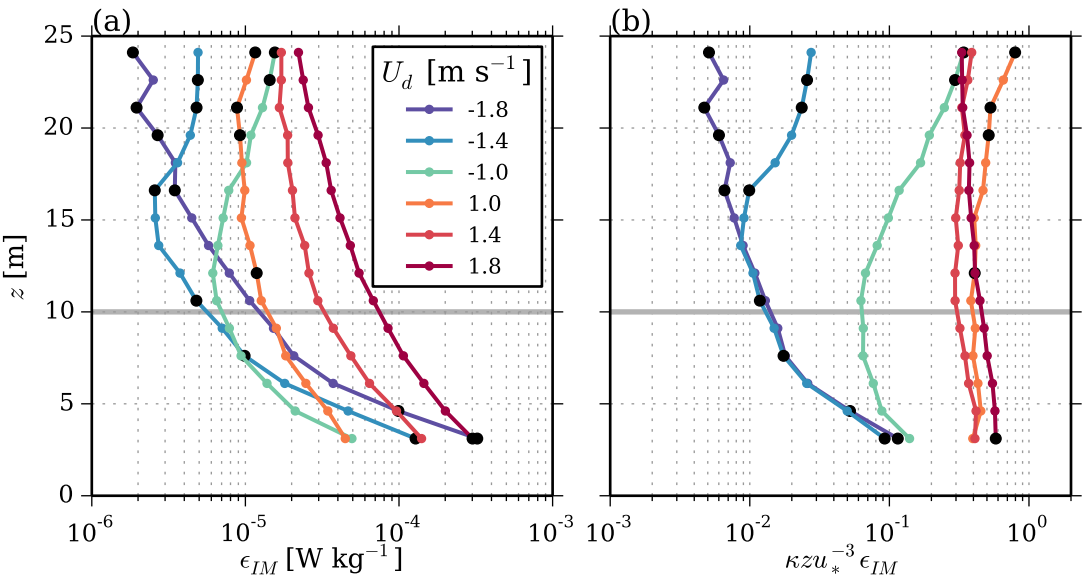

Figure 4.2: Dissipation rate, ϵ_{IM}, as a function of height above the bottom. Profiles have been averaged into 0.4 m s^{-1} speed bins based on the depth-averaged speed, U_d. The thick horizontal grey lines correspond to the nominal height of *Nemo*. Black markers are used to indicate points with high uncertainty (See Fig. 4.3 for vertical profiles of the measures of error).

Vertical profiles of the error measures in the ϵ_{IM} estimates are presented in Fig. 4.3. Near the bed, during strong flows, $\zeta > 0.2$ indicating that the aliasing generated by a low sample rate and high turbulence levels causes the spectra to deviate from the expected $k^{-5/3}$ shape. Near the surface on the ebb tide, the measurements are contaminated by wave-induced effects (Appendix C). Measurements at the Environment Canada meteorological station ("EC" in Fig. 3.3) indicated that the wind speed varied between 1 and 5 m s^{-1}, and the direction was predominantly southerly or southwesterly. Therefore, wind waves propagated against the southward current on the ebb, leading to wave height amplification on the ebb tide and not on the flood. Because the wave periods were small (ca. 5-6 s peak period) they are deep water waves and the increased variance associated with the wave motion does not penetrate to depths greater than 10 m.

The vertical profiles of the dissipation rate (Fig. 4.2a) indicate that turbulence levels are significantly higher on the flood tide compared with the ebb throughout the water column. For each profile, the highest dissipation rates are found near the bed, consistent with turbulence production in the bottom boundary layer. In Fig. 4.2b, the dissipation rates are scaled by the theoretical turbulent production given by Eq. (2.16) using u_* values

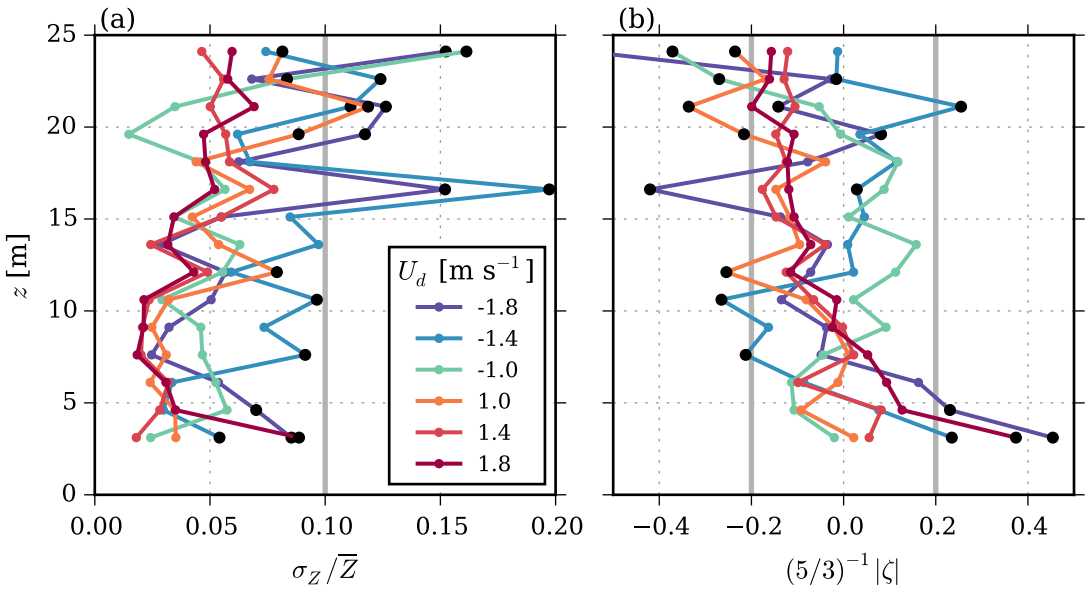

Figure 4.3: Vertical profiles of the measures of error in the ϵ_{IM} estimates. Profiles have been averaged into 0.4 m s^{-1} speed bins based on the depth-averaged speed, U_d. Grey lines correspond to the thresholds used to identify uncertain estimates, and black markers denote bins where at least one of the two criteria was not satisfied.

determined from fits to the law-of-the-wall (Eq. 2.12). On the flood tide, the profiles collapse to a constant value of about 0.3 to 0.6 for $5 < z < 15$ m, as expected for flow within a constant stress layer. In contrast, the ebb tide profiles do not collapse because the constant stress layer was very thin and not resolved by the ADCP, despite the logarithmic layer extending to 5 m above the bed. The observation of a near bed log-layer with non-uniform Reynolds stress has been observed both in Grand Passage (*Hay et al.*, 2013) and in other tidal channels (*Stacey et al.*, 1999; *Lu et al.*, 2000). Furthermore, using an ADCP positioned south of the ridge (Fig. 1), *Hay et al.* (2013) showed that when the log-layer was thin $u_*^2 \sim -0.4\,\langle u'w'\rangle$ at $z = 2.1$ m, as opposed to extending beyond 15 m, the expected result for a constant stress layer was obtained: i.e., $u_*^2 \sim -\langle u'w'\rangle$.

Dissipation rates were also estimated from the AD2CP vertical velocities, measured directly with beam 5. Spectra for the five minute bursts (2394 points) were obtained for each 12.5 cm vertical bin. Hanning windowed intervals of 300 points with 50% overlap were used, corresponding to 28 equivalent degrees of freedom (*Nuttall*, 1971) and a frequency resolution of 0.027 Hz. The resulting spectra were then averaged over 12 adjacent range bins to obtain a 1.5 m vertical average (as for the ADCP). Representative

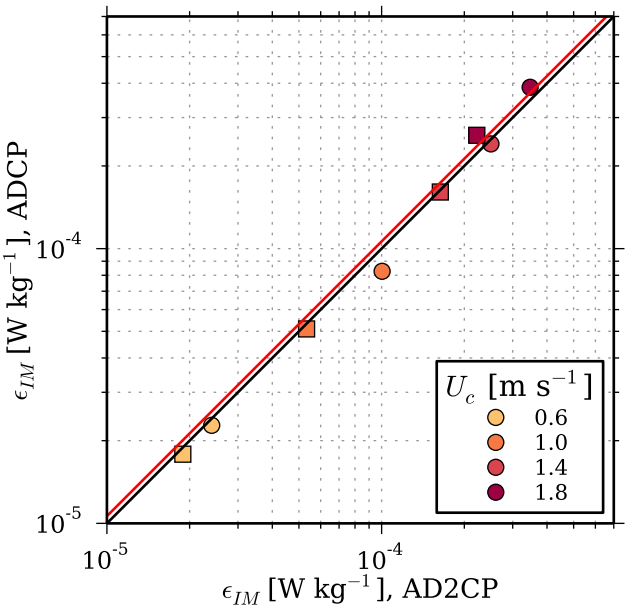

Figure 4.4: Speed-bin averaged dissipation rates from the ADCP and AD2CP at $z = 3.1$ m (circles) and 4.6 m (squares) height on the flood tide. Colours indicate the mean speeds over the 1.5 m vertical averaging intervals. The black line is the 1:1 line and the red line is the least-squares best fit where the proportionality constant is 1.06.

frequency and wavenumber spectra are shown in panels (c) and (d) of Fig. 4.1. Because of its higher sampling rate, the AD2CP spectra exhibit no sign of aliasing and a noise floor is apparent at 2.6×10^{-3} m^2 s^{-2} Hz^{-1} for all speed bins. Again, the inertial subrange is clearly evident and is resolved up to $\hat{k} \sim 3$ cpm at the highest flow speeds. The dissipation rate was estimated from the AD2CP data using Eq. (4.12), where $\widehat{S}_T$ and C are equivalent to $\widehat{S}_{55}$ and α_3 because the AD2CP directly measures the vertical velocity. This approach is termed "vertical beam" in Table 4.1.

The dissipation rates estimated via the Integral Method (IM) from the ADCP ("4 beam" approach) and the AD2CP ("vertical beam" approach) at 3.1 and 4.6 m above bottom are compared in Fig. 4.4. The ϵ_{IM} values from the two instruments are comparable, and a least-squares fit yields a proportionality constant of 1.06. This agreement indicates that errors introduced by the low sample rate and divergent beam geometry of the ADCP are small.

4.2.2 Dissipation Rates from Shear Probe Data

The one-minute mean dissipation rate was estimated from the shear probe measurements by averaging the frequency spectra computed from 119 one-second (2048 points) intervals

with 50% overlap. The frequency spectra were then converted to wavenumber spectra using Taylor's hypothesis with U in Eq. (2.39) equated to the average flow speed past the buoy, $|u_N|$, as interpolated from the two-minute ensembles of the velocity measurements from the ADV which was situated just aft of the MicroRider. Corrections to the spectra were made for both the spatial averaging due to the physical size of the shear probe (*Macoun and Lueck*, 2004) and for the vibration of the instrument (*Goodman et al.*, 2006). The 95% confidence intervals were estimated using the residual based bootstrapping method in the frequency domain with 1000 resamples (*Paparoditis*, 2002).

Representative shear spectra are shown in Fig. 4.5a for both a weakly-turbulent (lower curves) and a strongly-turbulent time interval (upper curves). It is clear that the spectral densities were nearly independent of probe number. The velocity spectra (Fig. 4.5b) were obtained by dividing the shear spectra by $(2\pi\hat{k})^2$ (*Wolk et al.*, 2002). For the smaller wavenumbers ($\hat{k} < 30$ cpm), the spectra for both low and high turbulence intensity exhibit a well-defined inertial subrange where $\psi \sim \hat{k}^{1/3}$ and $(2\pi\hat{k})^{-2}\psi \sim \hat{k}^{-5/3}$. For the weakly-turbulent case, the dissipation range—where ψ rolls off with $\hat{k}$—was observed, but only the ISR was resolved in the highly-turbulent example because the smallest eddies were not measured by the probes. For $\hat{k} > 150$ cpm, both spectra were dominated by the attenuation effects of the anti-aliasing filters. The inertial subrange was much better resolved in the shear probe data than in the ADCP data, spanning nearly two decades in Fig. 4.5b compared to less than one decade in Fig. 4.1b.

As outlined by *Lueck et al.* (2013), ϵ can be computed from the shear spectra using one of two methods. For dissipation rates smaller than 2×10^{-5} W kg^{-1}, the spectrum is integrated up to a maximum wavenumber, $\hat{k}_{max}$, to estimate the total variance using Eq. (2.34). For higher turbulence levels—since the dissipation range is not captured—the best proportional fit to the Nasmyth spectrum (Eq. 2.35) is obtained over the inertial subrange, i.e., $\hat{k} \in [0, \hat{k}_{max}]$. The dissipation estimates were deemed reliable if the following criteria were satisfied:

1) The largest ratio between the ϵ estimates from the four probes was $10^{0.8}$, i.e.,

$$\frac{\max(\epsilon_j)}{\min(\epsilon_j)} < 10^{0.8} = 6.3, \tag{4.15}$$

where j is the probe number, i.e., $j = 1, 2, 3$ or 4.

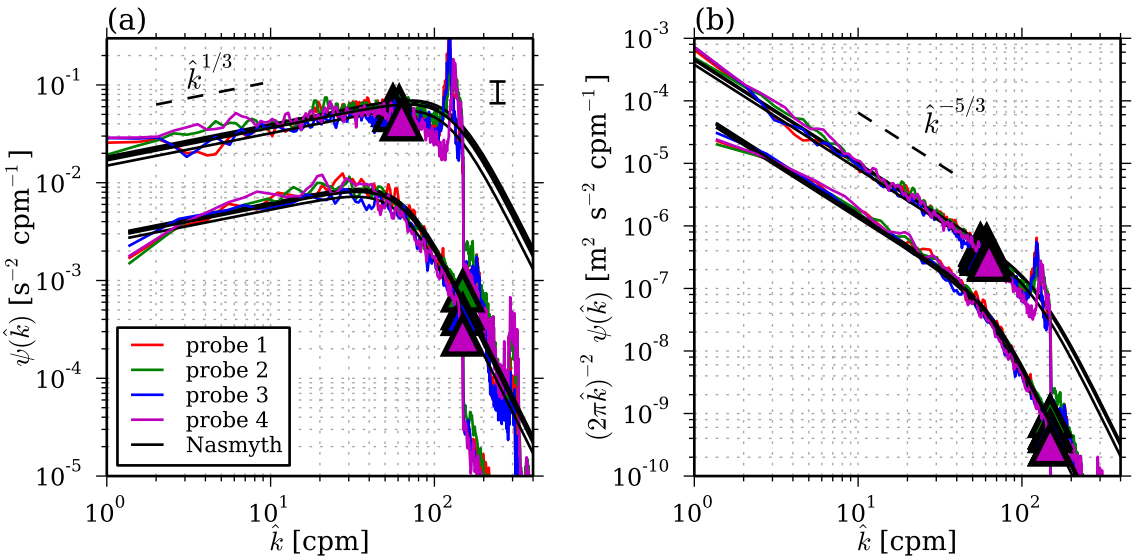

Figure 4.5: One-minute averaged (a) shear spectra and (b) velocity spectra for both a strongly turbulent region (upper curves) and a weakly turbulent region (lower curves). The triangles indicate the maximum wavenumbers, $\hat{k}_{max}$, that were used in the determination of ϵ for each method. The black lines represent the Nasmyth curves (Eq. 2.35) for the corresponding dissipation rates ($\epsilon \approx 1 \times 10^{-4}$ W kg^{-1} for the strongly turbulent region and $\epsilon \approx 6 \times 10^{-6}$ W kg^{-1} for the weakly turbulent region). The error bar in the upper right hand corner of (a) represents the mean size of the 95% confidence interval in the inertial subrange region.

2) The mean absolute deviation (MAD) of the spectra for all four probes was less than 0.4. This parameter, defined by *Ruddick et al.* (2000), is the average absolute deviation between the measured spectrum and the Nasmyth spectrum (Eq. 2.35), where the average is computed over all $\hat{k}$ up to a cutoff wavenumber, $\hat{k}_{max}$. Mathematically, the MAD value is given by

$$\text{MAD} = \frac{1}{n_k} \sum_{i=1}^{n_k} \left| \frac{\psi_{\text{meas}}(\hat{k}_i)}{\psi_{\text{Nasmyth}}(\hat{k}_i)} - 1 \right|, \tag{4.16}$$

where n_k is the number of discrete wavenumbers up to $\hat{k}_{max}$.

The time series of the four-probe-average dissipation estimates is presented in Fig. 4.6. The tidal variation of ϵ is clearly evident, with the flood tide values being significantly higher than those on the ebb (Figs. 4.6 and 4.7), which is qualitatively consistent with the ebb/flood asymmetry of the ADCP dissipation rates. The arithmetic mean of the values within 0.2 m s^{-1} speed bins are illustrated as the blue markers in Fig. 4.7. The error bars represent the range in the mean values amongst the probes and not the standard deviation of the raw measurements, which is clearly much larger. On the flood tide, ϵ is proportional to $|u_N|^3$ for $|u_N| > 1$ m s^{-1}. This scaling is consistent for flow in the boundary layer where turbulent production and dissipation are expected to be approximately in balance. The proportionality constant was estimated to be 7.8×10^{-6} from a least-squares fit to the mean values. A $|u_N|^3$ dependence of ϵ on flow speed is not apparent during the ebb tide.

4.3 Discussion

4.3.1 Inter-instrument Comparison of Dissipation Rates

The mean values of the dissipation rate at $z = 10.1$ m, computed from the ADCP data using the 4-beam Integral Method, are illustrated as black squares in Fig. 4.7. These points exhibit the same general trends as the shear probe results on both ebb and flood, but are higher by a factor of 1.3 to 2.1 (with one exception). There are a number of possible explanations for this systematic difference:

1) an error in the estimate of the mean velocity used in Eq. (2.39) due to the position of the ADV and flow distortion created by the *Nemo*

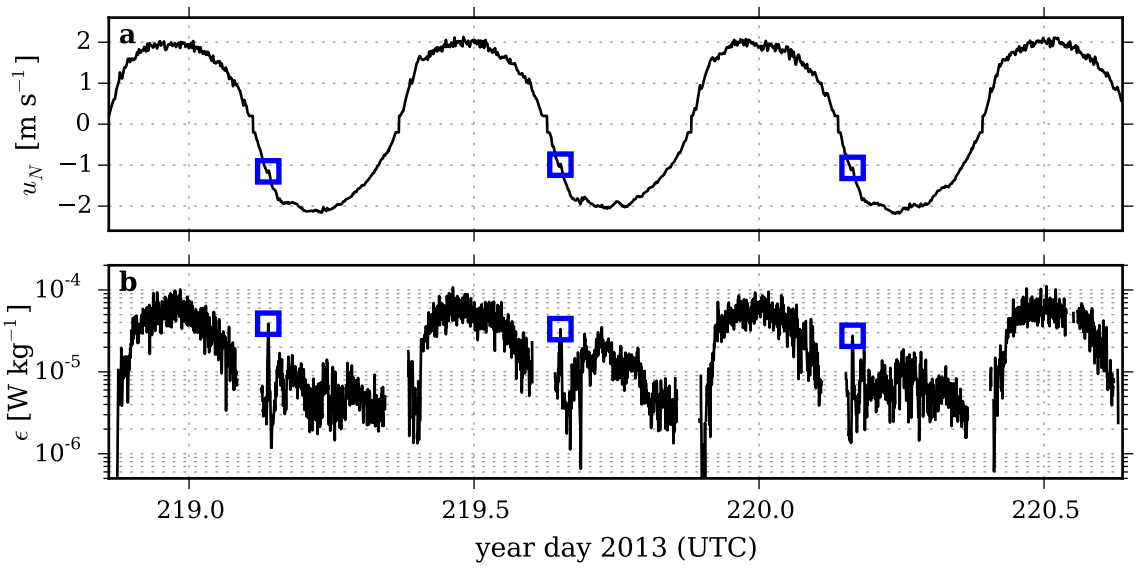

Figure 4.6: (a) The signed flow speed registered by the ADV (also shown in Fig. 3.7a). (b) The average dissipation rate computed from the four shear probes over one-minute intervals. High dissipation rates on the ebb tide are marked by the blue squares.

2) the tilt of the bottom mounted ADCP relative to the flow

3) aliasing of the ADCP spectra

4) the factor of 2 difference is real, and a consequence of the spatial separation of the two instrument platforms

The simplest of the above possibilities is an error in the mean velocity estimate used in the implementation of Taylor's hypothesis. The flood tide results in Fig. 4.7a indicate that 20% error in $|u_N|$ at the *Nemo* location would account for the difference in ϵ values. However, such a correction would lead to misalignment of the ebb results (Fig. 4.7b). Furthermore, the values of $|u_N|$ from the ADV differ from those computed from the downward looking AD2CP on *Nemo* by 5% on average. Thus, the possibility of an error in the estimate of mean velocity can be reasonably dismissed.

In the derivation of Eq. (4.7) it is assumed that the streamlines are orthogonal to the vertical axis of the instrument coordinates. If instead it is assumed that the angle between the instrument coordinates and the streamlines is non-zero and represented by β, Eq. (4.6)

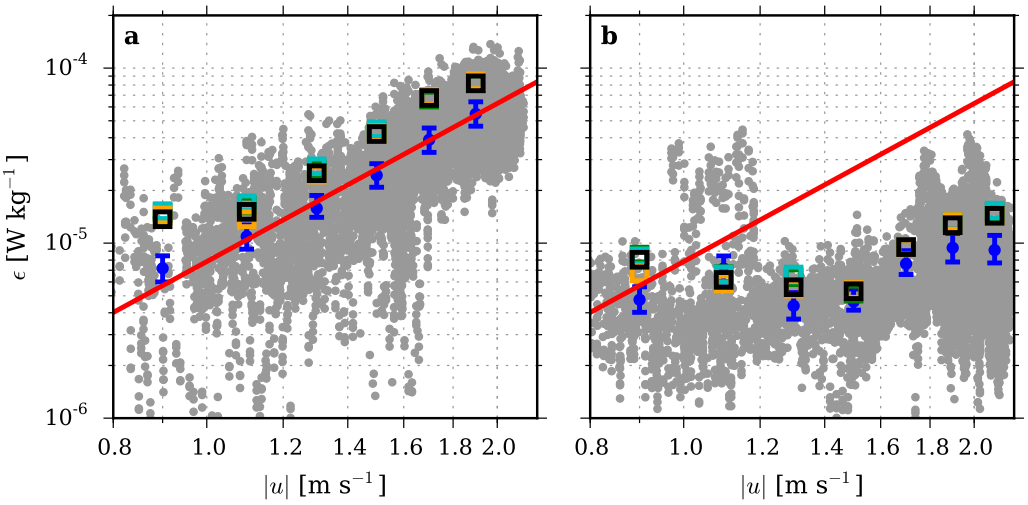

Figure 4.7: Dissipation rate as a function of flow speed on the (a) flood and (b) ebb tides. The grey points represent the one-minute averages from all four shear probes. The blue markers are the mean values within speed bins 0.2 m s^{-1} in width, and the error bars represent the range of mean estimates from the four probes. The red line is $\epsilon = 7.8 \times 10^{-6}|u|^3$, which is the least-squares fit to the flood tide estimates. The square markers correspond to the ϵ values computed from the ADCP data at $z = 10.1$ m using the 4-beam IM (black), 2-beam IM (green), 2-beam IM with tilt correction (cyan), and LS method (yellow).

becomes

$$\begin{aligned}\left(\sigma_{v_3}^2+\sigma_{v_4}^2\right)+&\Gamma\left(\sigma_{v_3}^2-\sigma_{v_4}^2\right)= \\ &\sigma_u^2\left[2\left(\sin^2\vartheta\cos^2\beta+\cos^2\vartheta\sin^2\beta\right)-\cos 2\vartheta\sin 2\beta\tan 2\beta\right] \\ &+\sigma_w^2\left[2\left(\cos^2\vartheta\cos^2\beta+\sin^2\vartheta\sin^2\beta\right)+\cos 2\vartheta\sin 2\beta\tan 2\beta\right] \\ &+\left(\sigma_{e_3}^2+\sigma_{e_4}^2\right)+\Gamma\left(\sigma_{e_3}^2-\sigma_{e_4}^2\right), \end{aligned} \tag{4.17}$$

where

$$\Gamma=\frac{\tan 2\beta}{\tan 2\vartheta}. \tag{4.18}$$

Replacing the variances with spectral densities and assuming that β is small, Eq. (4.7) can be obtained with $\widehat{S}_T$ and N_T given by

$$\widehat{S}_T=\frac{U}{2\pi}\left[\left(\widehat{S}_{33}+\widehat{S}_{44}\right)+\Gamma\left(\widehat{S}_{33}-\widehat{S}_{44}\right)\right], \tag{4.19}$$

$$N_T=\frac{U}{2\pi}\left[\left(N_3+N_4\right)+\Gamma\left(N_3-N_4\right)\right], \tag{4.20}$$

valid to $\mathcal{O}(\beta^2)$. The constant, C, is unchanged (Table 4.1). Thus, the effect of a non-zero β enters through a correction term applied to $\widehat{S}_T$ and N_T. This term, because it involves the product of β and the difference in spectral densities, is expected to be small.

For the Site 1 data, $\beta\approx 0.1$ rad, as determined from the slope of the speed-bin averaged estimates of w_I versus v_I. The corrected ϵ_{IM} values are illustrated in Fig. 4.7 by the cyan points and are indistinguishable from the values with $\beta=0$ (green markers).

The effect of aliasing on the dissipation rates was also considered by performing a least-squares fit to the speed-bin averaged spectra, taking into account the folding about the Nyquist frequency. Eq. (4.7) can be written in the form $\widehat{S}_T(k_i)=ak_i^*+N_T$, where k_i^* is a summation over M folds of the wavenumber given by

$$k_i^*=\left[\sum_{m=0}^{M}k_m^{-5/3}\right], \tag{4.21}$$

where

$$k_m=\begin{cases}mk_N+k_i & \text{if } m \text{ even}\\ \left(m+1\right)k_N-k_i & \text{if } m \text{ odd}\end{cases}, \tag{4.22}$$

k_N is the Nyquist wavenumber and k_i is the wavenumber in the resolved range, i.e., $k_i \in [0, k_N]$. With the noise level, N_T, known, the value of a minimizing the error in the fit is

$$a = \frac{\sum_{i=1}^{n_i} \widehat{S}_T(k_i) k_i^* - N_T \sum_{i=1}^{n_i} k_i^*}{\sum_{i=1}^{n_i} (k_i^*)^2}, \tag{4.23}$$

where n_i is the total number of discrete wavenumbers in the fitting region. The dissipation rate can then be computed by

$$\epsilon_{LS} = \left(aC^{-1}\right)^{3/2}, \tag{4.24}$$

where the subscript LS denotes "least-squares". Using a fitting region of $f \in [0.3, 0.72]$ Hz, the ϵ_{LS} estimates at $z = 10.1$ m are in good agreement with the ϵ_{IM} values (Fig. 4.7, red points) with the mean percent difference for all speed bins being less than 4%. It should also be noted that the minimum error in the fit was achieved with $M = 0$, thus indicating that the variance associated with the smaller, unresolved scales does not affect the spectral shapes at this depth. Closer to the bed, where aliasing is clearly prevalent (Fig. 4.1a), the best fits for the highest flow speeds are acquired with $M = 1$ (not shown).

It is possible that the differences between the ADCP and the shear probe measurements can be attributed to the 40 m cross-channel separation of the instruments. As was presented in *McMillan et al.* (2015), there is significant east-west variability in the dissipation rates near the deployment locations. A transect with a vertical microstructure profiler (VMP) during strong ebb flows indicated that dissipation rates at mid-depth were about 5×10^{-6} W kg^{-1} near the ADCP site and 2×10^{-6} W kg^{-1} near the *Nemo* location, which is consistent with the factor of two difference observed in Fig. 4.7. This east-west variability on the ebb tide is also consistent with visual observations that were made during the deployment period. Shear lines were visible at the surface originating at the northern point of Brier Island on the ebb flow, possibly bisecting the ADCP and *Nemo* locations. Similar spatial variability is expected on the flood tide.

4.3.2 Ebb/flood Asymmetry

The speed-bin averaged rates of dissipation on the flood and ebb tide are significantly different at both the ADCP and *Nemo* deployment locations (Figs. 4.2, 4.6, and 4.7). During strong flows, ϵ is about 10 fold higher on the flood tide than on the ebb. There is also a well-defined linear relationship between the dissipation rate and $|U|^3$ for flow

speeds greater than 1 m s^{-1} during the flood (Fig. 4.7a). On the ebb, however, the ϵ values are more scattered and the average is comparatively independent of flow speed (Fig. 4.7b).

Insight into this asymmetry can be gained from the velocity profiles obtained from the ADCP measurements (Fig. 3.11). On the flood tide, the logarithmic layer—and arguably the boundary layer—is thick and extends nearly all the way to the surface. Within a boundary layer, a balance between production and dissipation rates is expected, and hence, $\epsilon \sim |U|^3$ as observed. On the other hand, the logarithmic layer is very thin on the ebb tide, so the same assumption regarding the balance cannot be made.

The channel shape also affects the dissipation rates. On the northward flowing flood tide, the flow passes over several bathymetric features—including the CC ridge (Fig. 3.3)—before reaching the deployment locations. The complex bathymetry generates macro-turbulence near the bed which then propagates upward in the water column and results in high turbulence levels at the deployment locations. On the southward flowing ebb tide, the flow converges due to the channel shape. The associated acceleration suppresses the turbulence and hence results in lower dissipation rates. In addition, the bathymetry at the north entrance (upstream on ebb) to the channel is less variable than that within the passage to the south (upstream on flood) of the deployment locations.

The dissipation rates at the *Nemo* location on the ebb tide typically range between 2×10^{-6} and 2×10^{-5} W kg^{-1} (Figs. 4.6b and 4.7b). However, there are intermittent bursts where ϵ remains high for several minutes at a time. One such example occurs on all three ebb tides as the flow accelerates from 1 to 1.2 m s^{-1} (Fig. 4.6, blue squares). The bearing of the buoy, and hence, the incoming flow direction, is about 15° from true north at the time, in contrast to the mean flow direction of 5° during the stronger flows. This indicates that the flow becomes more turbulent if it passes over the shallow region to the NNE of the *Nemo* location. Greater insight into the dependence of dissipation rate on flow direction can be seen in Fig. 4.8, where ϵ is shown as a function of the buoy pitch and the colours of the markers correspond to the bearing direction. This figure therefore indicates that the dissipation rate is primarily related to the pitch of the buoy which appears to be loosely correlated to the flow direction. As the incoming flow deviates from true north, turbulence is generated by the shallow shoal, and the updrafts associated with this motion cause the nose of the buoy to pitch upward. The indication of higher turbulence levels on the eastern side of the passage is consistent with the VMP measurements that were made during the

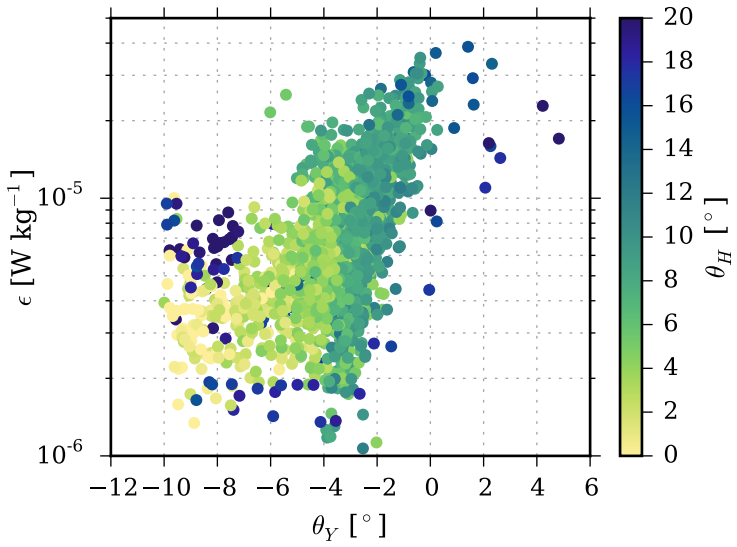

Figure 4.8: Dissipation rate on the ebb tide as a function of inclination angle, θ_Y. The colours of the markers correspond to the bearing of the buoy relative to true north.

deployment period (*McMillan et al.*, 2015).

4.3.3 Intermittency in the Dissipation Rate

The scatter in the one-minute estimates of ϵ (grey points in Fig. 4.7) is associated with small-scale intermittency, as demonstrated by the probability density functions (PDFs) of ϵ (Fig. 4.9). These PDFs, which were computed for $|u_N| > 1.8$ m s^{-1}, are lognormal on both the flood and ebb tide. The most probable values of ϵ differed by 20% amongst the probes. The differences cannot be attributed to anisotropy because probes 1 and 3 measured fluctuations in the vertical velocity, whereas probes 2 and 4 measured fluctuations in the horizontal velocity (Fig. 3.5).

The flood/ebb asymmetry discussed in Sec. 4.3.2 is again apparent in the PDFs. The broader probability distribution on the ebb tide (Fig. 4.9c)—indicating a higher degree of intermittency—is likely due to the log-layer being much thinner on the ebb compared to the flood (Fig. 3.11). On the ebb tide, the mean log-layer is about 5 m thick, however, large scale turbulence generates time variations in the boundary layer thickness that could cause it to periodically extend beyond 10 m. Thus, the *Nemo* float could have intermittently moved in and out of the boundary layer on the ebb tide, generating a greater spread in the ϵ values. On the other hand, the presence of an 18 m high log-layer on the flood tide resulted in reduced variability in ϵ because the measurements were all made within the boundary

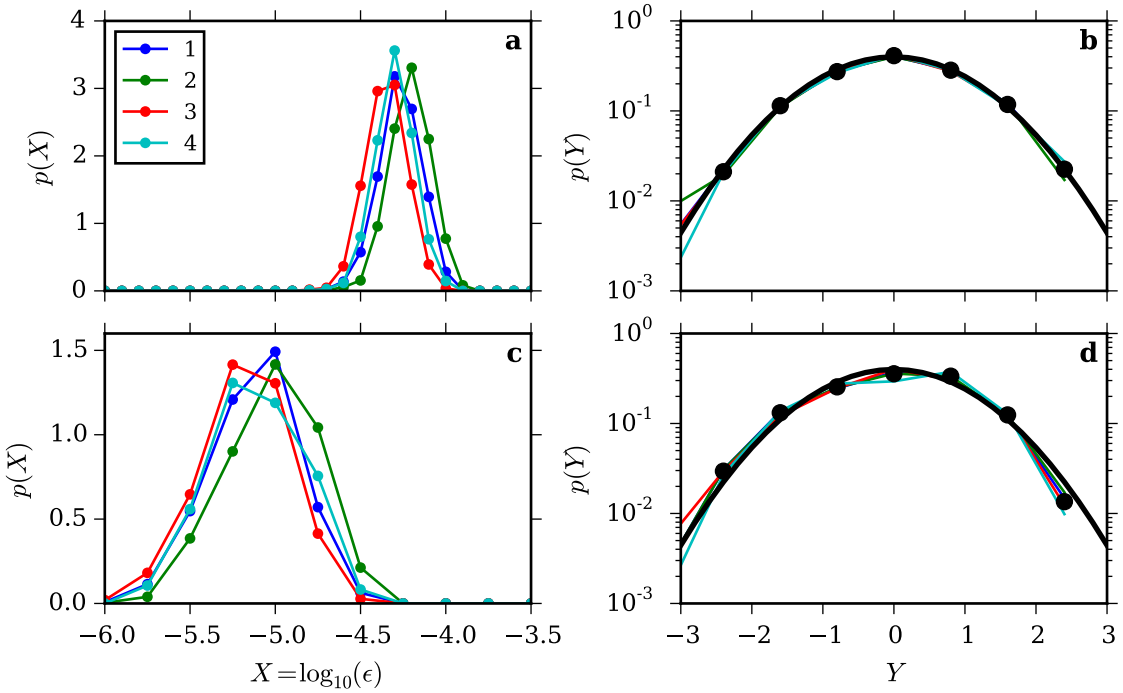

Figure 4.9: Probability density functions of the dissipation estimates from the four shear probes for flow speeds greater than 1.8 m s^{-1}. The distributions for the flood (a) and ebb (c) tides were based on 1143 and 1021 one-minute estimates, respectively. The standardized versions of (a) and (c) are shown in (b) and (d), respectively, where $Y = \sigma_X^{-1}(X - \overline{X})$, with $\overline{X}$ and σ_X being the mean and standard deviation of $X = \log_{10}(\epsilon)$. The black curves in the right panels are the normal distribution.

layer. Because the ϵ values conform to the lognormal distribution (Fig. 4.9b), the factor of 8 spread in the one-minute estimates for $u > 1.8$ m s^{-1} (Fig. 4.7a) is attributable to the small-scale intermittency in the boundary layer of a high Reynolds number flow.

The intermittency in the ADCP estimates of the dissipation rate was not investigated because the accuracy of the instantaneous velocity measurements is compromised by the Doppler noise. Both to properly estimate the noise level and to constrain the confidence intervals of the spectral densities, sufficient averaging of the spectra was required, allowing for an assessment of the speed bin averaged ϵ values. The variability of ϵ at small time scales is beyond the capability of the both the IM and LS methods presented in this chapter.

4.4 Conclusions

Speed-bin averaged rates of dissipation of TKE at mid-depth in a high flow tidal channel were estimated from bottom-mounted ADCP measurements (Site 1) and from shear probe measurements obtained using a horizontal profiler mounted on the *Nemo* turbulence system. The two sets of ϵ estimates agreed to within a factor of two, but the ADCP values were consistently higher. It was shown that the discrepancy cannot be explained by (1) errors in the estimation of the mean speed of the flow past the shear probes, (2) bias induced by the tilt of the ADCP frame relative to the streamlines, or (3) aliasing in the ADCP velocity spectra due to the low sampling rate. Thus, the differences were likely caused by the spatial separation of two instrument platforms. This argument is consistent with the cross-channel variation in ϵ that was observed by *McMillan et al.* (2015) using VMP measurements. Furthermore, comparisons between the estimates of ϵ from the standard, divergent beam ADCP were within 6% with those made by a co-located 1 MHz AD2CP (beta-test version) which collected velocity measurements along its vertical beam at a sampling rate of 8 Hz for $z < 5$ m.

The ADCP data captured both the variation of ϵ with flow speed and the ebb/flood asymmetry in the turbulence levels at mid-depth, consistent with the shear probe results. On the flood tide, the dissipation rate at $z = 10$ m—the nominal height of the buoy—varies with $|U|^3$ for flow speeds greater than 1 m s^{-1}, reaching a maximum value of 5×10^{-5} W kg^{-1} (as computed from the shear probe data) within the 1.9 m s^{-1} speed bin. On the ebb tide, the convergence of the flow in the narrowing channel resulted in lower dissipation rates with the maximum speed-bin averaged value of 9×10^{-6} W kg^{-1}.

The dissipation rates on the ebb tide are comparatively independent of flow speed. The ebb/flood asymmetry was also apparent in probability density functions of ϵ computed from the shear probe measurements for $|U| > 1.8$ m s^{-1}. A broader distribution on the ebb tide suggested that the dissipation rates reflected the time variations of the boundary layer thickness generated by the large scale turbulence.

The ADCP data were used to obtain vertical profiles of ϵ and, hence, the ebb/flood asymmetry in the flow throughout the water column. On the flood tide, complex bathymetric upstream of the site generates macro-turbulence causing the (logarithmic) boundary layer to extend beyond $z = 18$ m. Within this region, scaling the dissipation rates by $\mathcal{P}_h = (\kappa z)^{-1} u_*^3$ yields vertical profiles which are independent of height, and $\epsilon/\mathcal{P}_h \sim 0.4$. In contrast, on the ebb tide the logarithmic layer is much thinner and the $\epsilon/\mathcal{P}_h$ ratios were much lower and dependent on height above the bed—the maximum values were 0.1 near the bed, and decayed quasi-exponentially with height. Near the surface, the ebb tide estimates were contaminated with wave motion identified by the presence of a local maximum between 0.1 and 0.2 Hz in the velocity spectra.

The proven ability of standard, divergent beam ADCPs to make remote estimates of turbulence levels in a high Reynolds number flow is particularly promising for the tidal energy industry, which relies heavily on these instruments for assessments of the resource potential. Using the methods presented in this chapter, speed-bin averages of the dissipation rate can be quantified, however, the low sampling frequency and high Doppler noise levels of the ADCP limit its ability to resolve the small-scale variability in ϵ. On the other hand, the small physical size and fast response times of shear probes enable the high frequency fluctuations to be resolved. The present results using the MicroRider-*Nemo* combination demonstrate that time series measurements of high resolution velocity shear are attainable at mid-depth in high Reynolds number tidal flows. The high-sampling rate time series, spanning several tidal cycles, give rise to ϵ estimates that—for $|U| > 1.8$ m s^{-1}—are lognormally distributed and exhibit a factor of 8 spread within the boundary layer.

CHAPTER 5

SPECTRAL AND STRUCTURE FUNCTION ESTIMATES OF DISSIPATION RATES OF TKE USING BROADBAND ADCPS

In the previous chapter, it was shown that the shear probe estimates of the dissipation rate were log-normally distributed, suggesting that the intermittent nature of small scale turbulence was accurately captured. The same conclusion could not be made from the ADCP measurements because the implementation of the spectral method yielded only one estimate of ϵ per speed bin. In this chapter[1], the four-beam integral method is applied over shorter time intervals in an attempt to estimate ϵ on ca. 5-minute time scales. The use of structure functions (SF)—which were introduced in Chapter 2—is also explored as a possible means of estimating the temporal variability in ϵ.

In principal, ϵ can be estimated from diverging-beam ADCP data using either spectral or structure function methods. Both methods require the measurement of velocity fluctuations in the inertial subrange (ISR) where the assumption of local isotropy holds. Spectral methods require a high sampling rate to ensure that the ISR is captured in time, whereas structure function (SF) methods require the flow to be isotropic over the range of spatial scales included in the spatial differences. At high Reynolds numbers, the ISR spans several wavenumber decades, implying that the assumption of local isotropy should hold over a

[1]The majority of this chapter was first published in:
McMillan, J. M., and A. E. Hay, Spectral and structure function estimates of turbulence dissipation rates in a high-flow tidal channel using broadband ADCPs, *J. Atmos. Oceanic Technol.*, 34, 5–20, 2017.

correspondingly wide range of spatial scales. Thus, both spectral and SF methods should be applicable in high tidal flow environments.

Second-order structure functions appear to have been first used to compute ϵ from along-beam ADCP velocity measurements by *Wiles et al.* (2006). The method has been implemented in several subsequent turbulence investigations using Doppler profilers positioned in bottom-mounted configurations (*Lorke*, 2007; *Whipple and Luettich*, 2009; *Simpson et al.*, 2011; *Collignon and Stacey*, 2013; *Thomson et al.*, 2012; *Simpson et al.*, 2015), on mooring lines (*Lucas et al.*, 2014; *Simpson et al.*, 2015), and on drifting platforms (*Thomson*, 2012). The method has been shown to give ϵ values that are in good agreement with those obtained using acoustic Doppler velocimeters (*Mohrholz et al.*, 2008) and microstructure profilers (*Wiles et al.*, 2006; *Lucas et al.*, 2014). *Mohrholz et al.* (2008) also found the ϵ values obtained from the third-order structure function to be consistent with the second-order estimates.

The application of SF methods specifically to broadband ADCP data warrants caution as Doppler noise levels may contribute to high standard deviations in the instantaneous velocity differences. In addition, bin sizes of $\mathcal{O}(1)$ m may not adequately resolve the ISR and the assumption of isotropy may only be applicable over a few range bins. This isotropy assumption is particularly limiting in sheared flows where anisotropy is argued to generate large discrepancies in the ϵ estimates obtained along the individual beams (*Wiles et al.*, 2006). For similar reasons, stratified conditions also limit the range over which SF methods can be applied because the production scale is limited by the Ozmidov scale. To overcome these challenges, previous studies (*Mohrholz et al.*, 2008; *Whipple and Luettich*, 2009; *Simpson et al.*, 2011; *Thomson*, 2012; *Lucas et al.*, 2014; *Simpson et al.*, 2015) used pulse-coherent ADCPs which provide high-accuracy measurements using smaller bin sizes at the price of a reduced profiling range.

Spectral methods may be less affected by Doppler noise than structure function methods because the mean square sum of two positively correlated random variables is larger in amplitude than the mean square difference. Therefore, one might expect the dissipation estimates from a spectral method to be less noisy than those from a structure function approach. Spectral methods, however, are typically applied to point measurements of two- or three-dimensional current velocities, and the application to ADCP data is limited by the orientation of the diverging beams. In standard operation, the ADCPs do not directly

measure the along-stream or cross-stream velocity fluctuations, for which the theoretical spectral forms are known. *Lorke and Wüest* (2005) applied the inertial dissipation method to both 3-beam and 4-beam ADCP data to obtain an upper limit on ϵ by fitting the along-beam velocity spectra in the inertial subrange to the expected form for cross-stream fluctuations. The method showed good agreement with microstructure measurements, however, a pulse-coherent mode was needed to capture the low turbulence levels ($\epsilon < 10^{-8}$ W kg^{-1}). In Chapter 4, it was shown that, at higher turbulence levels, dissipation rates could be estimated from broadband ADCP measurements by using a spectral "integral method" that accounted for both Doppler noise and the orientation of the ADCP relative to the mean flow. Speed-bin averaged dissipation rates were shown to agree—to within a factor of two—with ϵ values obtained using shear probes moored at mid-depth for 2.5 days.

In this chapter, the dissipation rates estimated using the spectral integral method and structure function methods are compared. The analysis is carried out using mid-depth measurements acquired at all four ADCP locations (Fig. 3.3). The only other known comparison is that by *Lorke* (2007), who compared ϵ estimated from ADCP data via both the inertial dissipation method (i.e., a spectral method) and the second-order SF method to results from co-located, single-point measurements obtained with an acoustic Doppler velocimeter. In contrast to the results presented here, Lorke's data were acquired in a low dissipation rate ($\epsilon < 10^{-8}$ W kg^{-1}), bottom boundary layer, lacustrine environment at short $\mathcal{O}(1)$ m range, using a Doppler profiler in pulse-coherent mode.

In addition to the comparisons of ϵ, spectral and structure function methods are used to address the following questions:

1) Do estimates of ϵ obtained using structure functions explain the factor of two discrepancy between the ADCP and shear probe measurements presented in Chapter 4?
2) Can intermittency in ϵ be assessed using broadband diverging-beam ADCPs?
3) Do the broadband Doppler noise levels estimated from the structure function and spectral methods agree?
4) Do broadband Doppler noise levels depend on mean flow speed?

5.1 Methods

Spatial differences in the along-beam velocity fluctuations, $\hat{v}_i'$, lead directly to longitudinal structure function estimates. Recalling that $\hat{v}_i' = v_i' + e_i$, and letting $\widehat{D}_{LL}$ be the mean square difference in the measured velocities, then Eqs. (2.25) and (2.30) can be combined to yield

$$\widehat{D}_{LL}(r) = a_i r^{2/3} + b_i, \tag{5.1}$$

where, under the assumptions of local isotropy and homogeneity of the turbulence, $a_i = C_2 \epsilon_i^{2/3}$ and $b_i = 2\sigma_{e_i}^2$. A least squares regression of $\widehat{D}_{LL}$ versus $r^{2/3}$ can be used to give

$$\epsilon_i = \left(\frac{a_i}{C_2} \right)^{3/2}, \tag{5.2}$$

for each of the beams. The four ϵ_i estimates when averaged give ϵ_{S2}, i.e., the estimate of dissipation rate from the second-order structure function method.

Similarly, Eqs. (2.25) and (2.29) can be combined to show that if the Doppler noise is uncorrelated with $\hat{v}_i'$, the third-order moments of the along-beam velocity differences $\widehat{D}_{LLL}$ are

$$\widehat{D}_{LLL}(r) = m_i r, \tag{5.3}$$

where $m_i = -\frac{4}{5}\epsilon_i$ for locally isotropic turbulence. A least squares regression of $\widehat{D}_{LLL}$ versus r yields

$$\epsilon_i = -\frac{5}{4} m_i, \tag{5.4}$$

for each beam. Again, the four estimates of ϵ_i when averaged give ϵ_{S3}.

As in Chapter 4, the frequency spectra, $\widehat{S}_{ii}(f)$, of the along-beam fluctuations $\hat{v}_i'$ can be used to determine the dissipation rate using an integral method (IM). Here the "4 beam" approach is implemented where the theoretical form of the spectra, based on Eq. (2.31), is given by

$$\widehat{S}_T(k) = C\epsilon^{2/3} k^{-5/3} + N_T, \tag{5.5}$$

where

$$\widehat{S}_T = \frac{|U|}{2\pi} \left(\widehat{S}_{11} + \widehat{S}_{22} + \widehat{S}_{33} + \widehat{S}_{44} \right), \tag{5.6}$$

$$N_T = \frac{|U|}{2\pi} \left(N_1 + N_2 + N_3 + N_4 \right), \tag{5.7}$$

and $|U|$ is the mean flow speed. The constant C in Eq. (5.5) is

$$C = \left(\frac{14}{3} \sin^2 \vartheta + \frac{16}{3} \cos^2 \vartheta \right) \alpha_1, \tag{5.8}$$

where ϑ is the angle of the beams with respect to the vertical and α_1 is the streamwise Kolmogorov constant. The dissipation rate can then be expressed as

$$\epsilon_{IM} = \left[C^{-1} \left\langle (S_T - N_T)\, k^{5/3} \right\rangle_{\text{ISR}} \right]^{3/2}, \tag{5.9}$$

where $\langle \cdot \rangle_{\text{ISR}}$ represents an average over the inertial subrange and the IM subscript is used to identify the method.

5.2 Results

In this chapter, the analyses are focused on the measurements at mid-depth, which was chosen to be 10 m above bottom at all sites. A vertical averaging interval of 5 m (i.e., 9 range bins) was used (Fig. 3.11, grey region), and the depth-averaged horizontal velocity over this interval is denoted by U_r. This depth interval was chosen because along-beam velocity spectra (Fig. 4.1b) for $|U_r| > 1$ m s^{-1} exhibit a $k^{-5/3}$ range for scales below 5 m, thus the assumption of local isotropy—which is fundamental for both the spectral and structure function methods—is applicable over this depth interval.

The principal flood and ebb directions based on the depth-averaged flow are shown relative to both true north and the ADCP beam axes in Fig. 3.6. With the exception of Site 2a, the frames were well aligned with the streamwise flow. The deviations between the mean flow direction and the axis of the closest beam pair at Sites 3, 2b and 1 were 0.04°, 1.3°, and 15°, respectively.

5.2.1 Dissipation Rates from a Second-Order SF Method

For each ensemble (7-minutes at Site 1, 5-minutes otherwise), along-beam differences in the velocity fluctuations were computed to obtain estimates of $\widehat{D}_{LL}$ at $z = 10$ m. Because the velocities measured in adjacent bins are not independent (*Gordon*, 1996), differences were computed for all possible combinations of along-beam distance, r, ranging from 1.1 m (2 bins) to 4.3 m (9 bins) within the averaging region. This method resulted in 28 values of $\widehat{D}_{LL}$ and differs from the centre-differencing scheme described by *Wiles*

Table 5.1: Percentage of data rejected for flows with $|U_r| > 0.8$ m s^{-1}.

Site	IM method	SF2 method	SF3 method
1	44	34	84
2a	42	21	77
2b	40	10	72
3	58	4	76

et al. (2005) and subsequently implemented by others (e.g., *Wiles et al.*, 2006; *Mohrholz et al.*, 2008; *Lanckriet and Puleo*, 2013). It was confirmed that the centre-differencing scheme, which would have yielded only 10 values of $\widehat{D}_{LL}$, gives comparable estimates of the dissipation rate. However, because the approach adopted here makes use of all possible values of $\widehat{D}_{LL}$ at a given separation, it results in tighter confidence intervals for the estimates of ϵ_i and σ_{e_i}. Using all possible values at a given separation is also consistent with the assumption that the turbulence properties are homogeneous and isotropic.

A least-squares regression to Eq. (5.1) was performed for each ensemble and the ϵ_i value for each beam was obtained using Eq. (5.2) with $C_2 = 2.0$. An example is shown in Fig. 5.2b. The averages of the four ϵ_i values are shown as purple points in Fig. 5.1. The uncertainty, $\Delta\epsilon_i$, was estimated from the 95% confidence intervals on the slope and data were rejected if $\Delta\epsilon_i/\epsilon_i > 0.6$. Values were also rejected if $b_i < 0$, which corresponds to a negative estimate of σ_{e_i}. When taking the average of ϵ_i computed from all four beams, the data rejection rate for $|U_r| > 0.8$m s^{-1} ranged from 4% to 34% (Table 5.1).

5.2.2 Dissipation Rates from a Spectral Method

For each ensemble (7-minutes at Site 1, 5-minutes otherwise), along-beam frequency spectral densities, $\widehat{S}_{ii}(f)$, were computed for each vertical bin using Hanning-windowed intervals of 20 points (approximately 11-13 s) with 50% overlap. This resulted in spectra with a frequency resolution of approximately 0.075 Hz and up to 100 degrees of freedom (*Nuttall*, 1971). Spectra were then averaged over the 4.5 m range interval centred at $z = 10$ m.

For each beam, the Doppler noise floor, N_i, was estimated by computing the average spectral density from $f \in [0.5f_N, f_N]$ for the lowest flow speeds ($|U_r| < 0.25$ m s^{-1}). The corresponding σ_{e_i} values were computed using Eq. (4.1) and the four-beam mean, $\overline{\sigma}_{e_i}$, and standard deviation, $\Delta\sigma_{e_i}$, at each site are summarized in Table 5.2. These values are all within 6% of the expected accuracy of 4.66 cm s^{-1}.

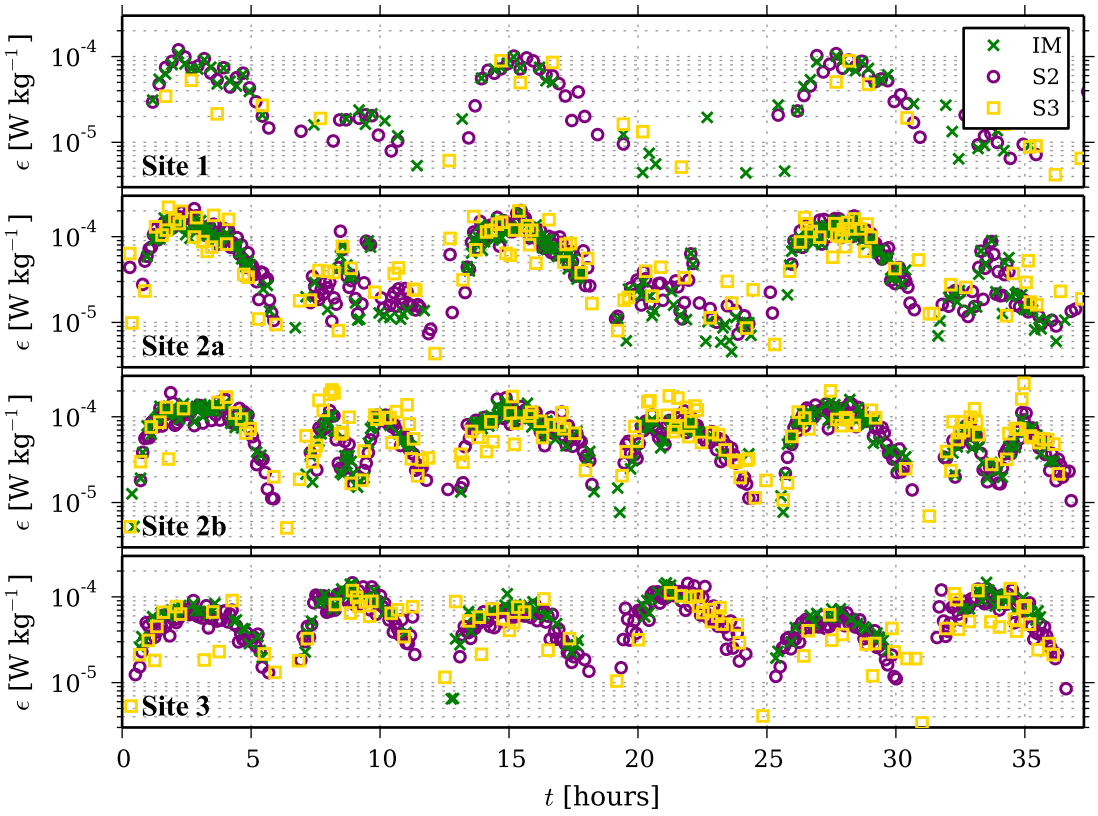

Figure 5.1: The computed dissipation rates over three tidal cycles at each location. In all subpanels, $t = 0$ coincides with the start of a flood tide and the corresponding year days are 212.1 (Site 1), 180.0 (Sites 2a and 2b), and 249.0 (Site 3). Gaps in the data correspond to ensembles for which the data were rejected (see Table 5.1).

Table 5.2: Summary of the computed Doppler noise levels. The IM column gives the four-beam mean $\overline{\sigma}_{e_i}$ and standard deviation $\Delta\sigma_{e_i}$ as computed from the velocity spectra at low flow speeds. The SF2 column gives the corrected values determined via Eq. (5.18), where the statistics are amongst all beams and all speed bins. The manufacturer-specified accuracy is 4.66 cm s^{-1}.

	IM	SF2
Site	$\overline{\sigma}_{e_i} \pm \Delta\sigma_{e_i}$ [cm s^{-1}]	$\widetilde{\overline{\sigma}}_{e_i} \pm \Delta\widetilde{\sigma}_{e_i}$ [cm s^{-1}]
1	4.58±0.08	4.55±0.12
2a	4.66±0.04	4.64±0.11
2b	4.81±0.03	4.77±0.09
3	4.92±0.02	4.98±0.08

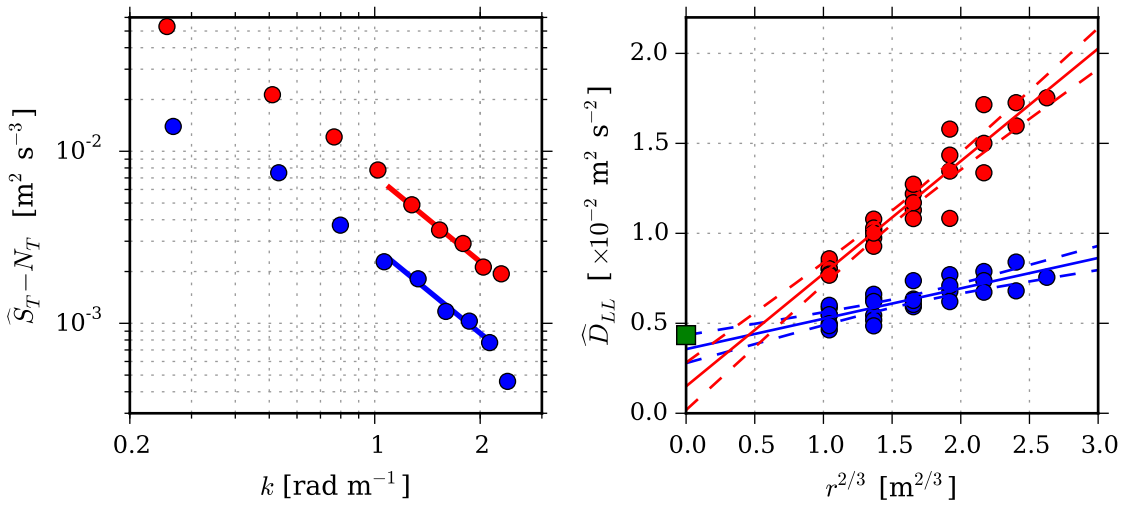

Figure 5.2: Representative data at Site 2a for $|U_r| = 2$ m s^{-1} on flood (red) and ebb (blue). The left panel shows the denoised velocity spectra with fits to Eq. (5.5) shown by the solid lines. The right panel shows the second-order structure functions (beam 3) with fits to Eq. (5.1) and 95% confidence intervals plotted as solid and dashed lines, respectively. The green square at $r = 0$ corresponds to the expected y-intercept based on the manufacturer-specified Doppler noise level.

The dissipation rate ϵ_{IM} was computed by applying Eq. (5.9) over the inertial subrange given by $k \in [1.1, 2.1]$ rad m^{-1}. The same wavenumber interval was used for all ensembles. Examples of the computed spectra are shown in Fig. 5.2b, and time series of the ϵ_{IM} values are shown in Fig. 5.1 (green points). A clear tidal modulation is apparent at all sites.

At low flow speeds, the low frequency resolution of the spectra resulted in only one spectral value in the inertial subrange. Consequently, data for these flow speeds were not given further consideration. Data were also rejected for ensembles for which the spectral shape of $\widehat{S}_T - N_T$ deviated from the expected -5/3 slope in the inertial subrange by more than 20%, i.e.

$$\frac{3}{5}|\zeta| > 0.2, \tag{5.10}$$

where ζ is defined such that $(\widehat{S}_T - N_T) \sim k^{-5/3+\zeta}$. For all sites, nearly half the data for $|U_r| > 0.8$ m s^{-1} were rejected on the basis of spectral shape (Table 5.1).

5.2.3 Comparison of Dissipation Rates from IM and SF2 Methods

The time series of the ϵ values (Fig. 5.1) from the second-order structure function method (purple points) and the spectral integral method (green points) track each other closely.

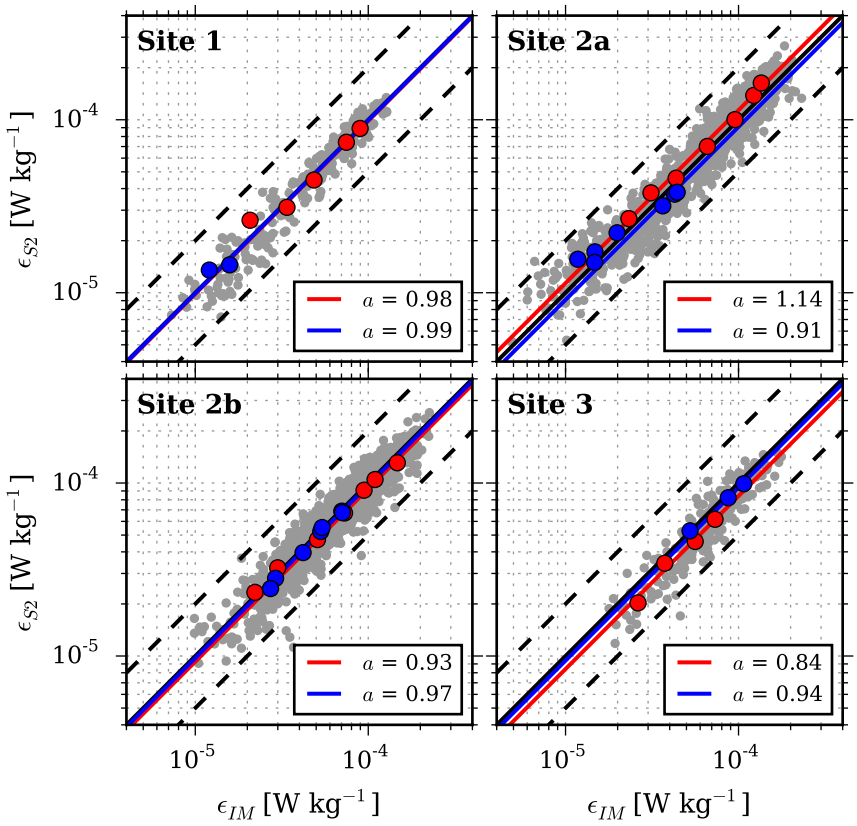

Figure 5.3: Comparison of the dissipation rates at each site as computed from the second-order structure function (ϵ_{S2}) and the integral method (ϵ_{IM}). Averages within 0.2 m s^{-1} speed-bins are plotted in red and blue for the flood and ebb tides, respectively. The values of the best-fit slope, a, to the speed bin averages are shown in the legend. The 1:1 line is solid black, whereas the 1:2 and 2:1 lines are dashed.

These estimates are plotted one against the other in Fig. 5.3 (gray points). The points corresponding to individual estimates are scattered about the 1:1 line, and are typically within a factor of two of each other (dashed lines). Speed-bin averaged dissipation rates were determined by averaging the ϵ values within 0.2 m s^{-1} speed-bins (Fig. 5.3, red and blue markers). The least-squares best fit lines indicate that the ϵ_{S2} values tend to be within 16% of the ϵ_{IM} values, with the tendency that $\epsilon_{S2}<\epsilon_{IM}$. The agreement between ϵ_{IM} and ϵ_{S2} at all four sites indicates that the methods are insensitive to the orientation of the ADCP relative to the flow direction. This is somewhat surprising as the IM method was derived under the assumption that one of the beam pairs is oriented close to the streamwise direction (Chapter 4).

Table 5.3: Mean $\overline{X}$ and standard deviations σ_X of $X = \log_{10}\epsilon$. Values are given with reference to 1 W kg^{-1}. The "SP" site is the location of the shear probe measurements (Fig. 3.3.)

Site	ϵ	**Flood**		**Ebb**	
		$\overline{X}$	σ_X	$\overline{X}$	σ_X
SP	-	-4.28	0.12	-5.11	0.26
1	ϵ_{IM}	-4.16	0.15	-4.88	0.22
	ϵ_{S2}	-4.17	0.17	-4.87	0.14
2a	ϵ_{IM}	-3.99	0.11	-4.50	0.33
	ϵ_{S2}	-3.96	0.13	-4.52	0.26
2b	ϵ_{IM}	-3.98	0.12	-4.26	0.24
	ϵ_{S2}	-4.00	0.12	-4.27	0.24
3	ϵ_{IM}	-4.20	0.09	-4.01	0.14
	ϵ_{S2}	-4.29	0.11	-4.03	0.12

5.2.4 Probability Density Functions of the Dissipation Rate

The probability density functions of $X = \log_{10}\epsilon$—computed for $|U_r| > 0.75\ \max(|U_r|)$—are provided in Fig. 5.4. The values for the mean, $\overline{X}$, and standard deviation, σ_X, of the PDFs are very similar for the IM and SF2 methods at each site (Table 5.3). In a similar comparison between the inertial dissipation method and the SF2 method, *Lorke* (2007) obtained log-normal distributions of ϵ using 21-minute temporal averages of pulse-coherent Doppler profiler data. The distributions for both methods had the same variance, however the mean value was 2.5 fold greater for the SF2 method. For the Grand Passage data, however, the mean values from the two methods are in close agreement (Table 5.3), differing in linear space by at most 23% in one instance (Site 3, flood) and by less than 5% in the remaining seven, with no systematic bias.

The variance, σ_X^2, of the PDFs is dependent on both the site and the tidal phase (i.e., ebb/flood). The widest distributions occur on the ebb tide at Sites 1, 2a and 2b. At these locations the vertical averaging region is just above the logarithmic layer on the ebb tide (Fig. 3.11), suggesting that time variations in the boundary layer thickness lead to increased variability in ϵ. The intermittency exponent μ is also larger because $\sigma_X^2 = \ln A + \mu \ln(\mathscr{L}/r)$ where A is a positive constant (*Pope*, 2000).

Standardized PDFs are shown in Fig. 5.5 for two speed ranges, and compared to the log-normal distribution that is expected for a high Reynolds number flow. For each site, tidal phase, and speed range, Y—given by $Y = \sigma_X^{-1}(X - \overline{X})$—was computed. The values

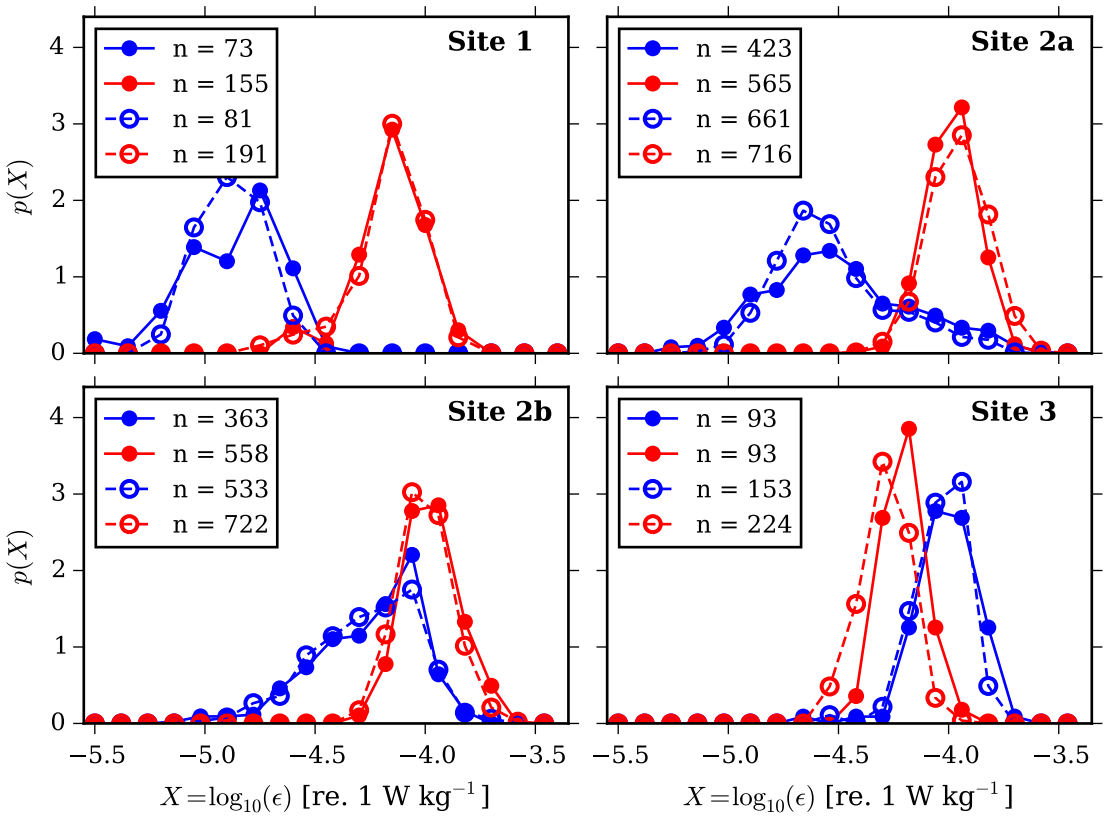

Figure 5.4: Histograms of dissipation rates for $|U_r| > 0.75 \max(|U_r|)$. Solid lines and filled circles indicate the IM method, dashed lines and open circles the SF2 method. Blue and red indicate ebb and flood, respectively. The number of ensembles n for each PDF is indicated in the legend.

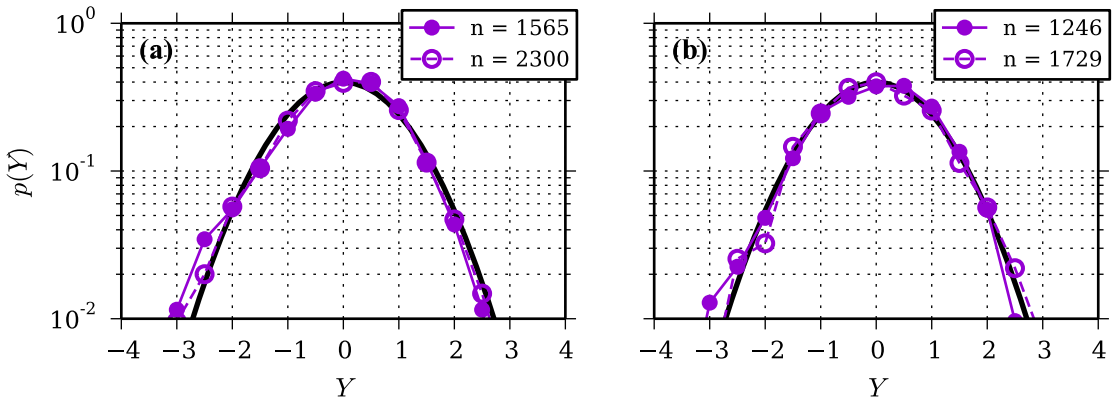

Figure 5.5: Standardized PDFs of $Y = \sigma_X^{-1}(X - \overline{X})$ for (a) $1.4 < |U_r| < 1.8$ m s^{-1}, and (b) $1.8 < |U_r| < 2.2$ m s^{-1}, where $X = \log_{10}\epsilon$. Solid lines and filled circles indicate the IM method, dashed lines and open circles the SF2 method. The number of ensembles n is indicated in the legend and the black curves are the normal distributions.

for ebb and flood at all four sites were then combined to yield better statistics. The resulting PDFs for both the IM and SF2 methods agree well with the log-normal distributions for both speed ranges. This further indicates that the intermittency in the dissipation rate is detectable in high speed flows using diverging-beam ADCP data.

5.2.5 Dissipation Rates from a Third-Order SF Method

Third-order structure functions, $\widehat{D}_{LLL}$, were computed using the same method and depth range described in Section 5.2.1. The values were regressed against Eq. (5.3) to determine ϵ_i using Eq. (5.4). The four ϵ_i values were then averaged to give ϵ_{S3}, and are shown as yellow squares in Fig. 5.1. The ϵ_{S3} values track the ϵ_{S2} estimates reasonably well. Data were rejected if $m_i > 0$, which gives a negative value for ϵ_i. This criterion resulted in 72% to 84% of the ϵ_{S3} estimates being rejected, indicating that, for these data, the third-order method is much less robust, despite the form of $\widehat{D}_{LLL}$—given by Eq. (5.3)—being independent of σ_{e_i}.

Despite the high percentage of data rejected for the third-order method, a comparison of ϵ_{S3} and ϵ_{S2} is relevant. The estimates from all four sites are shown one against the other in Fig. 5.6. The data are scattered about the 1:1 line, with the tendency that $\epsilon_{S3} > \epsilon_{S2}$. This bias was exhibited at all four sites. Because the theoretical form of the third-order structure function, given by Eq. (2.29), is known exactly and $\widehat{D}_{LLL}$ is independent of noise, these results validate the use of $C_2 = 2.0$. The ϵ_{S2} estimates would be 7% lower—resulting in a larger discrepancy between ϵ_{S3} and ϵ_{S2}—if a value of $C_2 = 2.1$ had been used.

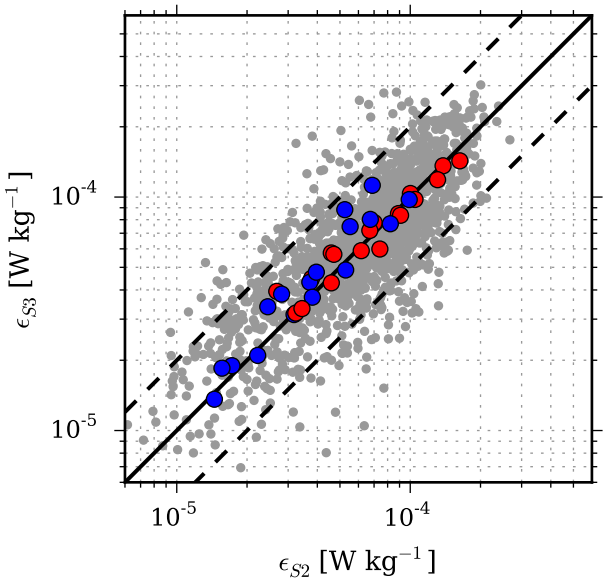

Figure 5.6: Comparison of the dissipation rates at all sites as computed from the third-order (ϵ_{S3}) and second-order (ϵ_{S2}) structure functions. Averages within 0.2 m s^{-1} speed-bins were computed separately for each site and are plotted in red and blue for the flood and ebb tides, respectively. The 1:1 line is solid black, whereas the 1:2 and 2:1 lines are dashed.

5.3 Discussion

5.3.1 Discrepancy with Shear Probe Estimates

One of the objectives of work related to this chapter was to determine whether the factor of two discrepancy between the estimates of ϵ from the shear probe and ADCP data (Chapter 4) could be attributed to the use of a spectrum-based method. The agreement between the IM and SF2 methods in both the means (Fig. 5.3) and the PDFs (Fig. 5.4) indicates otherwise. In addition, the third-order estimates—which are unaffected by noise and do not involve a universal constant—were higher than ϵ_{S2} (Fig. 5.6) and thus in greater disagreement with the shear probe results. These conclusions are further evidence that the observed differences are real and are likely explained by the 40 m spatial separation of the instruments.

The mean, $\overline{X}$, and standard deviation, σ_X, of the shear probe estimates of $X = \log_{10} \epsilon$ are included in Table 5.3 for additional comparison. The statistics are more different between the shear probe site and nearby Site 1 than between the SF2 and IM methods applied to the Site 1 data. However, the observation of a higher mean and lower variance on the flood tide compared to the ebb, is consistent with both the shear probe and ADCP

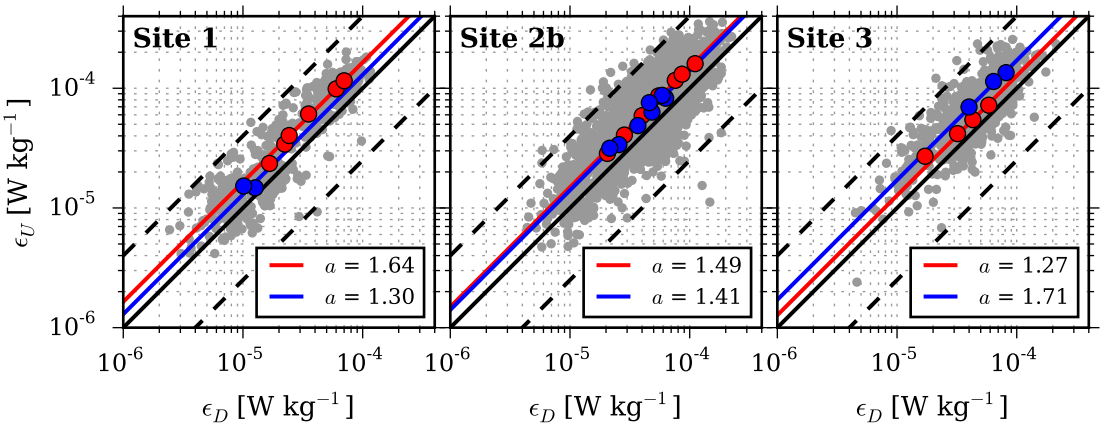

Figure 5.7: Comparisons of ϵ_i determined using the SF2 method for the upstream (ϵ_U) and downstream (ϵ_D) facing beams. The coloured markers and lines correpond to speed-bin averaged values and lines of best fit on the flood (red) and ebb (blue). The legend indicates best fit values of the slope, a, obtained by regression: i.e. $\epsilon_U = a\,\epsilon_D$. The solid black line is the 1:1 line and the dashed lines show the 4:1 and 1:4 relationships.

estimates of ϵ. Spatial variability in ϵ within the passage is also apparent in the differences between ADCP Sites 2a and 2b. The ADCPs at these sites were deployed concurrently about 190 m apart in the streamwise direction (Fig. 3.3). On the flood tide, both $\overline{X}$ and σ_X are comparable, whereas on the ebb tide, the dissipation rates are lower, but more variable, at Site 2a.

5.3.2 Streamwise Biases in SF2 Estimates

Wiles et al. (2006) found that dissipation rates were consistently higher for the upstream-facing beam. Dissipation estimates from the upstream- and downstream-facing beams in the Grand Passage data are compared in Fig. 5.7. Speed-bin averaged ϵ_i estimates from the upstream-facing beam tend to be greater than the downstream-facing beam by a factor ranging from 1.27 to 1.71, consistent with the observation by *Wiles et al.* (2006). Thus, there is a tendency for dissipation rates estimated via the SF2 method to be biased high in the upstream-facing direction relative to the downstream facing direction. An explanation for this result is provided below.

Consider an ADCP oriented such that beam 1 faces upstream into the flow and beam 2

downstream, then from Eq. (2.25), D_{LL} for each beam is given by

$$D_{11} = D_{uu}\sin^2\vartheta + D_{ww}\cos^2\vartheta - 2D_{uw}\sin\vartheta\cos\vartheta, \tag{5.11}$$

$$D_{22} = D_{uu}\sin^2\vartheta + D_{ww}\cos^2\vartheta + 2D_{uw}\sin\vartheta\cos\vartheta, \tag{5.12}$$

where D_{uu} and D_{ww} are the second-order moments of the streamwise and vertical velocity differences, respectively, and D_{uw} is given by

$$D_{uw} = \langle u_0' w_0' \rangle + \langle u_r' w_r' \rangle - \langle u_r' w_0' \rangle - \langle u_0' w_r' \rangle \,, \tag{5.13}$$

where u' and w' are the turbulent velocities at the positions denoted by the subscripts (e.g., $u_0' = u'(r_0)$). Because the correlations at spatially-separated points are expected to be less than the correlations at the same point, D_{uw} can be approximated as

$$D_{uw} \approx \langle u_0' w_0' \rangle + \langle u_r' w_r' \rangle \approx 2\langle u'w' \rangle \,. \tag{5.14}$$

Invoking the standard assumption of horizontal homogeneity of second-order moments of the turbulence (e.g., *Stacey et al.*, 1999), Eqs. (5.11), (5.12), and (5.14) can be combined to give $D_{11} - D_{22} \sim -4\langle u'w' \rangle$. Since $\langle u'w' \rangle < 0$ within the log-layer, the upstream facing beam is expected to yield a higher dissipation rate than the downstream facing beam. This result is consistent with the lines of best fit shown in Fig. 5.7: high Reynolds stresses of $-\langle u'w' \rangle \sim 3 \times 10^{-3}$ m^2 s^{-2} are associated with the flood tides at Sites 1 and 2b, and with the ebb tide at Site 3. These high Reynolds stresses—which yield equivalent dissipation rates of approximately 3×10^{-5} W kg^{-1} via Eq. (2.30)—occur when the mid-depth location ($z = 10$ m) is within the logarithmic layer (Fig. 3.11).

Assuming statistical homogeneity across the beams, the average of Eqs. (5.11) and (5.12) can be computed to eliminate the D_{uw} terms. This demonstrates that averaging the along-beam estimates of ϵ_i is important for achieving accurate results when implementing the structure function methods for diverging-beam ADCPs in situations where the Reynolds stress is significant.

5.3.3 Doppler Noise Levels

In the implementation of the IM method, the standard deviation of the Doppler noise σ_{e_i} is determined for each beam from the spectral levels at high frequencies and low flow

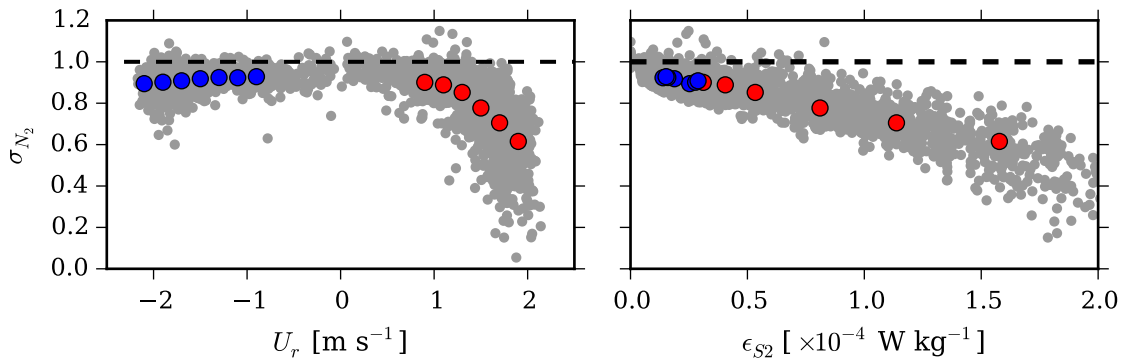

Figure 5.8: Normalized Doppler noise standard deviations, σ_{N_i}, as a function of flow speed (U_r, left) and dissipation rate (ϵ_{S2}, right) for beam 2 at Site 2a. Averages within 0.2 m s^{-1} speed-bins are plotted in red and blue for the flood and ebb tides, respectively. The black dashed line represents $\sigma_{N_i} = 1$, i.e. the expected value based on the velocity spectra at low flow speeds.

speeds (Table 5.2). To estimate ϵ_{IM} via Eq. (5.9), σ_{e_i} is assumed to be constant—i.e., speed-independent. On the other hand, the SF2 method yields an estimate of σ_{e_i} for each 5- to 7-min data record via $\sigma_{e_i} = \sqrt{b_i/2}$. Scatter plots of σ_{N_i}—i.e., σ_{e_i} normalized by the IM estimate for the appropriate beam—are shown in Fig. 5.8 as a function of both flow speed (left panel) and dissipation rate (right panel). Fig. 5.8 is representative of σ_{N_i} computed for all the beams at all ADCP locations, and not only shows that the speed-bin averages are all below the expected value of unity, but also that the σ_{N_i} estimates decrease with increasing flow speed and increasing dissipation rate. The 95% confidence limits on σ_{N_i} increase significantly with flow speed (not shown), and typically include unity. However, the increased uncertainty during strong flows cannot account for the observed systematic bias in the apparent noise levels.

The variation of the Doppler noise is the opposite of the expected trend: flow-speed dependent decorrelation mechanisms—advection and turbulence—are expected to yield higher Doppler noise levels at higher flow speeds (e.g., *Brumley et al.*, 1991). In addition, the correlations (see Appendix B) were essentially independent of flow speed and near the value of 128, which is the expected level for high quality velocity measurements (*Gordon*, 1996). The backscatter amplitude (see Appendix B) did increase slightly with increasing flow speed, however, the signal strength was nearly equal on both phases of the tide. Thus, the variation in the amplitude does not explain the flood/ebb asymmetry in σ_{N_i} that is apparent in Fig. 5.8 (and at other sites).

Insight into the low values of σ_{N_i} was obtained by applying the SF2 method to synthetic time series generated by a linear superposition of sinusoids of frequency f_i and amplitude $A_i = C_s f_i^{-5/6}$, where C_s is a constant dependent on the flow speed and dissipation rate. The phases of the frequency constituents were randomly distributed with uniform probability between 0 and 2π. The resulting time series yielded Gaussian-distributed velocities and spectral densities proportional to $\epsilon^{2/3} f^{-5/3}$, as in real, locally isotropic, homogeneous turbulence (*Batchelor*, 1953, p. 169). Additional noise with a Gaussian distribution and variance $\sigma_{v_b}^2$ was added to the time series to simulate the influence of Doppler noise. To apply the SF2 method, spatial lags, r, were computed using Taylor's hypothesis and the ϵ_i and σ_{e_i} values were determined via Eq. (5.1) for $r < 6$ m. The resulting noise levels $\overline{\sigma}_{N_i}$, based on 500 realizations for each specified dissipation rate, are shown in Fig. 5.9. The $\overline{\sigma}_{N_i}$ values follow the same trend with dissipation rate as the ADCP estimates, but—notably—the results from the synthetic time series are also dependent on the maximum frequency f_M included in the Fourier series. The dependence of $\overline{\sigma}_{N_i}$ on f_M indicates that the exclusion of the small scale motion may be influencing the value of the SF2 y-intercept.

Exactly how truncating the Fourier series affects the D_{LL} results is not readily obvious. Using the same notation as Section 5.3.2, the second-order structure function defined in Eq. (2.25) can be written as

$$D_{LL} = \left\langle u_0'^2 \right\rangle + \left\langle u_r'^2 \right\rangle - 2 \left\langle u_0' u_r' \right\rangle \approx 2 \left\langle u_0'^2 \right\rangle - 2 \left\langle u_0' u_r' \right\rangle , \tag{5.15}$$

where the assumption of homogeneity has been invoked. The influence of f_M on both $\langle u_0'^2 \rangle$ and $\langle u_0' u_r' \rangle$ was determined using the synthetic time series (described above) without the addition of Gaussian noise. For a given dissipation rate ϵ_o and flow speed $|U|$, decreasing f_M yielded a smaller variance, whereas the covariance remained constant (Fig. 5.10). Using values of $\epsilon_0 = 10^{-4}$ W kg^{-1} and $U = 2$ m s^{-1} for the synthetic time series, $\langle u_0'^2 \rangle$ was about 1% smaller for $f_M = 2$ Hz compared to $f_M = 16$ Hz. However, the corresponding decrease in D_{LL} was approximately 10%. Because the variance is independent of r, this decrease corresponds to a downward shift of the D_{LL} versus $r^{2/3}$ curve, yielding smaller b_i values, while the slopes, and hence ϵ_i, remain unaffected. This is consistent with the results shown in Fig. 5.11, where the dissipation rates computed from the noise-free synthetic time series are within 2% of the specified value ϵ_0. The y-intercepts, on the other hand, are

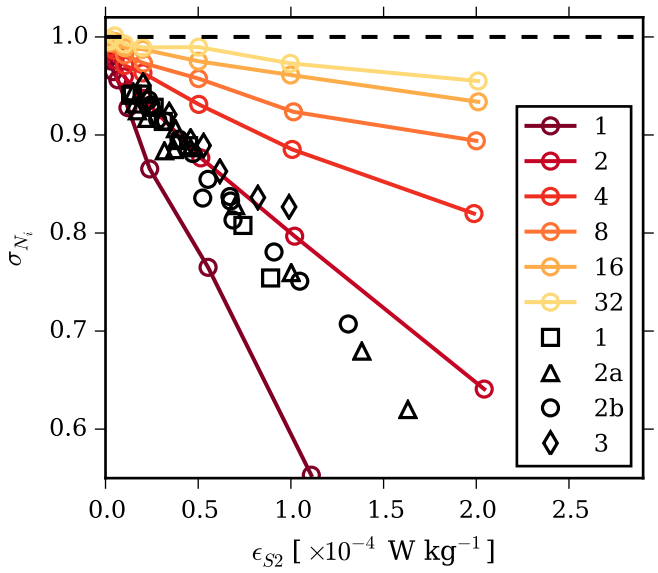

Figure 5.9: Normalized noise levels as a function of dissipation rate computed from the SF method applied to ADCP data (black markers) and the synthetic time series (coloured circles and lines). The ADCP markers represent averages amongst the four beams and within 0.2 m s^{-1} speed bins. The coloured circles represent the average values from 500 realizations of the synthetic time series. The legend indicates the maximum frequency, f_M, of the Fourier series (in Hz) and the ADCP deployment sites.

less than zero and strongly dependent on f_M and ϵ_0.

Given the maximum frequency in the time series is f_M, let $r_m = |U| f_M^{-1}$ be a representative scale of the unresolved eddies. A modified SF2 method is introduced by assuming that the velocity fluctuations associated with an eddy of size r_m scale as

$$u'_m \sim (\epsilon r_m)^{1/3}, \tag{5.16}$$

with a corresponding variance $\langle u'^2_m \rangle = 0.5|u'_m|^2 = 0.5K\,(\epsilon r_m)^{2/3}$, where K is a scaling factor of order one. Writing the true variance as the sum of the resolved and unresolved components, yields

$$\widehat{D}_{LL}(r) = C_2 \epsilon_i^{2/3} r^{2/3} + 2\widetilde{\sigma}^2_{e_i} - K(\epsilon r_m)^{2/3}, \tag{5.17}$$

where the tilde is used to distinguish the corrected Doppler noise standard deviation $\widetilde{\sigma}_{e_i}$ from the value determined via Eq. (5.1).

The value of K was determined by applying the SF2 method to synthetic time series

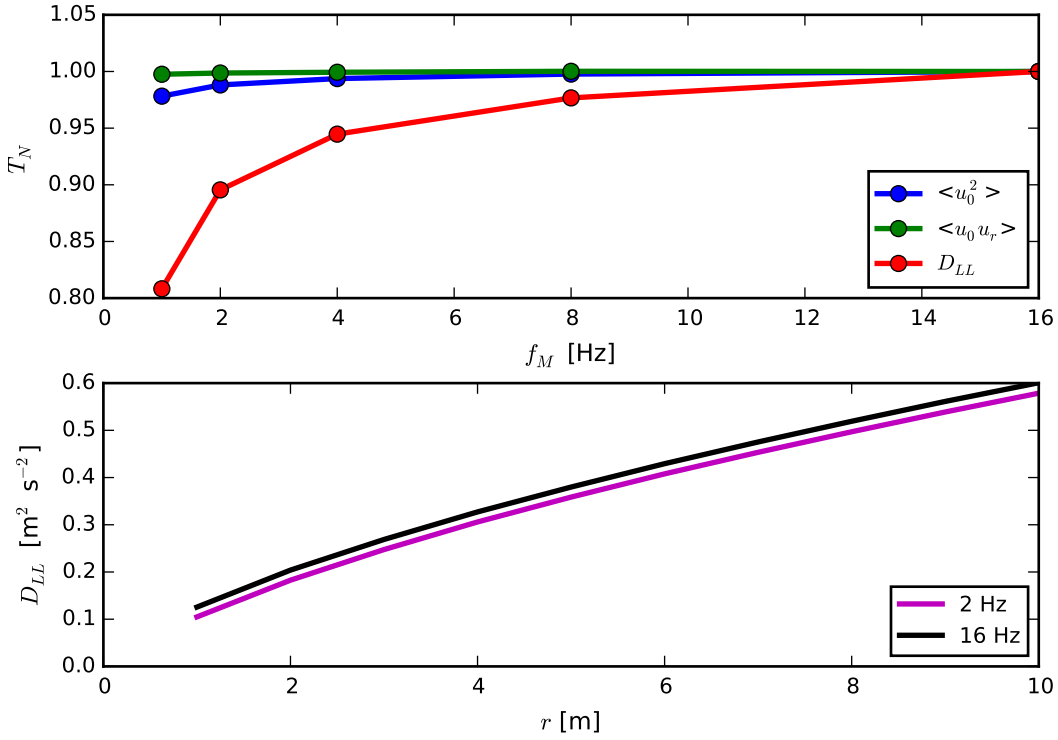

Figure 5.10: Effects of truncating the Fourier series on the second-order structure function as determined using 100 realizations of synthetic time series generated with $U = 2$ m s^{-1} and $\epsilon_0 = 10^{-4}$ W kg^{-1}. (Top panel) The variance $\langle u_0^2 \rangle$, covariance $\langle u_0 u_r \rangle$ and D_{LL} terms evaluated at $r = 2$ m where each term T_N is normalized by its value at 16 Hz. (Bottom panel) Computed D_{LL} curves as a function of r.

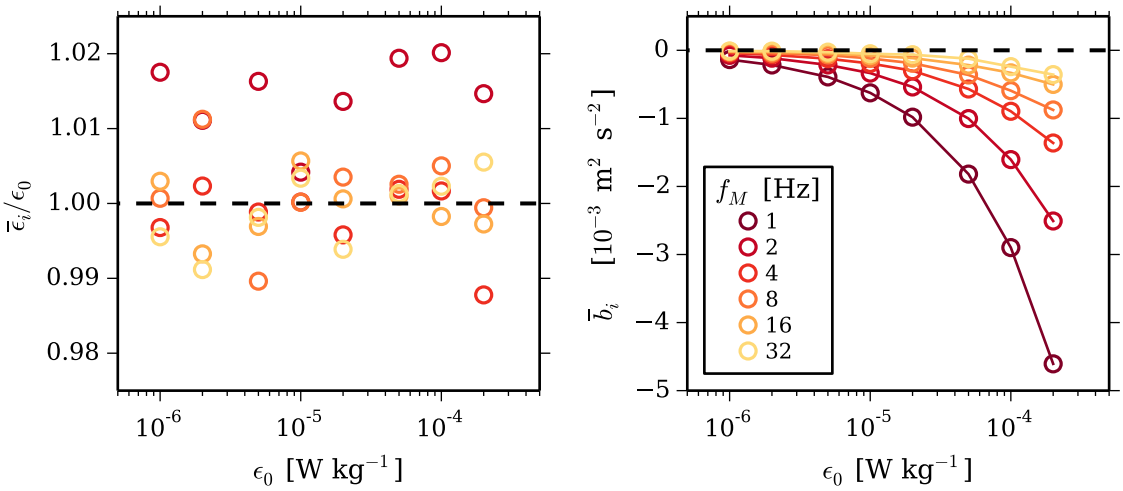

Figure 5.11: Average dissipation rate ($\bar{\epsilon}_i$, left) and y-intercept ($\bar{b}_i$, right) computed by applying the SF2 method to 500 realizations of a synthetic time series generated with a mean flow speed $|U| = 2$m s^{-1}, dissipation rate ϵ_0, and maximum frequency f_M.

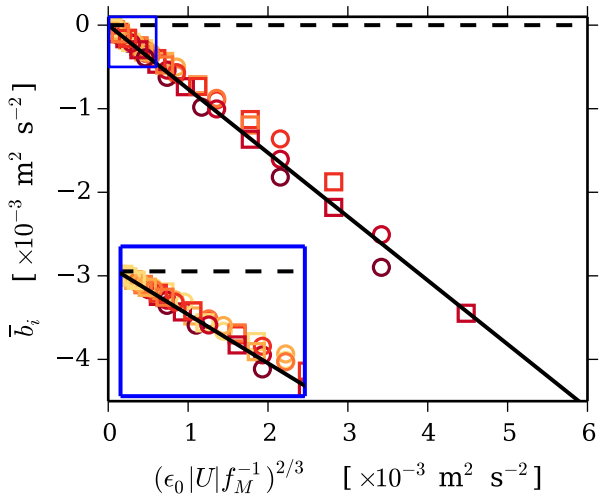

Figure 5.12: Average y-intercept, $\overline{b}_i$, computed by applying the SF2 method to 500 realizations of a synthetic time series with mean flow speeds of 2 m s^{-1} (circles) and 3 m s^{-1} (squares). The colours correspond to the f_M values given in Fig. 5.11. The solid black line is $\overline{b}_i = -K\left(\epsilon_0 |U| f_M^{-1}\right)^{2/3}$ with $K = 0.764$ determined using a least-squares regression. The inset highlights the data near the origin. The dashed black line is $\overline{b}_i = 0$.

with various $|U|$, ϵ_0, and f_M. Since no noise was added, then $\widetilde{\sigma}_{e_i}^2 = 0$, and it is expected that $b_i = -K\left(\epsilon_0 r_m\right)^{2/3}$. The results from all combinations of input parameters are shown in Fig. 5.12. It is clear that a linear relationship holds for the range of values considered. By least squares regression, $K = 0.764$, and importantly, this value is independent of the mean speed, maximum frequency, and dissipation rate.

Because of the finite ADCP pulse length, eddies smaller than twice the range bin size cannot be resolved. Thus, an ADCP acts as a low-pass filter, having a similar effect to the truncation of a Fourier series. Using $K = 0.764$ and $r_m = 1.06$ m—i.e., the minimum resolvable scale along the beam axis with a 0.5-m user-specified vertical cell size and 20° beam angle—the corrected Doppler noise levels from the ADCP data are determined via

$$\widetilde{\sigma}_{e_i} = \sqrt{\sigma_{e_i}^2 + \frac{K}{2}\left(\epsilon_i r_m\right)^{2/3}}. \tag{5.18}$$

Applying this correction yields $\widetilde{\sigma}_{N_i}$ values that range between 0.96 and 1.02 for all sites and—importantly—show no systematic trend with dissipation rate (Fig. 5.13). The average and standard deviation of $\widetilde{\sigma}_{e_i}$ amongst all beams and speed bins are reported in Table 5.2. For all sites, the values agree with the estimates determined from the IM method.

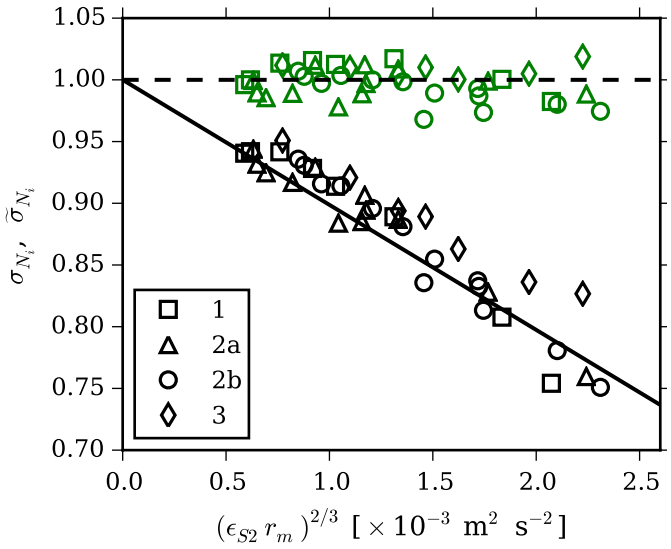

Figure 5.13: Normalized Doppler noise standard deviations for all four sites. The plotted values are averages amongst the four beams where the black and green markers correspond to the uncorrected (σ_{N_i}) and corrected ($\widetilde{\sigma}_{N_i}$) values, respectively. The marker shapes correspond to the sites as indicated in the legend. The solid black line is the expected value of σ_{N_i} based on the modified SF2 method and the manufacturer-specified accuracy, i.e. $\sigma_{N_i} = \left[1 - 0.5\sigma_{v_i}^{-2} K(\epsilon_{S2} r_m)^{2/3}\right]^{1/2}$ with $K = 0.764$.

5.4 Conclusions

Broadband ADCP data from mid-depth at four locations within a high flow tidal channel have been used to compare dissipation rates computed using spectral and structure function methods. The results indicate that the spectral integral method (IM) and the second-order structure function (SF2) method yield speed-bin averaged dissipation rates that agree to within 16%, depending on the location and flow direction (ebb vs. flood) with the tendency that $\epsilon_{S2} < \epsilon_{IM}$. The agreement between the methods appears to be independent of the orientation of the ADCP relative to the mean flow direction.

The dissipation rate estimates from the IM and SF2 methods provide the following answers to the questions posed in the introduction:

1) Because the ϵ_{IM} and ϵ_{S2} estimates agree to within 16%, the factor of two discrepancy between the ADCP and shear probe measurements found in Chapter 4 cannot be attributed to a particular analysis method. Consequently, spatial (i.e., cross-channel) variability in turbulence statistics remains the likely explanation for the observed

discrepancy.

2) The dissipation rate computed from broadband ADCP measurements is log-normally distributed as expected for high Reynolds number flows, indicating that the intermittency in ϵ on 5-minute time scales can be captured using broadband diverging-beam ADCPs.

3) The apparent Doppler noise levels σ_{e_i} computed using the traditional SF2 method decrease with increasing dissipation rate and are lower than the values determined from the IM method. It is shown that the low-pass filtering effect associated with the finite ADCP pulse length (and therefore cell size) results in a $\mathcal{O}(1\%)$ reduction in the measured variance, which in turn shifts the $\widehat{D}_{LL}$ versus $r^{2/3}$ curve downward, yielding smaller σ_{e_i} values, while not affecting ϵ_i. A modified SF2 method—that accounts for the unresolved variance and involves a constant factor K—yields noise levels that are in agreement with the estimates from the IM method. The 0.764 value of K used to correct the ADCP noise levels was determined from synthetic time series generated by a Fourier series representation of inertial subrange turbulence.

4) The corrected SF2 noise level estimates show no dependence on flow speed or dissipation rate. This result is consistent with the use of a constant spectral noise level in the IM method.

The results of this work validate the use of $C_2 = 2.0$ for the SF2 universal constant, which is consistent with the estimate of $\alpha_1 = 0.5$ obtained by *Sreenivasan* (1995) for the Kolmogorov constant in the streamwise velocity spectrum. Had a value of $C_2 = 2.1$—frequently used in previous studies—been implemented, the ϵ_{S2} values would have been 7% lower and resulted in greater discrepancy with the ϵ_{IM} estimates. In addition, the third-order SF—which does not involve an empirical constant—showed good agreement with the ϵ_{S2} estimates, with the tendency that $\epsilon_{S2}<\epsilon_{S3}$. The SF3 method, however, was less robust with a rejection rate that exceeded 72% at all sites.

The results of this work indicate that the SF2 method can be more robust in comparison to the IM method when estimating ϵ on 5-min time scales from broadband ADCP data in high speed tidal flows. For these data, the SF2 method yields reliable estimates of ϵ for up to 90% of the ensembles, compared with a maximum of 60% for the IM method.

Regardless of the choice of method, broadband ADCPs can be used to estimate ϵ remotely, provided stratification and vertical velocity shear are both sufficiently weak. It is

expected that these results—which specifically considered the estimation of ϵ on shorter time scales corresponding to intermittency (in the statistical sense)—can be extended to examine variability on longer time scales corresponding to tidal frequencies.

CHAPTER 6

TEMPORAL AND SPATIAL VARIATIONS IN THE TKE BALANCE

In this chapter, insight into the dynamics that drive the spatial and temporal variability in ϵ and other turbulence parameters is obtained by estimating the dominant terms in the turbulent kinetic energy (TKE) equation at the four ADCP locations. The TKE, production, dissipation, and transport terms are computed throughout the water column, and the energy balance during peak flood and ebb conditions is discussed. Spatial variability and ebb/flood asymmetries are shown to be related to the RMS upstream bottom roughness, and temporal variability at Site 2b is shown to be dependent on the upstream flow direction.

The governing equation for TKE in an unstratified boundary layer (Section 2.1.2) is given by

$$\frac{D}{Dt}\left(\frac{q^2}{2}\right) = T_d + T_p + \mathcal{P}_h - \epsilon. \tag{6.1}$$

For steady conditions over a uniform bed, it is typically assumed that the left hand side and the transport terms (T_p and T_d) are small, yielding a balance between $\mathcal{P}_h$ and ϵ.

The validity of $\mathcal{P}_h = \epsilon$ in tidal flows has been investigated in several studies using a variety of approaches and instrumentation (*Lu et al.*, 2000; *Rippeth et al.*, 2003; *Walter et al.*, 2011; *Thomson et al.*, 2012; *Korotenko et al.*, 2013; *Talke et al.*, 2013). The results from the cited studies are inconclusive and site-dependent. *Lu et al.* (2000) and *Thomson et al.* (2012) used measurements at $z = 15$ and 5 m, respectively, to show that there was significant scatter in $\mathcal{P}_h/\epsilon$, with the rates agreeing to within a factor of 5. On the other hand, *Rippeth et al.* (2003) concluded that the production rate was consistently 1.5 fold greater than the dissipation rate for $z > 4$ m, whereas *Walter et al.* (2011) found that $\mathcal{P}_h$

was consistently smaller than ϵ by a factor of 3 at $z = 1$ m. The most recent measurements by *Korotenko et al.* (2013) and *Talke et al.* (2013), both yielded $\mathcal{P}_h/\epsilon$ ratios that varied through the water column: for strong flows, $\mathcal{P}_h/\epsilon$ ranged from 5–10 near the bed and decreased with height to unity near mid-depth.

An imbalance between $\mathcal{P}_h$ and ϵ suggests that other terms in the TKE equation are significant. In particular, for a high Reynolds number flow in a channel with variable bathymetry, advection in the streamwise direction is expected to be significant, and greater than that in the lateral and vertical directions. In addition, the vertical diffusive transport, T_d, is likely non-negligible, whereas the pressure transport term, T_p—i.e., the vertical gradient of $\langle P'w' \rangle$ (Eq. 2.9)—is expected to be small, except near the surface where pressure fluctuations may be correlated with upwelling motion (*Stacey*, 2003). Direct numerical simulations of channel flow over smooth walls yield T_p that is an order of magnitude smaller than both $\mathcal{P}_h$ and ϵ for $z < 15\nu/u_*$, and T_d is negligible at greater distances from the bed (*Kim et al.*, 1987; *Alfonsi et al.*, 2016). These assumptions allow Eq. (6.1) to be written as

$$\frac{\partial}{\partial t}\left(\frac{q^2}{2}\right) + U\frac{\partial}{\partial x}\left(\frac{q^2}{2}\right) = T_d + \mathcal{P}_h - \epsilon. \tag{6.2}$$

For steady flows it can be further assumed that the time derivative is small, yielding a balance between advection, production, dissipation and transport.

In this chapter, the time rate of change in TKE and the terms on the right hand side of Eq. (6.2) are computed. Relevant background information is presented in Section 6.1 and the methods for estimating the turbulence parameters from ADCP data are outlined in Section 6.2. The results are presented in Section 6.3. More specifically, the time variability in the turbulence parameters is described, and averages of T_d, $\mathcal{P}_h$, and ϵ are computed for the one-hour interval centred on peak ebb and flood conditions. In Section 6.4, the results are compared to previous studies, and the influence of the upstream roughness and flow direction is discussed. Concluding remarks are given in Section 6.5.

6.1 Background

The vertical variation in turbulence parameters in open channels and boundary layers has been examined in previous studies. At high-Reynolds numbers, the turbulence structure

over smooth- and rough-walls is self-similar outside of the region nearest the bed (*Raupach et al.*, 1991). In particular, second-order turbulence statistics reduce to universal forms when scaled by the friction velocity, u_*, and a relevant length scale. The appropriate scaling is dependent on the height above bed and is shown schematically in Fig. 6.1. The framework used here combines that used by *Nezu and Nakagawa* (1993) for open channel flows, and by *Raupach et al.* (1991) for rough wall turbulent boundary layers. The fundamental properties of each of the layers are as follows:

1) *Roughness sublayer*: The turbulence parameters are controlled by viscosity and the properties of the roughness elements. The relevant velocity scale is u_*. For a smooth wall, the corresponding length scale is ν/u_*, whereas for a rough wall, additional length scales associated with the dimensions of the roughness elements are required to characterize the flow. The height of the bathymetric features, h, is referred to as the roughness height. In tidal channels with high Reynolds number flows, $h >> \nu/u_*$, and hence, viscous effects are negligible throughout most of the roughness sublayer. The vertical extent of the layer is dependent on h, as well as both the lateral dimension and the spacing between the roughness elements. A typical range of $z \approx 2h$ to $5h$ has been observed in wind tunnel experiments with uniform roughness elements (*Raupach et al.*, 1991). This region is also called the "wall region" (*Nezu and Nakagawa*, 1993) or "surface layer" (*Tennekes and Lumley*, 1972).

2) *Equilibrium layer*: An intermediate region where the turbulence dynamics are neither controlled by the small roughness elements or the boundary layer thickness, δ. Thus, the relevant scales are z and u_*. Within the equilibrium layer, the Reynolds stress is constant, and the rates of production and dissipation are approximately equal. *Raupach et al.* (1991) used measurements in wind tunnels to conclude that the constant stress region was confined to $z < 0.2\delta$, where δ is defined as the height at which the Reynolds stress reduces to zero. It is expected that the thickness of the equilibrium layer is dependent on the Reynolds number, i.e., this region is analogous to the inertial subrange in the spectral distribution (*Tennekes and Lumley*, 1972). This region is also referred to as the "intermediate region" (*Nezu and Nakagawa*, 1993, e.g) or "inertial sublayer" (*Tennekes and Lumley*, 1972).

3) *Log-layer*: The velocity profile is logarithmic and the Reynolds stress decreases

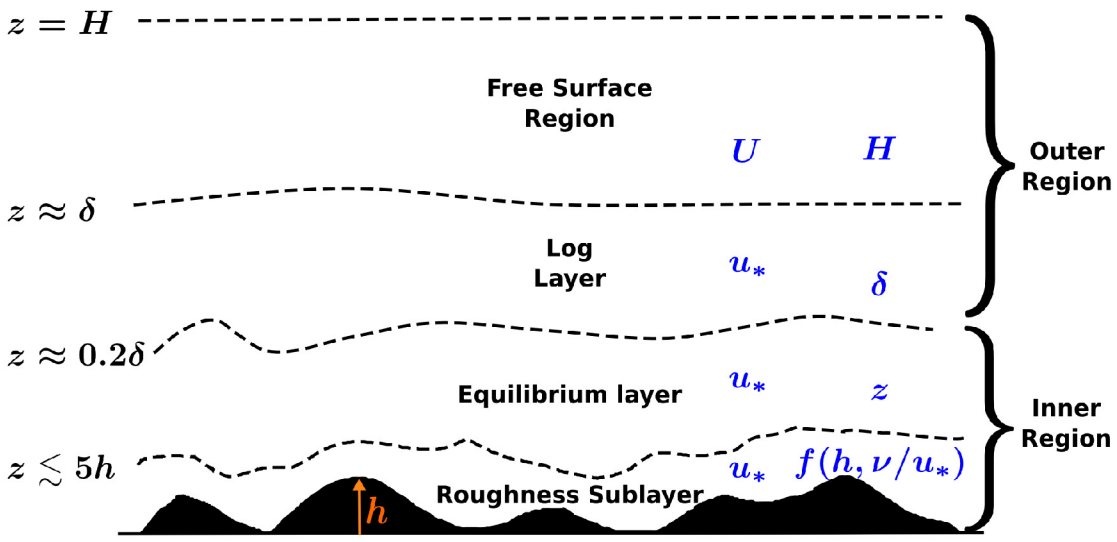

Figure 6.1: Subdivision of the water column into regions referred to in the text. The relevant velocity and length scales are given in blue and the approximate height of each layer is based on *Raupach et al.* (1991).

linearly with height above bottom, reducing to zero at $z = \delta$. The turbulence properties are not strongly influenced by the properties at the bed and the characteristic eddies scale with δ and u_*. In boundary layer flows—where a free surface does not exist—the "outer region" consists of the log-layer only.

4) *Free surface region*: The velocity profile is nearly uniform and the relevant scales are the mean velocity, U, and the flow depth, H. Turbulence is expected to be low in this region in the absence of breaking surface gravity waves.

6.2 Methods

The along-beam ADCP velocity measurements were used to estimate the turbulence parameters (q^2, $\mathcal{P}_h$, ϵ, T_d) throughout the water column at each of the ADCP locations. The dissipation rate was estimated using the modified second-order structure function method introduced in Chapter 5 (Eq. 5.17). The TKE and production terms were computed using the variance method (see Section 6.2.1), and the vertical diffusive transport was estimated by summing the third order moments of the along-beam velocity measurements (see Section 6.2.2). Because these methods rely on assumptions regarding both the anisotropy of the flow, and the statistical homogeneity of the velocity moments across the beam spread,

they provide a first-order approximation to the turbulence quantities. Quantification of the errors and uncertainties is limited to assessing the variability in the estimates across multiple tidal cycles.

6.2.1 Variance Method (Reynolds Stresses, Production, and TKE)

The variance method was first introduced by *Plueddemann* (1987) and *Lohrmann et al.* (1990), and has been implemented in many studies to estimate the Reynolds stresses and TKE using standard diverging-beam ADCP data (e.g., *Stacey et al.*, 1999; *Lu et al.*, 2000; *Rippeth et al.*, 2003). Assuming that (1) the second-order statistical properties of the flow are homogeneous across the beam spread, and (2) that differences in the along-beam noise levels are small, then differences of the along-beam velocity variances (Eqs. 4.2–4.5) yield

$$-\left\langle u_I' w_I' \right\rangle = \frac{\sigma_{v_2}^2 - \sigma_{v_1}^2}{2\sin 2\vartheta}, \tag{6.3}$$

$$-\left\langle v_I' w_I' \right\rangle = \frac{\sigma_{v_4}^2 - \sigma_{v_3}^2}{2\sin 2\vartheta}, \tag{6.4}$$

which are the Reynolds stresses in instrument coordinates (defined in Appendix F). By computing the vertical shear of the mean velocity components, $\langle u_I \rangle$ and $\langle v_I \rangle$, the total turbulent production, $\mathcal{P}_h$, can be estimated by

$$\mathcal{P}_h = -\left\langle u_I' w_I' \right\rangle \frac{\partial \left\langle u_I \right\rangle}{\partial z} - \left\langle v_I' w_I' \right\rangle \frac{\partial \left\langle v_I \right\rangle}{\partial z}. \tag{6.5}$$

The sum of the along beam velocity variances (Eqs. 4.2–4.5) yields

$$\sum_{i=1}^{4} (\sigma_{v_i}^2 - \sigma_{e_i}^2) = 2\sin^2\vartheta(\sigma_{u_I}^2 + \sigma_{v_I}^2) + 4\cos^2\vartheta\sigma_{w_I}^2, \tag{6.6}$$

which gives an estimate of the TKE

$$\frac{q^2}{2} = \frac{\gamma_2 + 1}{4\sin^2\vartheta}\left[1 + \frac{2\gamma_2}{\tan^2\vartheta}\right]^{-1}\left(\sum_{i=1}^{4}(\sigma_{v_i}^2 - \sigma_{e_i}^2)\right), \tag{6.7}$$

where

$$\gamma_2 = \frac{\sigma_w^2}{\sigma_u^2 + \sigma_v^2}, \tag{6.8}$$

is a measure of the anisotropy, ranging from 0 for highly anisotropic turbulence to 0.5 for

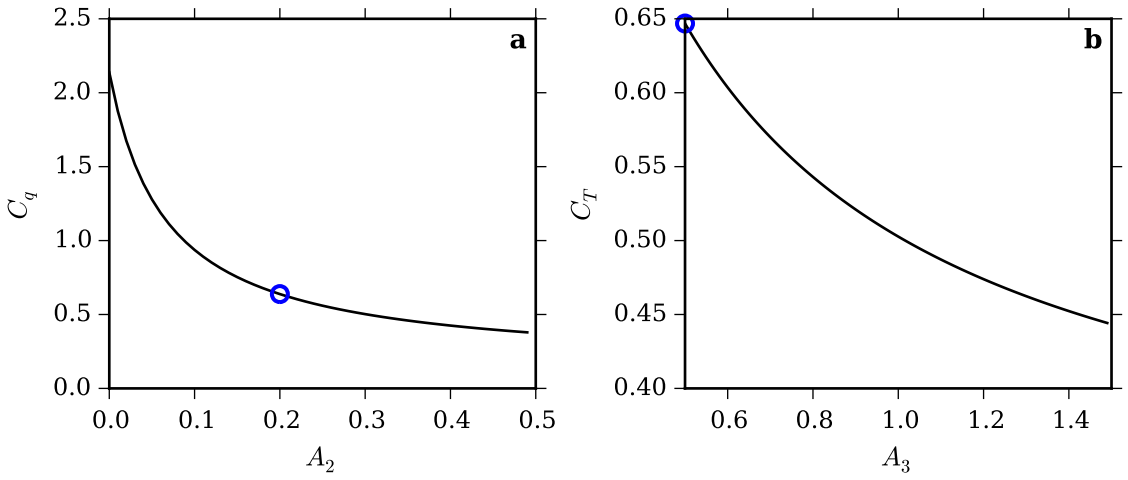

Figure 6.2: Coefficients C_q and C_T for the estimation of (a) TKE and (b) T_d as a function of the appropriate anisotropy ratio with $\vartheta = 20°$. The blue markers indicate the values used in this thesis.

fully isotropic conditions. For an ADCP with a beam angle of $\vartheta = 20°$, the coefficient, C_q, defined as

$$C_q = \frac{\gamma_2 + 1}{4 \sin^2 \vartheta} \left[1 + \frac{2\gamma_2}{\tan^2 \vartheta} \right]^{-1}, \tag{6.9}$$

varies by a factor of five over the possible range of γ_2 values (Fig. 6.2a), thus the TKE estimates are sensitive to the value of γ_2. Using two coupled ADCPs in a 17 m deep tidal river, *Vermeulen et al.* (2011) showed that γ_2 increased with distance away from the bed. On the ebb tide, the mean values ranged from 0.15 to 0.21, whereas the corresponding range on the flood tide was 0.2 to 0.4. A constant value of 0.2 has been used in several studies in tidal channels (*Stacey et al.*, 1999; *Lu and Lueck*, 1999; *Osalusi et al.*, 2009).

The TKE estimates must include a correction for the Doppler noise variance, $\sigma_{e_i}^2$, estimated here using a spectral method. For each depth and beam, the velocity spectra for the lowest flow speeds ($|U_c| < 0.2$ m s^{-1}) are computed, and the average spectral level, N_i, from $f \in [0.5 f_N, f_N]$ is determined, where f_N is the Nyquist frequency (see Appendix D for details). The variance is then given by $\sigma_{e_i}^2 = N_i f_N$.

6.2.2 Vertical Diffusive Transport

The vertical diffusive transport, T_d, was defined in Eq. (2.10) as

$$T_d = -\frac{1}{2} \frac{\partial F_d}{\partial z}, \tag{6.10}$$

where $F_d = \langle w' q^2 \rangle$ is the vertical diffusive flux of TKE. For energetic conditions where the signal-to-noise ratio is high, *Stacey* (2003) introduced a method to estimate T_d from the third-order moments of the along-beam velocities, showing that the flux can be written as

$$F_d = -C_T \left[\left\langle v_1'^3 \right\rangle + \left\langle v_2'^3 \right\rangle + \left\langle v_3'^3 \right\rangle + \left\langle v_4'^3 \right\rangle \right], \tag{6.11}$$

where C_T is a coefficient that involves triple products of $\cos\vartheta$ and $\sin\vartheta$. For a four-beam ADCP with a beam angle of $\vartheta = 20°$, C_T is given by

$$C_T = \frac{1 + \gamma_3}{0.6595 + 3.3191\gamma_3}, \tag{6.12}$$

where γ_3 is an anisotropy factor for the third-order moments defined as

$$\gamma_3 = \frac{\langle w'^3 \rangle}{\langle w' u'^2 \rangle + \langle w' v'^2 \rangle}. \tag{6.13}$$

Stacey (2003) used the results from the DNS simulations of *Briggs et al.* (1998) to suggest that γ_3 ranges between 0.5 for perfectly isotropic conditions to 1.5 for the highly anisotropic conditions within a density interface. For $\vartheta = 20°$, the corresponding C_T values span a range of 1.5 (Fig. 6.2b). An upper limit for F_d can be obtained using $\gamma_3 = 0.5$, and thus $C_T = 0.65$. The estimate of T_d can then be obtained from Eq. (6.10), using a centre differencing approach to compute the vertical derivative.

Stacey (2003) showed that the estimates of T_d obtained using Eqs. (6.10) and (6.11) agreed well with those made directly using measurements from a nearby ADV; however, sufficient averaging was required to reduce the large uncertainties generated by high Doppler noise levels. Using a pulse-coherent ADCP, which has lower noise levels than a standard broadbeam ADCP, *Talke et al.* (2013) obtained estimates of T_d that were comparable to $\mathcal{P}_h - \epsilon$, as expected for steady flow in a boundary layer where advection is small (Eq. 6.2).

6.3 Results

6.3.1 Time Series of TKE, Production, Dissipation, and Transport

For each 5- or 7-minute ensemble, the Reynolds stresses and F_d, $\mathcal{P}_h$, and ϵ were computed using the methods described in Section 6.2. One-day time series of these parameters at

each of the sites are shown in Fig. 6.3. To allow comparison among the sites, the Reynolds stresses were converted to frame coordinates—i.e., (x_F, y_F, z_F)—which are identical to instrument coordinates, except for a 90-degree rotation at Sites 1 and 2b to preserve $u > 0$ on the flood tide (See Fig. 3.6, Table A.1). Because the ADCPs at Sites 1, 2b, and 3 were well-aligned with the flow direction (Fig 3.6), the along-channel and transverse Reynolds stresses can be approximated by $-\langle u'_F w'_F \rangle$ and $-\langle v'_F w'_F \rangle$, respectively. At Site 2a, the ADCP was oriented at about a 45° angle to the flow and thus both stress components are oblique to the principal flow direction. Blank regions in the time series of $\mathcal{P}_h$ (Fig. 6.3m–p) correspond to $\mathcal{P}_h < 0$, which often arise during the turning of the tide and near the surface when turbulence levels are low.

The corresponding TKE and its time derivative are shown in Fig. 6.4. The estimates of TKE were obtained using Eq. (6.7) with $\gamma_2 = 0.2$. The time derivative was computed using a centre-differencing scheme. The TKE estimates do not extend to the surface because the variances associated with Doppler noise were only realistic to within approximately 90% of the lowest water level.

Several common patterns emerge in the time series in Figs. 6.3 and 6.4. Most notably, the parameters track each other well and exhibit variations on tidal time scales. Significant ebb/flood asymmetries are also apparent at all sites. Other commonalities include:

1) The estimates of $\mathcal{P}_h$ and ϵ vary by more than two orders of magnitude. The highest values are approximately 10^{-3} W kg^{-1} near the bed, whereas values less than 10^{-5} W kg^{-1} occur near slack water.

2) On the ebb tides at Sites 1, 2a, and 2b, the highest values of $\mathcal{P}_h$ are confined to a thin region near the bed. For $z > 12$ m, the production of turbulence is reduced because the velocity shear is much lower (see Fig. 3.11 for velocity profiles). The same pattern is observed in ϵ at Sites 1 and 2a (on ebb), but the decrease is less abrupt, due in part to the use of 4.5 m range intervals in SF2 method to compute ϵ.

3) On the flood tide at Sites 1, 2a, 2b, and ebb at Site 3, the turbulence parameters decrease with height above bed, but remain high throughout the water column. Thick log-layers are observed during these flow conditions (Fig. 3.11).

4) Near the bed, the dissipation rate tends to be lower than the production rate and $F_d > 0$, indicating a flux of TKE away from the bed.

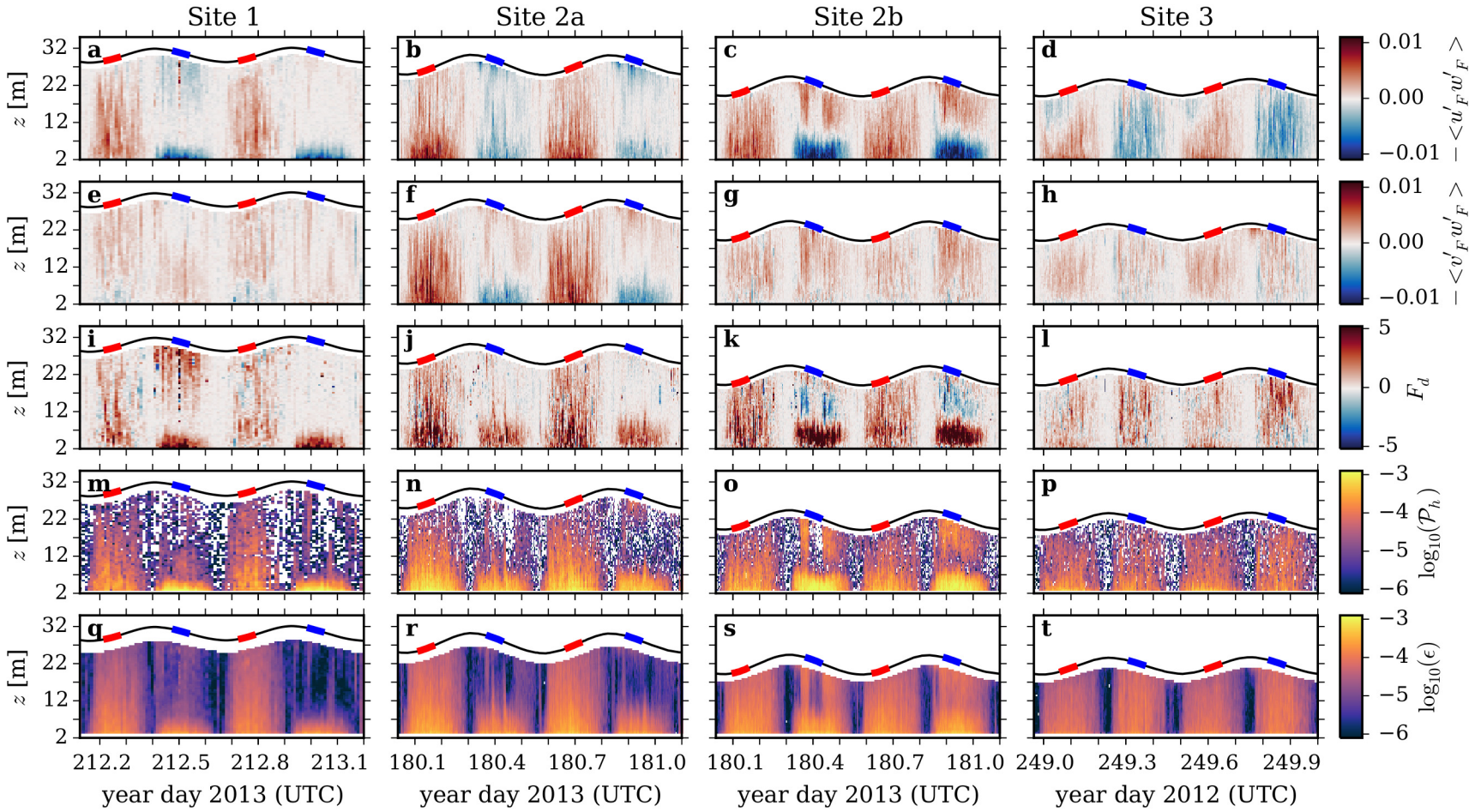

Figure 6.3: Time series of Reynolds stresses (a-h), vertical flux of TKE (i-l), production (m-p) and dissipation (q-t) at each site. The black line corresponds to the sea surface, and the red and blue segments highlight the one-hour intervals centred on maximum flow. Units are $m^2\ s^{-2}$ for the Reynolds stresses, $10^{-4}\ m^3\ s^{-3}$ for F_d and $W\,kg^{-1}$ for $\mathcal{P}_h$ and ϵ.

5) At Sites 1, 2b, and 3, the transverse Reynolds stresses are significantly less than the along-channel stresses.

6) The time derivative of TKE is always less than 10^{-5} W kg^{-1}. This implies, that during strong flows, when $\mathcal{P}_h$ and ϵ are high, the assumption of statistically steady turbulence is appropriate.

Two noteworthy, site-specific features also emerge in the time series. At Site 2b, turbulence appears to be generated near the surface on the ebb tide and transported downward because $F_d < 0$ (Fig. 6.3k). The velocity profiles on the ebb tide at this site (Fig. 3.11) have a maximum near $z = 10$ m, which coincides with a region of reversed shear near the surface, thus allowing for the production of turbulence. Interestingly, this production mechanism is essentially shut off during the strongest ebb flows on day 180.4. This variability was observed at 10 m above the bottom in Fig. 5.1 and is present throughout the 12 day period that was analyzed. Further discussion is presented in Sec. 6.4.3.

A similar production mechanism may be generating high $\mathcal{P}_h$ and ϵ values throughout the water column at Site 3 on the flood tide. At this site, the log-layer only extends to 5 m above the bed, thus—based on the results at the other sites—it would be expected that the highest turbulence levels would be confined to a thin region near the bed. However, near the surface, $-\langle u'_F w'_F \rangle$ is negative at the onset of the flood tide (Fig. 6.3k), and the velocity profiles exhibit a region of reversed shear near the surface (Fig. 3.11), leading to the production of turbulence.

6.3.2 Velocity, TKE, and Reynolds Stresses At Peak Flow

The time series in Fig. 6.3 show that the turbulence levels are asymmetric with respect to the ebb/flood tides and are arguably dependent on the thickness of the log-layer (see points 2 and 3 in Section 6.3.1). To examine this behaviour in more detail, mean velocity profiles were computed for the 60-minute interval centred on the peak flood and ebb flows (red and blue segments in Fig. 6.3). An average over all tidal cycles was then computed and a least-squares best fit to the law-of-the-wall (Eq. 2.12) was obtained for $z < 5$ m (Fig. 6.5, left panels). The resulting u_* and z_0 values are listed in Table 6.1.

The thickness of the log-layer, δ_L, was estimated as the height at which the measured profile deviated from the law-of-the-wall fit by 1%. The subscript L is used to distinguish δ_L from δ, which is the height at which the Reynolds stress goes to zero. The values of δ_L

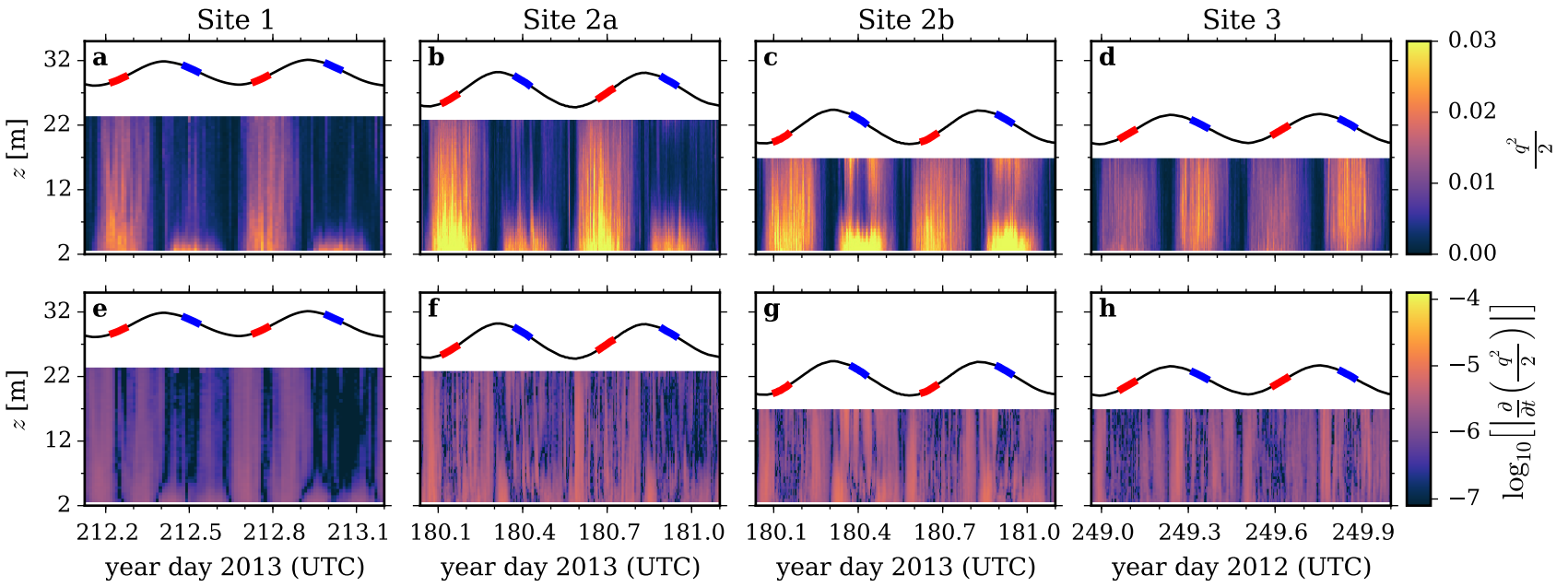

Figure 6.4: Time series of TKE (a-d) and its time derivative (e-h). The black line corresponds to the sea surface, and the red and blue segments highlight the one-hour intervals centred on maximum flow. Units are $m^2\ s^{-2}$ for the TKE, and $m^2\ s^{-3}$ for $0.5\ \partial q^2/\partial t$. The colour bar in the lower panels has limits that are one order of magnitude smaller than those for $\mathcal{P}_h$ and ϵ in Fig. 6.3.

ranged from 5.1 m on the ebb tide at Site 1 and the flood tide at Site 3 to 25 m on the flood tide at Site 2a (Fig. 6.5, circular markers).

Reynolds stresses were averaged over the same intervals, and normalized using the u_*^2 values determined from nonlinear least squares best fits to the law-of-the wall (Fig. 6.5, right panels). At all sites, the normalized streamwise Reynolds stresses are less than unity throughout the water column, indicating that the bottom stress estimated via the law-of-the-wall is higher than that estimated using the variance method, consistent with previous studies in tidal channels (*Lu et al.*, 2000; *Rippeth et al.*, 2002). At Sites 1, 2b and 3—which were all well-aligned with the flow—the transverse Reynolds stresses are near zero at the bed and remain negligible throughout the water column on the ebb tide. On the flood tide, however, the transverse stresses peak above mid-depth and are comparable in magnitude to the streamwise stresses near the surface at Sites 1 and 2b.

A constant stress region, ranging in thickness from 3–7 m, exists when the log-layer extends beyond $z = 6$ m (flood at Sites 1, 2a, 2b, and ebb at Sites 2a, 2b, and 3). The magnitude of the normalized stress ranges from 0.2 at Site 2a (ebb, solid blue line) to 0.8 at Site 3 (ebb, solid blue line). Above this region, the stress decreases toward zero at the surface, except on the ebb tide at Site 2b where the stress goes to zero at mid-depth. On the other hand, when the log-layer is confined to $z < 6$ m (ebb tide at Sites 1 and flood tide at Site 3), the along-channel stresses have a near-linear dependence on z, indicating that the constant stress layer is confined to the region below the first ADCP bin.

The averaged vertical profiles of TKE during peak flow conditions are dependent on the site and tidal phase (Fig. 6.5, middle panels). The highest TKE occurs in the lowest range bin at all locations, except on the ebb tide at Site 3, where the maximum is at $z = 8$ m. The magnitude of the normalized TKE is highest (4.5) on the ebb tide at Site 3. In all other cases, the maximum values of TKE/u_*^2 range between 0.9 and 3. Above the lowest range bin, TKE decreases with height, remaining greater than u_*^2 throughout the water column except on the ebb tides at Sites 1, 2a, and 2b. The TKE profiles are discussed further in Chapter 7, in relation to the best-fit energy spectra spanning low and high wavenumbers—i.e., including both the production and inertial subranges.

6.3.3 Turbulent Kinetic Energy Balance At Peak Flow

Near peak flood and ebb flows, the current is quasi-stationary, and the time rate of change of TKE is small (Fig. 6.4e-h) compared to $\mathcal{P}_h$ and ϵ (Fig. 6.3m-t). The terms in the TKE

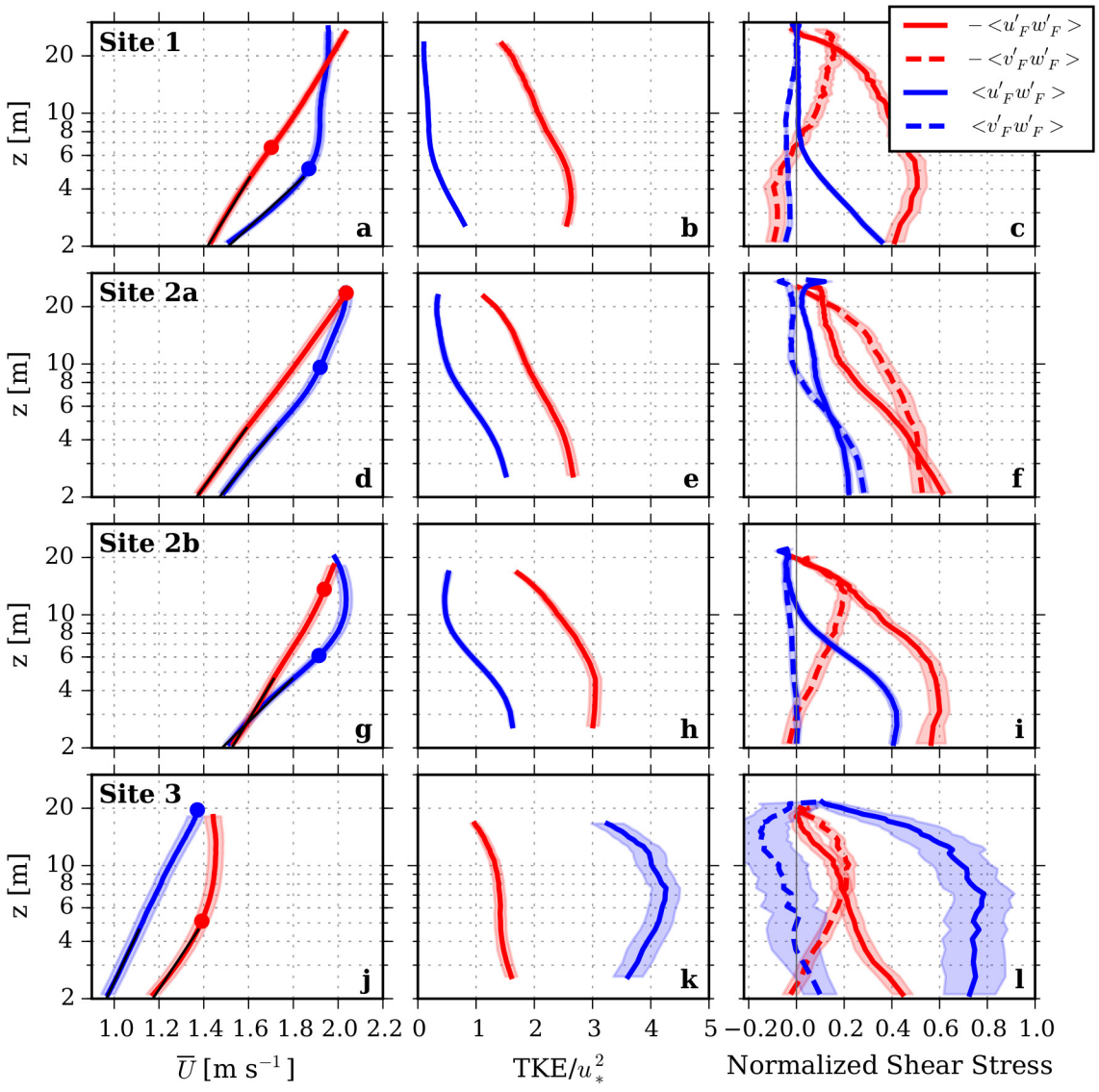

Figure 6.5: Vertical profiles of velocity (left), TKE (middle), and Reynolds stresses (right). Red and blue lines correspond to the flood and ebb tides, respectively. TKE and Reynolds stresses have been normalized by u_*^2, determined from fits to the law of the wall (left panel, black lines). The circular markers in the left panels correspond to the computed thickness of the log-layer, δ. Shaded regions identify the standard errors in the estimates based on the number of tidal cycles included in the average.

Table 6.1: Friction velocity, u_*, and roughness length scale, z_0, determined from nonlinear least squares regression to the law-of-the-wall (Eq 2.12).

Site	u_* [10^{-2} m s^{-1}]		z_0 [10^{-2} m]	
	Flood	**Ebb**	**Flood**	**Ebb**
1	9.1	16.1	0.4	4.7
2a	10.7	12.1	1.2	1.6
2b	9.0	15.0	0.2	3.9
3	9.8	7.0	1.6	0.8

equation were therefore examined using the same averaging approach described for the velocity profiles: i.e., the data for 60-minute intervals centred on the peak flood and ebb flows (red and blue dots in Fig. 6.3) were extracted and an average for all tidal cycles was computed.

The resulting vertical profiles of $\mathcal{P}_h$, T_d, ϵ, and $\mathcal{P}_h/\epsilon$ are shown in Fig. 6.6. For $z < 5$ m, $\mathcal{P}_h/\epsilon > 1$ and reaches a maximum of 3.7 on the ebb tide at Site 2b. Near mid-depth, $\mathcal{P}_h/\epsilon \approx 1$, except on the ebb tide at Site 1, where $\mathcal{P}_h = 2.4 \times 10^{-5}$ W kg^{-1} and is a factor of two larger than ϵ. Near the surface, the dissipation exceeds production at all sites on the flood tide, yielding $\mathcal{P}_h/\epsilon < 1$. The near-surface ratio on the ebb tide is much more variable, likely due to the presence of waves during several tidal cycles (Appendix C).

The local imbalance in $\mathcal{P}_h$ and ϵ at a given height cannot be accounted for by vertical transport of TKE from the boundary layer because, given the standard errors, the T_d values are rarely significantly different from zero (Fig. 6.6, yellow lines). This is somewhat surprising given that F_d is consistently greater than zero near the bed (Fig. 6.3), indicating an upward flux of TKE from the boundary layer. However, at most sites, because the magnitude of F_d is nearly uniform, Eq. (6.10) yields $T_d \approx 0$ and hence there is no net export of TKE from the boundary layer. There are three exceptions (i.e., cases for which $|T_d| > 0$): on the ebb tides at Sites 1, 2a, and 2b. At Site 1, $T_d > 0$ for $z < 7$ m, indicating that TKE is being imported into the near-bed layer. A layer of positive vertical transport also occurs on the ebb tides at Sites 2a and 2b for z ranging from 5 to 10 m, although the magnitude of T_d is much smaller at Site 2a than 2b. At Site 2b, the influx of TKE arises from both the downward flux from the surface (Fig. 6.3k, blue regions) and the upward flux from the near bed layer (Fig. 6.3k, red regions). At Sites 2a and 2b, $T_d < 0$ for $z < 5$ m, indicating that TKE is being exported upward and out of the near-bed layer.

Table 6.2: Depth-averaged dissipation, production, and transport terms. Values are given in units of 10^{-5} W kg^{-1}. The averages were computed from $z = 3$ m to ca. 90% of the water depth.

Site	Flood		Ebb		
	$\overline{\epsilon}$	$\overline{\mathcal{P}}_h$	$\overline{\epsilon}$	$\overline{\mathcal{P}}_h$	$\overline{T}_d$
1	7.6	8.6	2.2	4.6	1.5
2a	11.4	15.9	3.9	6.4	0.9
2b	11.3	10.6	9.4	18.8	2.1
3	5.9	6.3	9.2	7.9	-

At most sites, $\mathcal{P}_h(z) + T_d(z) - \epsilon(z) \neq 0$, particularly as the bed is approached (Fig. 6.6, black lines). Although the terms are not in balance locally, a balance in the depth-averaged sense may exist. Due to the condition of no normal flow at the sea bed and at the surface, the integral of the diffusive transport term is expected to approach zero. Thus, averaging Eq. (6.2) over the water depth, H, yields

$$\frac{1}{H}\int_0^H U\frac{\partial}{\partial x}\left(\frac{q^2}{2}\right)dz = \overline{\mathcal{P}}_h - \overline{\epsilon}, \tag{6.14}$$

where $\overline{\mathcal{P}}_h$ and $\overline{\epsilon}$ are the depth-averaged rates of production and dissipation, respectively. The vertical integrals of $\mathcal{P}_h$ and ϵ were computed from $z = 3$ m to 90% of the surface (Table 6.2). On the flood tide at Sites 1, 2b, and 3, and on the ebb tide at Site 3, $\overline{\mathcal{P}}_h$ and $\overline{\epsilon}$ are within 15% of each other, whereas, the depth-averaged production exceeds the dissipation on the flood at Site 2a and on the ebb tide at Sites 1, 2a, and 2b, by up to a factor of two, indicating that the streamwise advection term could be significant and greater than zero (Eq. 6.14).

The depth-averaged T_d was also computed for the profiles for which T_d was significantly different from zero (Table 6.2). While the $\overline{T}_d$ values are smaller than $\overline{\mathcal{P}}_h$ and $\overline{\epsilon}$, they are nonzero—in contrast to the results obtained by *Talke et al.* (2013)—likely because, in part, the $z < 3$ m region is not captured in the ADCP data.

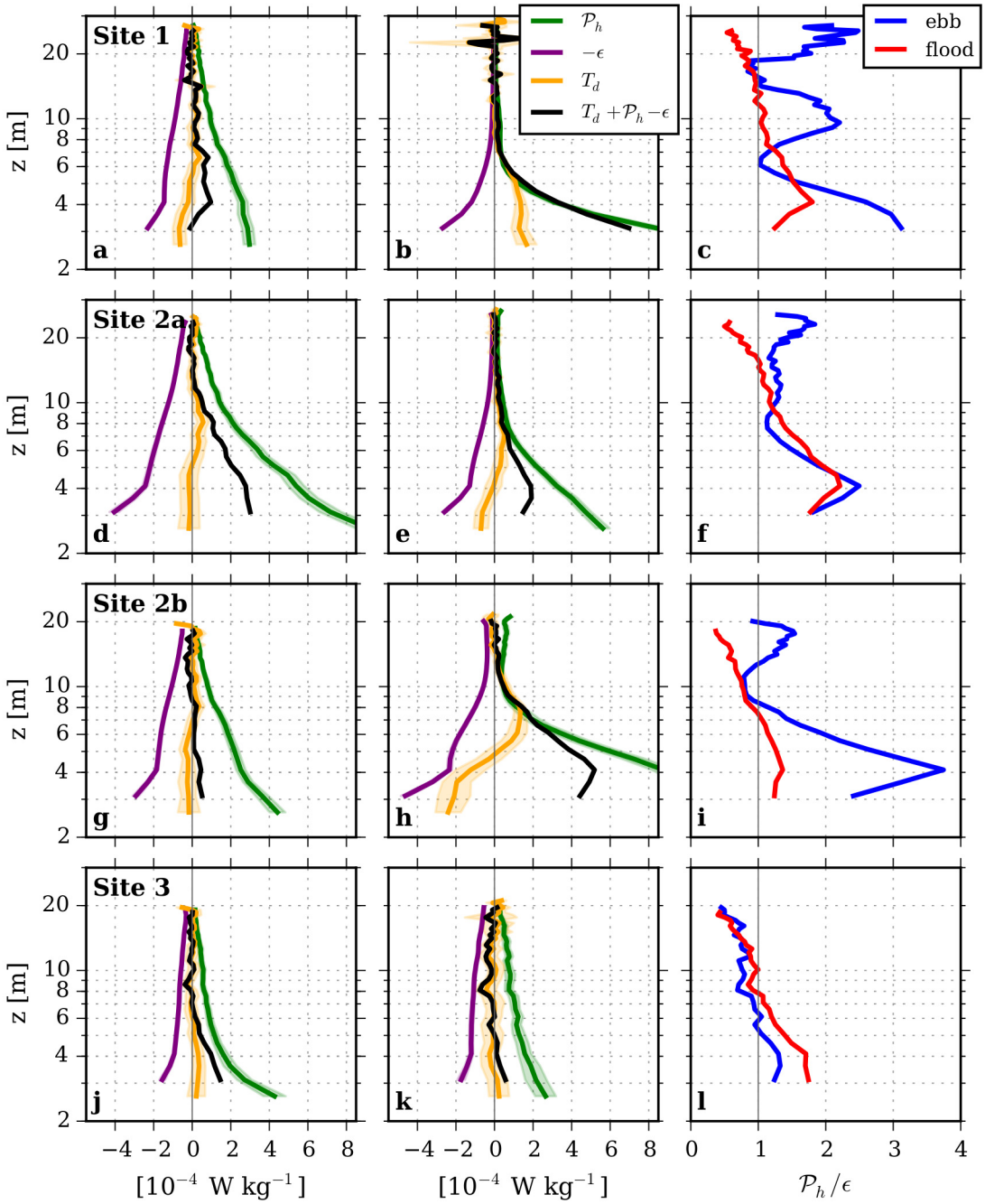

Figure 6.6: Balance of the terms in the TKE equation at each of the sites during maximum flood (left panels) and ebb (middle panels) tides. The corresponding ratios of production and dissipation are also shown (right panels). Shaded regions in the left and middle panels identify the standard errors in the estimates based on the number of tidal cycles included in the average.

6.4 Discussion

6.4.1 Comparison to Previous Studies

The velocity profiles and Reynolds stresses presented in Fig. 6.5 demonstrate that the ADCP measurements resolve the outer region (Fig. 6.1), including the log-layer, at all sites. Because a constant stress region was not resolved on the ebb tide at Site 1 or on the flood tide at Site 3 (Fig. 6.5c and l), it is assumed that, at these locations, the equilibrium layer was thinner than 2.1 m, which is the height of the lowest range bin. Furthermore, the velocity profiles do not deviate from the law-of-the-wall fits near the bed, indicating that the roughness sublayer was also thinner than 2.1 m at all sites. This is not surprising because the roughness height scales with $h \approx 30 z_0$ (*Raupach et al.*, 1991), which—using a typical value of $z_0 = 0.01$ m (Table 6.1)—yields $h = 0.3$ m. Thus, the maximum height of the roughness sublayer, i.e., $5h$, is approximately 1.5 m.

6.4.1.1 Reynolds Stresses

Previous field campaigns carried out in unstratified tidal channels using ADCPs have not consistently revealed the presence of a constant stress layer. Instead, the Reynolds stresses have been shown to vary linearly away from the bed (*Stacey et al.*, 1999; *Rippeth et al.*, 2002; *Osalusi et al.*, 2009), consistent with the theoretical expectation outside the constant stress region (*Nezu and Nakagawa*, 1993). Other studies (e.g., *Lu et al.*, 2000) have obtained more complex profiles of Reynolds stress that were neither constant nor linear. With the exception of the study by *Osalusi et al.* (2009), these earlier investigations were carried out in channels where the Reynolds number was approximately half that in Grand Passage (Fig. 1.1). Thus, it is likely that the constant stress region was not resolved, as is argued for the ebb tide at Site 1 and the flood tide at Site 3.

For high Reynolds number flows over rough walls in wind tunnels, *Raupach et al.* (1991) showed that a constant stress region was consistently resolved for $z < 0.2\delta$. Above this region, the stress decreased linearly toward zero at the top of the boundary layer at $z = \delta$. In the Grand Passage data, the Reynolds stress typically approaches zero near the surface (Fig. 6.5), thus for $\delta \approx 20$ m, a constant stress region is expected to extend to 4 m, consistent with the 3 to 4 m upper limit observed on the flood tides at Sites 1, 2a, and 2b and ebb tides at Sites 2a and 2b. On the ebb tide at Site 3, the constant stress region extends to approximately 7 m, possibly due to greater influence of the upstream bathymetry. This possibility is discussed further in Section 6.4.2.

6.4.1.2 Production, Dissipation, and Transport

In the constant stress layer—i.e., the equilibrium layer—the rates of production and dissipation are expected to be in balance; however, this balance was not observed in the Grand Passage data (Section 6.2.3). Instead, production exceeds dissipation near the bed at all sites, and $\mathcal{P}_h/\epsilon$ approaches unity near mid-depth. The precise height at which this balance is observed is seemingly independent of the estimated log-layer thickness, δ_L.

Two previous field campaigns in tidal flows have obtained comparable results. Using ADCP measurements in the English Channel, where the mean water depth was 17 m and the maximum current speed was 1.5 m s^{-1}, *Korotenko et al.* (2013) found that the vertical profiles of $\mathcal{P}_h/\epsilon$ were asymmetric with respect to the flood and ebb tides. On the flood, $\mathcal{P}_h/\epsilon > 10$ at $z = 1.5$ m and decreased with height, with the ratio remaining larger than unity throughout the 6 m measurement region. On the ebb tide, however, $\mathcal{P}_h/\epsilon \approx 2$ at $z = 1.5$ m and approached unity near $z \approx 4$ m.

The second relevant study was carried out by *Talke et al.* (2013) in a shallow tidal river with a maximum water depth of 5 m. Using measurements from an ADCP and an ADV, they showed that production exceeded dissipation by more than a factor of two in the lower half of the water column, above which the production was insignificant while the dissipation remained high. This variation of ϵ and $\mathcal{P}_h$ with height is consistent with the observations in Grand Passage, particularly on the flood tide at all sites and on the ebb tide at Site 3 (Fig. 6.6, right panels). Furthermore, *Talke et al.* (2013) obtained a depth-integrated value of $\mathcal{P}_h$ that exceeded that of ϵ, a result in agreement with all of the Grand Passage sites, except the flood tide at Site 2b and the ebb tide at Site 3 (Table 6.2).

The diffusive transport term estimated by *Talke et al.* (2013) is also qualitatively consistent with the observations at Sites 2a and 2b. *Talke et al.* (2013) obtained a negative value for $z < 0.3H$ and a positive value—approximately three fold smaller in magnitude—for $z > 0.45H$. However, unlike the present results, *Talke et al.* (2013) found that the magnitude of T_d was comparable to $\mathcal{P}_h - \epsilon$ near the bed, thus closing the local TKE balance. Based on the T_d estimates, and the vertical variation of $\mathcal{P}_h$ and ϵ, *Talke et al.* (2013) suggested that excess TKE was being removed from the near bed region and transported upward where it was subsequently dissipated.

Additional insight into the vertical structure of $\mathcal{P}_h$, ϵ, and T_d, can be gained from DNS simulations of channel flow. Because of computing power limitations, to date,

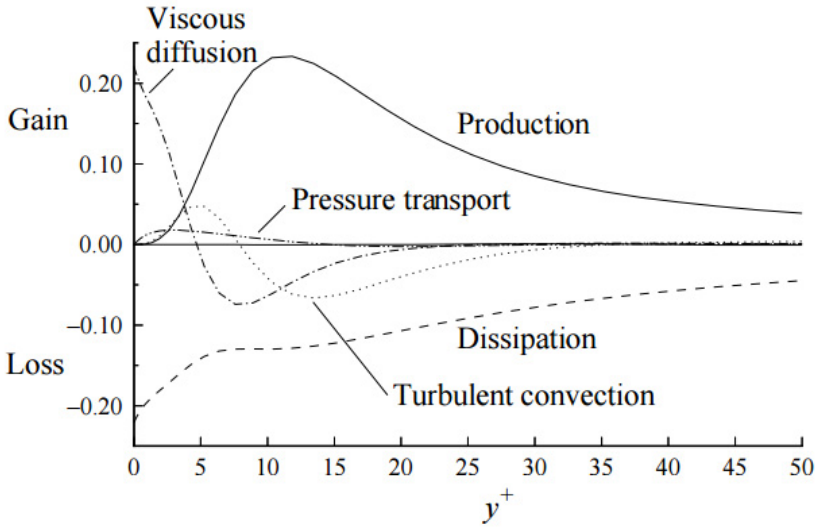

Figure 6.7: Turbulent kinetic energy budget in the viscous wall region of channel flow as determined from the DNS data of *Kim et al.* (1987) with $Re_\tau = 395$. The wall coordinate is defined as $y^+ = u_* z/\nu$, where z is the height above bottom. The relevant terms discussed in the text are: production ($\mathcal{P}_h$), dissipation (ϵ), and turbulent convection, (T_d). This figure is Fig. 7.18 in *Pope* (2000), and is available online at https://pope.mae.cornell.edu/TurbulentFlows/popefigures/pdf/chapter7Figures.pdf (Accessed on Feb. 15, 2017).

the highest attainable Reynolds number—based on the boundary layer properties—is $\mathrm{Re}_\tau = u_* \delta/\nu \approx 600$ (*Alfonsi et al.*, 2016; *Moser et al.*, 1999). In comparison, the equivalent Reynolds number for the Grand Passage dataset is $\mathcal{O}(10^6)$. Thus, the DNS models resolve turbulence that is significantly less energetic than in a tidal channel. Despite this limitation, however, the simulations reveal a thin constant stress layer (*Alfonsi et al.*, 2016) and a region over which the production and dissipation rates are in balance (*Moser et al.*, 1999). Furthermore, the thickness of this equilibrium layer is shown to increase for increasing Re_τ.

Closer to the wall, but above the viscous sublayer—i.e., in the region analogous to the roughness sublayer—production, dissipation and vertical diffusive transport vary significantly as shown in Fig. 6.7 for a simulation with $\mathrm{Re}_\tau = 395$ (*Kim et al.*, 1987). For $y^+ = u_* z/\nu < 7$, T_d (i.e., turbulent convection) is positive, whereas, for $y^+ > 7$, T_d is negative and $\mathcal{P}_h > \epsilon$. Because the ADCP measurements do not resolve a maximum in production (Fig. 6.6, left and middle panels), the relevant region for comparison is $y^+ > 10$, where $\mathcal{P}_h > \epsilon$, consistent with the near bed observations in Grand Passage.

Furthermore, for $y^+ > 10$ the DNS simulation indicates that $T_d < 0$, in agreement with the observations at Sites 2a and 2b for $z < 5$ m. The observation that $T_d > 0$ near the bed at Site 1, and for $z \in [5, 10]$ m at Sites 2a and 2b is not consistent with the DNS results.

These comparisons indicate that the fundamental properties of the turbulent flow in Grand Passage are qualitatively consistent with previous studies in both natural systems and virtual channels. Significant differences arise, especially regarding the thickness of the constant stress layer and the height at which a balance between production and dissipation is observed. These differences, in addition to the ebb/flood asymmetry and site-dependence of the turbulence parameters, indicate that the streamwise advection is non-negligible and positive (via Eq. 6.14)—a result that is not surprising for a high Reynolds number flow in a passage with significant variability in the bottom roughness and water depth along the flow path.

6.4.2 Dependence on Upstream Roughness

The variability in the upstream bathymetry was estimated using 2 m resolution multibeam data. The demeaned water depths, $H - \overline{H}$, along transects in the principal flow direction (Fig. 3.8) are shown as a function of normalized upstream distance, x_U/H_0, where H_0 is the depth at the ADCP site (Figs. 6.8a,b). The roughness was quantified by first applying a moving average filter over 40 m scales to obtain a smoothed transect, H_{SM}, and then computing the root-mean-square of $h' = H - H_{SM}$ for $x_U/H_0 < 20$ (Figs. 6.8c,d). The resulting h'_{rms} values range from 0.15 to 0.35 m (Fig. 6.9a).

At Sites 2a, 2b, and 3, the thickness of the log-layer, δ_L, is positively correlated with h'_{rms}, i.e., the larger the upstream roughness, the thicker the boundary layer (Fig. 6.9a, filled markers). For the range of values that were observed, the relationship between h'_{rms} and δ_L appears to be linear; however, the y-intercept would yield a non-physical δ_L value for $h'_{\text{rms}} = 0$. Other roughness metrics, weighted to account for proximity, such as $\int h' x_U^{-1} dx_U$ and $\int h' x_U^{-1/2} dx_U$, were also investigated, yielding similar trends with δ_L, but greater scatter was observed (not shown). In addition, both of these integral metrics were small for the ebb tide at Site 3, where the presence of the cross-channel (CC) ridge (Fig. 3.3) at $x_U/H_0 = 15$ is considered to have a significant effect on the flow (*Hay et al.*, 2013), despite its distance far upstream.

The thickness of the log-layer is shown as a function of the drag coefficient, C_d, (referenced to the velocity at $z = 1$ m, Section 3.4.2) in Fig. 6.9b. Although there is substantial

scatter among the data, the overall trend is that δ_L decreases with increasing C_d. In Fig. 6.5, it is also apparent that larger δ_L values coincide with thicker constant stress regions. Thus, for a given mean flow speed, the presence of a thick log-layer allows the frictional force imparted by the bed to be distributed over a larger range of depths, thus reducing the velocity shear at the bed and lowering the value of C_d.

The effects of variable topography on turbulence in the atmospheric boundary layer have been considered by *Kaimal and Finnigan* (1994). In the turbulent wake in the lee of a topographic feature like a hill, increased vertical mixing thickens the boundary layer and reduces the velocity shear near the bed. Consequently, within the wake of a prominent bathymetric feature like a ridge, the bottom stress, and hence C_d, are lower than obtained for a similar flow speed over a flat bottom.

The largest C_d values occur on the ebb tides at Sites 1 and 2b (Fig. 6.9b), which also correspond to the greatest imbalances in $\overline{\mathcal{P}}_h$ and $\overline{\epsilon}$ (Table 6.2). In these instances, the log-layer is also thin, thus the region over which significant production and dissipation occur is below the resolvable range of the ADCP. It is likely that, in these cases with high bottom drag, other terms in the TKE equation are significant.

6.4.3 Temporal Variability on the Ebb Tide at Site 2b

The turbulence parameters on the ebb tide at Site 2b vary with time and depth differently than at the other sites. Near the surface, $\mathcal{P}_h$ and ϵ are high and $F_d < 0$ as the flow accelerates and decelerates (Figs. 6.3k,o,s), but, the turbulence levels occasionally drop off abruptly during peak flows (e.g., day 180.4). These "peak flow ϵ minima" are also captured at $z = 10$ m using both the spectral and structure function approaches (Fig. 5.1, third panel), and are present in 14 of the 23 ebb cycles that were analyzed (not shown). Importantly, this temporal variability on the ebb tide is not present at Site 2a (Figs. 6.3j,n,r), which was deployed concurrently about 190 m to the north of Site 2b (Fig. 3.3). Surface waves were present at both sites during the deployment period (Appendix C), and thus the influence of waves alone cannot explain the variability at Site 2b.

The high production and dissipation rates near the surface are driven by vertical shear in the mean flow velocity, i.e., both speed and direction. A time series of the dissipation rate averaged over $z = 12$ to 17 m is shown in Fig. 6.10 (top panel). The chosen interval includes two ebb tides—one ebb cycle with a peak flow ϵ minimum (year day 180.4) and one without (year day 179.9). Profiles of flow speed and direction are shown for the

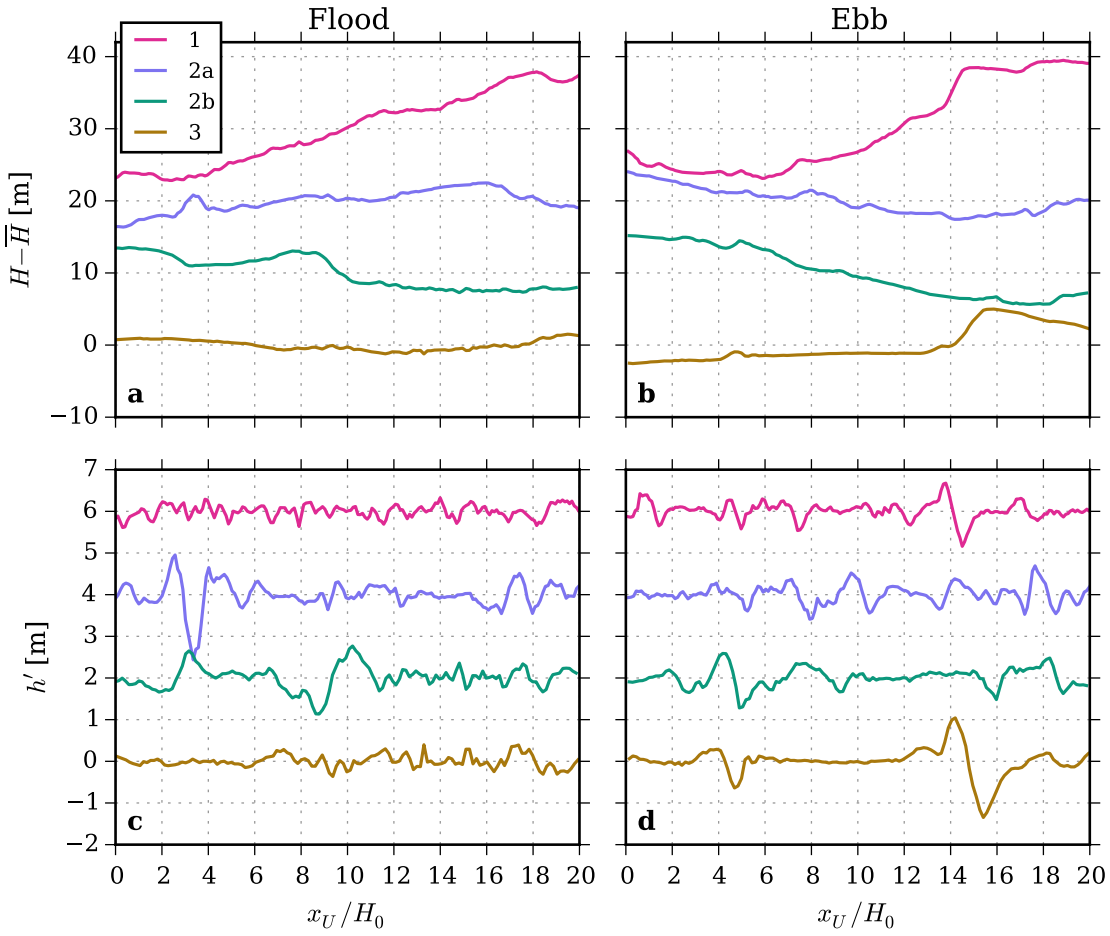

Figure 6.8: Demeaned water depths, $H - \overline{H}$, and roughness metric, h', as a function of normalized upstream distance, x_U/H_0, on the flood (a, c) and ebb (b, d) tides. The colours correspond to the sites given in the legend. The curves have been vertically offset by 10 m in (a) and (b) and by 1 m in (c) and (d).

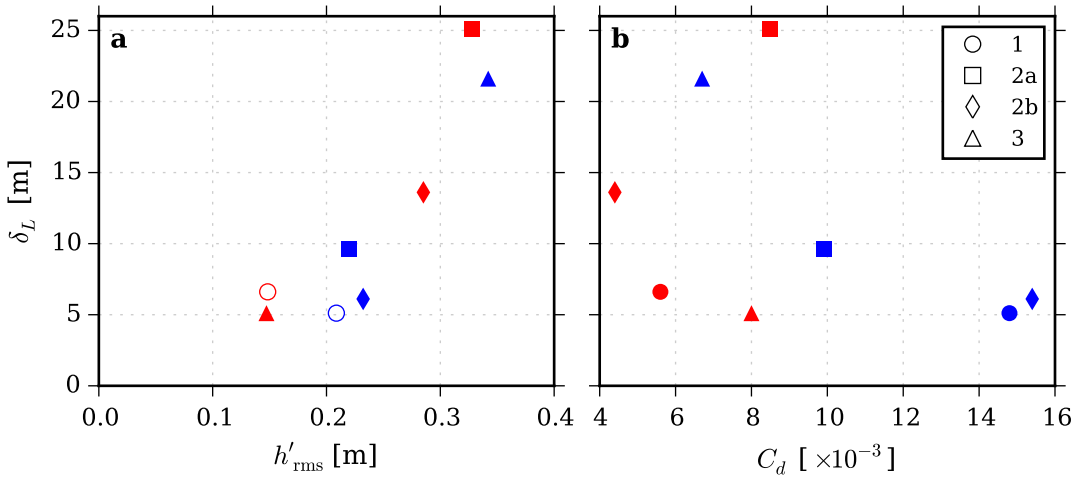

Figure 6.9: Log-layer thickness, δ, as a function of (a) upstream roughness (h'_{rms}) and (b) local drag coefficient, C_d. Red and blue markers correspond to flood and ebb tides for the sites indicated in the legend. In the left panel, unfilled markers are used for Site 1 because the exact location of the ADCP is not known, and hence h'_{rms} is likely not representative of the upstream conditions.

acceleration (green), maximum flow (blue), and deceleration (red) phases of the ebb tide. Five of the six profiles show the presence of vertical shear in the flow speed and direction in the top 10 m of the water column. More specifically, the flow at the surface is slower and from a direction approximately five degrees east of that at mid-depth. The solid blue lines, on the other hand, indicate a comparatively uniform speed and direction during the peak flow ϵ minimum near day 180.4.

The observed tidal variation of ϵ on the ebb tide at Site 2b is consistently like that observed near day 180.4. At the onset of the ebb tide, the dissipation rate increases rapidly due to the presence of reversed shear at the surface, then ϵ falls off near peak flow when the velocity becomes uniform. As the flow decelerates, the reversed shear then redevelops leading to an increase in ϵ, but, the formation of the reversed shear on the deceleration phase is less consistently observed than on the the acceleration phase.

The reversed shear is likely caused by lateral entrainment of slower surface water just to the northeast of Site 2b on the upstream side of the cross-channel (CC) ridge. The direction of the flow at the surface is typically 200-205° from north (Fig. 6.10), however, when the reversed shear is not present, the flow direction is 197°. The deviation of 3-8° degrees significantly affects the turbulence levels in the upper water column.

Additional insight into the spatial variability of the surface flow is obtained using a

3D simulation of the region performed with the Finite Volume Community Ocean Model (FVCOM, Appendix E), which was validated for the Grand Passage region by *O'Flaherty-Sproul* (2013). Snapshots of the simulated velocity field for two instances on an ebb tide are shown in Fig. 6.11. The panels in the top (bottom) row correspond to an instance when reversed shear was (was not) present at the surface in the model results. The left and middle panels illustrate relative flow speeds near the surface (U_2) and near mid-depth (U_5), respectively. The reference speed, U_r, is equivalent to U_2 at the ADCP location (black circle). The right panels show the difference between the flow at these two depths, i.e., $|U_5| - |U_2|$. In Fig. 6.11a, Site 2b is located very close to a region of high lateral shear. The flow speed varies by more than $0.5\,\mathrm{m\,s^{-1}}$ over a cross-channel distance of $\mathcal{O}(100)$ m. The position of the front varies with both time and depth. When reversed shear is present in the velocity profile (top row), a near-surface, lateral velocity gradient is present Site 2b (Fig. 6.11a), whereas the front at mid-depth is to the east of Site 2b (Fig. 6.11b). A local vertical velocity gradient is therefore generated with slower flow at the surface than at mid-depth (Fig. 6.11c). On the other hand, when the reversed shear is not present (bottom row), the front is to the east of Site 2b, both near the surface (Fig. 6.11d) and near mid-depth (Fig. 6.11e).

These results suggest that the variability in the turbulence levels on the ebb tide at Site 2b arises because the position of the ADCP is near the edge of the main current. As the flow accelerates and decelerates, the position of this lateral shear zone shifts relative to the ADCP site and is accompanied by significant negative vertical shear in the upper half of the water column. The position of this front at the surface will be further affected by the wind direction. For example, on day 179.9, the winds were approximately $25\,\mathrm{km\,h^{-1}}$ and south-south-easterly (Appendix C). The easterly component of the wind was pushing the front westward, and hence, the reversed shear at Site 2b was present throughout the tidal cycle and the peak flow ϵ minimum did not occur. The opposite conditions occurred on day 178.9 (not shown) when the wind was approximately $10\,\mathrm{km\,h^{-1}}$ and north-north-westerly. Because the front was pushed eastward, the initial increase in ϵ during the accelerating flow did not occur, and the dissipation rate remained below $5 \times 10^{-5}\,\mathrm{W\,kg^{-1}}$ in the top half of the water column throughout the entire ebb tide.

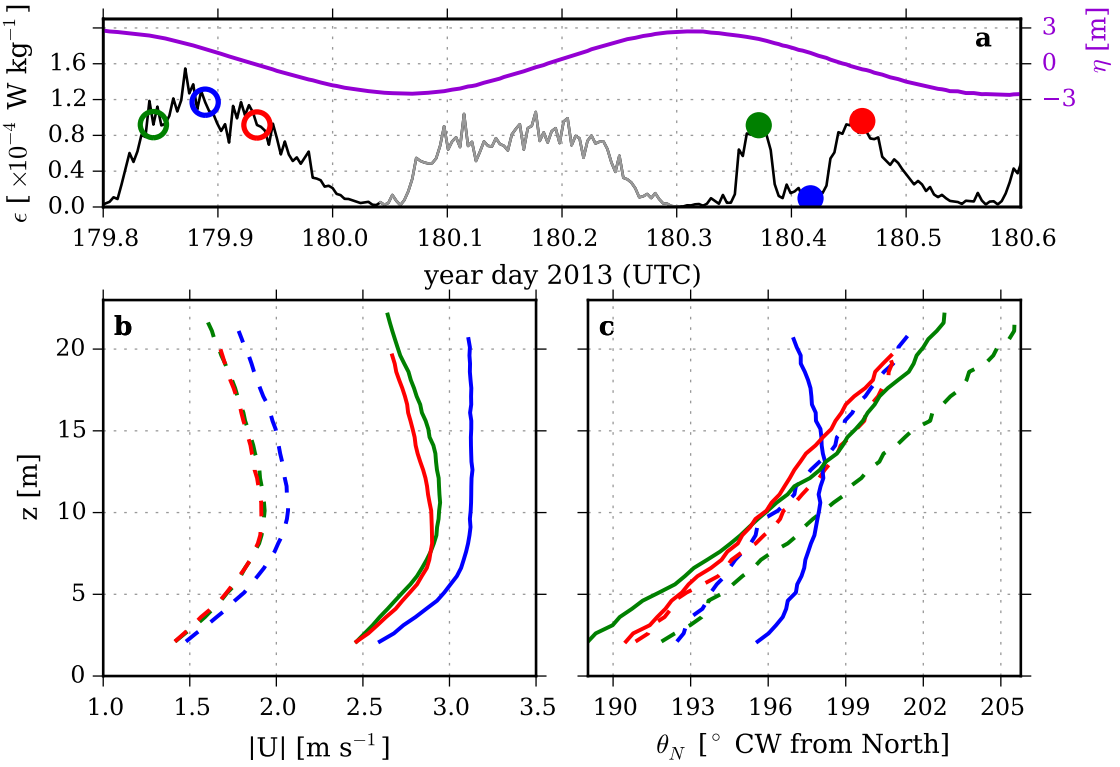

Figure 6.10: (a) Surface elevation (purple), and average dissipation rate from $z = 12$ to 17 m (black, grey). Ebb tides are shown in black and the flood tides are in grey. The circular markers indicate the times of the profiles shown in the bottom two panels. Open and closed circles correspond to dashed and solid lines, respectively. (b) Velocity profiles at the times highlighted in the top panel. The solid lines have been shifted to the right by 1 m s^{-1}. (c) Profiles of the flow direction at the times highlighted in the top panel.

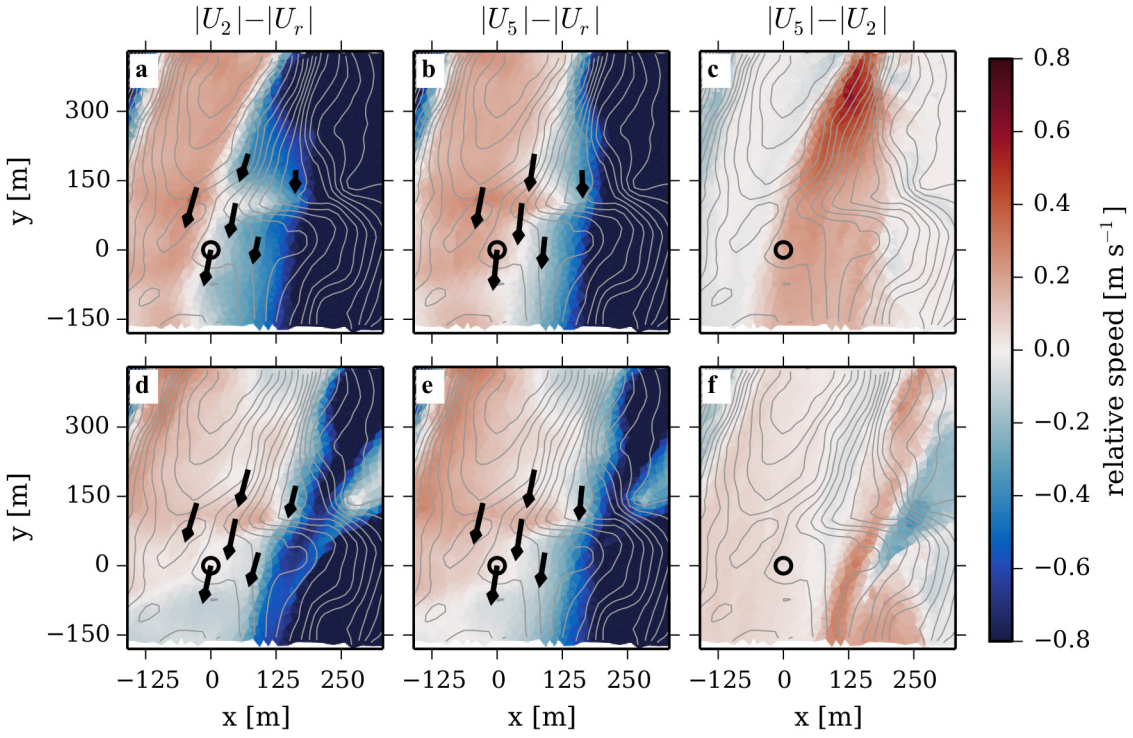

Figure 6.11: Snapshots of the simulated flow speed on the ebb tide computed using the FVCOM model. The left (a,d) and middle (b,e) panels illustrate relative flow speeds near the surface (U_2) and near mid-depth (U_5), respectively. The reference speed, U_r, is equivalent to U_2 at Site 2b (black circle). The red (blue) colours indicate that the flow is moving faster (slower) that at Site 2b. The right panels show the difference in the flow speeds at the two depths. Reversed shear at Site 2b is present for the results shown in the top row (a-c) and absent for the results shown in the bottom row (d-f). Black arrows are velocity vectors and grey lines are bathymetric contours in 2 m intervals.

6.5 Conclusions

ADCP data at four locations in Grand Passage have been used to assess the TKE balance throughout the water column during peak flood and ebb flows. Rates of production and dissipation are shown to agree to within a factor of two throughout most of the water column, with the tendency that $\mathcal{P}_h > \epsilon$ near the bed, $\mathcal{P}_h \approx \epsilon$ at mid-depth, and $\mathcal{P}_h < \epsilon$ near the surface. This result is somewhat surprising, given that the constant stress layer—where it is typically assumed that $\mathcal{P}_h = \epsilon$—was confined to $z = 3$ to 7 m. However, the vertical variation in $\mathcal{P}_h$ and ϵ is qualitatively consistent with DNS simulations of channel flows and the observations obtained by *Talke et al.* (2013) in a shallow tidal river.

The local imbalance in $\mathcal{P}_h$ and ϵ cannot be fully accounted for by the vertical diffusion of TKE, T_d, which is significantly different from zero on the ebb tide at Sites 1, 2a, and 2b. Near the bed at Sites 2a and 2b, $T_d < 0$, indicating the export of TKE from the high production region nearest the bed. Regions of import, i.e., $T_d > 0$, exist for $z < 7$ m at Site 1, and for $z \in [5, 10]$ m at Sites 2a and 2b.

Depth averages of $\mathcal{P}_h$ and ϵ agree to within 15% in four of the eight cases (flood tide at Sites 1, 2a, and 2b, and ebb tide at Site 3), whereas the depth-averaged production exceeds dissipation otherwise. It is suggested that the observed imbalance is due to the streamwise advection of TKE in these cases. While the streamwise derivative of TKE cannot be estimated from the ADCP measurements, variations in the upstream conditions are shown to affect the flow in two ways. First, the log-layer thickness—and hence the vertical distribution of velocity shear and production—is positively correlated with the RMS bottom roughness, estimated over an upstream range of 20 water depths. In addition, minima in ϵ during peak ebb flows at Site 2b arise when changes in the upstream flow direction shift the position of a lateral shear zone relative to the ADCP site.

CHAPTER 7

TURBULENCE SPECTRA AT LARGE SCALES: VON KÁRMÁN VERSUS KAIMAL

In this chapter, investigation of the turbulent kinetic energy spectrum is extended into the production range, where large eddies contribute most of the total velocity variance. The analysis is based on the von Kármán and Kaimal semi-empirical spectra, which were developed initially in relation to atmospheric boundary layer turbulence. The von Kármán and Kaimal spectra are used to obtain a predicted spectral form applicable to diverging-beam ADCP data. The modified forms are compared to the spectra observed during peak flood and ebb conditions at Sites 2b and 3, where the instruments sampled continuously and were well aligned with the flow direction (Fig. 3.6). The applicability of the von Kármán and Kaimal forms is shown to depend on z because the anisotropy and length scales vary with height above bottom.

Both the Kaimal and von Kármán spectra have been shown to describe turbulence measurements in atmospheric boundary layer flows (e.g., *Kaimal et al.*, 1972; *Morfiadakis et al.*, 1996; *Petersen et al.*, 1998). In unstratified tidal flows, the validity of the Kaimal form has been investigated by *Walter et al.* (2011) and *Lien and Sanford* (2000) using measurements acquired with an ADV and an electromagnetic vorticity meter, respectively. Both studies concluded that the semi-empirical spectra captured the general shape of the measured spectra in the near bed region; however, the Kaimal spectra underestimated the variance at low frequencies. In contrast, the von Kármán spectra have been shown to overestimate the variance in the production range when compared to ADV measurements

acquired at 5 m above the bottom in a 2 m s^{-1} tidal flow (*Milne et al.*, 2013).

The ability to predict the spectral properties of large scale fluctuations is desired, specifically regarding tidal energy developments. Models used to estimate turbine performance are often initialized by specifying the spectral densities based on theoretical curves. Both *Tidal Bladed* and *TurbSim*—two of the most commonly used models—allow for the spectra to be specified by either the Kaimal or von Kármán forms (*Burton et al.*, 2011; *Jonkman*, 2009). The input spectra are dependent upon appropriate length scales and velocity variances, which—in principle—can be estimated from field measurements.

In this chapter, the derivation and properties of the longitudinal and vertical von Kármán and Kaimal spectra are presented and discussed in Section 7.1. New values for the empirical constants in the Kaimal spectra are proposed. In Section 7.2, modified forms are obtained for both spectra that are applicable to diverging-beam ADCP data. In addition, a measure of anisotropy—which affects the numerical values of the empirical constants—is introduced and the method used to estimate the integral length scale is described. Comparisons between the measured spectra and predicted forms are presented in Section 7.3, and the results are discussed in Section 7.4. Conclusions are summarized in Section 7.5.

7.1 Semi-Empirical Velocity Spectra

7.1.1 von Kármán Spectra

von Kármán (1948) obtained a spectral form for isotropic turbulence. He represented the shape of the three-dimensional spectrum by $k^4[1 + (k/k_0)^2]^{-17/6}$: i.e., in essence an interpolation between the k^4 dependence at low frequencies and the $k^{-5/3}$ dependence at high frequencies. The cutoff wavenumber, k_0, is related to the integral scale of the turbulence, and the proportionality constant is obtained by ensuring that the integral of the spectrum is equal to the total variance (*Diedrich and Drischler*, 1957). Under the assumption of isotropy $\sigma^2 = \sigma_u^2 = \sigma_w^2$ and the longitudinal integral length scale, L_{vK}, is twice the lateral integral length scale (*Diedrich and Drischler*, 1957). In frequency space, these assumptions yield one-dimensional longitudinal and vertical spectra—i.e., Φ_{uu} and

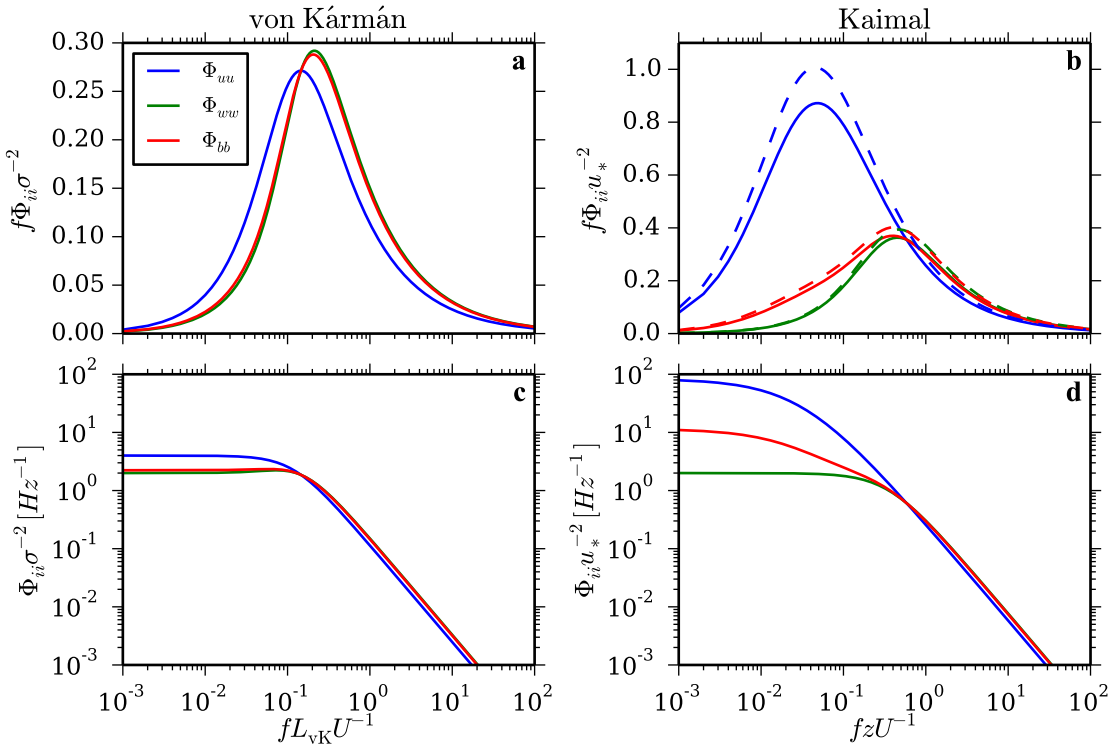

Figure 7.1: The semi-empirical von Kármán and Kaimal spectra. Kaimal spectra are shown for the atmospheric coefficients (dashed lines) given by *Kaimal and Finnigan* (1994) and modified coefficients based on anisotropic relationships obtained by *Raupach et al.* (1991) (solid lines).

Φ_{ww}, respectively—given by

$$\frac{f\Phi_{uu}(f)}{\sigma^2} = \frac{4\tilde{f}_{\mathrm{vK}}}{\left[1+70.8\tilde{f}_{\mathrm{vK}}^2\right]^{5/6}}, \tag{7.1}$$

$$\frac{f\Phi_{ww}(f)}{\sigma^2} = \frac{2\tilde{f}_{\mathrm{vK}}\left(1+188.7\tilde{f}_{\mathrm{vK}}^2\right)}{\left[1+70.8\tilde{f}_{\mathrm{vK}}^2\right]^{11/6}}, \tag{7.2}$$

where $\tilde{f}_{\mathrm{vK}}$ is a non-dimensional frequency defined as $\tilde{f}_{\mathrm{vK}} = fL_{\mathrm{vK}}/|U|$. As shown in Fig. 7.1, the longitudinal and vertical spectra have similar shapes, with the maximum of $f\Phi_{ww}$ occurring at an $\tilde{f}_{\mathrm{vK}}$ value that is 45% higher than the maximum of $f\Phi_{uu}$ (Table 7.1). At high frequencies, $\Phi_{ww}/\Phi_{uu} = 4/3$, which is the expected ratio in the inertial subrange.

7.1.2 Kaimal Spectra

Using the data from the 1968 Kansas Experiment, *Kaimal et al.* (1972) obtained "universal" forms for the spectra under neutral conditions that depend only on the mean velocity, the friction velocity, and the height above ground. The spectra can be written in a general form as

$$\frac{f\Phi_{uu}(f)}{u_*^2} = \frac{A\tilde{f}_{\mathrm{K}}}{\left(1 + B\tilde{f}_{\mathrm{K}}\right)^{5/3}}, \tag{7.3}$$

$$\frac{f\Phi_{ww}(f)}{u_*^2} = \frac{C\tilde{f}_{\mathrm{K}}}{1 + D\tilde{f}_{\mathrm{K}}^{\,5/3}}, \tag{7.4}$$

where $\tilde{f}_{\mathrm{K}}$ is a non-dimensional frequency defined as $\tilde{f}_{\mathrm{K}} = fz/|U|$ and A, B, C, and D are empirical constants (*Kaimal and Finnigan*, 1994).

Relationships between the constants can be obtained by ensuring that the integral of the spectrum is equal to the variance, yielding

$$\frac{A}{B} = \frac{2}{3}\frac{\sigma_u^2}{u_*^2}, \tag{7.5}$$

$$\frac{C}{D^{3/5}} = \frac{1}{2}\frac{\sigma_w^2}{u_*^2}. \tag{7.6}$$

Additional equations can be obtained by requiring the spectra to reduce to the ISR form in the high frequency limit. Also assuming that $\epsilon = (\kappa z)^{-1}u_*^3$, i.e., a balance between production and dissipation, yields

$$\frac{A^3}{B^5} = \frac{\alpha_1^3}{(2\pi\kappa)^2}, \tag{7.7}$$

$$\frac{C}{D} = \frac{4\alpha_1}{3(2\pi\kappa)^{2/3}}, \tag{7.8}$$

where κ and α_1 are the von Kármán constant and the longitudinal Kolmogorov constant, respectively. Thus, from known relationships between the velocity variances, spectra spanning the production and inertial subranges can be predicted for a given value of u_*.

The Kaimal curves used most often in atmospheric applications have $A = 102$, $B = 33$, $C = 2.1$ and $D = 5.3$ (Figs. 7.1b and d, dashed lines). These values can be obtained using $\sigma_u = 2.15u_*$, $\sigma_w = 1.24u_*$, $\kappa = 0.4$ and $\alpha_1 = 0.55$ (*Kaimal and Finnigan*, 1994).

Table 7.1: Properties of the maxima of the semi-empirical spectra.

	von Kármán		Kaimal*		Kaimal†	
	$\tilde{f}_{\mathrm{vK}}$	$\max\left(\frac{f\Phi_{ii}}{\sigma^2}\right)$	$\tilde{f}_{\mathrm{K}}$	$\max\left(\frac{f\Phi_{ii}}{u_*^2}\right)$	$\tilde{f}_{\mathrm{K}}$	$\max\left(\frac{f\Phi_{ii}}{u_*^2}\right)$
Φ_{uu}	0.146	0.271	0.045	1.007	0.048	0.872
Φ_{ww}	0.212	0.292	0.469	0.394	0.454	0.363
Φ_{bb}	0.205	0.288	0.411	0.402	0.399	0.370

* *Kaimal and Finnigan* (1994): $\sigma_u = 2.15\,u_*$, $\sigma_w = 1.24\,u_*$, $\alpha_1 = 0.55$.
† *Raupach et al.* (1991): $\sigma_u = 2.0\,u_*$, $\sigma_w = 1.2\,u_*$, $\alpha_1 = 0.5$.

However, using the data acquired at Site 3 on the ebb tide, *Hay et al.* (2013) showed that $\sigma_u = 2.0u_*$ and $\sigma_w = 1.2u_*$, agreeing favourably with wind tunnel measurements (*Raupach et al.*, 1991). Using these ratios with $\kappa = 0.4$ and $\alpha_1 = 0.5$ yields $A = 83$, $B = 31$, $C = 2$ and $D = 5.6$ (Figs. 7.1b and d, solid lines).

The spectral densities and frequencies corresponding to the peaks of $f\Phi_{ii}$ are given by

$$\max\left(\frac{f\Phi_{uu}}{u_*^2}\right) = 0.3257\frac{A}{B} \qquad \text{at } \tilde{f}_{\mathrm{K}} = \frac{3}{2B}, \tag{7.9}$$

$$\max\left(\frac{f\Phi_{ww}}{u_*^2}\right) = 0.5102\frac{C}{D^{3/5}} \qquad \text{at } \tilde{f}_{\mathrm{K}} = \left(\frac{3}{2D}\right)^{3/5}. \tag{7.10}$$

The numerical values are listed in Table 7.1. The modified constants result in 8% and 15% decreases in the amplitude of the spectral peaks of $f\Phi_{ww}$ and $f\Phi_{uu}$, respectively, but have little effect on the $\tilde{f}_{\mathrm{K}}$ values at which the peaks occur.

The Kaimal curves in Fig. 7.1 illustrate the effect of anisotropy. At low frequencies, the variance is dominated by horizontal fluctuations, and the maximum in $f\Phi_{uu}$ occurs at a $\tilde{f}_{\mathrm{K}}$ value that is approximately 10-fold smaller than the corresponding value for $f\Phi_{ww}$ (Table 7.1). Thus, the most energetic eddies in the flow have much larger horizontal scales than vertical scales, as expected for turbulence within the boundary layer. For high frequencies, the spectral densities decrease as $\tilde{f}_{\mathrm{K}}^{-5/3}$, as expected in the inertial subrange, and the ratio of Φ_{ww}/Φ_{uu} is $CB^{5/3}/AD$, which is equal to 1.32 (i.e., 4/3) for both sets of coefficients used in Fig. 7.1.

7.1.3 Comparison of von Kármán and Kaimal Spectra

The von Kármán and Kaimal spectra are inherently different because they are applicable in isotropic and anisotropic conditions, respectively. Insight into the similarities and

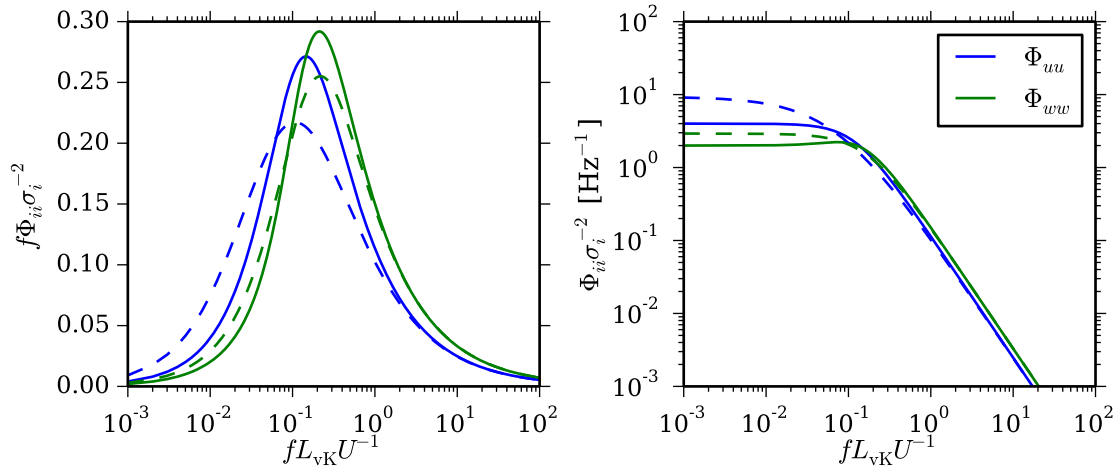

Figure 7.2: Comparison of von Kármán spectra (solid lines) and Kaimal spectra (dashed lines). Kaimal spectra are based on anisotropic relationships obtained by *Raupach et al.* (1991), i.e. $\sigma_u = 2.0u_*$, $\sigma_w = 1.2u_*$, and $\alpha_1 = 0.5$.

differences between these spectral shapes can be obtained by ensuring that the spectra tend to the same result in the inertial subrange. Equating Eqs. (7.1) and (7.3) for large f and using Eq. (7.5) to relate u_* and σ_u, yields $L_{\mathrm{vK}} = 2.2z$ for $B = 31$. The non-dimensional frequencies are therefore related by $\tilde{f}_{\mathrm{K}} = 0.45\tilde{f}_{\mathrm{vK}}$, allowing the longitudinal Kaimal spectrum to be plotted as a function of $\tilde{f}_{\mathrm{vK}}$ (Fig. 7.2, blue dashed line). The same procedure can be applied to the vertical velocity spectra, yielding $\tilde{f}_{\mathrm{K}} = 2.09\tilde{f}_{\mathrm{vK}}$ for $D = 5.6$ (Fig. 7.2, green dashed line). This direct comparison of the spectra reveal that the peak of $f\Phi_{ii}$ is lower and broader for the Kaimal spectra than for the von Kármán spectra.

7.2 Methods

7.2.1 A Measure of Anisotropy

A direct measure of anisotropy would require independent estimates of σ_u^2, σ_v^2, and σ_w^2, which cannot be obtained using data from a 4-beam, Janus configuration ADCP. However, combining the equations for the beam velocity variances—Eqs. (4.2) to (4.5)—and assuming statistical homogeneity across the spread of the beams, yields

$$\sigma_{u_I}^2 - \sigma_{v_I}^2 = \frac{\left(\sigma_{v_1}^2 - \sigma_{e_1}^2\right) + \left(\sigma_{v_2}^2 - \sigma_{e_2}^2\right) - \left(\sigma_{v_3}^2 - \sigma_{e_3}^2\right) - \left(\sigma_{v_4}^2 - \sigma_{e_4}^2\right)}{2\sin^2\vartheta}, \tag{7.11}$$

where u_I and v_I are the horizontal velocity components in instrument coordinates (Appendix F), and $\sigma_{v_i}^2$ and $\sigma_{e_i}^2$ are the variances of the along-beam velocities and the Doppler noise, respectively. For an instrument that is well-aligned with the flow, $\sigma_{u_I}^2 - \sigma_{v_I}^2$ is expected to equal zero in isotropic conditions with the magnitude of the difference increasing as the anisotropy of the turbulence increases.

7.2.2 Pairwise-Summed Beam Velocity Spectra

For instrument beam-pairs aligned with the flow direction, the summed beam velocity spectra can be related to the longitudinal and transverse spectra. The spectral representation of Eq. (4.6) for the streamwise beam pair, i.e., denoted by beams i and j, is

$$\widehat{S}_{ii} + \widehat{S}_{jj} = 2S_{uu}\sin^2\vartheta + 2S_{ww}\cos^2\vartheta + N_i + N_j, \tag{7.12}$$

where, as before, the Reynolds stress has been eliminated by assuming statistical homogeneity across the beam spread. A denoised mean velocity spectrum, S_{bb}, can then be defined as

$$S_{bb} \equiv \frac{1}{2}\left(\widehat{S}_{ii} - N_i + \widehat{S}_{jj} - N_j\right), \tag{7.13}$$

yielding

$$S_{bb} = S_{uu}\sin^2\vartheta + S_{ww}\cos^2\vartheta. \tag{7.14}$$

The predicted form of S_{bb}, i.e., Φ_{bb}, for $\vartheta = 20°$ is illustrated in Fig. 7.1 (red lines) for both the von Kármán and Kaimal representations. The coordinates of the maxima of $f\Phi_{bb}$ are given in Table 7.1. The dominance of $\cos^2\vartheta$ over $\sin^2\vartheta$ yields Φ_{bb} spectra that are closer to Φ_{ww} than Φ_{uu}, especially for the von Kármán form. At low frequencies, the contribution from Φ_{uu} dominates the Kaimal form. This difference between the two predicted spectral shapes has an important bearing on the results presented later.

7.2.3 Comparisons to von Kármán and Kaimal spectra

The von Kármán spectra are dependent upon the variance, σ^2, and the longitudinal integral length scale, L_{vK}. Because the turbulence is assumed to be isotropic, $\sigma^2 = \sigma_u^2 = \sigma_v^2$, and thus the integral of Eq. (7.14) yields

$$\sigma^2 = \int_0^\infty S_{bb}\, df. \tag{7.15}$$

The length scale can be determined from the $\tilde{f}_{\mathrm{vK}}$ value at the peak of fS_{bb}. Because the maximum is expected to occur at $\tilde{f}_{\mathrm{vK}} = 0.205$ (Table 7.1), the equivalent length scale is $L_{\mathrm{vK}} = 0.205|U|/f_{\mathrm{max}}$, where f_{max} is the frequency at the observed spectral peak.

In their universal form, the Kaimal spectra are dependent on the friction velocity, u_*, and the height above bed, z. For the Kaimal spectra to reduce to the ISR form in the high frequency limit, the assumption that $\epsilon = (\kappa z)^{-1} u_*^3$ is required, which assumes that (1) the Reynolds stress is equal to u_*^2, and (2) that production and dissipation are in balance. Because neither of these assumptions are valid (Figs. 4.2, 6.5, and 6.6), the use of u_* from the law-of-the-wall fits does not yield spectra that are directly comparable to the Kaimal form. Thus, a scaling coefficient, a_{K}, is introduced, and Eqs. (7.3) and (7.4) are normalized by $a_{\mathrm{K}} u_*^2$, instead of simply u_*^2. The value of a_{K} was determined so that the spectral peak of $fS_{bb}/a_{\mathrm{K}} u_*^2$ coincided with the predicted maximum of 0.370 (Table 7.1). The $\tilde{f}_{\mathrm{K}}$ value at the spectral peak was also used to compute $L_{\mathrm{K}} = 0.399|U|/f_{\mathrm{max}}$, which was used in place of z as the relevant length scale. This construction of the relevant parameters ensures that the measured and predicted spectra are in agreement at the spectral peak, but it does not ensure that they tend to the same limit in the ISR.

7.2.4 Integral Length Scale

An independent measure of the integral length scale can be obtained by computing autocorrelation functions of the along-beam velocity measurements, $\widehat{R}_{ii}$. Recalling that the beam velocity registered by the i-th transducer is given by $\hat{v}_i' = v_i' + e_i$, the definition of the autocorrelation yields

$$\widehat{R}_{ii}(\tau) = \langle v_i'(t) v_i'(t+\tau) \rangle + \langle e_i(t) e_i(t+\tau) \rangle \tag{7.16}$$

$$= R_{ii}(\tau) + R_{e_i e_i}(\tau), \tag{7.17}$$

where τ is the time lag, and R_{ii} and $R_{e_i e_i}$ are the autocorrelation functions of the true turbulent fluctuations and the Doppler noise, respectively. Because the Doppler noise is assumed to be white, $R_{e_i e_i}(0) = \sigma_{e_i}^2$ and $R_{e_i e_i} = 0$ for $\tau \neq 0$. Thus,

$$R_{ii}(\tau) = \begin{cases} \widehat{R}_{ii}(\tau) - \sigma_{e_i}^2 & \text{if } \tau = 0 \\ \widehat{R}_{ii}(\tau) & \text{otherwise.} \end{cases} \tag{7.18}$$

The corresponding integral length scale for the i-th beam is given by

$$L_i = |U| \int_0^\infty \frac{R_{ii}(\tau)}{R_{ii}(0)} d\tau, \tag{7.19}$$

where Taylor's hypothesis has been invoked to convert time to distance.

For the beams oriented in the cross-stream direction, i.e., denoted by subscripts k and ℓ, the expressions for the velocity components (see Appendix F) can be used to show that

$$\widehat{R}_{kk} = R_{vv} \sin^2 \vartheta + R_{ww} \cos^2 \vartheta + 2R_{vw} \sin \vartheta \cos \vartheta + R_{e_k e_k}, \tag{7.20}$$

$$\widehat{R}_{\ell\ell} = R_{vv} \sin^2 \vartheta + R_{ww} \cos^2 \vartheta - 2R_{vw} \sin \vartheta \cos \vartheta + R_{e_\ell e_\ell}, \tag{7.21}$$

where the subscripts represent the Cartesian velocity components, and $R_{xy} = \langle x(t)y(t+\tau) \rangle$. Summing the equations and assuming statistical homogeneity yields

$$\frac{\widehat{R}_{kk} + \widehat{R}_{\ell\ell}}{2} = R_{vv} \sin^2 \vartheta + R_{ww} \cos^2 \vartheta. \tag{7.22}$$

For isotropic turbulence $R_{vv} \approx R_{ww}$, thus the average of $\widehat{R}_{kk}$ and $\widehat{R}_{\ell\ell}$ yields an estimate for R_{ww}. The velocity variances for the cross stream beams are also approximately equal, yielding $\sigma_k^2 = R_{kk}(0) \approx R_{\ell\ell}(0)$, thus the vertical integral length scale—i.e., $L_w = |U|\sigma_w^{-2} \int_0^\infty R_{ww} d\tau$—can be approximated by

$$L_{Iw} = \frac{L_k + L_\ell}{2}, \tag{7.23}$$

where I in the subscript denotes the integral scale.

7.3 Results

7.3.1 A Measure of Anisotropy

For each 5-minute ensemble, the along-beam velocity variances, $\sigma_{v_i}^2$ at Sites 2b and 3 were computed. The Doppler noise variances, $\sigma_{e_i}^2$, were estimated using the spectral method described in Section 6.2.1 (see Appendix D for more details). An estimate of $\sigma_{u_I}^2 - \sigma_{v_I}^2$, i.e., the anisotropy in the horizontal, was then obtained using Eq. (7.11), and averages were calculated for the 60-minute intervals centred on peak flood and ebb flows (red and

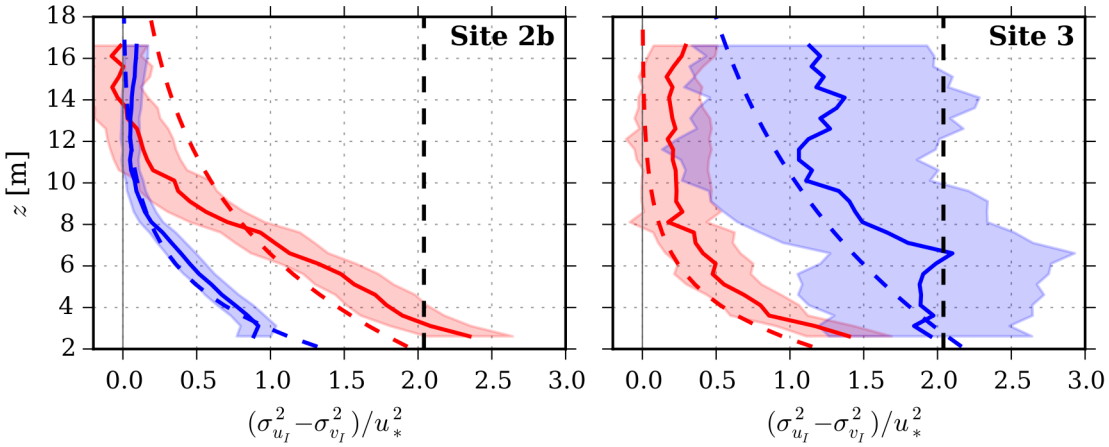

Figure 7.3: Difference between streamwise and cross-stream variances during peak flow conditions. Solid lines correspond to the measured estimates obtained via Eq. (7.11). The shaded regions identify the standard errors in the estimates based on the number of tidal cycles included in the average. The dashed lines correspond to the empirical estimates based on *Raupach et al.* (1991) (black) and *Nezu and Nakagawa* (1993) (red, blue). Red and blue colours correspond to the flood and ebb, respectively.

blue segments in Fig. 6.3). The mean values over all tidal cycles are shown in Fig. 7.3, where the estimates have been normalized by u_*^2 as determined from the law-of-the-wall fits (Table 6.1). The magnitude of $\sigma_{u_I}^2 - \sigma_{v_I}^2$ is highest near the bed, where the flow is expected to be most anisotropic. For $z > 10$ m, $\sigma_{u_I}^2 - \sigma_{v_I}^2$ is near zero on both phases of the tide at Site 2b, and on the flood tide at Site 3, indicating a tendency toward isotropy with increasing height above bottom.

In Fig. 7.3, the measured differences in the streamwise and cross-stream variances are compared to two empirical estimates. The first is based on $\sigma_u = 2.0u_*$ and $\sigma_v = 1.4u_*$, which are the anisotropic ratios in the constant stress layer obtained by *Raupach et al.* (1991) for wind tunnel measurements. The corresponding value of $(\sigma_u^2 - \sigma_v^2)/u_*^2$ is 2.06 (Fig. 7.3, black line) which agrees well with the data at $z \approx 3$ m on the flood tide at Site 2b and for $z < 7$ m on the ebb tide at Site 3. The second empirical estimate is based on the vertical distributions of the variances given by *Nezu and Nakagawa* (1993) for open channel flow, which decrease exponentially with height above bed according to

$$\sigma_u^2/u_*^2 = 5.29e^{-2z/H}, \tag{7.24}$$

$$\sigma_v^2/u_*^2 = 2.66e^{-2z/H}, \tag{7.25}$$

$$\sigma_w^2/u_*^2 = 1.61e^{-2z/H}, \tag{7.26}$$

where H is the channel depth. Replacing H with δ_L—i.e., the thickness of the log-layer (Section 6.4.2)—and combining Eqs. (7.24) and (7.25), yields $\left(\sigma_u^2 - \sigma_v^2\right)/u_*^2 = 2.63e^{-2z/\delta_L}$ which is illustrated in Fig. 6.2 as the red and blue dashed lines, for the flood and ebb tides, respectively. The predicted estimate for the variance difference agrees best with the measurements on the ebb tide at Site 2b and on the flood tide at Site 3. On the flood tide at Site 2b and the ebb tide at Site 3, the measured differences are comparable in magnitude but deviate from the expected exponential form. The site-dependence of anisotropy is discussed further in Section 7.4.3.

7.3.2 Pairwise-Summed Beam Velocity Spectra

The along-beam velocity spectra were computed for the 60-minute interval around maximum flood and ebb flows. Hanning-windowed, four-minute segments were used with 50% overlap yielding spectra with a frequency resolution of approximately 0.004 Hz and 51 and 55 equivalent degrees of freedom at Sites 2b and 3, respectively (*Nuttall*, 1971). The spectra for all tides were then averaged and the z-dependent noise levels—estimated from the spectra at slack water—were removed, yielding an estimate of S_{bb} via Eq. (7.13). The S_{bb} estimates were further averaged over 1.5 m in the vertical.

A subset of the resulting spectra is shown in variance preserving form in Fig. 7.4. The spectral levels do not vary significantly with depth, except on the ebb tide at Site 2b where the variances are very high near the bed and drop off quickly with increasing z, consistent with the large gradients in $\mathcal{P}_h$ and ϵ (Figs. 6.3 and 6.6).

On the ebb tide at both sites, there is a sharp peak near 0.15 Hz for $z > 11.6$ m, which corresponds to the increased variance associated with wave motion (Appendix C). Excluding these wave peaks, the maxima of fS_{bb} typically occur between 0.04 and 0.25 Hz. A least squares regression of a second order polynomial to fS_{bb} vs $\log_{10} f$ was used over approximately a one decade interval near the spectral peak. The resulting polynomial was then used to both estimate the frequency at the spectral peak, $f_{\max}$, and interpolate the spectra over the frequency range containing the wave peak (Fig. 7.6, grey lines).

At high frequencies—i.e., $f > 0.6$ Hz—fS_{bb} often increases with f, deviating from the expected $f^{-2/3}$ form. Because this is most apparent for the spectra nearest the bed where the turbulence levels are the highest, it is likely that the $\mathcal{O}(1)$ Hz sample rate leads to aliasing in the spectra. Because the focus of this chapter is on turbulence in the production range, no corrections to the spectra were made to reduce this effect.

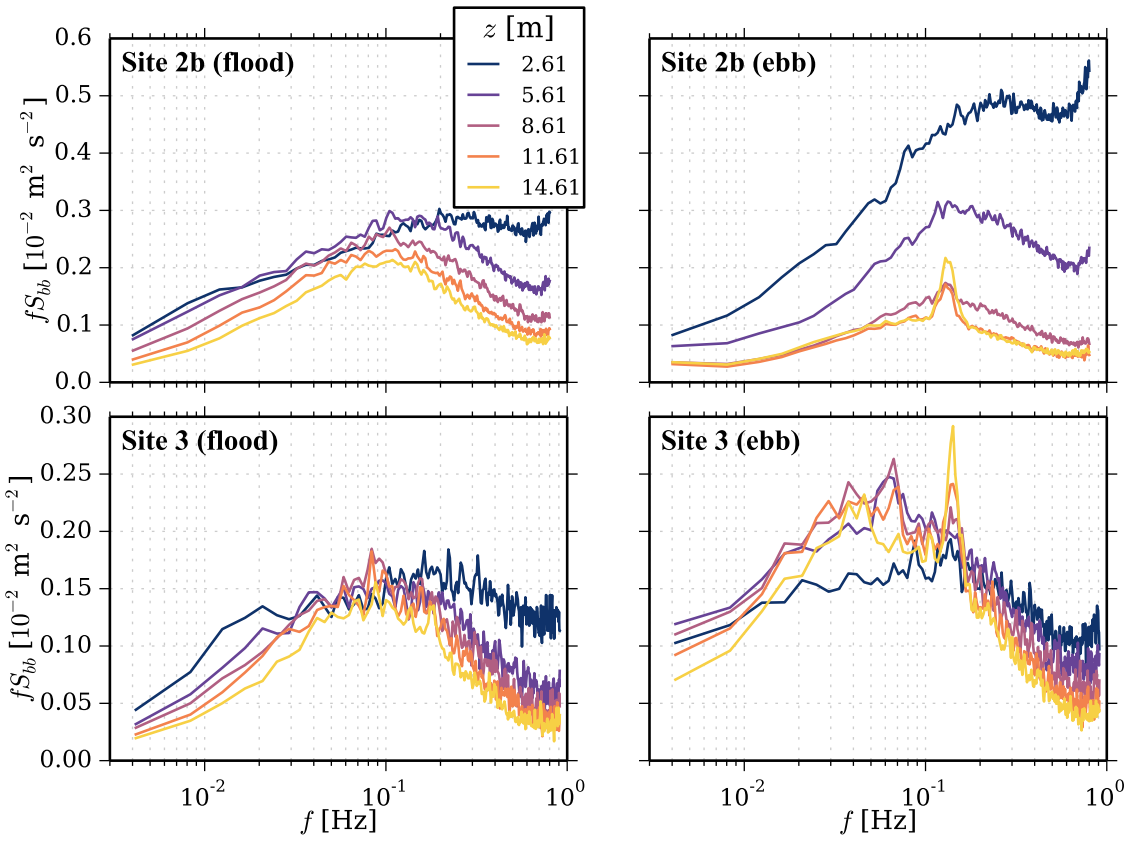

Figure 7.4: Average pairwise-summed beam velocity spectra, S_{bb}, for the beam pair oriented in the streamwise direction (Eq. 7.13). Averages were computed over all tides and over 1.5 m in the vertical. The colours represent the heights given in the legend.

7.3.3 Length Scales

The values of $f_{\max}$ estimated from the polynomial fits were used to determine the length scales associated with the spectral peaks. For the von Kármán spectra, $L_{\mathrm{vK}} = 0.205|U|/f_{\max}$, and for the Kaimal spectra $L_{\mathrm{K}} = 0.399|U|/f_{\max}$ (Table 7.1), thus the two length scales are related by $L_{\mathrm{K}} = 1.95L_{\mathrm{vK}}$. Both the L_{vK} and L_{K} estimates are shown in Fig. 7.5 (solid lines), though the reader should bear in mind that they are directly proportional, so the profile shapes are identical except for the constant scaling factor. The L_{vK} and L_{K} values increase with distance from the bed to a broad maximum between 10 to 15 m height and then decrease toward the surface, particularly at Site 2b. Near the bed, $L_{\mathrm{K}} \approx z$ (Fig. 7.5, black line) as expected from the general form of the Kaimal spectra. In the upper half of the water column $L_{\mathrm{K}} < z$ because the free-surface necessarily limits the maximum size of the eddies.

The integral length scales, L_i, were estimated from the along-beam velocity measurements using the autocorrelation function for each five-minute ensemble and Eq. (7.19) with the upper limit of integration being the first zero crossing of $R_{ii}(\tau)$. The mean values over all tides for the 60-minute intervals around maximum flood and ebb flows were then determined and the average of the cross-stream beams—i.e., L_k and L_ℓ—was calculated, yielding L_{Iw} via Eq. (7.23). Vertical profiles of the resulting integral scales are shown in Fig. 7.5 (dashed lines). With the exception of the ebb tide at Site 3, the L_{Iw} values closely track the L_{vK} values determined from the von Kármán spectra. This result is surprising because L_{vK} and L_{Iw} are estimates of the longitudinal and vertical integral scales, respectively, which—for isotropic turbulence—are expected to be related by $L_{\mathrm{vK}} = 2L_{Iw}$ (*Diedrich and Drischler*, 1957; *Kaimal and Finnigan*, 1994). Length scales are discussed further in Section 7.4.2.

7.3.4 Comparison to the Predicted Spectral Forms

The measured spectra and the von Kármán and Kaimal forms are compared in Fig. 7.6. The non-dimensional frequencies were computed using L_{vK} and L_{K}, thus forcing the spectral peaks to align. The velocity parameters used to non-dimensionalize the spectral densities—i.e., σ^2 for von Kármán and $a_{\mathrm{K}}u_*^2$ for Kaimal—are shown in Fig. 7.7. Qualitatively, the variance profiles exhibit patterns similar to those for TKE (Figs. 6.5h,k) with a significant increase toward the bed, except on the ebb tide at Site 3, where the maximum occurs at $z \approx 7$ m. The values of a_{K} used to scale the Kaimal spectra vary by more than an order of

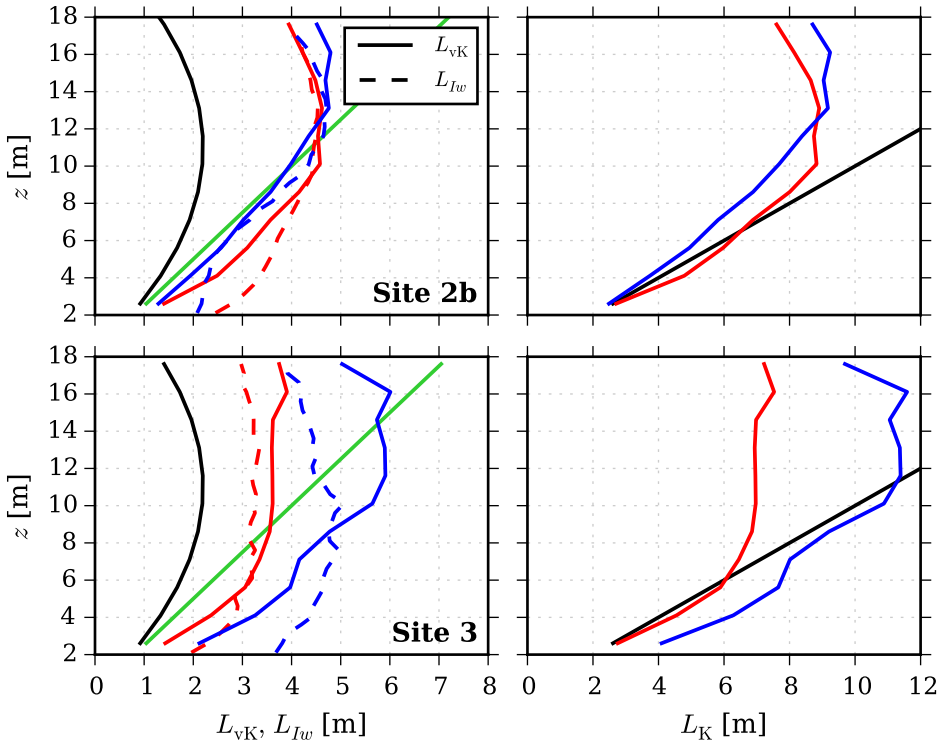

Figure 7.5: Length scales determined from the spectral maxima (L_{vK}, L_{K}) and integral length scales determined from the autocorrelation functions (L_{Iw}). Red and blue correspond to flood and ebb tides, respectively, and linetypes are specified in the legend. In the left panels, the solid black line is $L = \kappa z(1 - z/H)$ and the green line is $L = \kappa z$. In the right panels, the black line is $L = z$.

magnitude. Near the surface at Site 2b, $a_{\mathrm{K}} \approx 0.1$ on the ebb tide, whereas $a_{\mathrm{K}} > 1.2$ near mid-depth on the ebb tide at Site 3. The expected value of a_{K}—based on the universal Kaimal scaling—is 1, which is most consistent on the flood tide at Site 2b and on the ebb tide at Site 3, for which the normalized Reynolds stresses, i.e., $-\langle u'w' \rangle / u_*^2$, were greater than 0.5 (Figs. 6.5i,l).

The agreement between the measured spectra and the von Kármán and Kaimal forms varies with site, tidal phase (ebb/flood) and height above bed. The RMS errors between the measured and predicted spectra are shown in Fig. 7.8. The errors were computed for the non-dimensional frequency range below 60% of the maximum (Fig. 7.6, black markers), thus excluding the high frequency range affected by aliasing. For $z < 5$ m, the measured spectra conform better to the Kaimal form than the von Kármán form, whereas the opposite is true near the surface, indicating—as expected—that the flow closer to the bed is more anisotropic. Furthermore, at all depths, the von Kármán spectra underestimate the variance at low frequencies; however, the discrepancy decreases with height above bed, indicating the need for a z-dependent measure of anisotropy in the formulation of the semi-empirical spectra.

7.3.5 Varying σ_u/u_*

The discrepancy at low frequencies between the measured spectra and the Kaimal forms, as well as the observation that $\sigma_{u_I}^2 - \sigma_{v_I}^2$ varies throughout the water column (Fig. 7.3), suggests that the use of a constant value for σ_u/u_* may be inappropriate. Near the bed, the Kaimal spectra underpredict the variance at low frequencies, whereas for $z > 8$ m, the measured spectral densities are lower than the Kaimal curves (Fig. 7.6, right panels). Because Φ_{bb} is dominated at low frequencies by Φ_{uu} (Fig. 7.2) a z-dependent σ_u/u_* was implemented, with σ_w/u_* fixed at the *Raupach et al.* (1991) value of 1.2. Example comparisons are shown in Fig. 7.9 for $z = 8.61$ m at Site 2b. On the flood tide, a value of $\sigma_u/u_* = 1.6$ yields the lowest RMS error (Figs. 7.9a,b). However, on the ebb tide, a local minimum was not observed over the range of σ_u/u_* values considered (Fig. 7.9d). In cases like this—i.e., where no local minimum was found—the best-fit value was selected as the highest σ_u/u_* ratio where the derivative with respect to z of the RMSE was below 5×10^{-5} m^{-1} (e.g., green marker in Fig. 7.9d).

The best-fit values of σ_u/u_* and the corresponding RMS errors are shown as functions of z in Figs. 7.10 and 7.11, respectively. The optimal σ_u/u_* values typically decrease

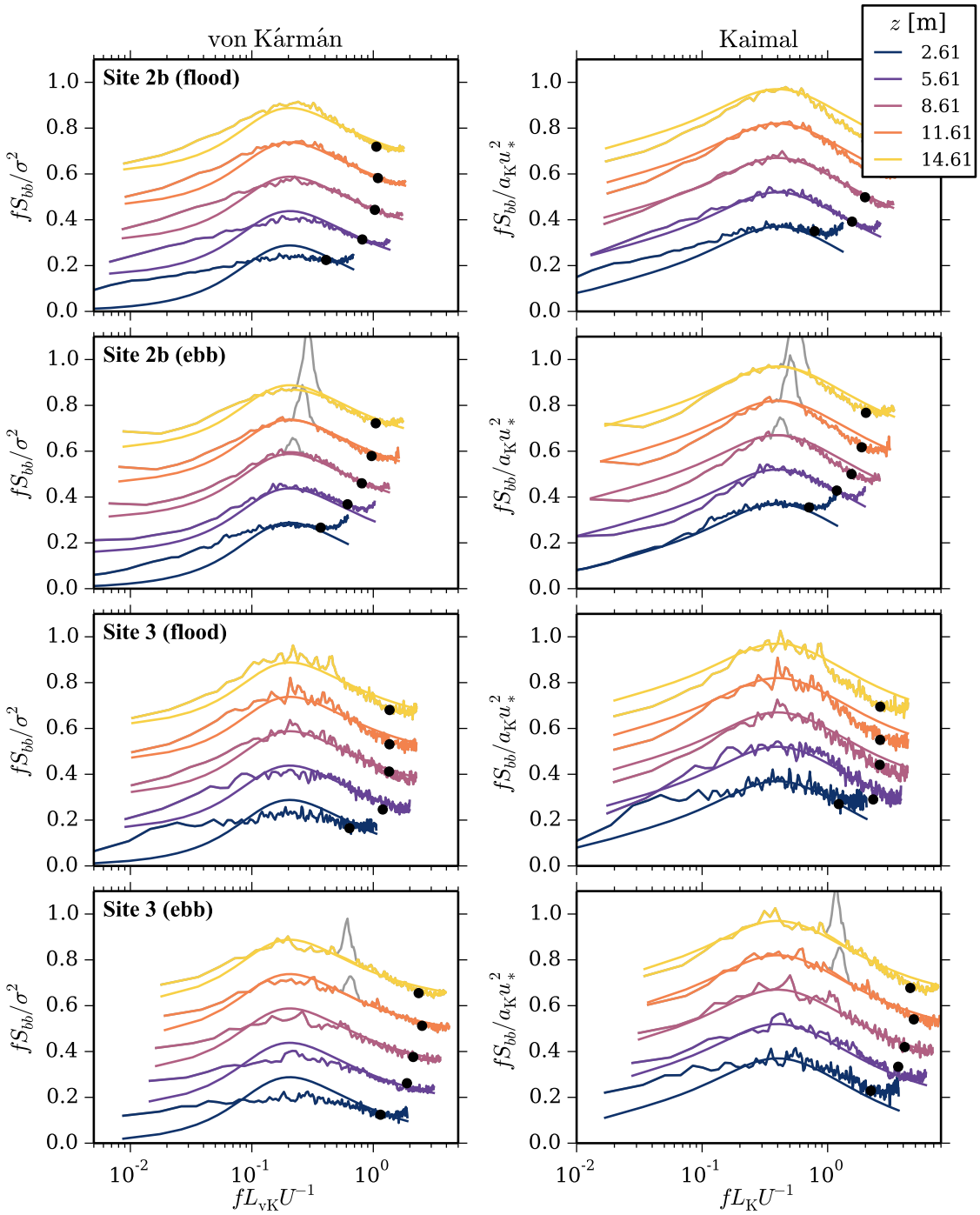

Figure 7.6: A subset of the non-dimensionalized velocity spectra with comparisons to the von Kármán curves (left panel, smooth curves) and Kaimal curves (right panel, smooth curves). The grey segments of the spectra represent wave peaks that were interpolated over. For increasing z, the curves have been shifted vertically by 0.15 units. The black markers correspond to the maximum frequency used in the computation of the RMS error between the observed and predicted spectra.

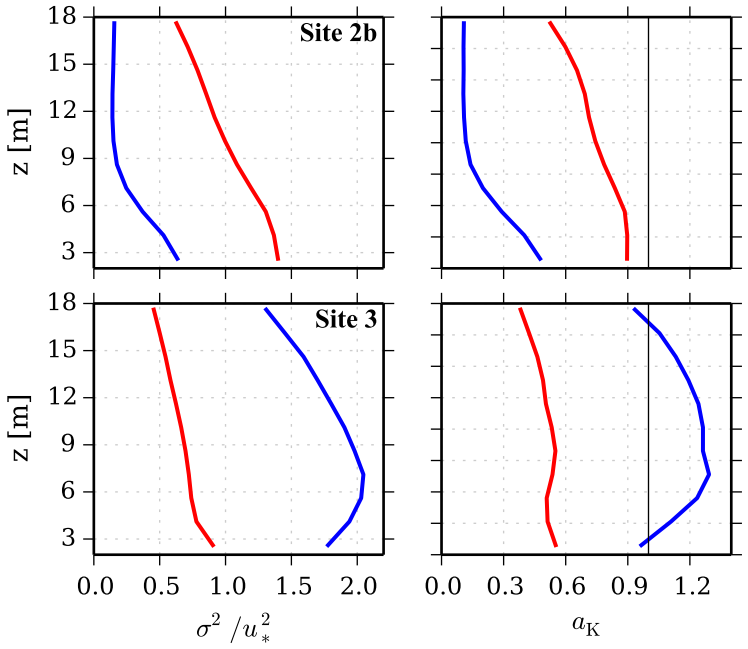

Figure 7.7: Parameters used to non-dimensionalize the spectral fits. The variance computed using Eq. (7.15) is plotted in the left panels and the variance scaling coefficient a_K (used for fitting to the Kaimal spectra) is plotted in the right panels. Flood and ebb tides are represented by the red and blue lines, respectively.

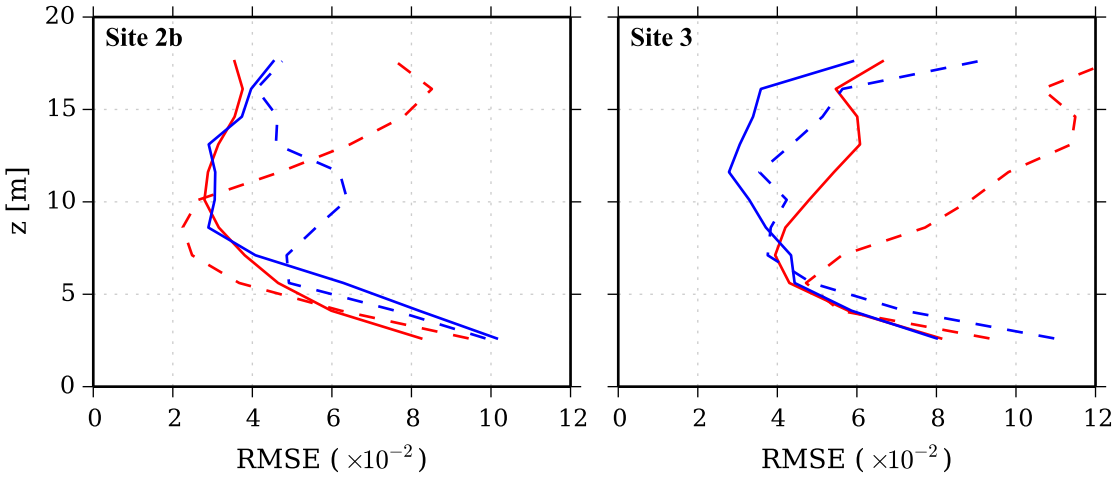

Figure 7.8: RMS errors between the measured spectra and the predicted forms (solid: von Kármán, dashed: Kaimal). Red and blue lines correspond to the flood and ebb tides, respectively.

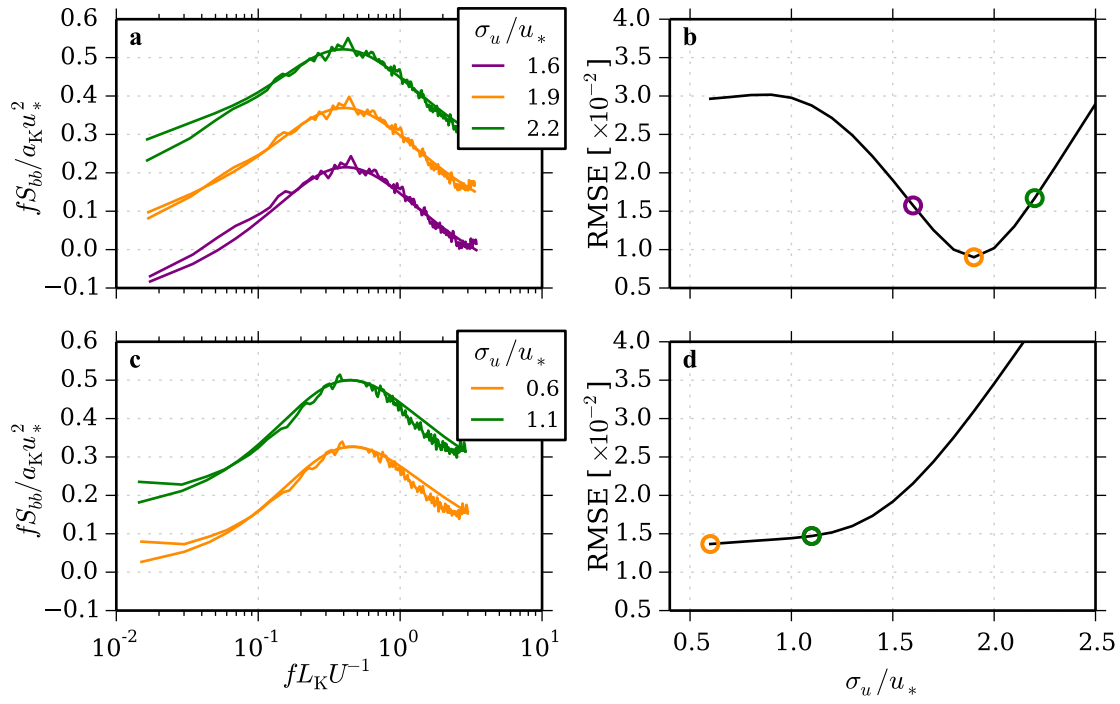

Figure 7.9: Non-dimensional velocity spectra at $z = 8.61$ m at Site 2b on the (a) flood, and (c) ebb tides, compared to the Kaimal curves for various σ_u/u_* values. The purple and green curves are offset vertically by -0.15 and 0.15 units, respectively. (b) The corresponding RMS errors between the measured spectra and the Kaimal curves are shown in (b) and (d) for the full range of σ_u/u_* values considered. The errors were computed for the frequencies below the $fS_{bb}/a_K u_*^2$ maximum.

with height above bottom, consistent with the tendency toward more isotropic turbulence near the surface. One exception occurs at Site 2b on the ebb tide where the lowest σ_u/u_* values occur near mid-depth. On the flood tide at Site 2b and the ebb tide at Site 3, the vertical variation is well predicted by $\sigma_u/u_* = 3.45e^{-z/\delta_L}$ (dashed lines)—i.e., Eq. (7.24) multiplied by 1.5 —indicating that the longitudinal variances are more than double those predicted by *Nezu and Nakagawa* (1993) throughout the water column.

7.4 Discussion

7.4.1 Comparison to Previous Studies

To my knowledge, this is the first study to compare diverging-beam ADCP data to suitably modified forms of the Kaimal and von Kármán velocity spectra. Previous comparisons in

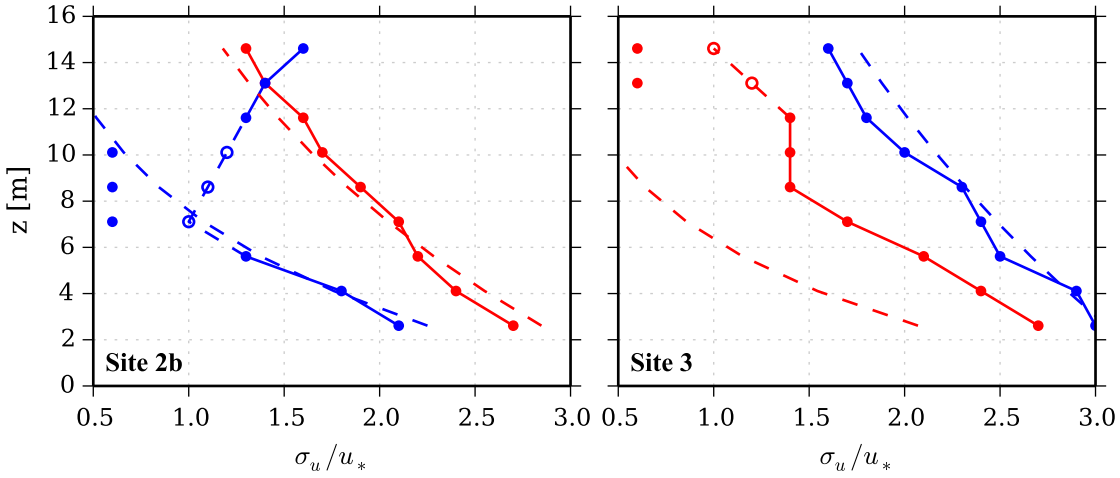

Figure 7.10: Best-fit σ_u/u_* values as a function of height above bottom (solid lines) and $\sigma_u/u_* = 3.45e^{-z/\delta_L}$ (dashed lines). Flood and ebb tides are represented by the red and blue lines, respectively. Closed markers denote the best-fit values determined by the lowest RMS errors between the measured spectra and the Kaimal curves (e.g. yellow lines and markers in Fig 7.9). Open markers correspond to optimal σ_u/u_* values determined using a minimum threshold on the derivative of the RMS error (e.g. green line and marker in Figs. 7.9c,d).

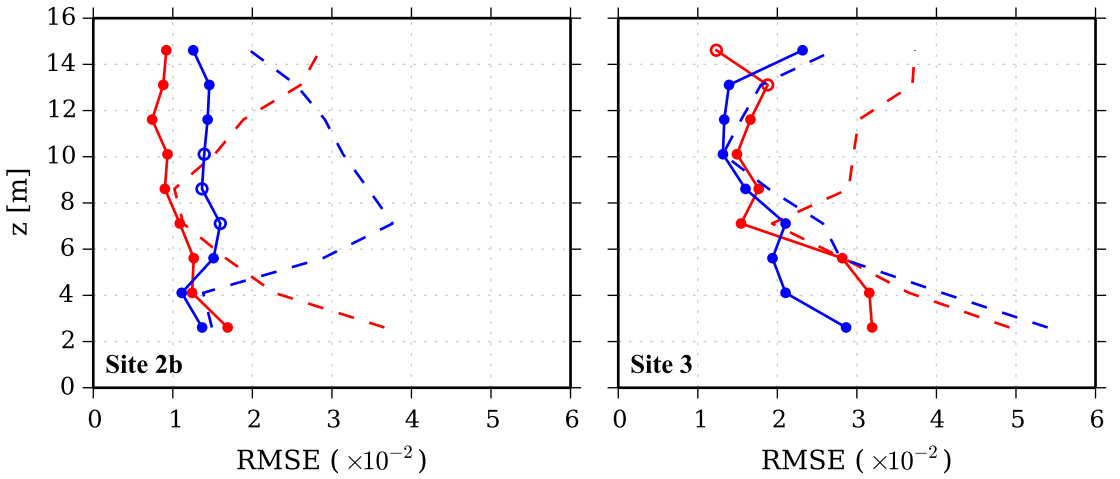

Figure 7.11: RMS errors between the measured spectra and the Kaimal spectra with the best-fit σ_u/u_* ratio. The errors were computed for frequencies below the fS_{bb}/au_*^2 maximum. Dashed lines correspond to the equivalent errors with $\sigma_u = 2.0u_*$. Red and blue correspond to flood and ebb tides, respectively. The open and closed markers are consistent with those used in Fig. 7.10.

unstratified tidal flows have been limited to single-point time series measurements of u, v, and w obtained at a single depth (*Walter et al.*, 2011; *Milne et al.*, 2013) or obtained successively at several depths by moving a single sensor through the water column (*Lien and Sanford*, 2000). While ADCPs yield simultaneous estimates of velocity throughout the water column, direct estimates of u, v, and w cannot be obtained due to the divergent beam geometry. Neither can the length scale in the von Kármán spectrum be estimated directly from the ADCP data, and so must instead be obtained by forcing the observed and predicted spectra to coincide at the peak of $f\Phi_{bb}$.

Given these limitations, it is nevertheless promising that the ADCP results presented in this chapter are consistent with the earlier comparisons to the Kaimal spectra cited above. Near the bed—i.e., at $z = 2.61$ m and occasionally greater heights—the observed spectral densities are higher than the Kaimal spectra at low frequencies (Fig. 7.6, left panels), in agreement with the results obtained by both *Walter et al.* (2011) and *Lien and Sanford* (2000) at $z = 1$ m and $z < 9$ m, respectively. Note that *Walter et al.* (2011) used the values for the constants A, B, C, and D in *Kaimal et al.* (1972), and *Lien and Sanford* (2000) used the slightly modified values given by *Kaimal and Finnigan* (1994): i.e., both different from the initial values used here, which were based on wind tunnel measurements by *Raupach et al.* (1991) and $\alpha_1 = 0.5$ rather than 0.55. The underestimation of the spectral densities in the low frequency region of the spectrum prompted the use of a variable σ_u/u_* ratio, resulting in better agreement between the measurements and the Kaimal form of S_{bb} (Fig. 7.11).

Comparisons of the Grand Passage data to the von Kármán spectra are inconsistent with the ADV measurements of *Milne et al.* (2013) because, at low frequencies, the velocity spectra in Grand Passage are all underpredicted by the von Kármán spectra (Fig. 7.6, left panels). While the method implemented by *Milne et al.* (2013) did not force the spectra to coincide at the spectral peaks, the observed spectra were narrower than the von Kármán forms, unlike the results presented in this chapter.

The method implemented in this study to estimate length scales from the spectral peak is commonly used to compare measurements obtained in the atmospheric boundary layer to the von Kármán and Kaimal forms (e.g., *Mann*, 1994; *Peña et al.*, 2010). Other approaches have estimated the length scales by matching the measured spectra to the appropriate limit in the inertial subrange (e.g *Morfiadakis et al.*, 1996). In many of these

investigations—particularly when the von Kármán form was considered—the length scales were determined separately for each velocity component: i.e., it was not assumed that the longitudinal integral scale was a factor of two larger than the transverse scale. In addition, the use of von Kármán spectra where $\sigma_u^2 \neq \sigma_w^2$ is common in simulations of atmospheric turbulence (*Burton et al.*, 2011). Other modifications that incorporate anisotropy have been suggested, including a spectral model developed by *Mann* (1994, 1998) based on Rapid Distortion Theory (*Townsend*, 1976). Although these modified forms—unlike Eqs. (7.1) and (7.2)—are inconsistent with the analytical equations governing the autocorrelation functions (*Diedrich and Drischler*, 1957), they have been shown to agree well with measurements obtained in neutral atmospheric boundary layers. Thus, the modified forms could be applicable to unstratified tidal flows.

7.4.2 Physical Interpretation of the Length Scales

The length scales relevant to the von Kármán and Kaimal spectra are both related to the size of the eddies contributing to the variance in the production range. For the Kaimal spectra in their general form, z is the relevant length scale, indicating that the distance from the boundary controls the vertical scale of the eddies, which is consistent with longstanding ideas associated with Prandtl's mixing length and the eddy viscosity, $\kappa u_* z$, arising from the law-of-the-wall. The Grand Passage data confirm this scaling in the near bed region, since the length scale estimated from the spectral peak—i.e., L_{K}—is within 25% of z for $z < 8$ m. On the ebb tide at Site 3, the scaling with z extends farther upward to a height of 12 m. Near mid-depth, L_{K} tends to be independent of height, whereas in the upper half of the water column, the distance to the free surface limits the vertical extent of the eddies. A consistent decrease in L_{K} was only observed on the flood tide at Site 2b. However, the uppermost 4 m—where the free surface will have the greatest effect—is not resolved in the ADCP data.

The relevant length scale for the von Kármán spectra, L_{vK}, is, by definition, the longitudinal integral scale. Under the assumption of isotropy, the vertical integral length scale is equal to $L_{\mathrm{vK}}/2$; however, the L_{Iw} estimates—which are an approximation for the vertical scale—reveal that this relationship does not hold, and instead, $L_{\mathrm{vK}} \approx L_{Iw}$ (Fig. 7.5, left panels). Importantly, neither length scale is based on the fundamental definition as the integral of the autocorrelation function, and hence cautious interpretation is warranted. In addition, the turbulence—particularly near the bed—is anisotropic although the deviation

from isotropy is expected to yield $L_{\mathrm{vK}} > 2L_{Iw}$, which is not observed in the data.

Bearing this in mind, comparison to theoretical length scale estimates is useful. In the inertial sublayer, *Tennekes and Lumley* (1972) (p. 159) suggest that the relevant vertical scale is κz based on a scaling of the velocity shear as $dU/dz = u_*/\kappa z$, i.e., the-law-of-the-wall assumption. This relationship appears to be consistent with L_{Iw} at Site 2b on the ebb tide (Fig. 7.5, green line). The mixing length scale for channel flow, given by $L = \kappa z(1 - z/H)$, is illustrated in black in Fig. 7.5 (left panels) and is shown to be about a factor of two less than the measured length scales throughout the water column, consistent with the comparisons made by *Stacey et al.* (1999).

7.4.3 Vertical Variation of Anisotropy

Anisotropy was assessed in two ways. First, the difference in the streamwise and cross-stream variances (Fig. 7.3) was estimated via Eq. (7.11), and best-fit σ_u/u_* values were determined from spectral fits to the Kaimal form of fS_{bb} in the low frequency range (Fig. 7.10). In all cases, except on the ebb tide at Site 2b, both measures of anisotropy decrease with height above bottom and vary with both site and tidal phase.

On the ebb tide at Site 3, the estimated length scales were the largest (Fig. 7.5) and the differences in the streamwise and cross-stream variances (Fig. 7.3) were the greatest. These observations indicate that the turbulence generated at the cross-stream ridge located ca. 300 m upstream remains highly energetic and anisotropic as it is advected past the ADCP site. The best-fit σ_u/u_* values were also the highest at this site (Fig. 7.10) with an optimal value of 3 at $z = 2.61$ m, inconsistent with the results of *Hay et al.* (2013) who showed that $\sigma_u/u_* = 2$ and $\sigma_w/u_* = 1.2$ yielded the expected along beam velocity variances at $z = 2.1$ m.

The vertical variation in σ_u/u_* on the ebb tide at Site 2b is inconsistent with the other cases (Fig. 7.3), exhibiting a minimum at mid-depth and then increasing with z as the surface is approached. In the previous chapter, it was shown that the ebb tide at Site 2b is characterized by a thin log-layer within which the turbulence levels are very high. Turbulence is also generated near the surface during several tidal cycles, thus leading to increased variance and increasing σ_u/u_* since u_* remains constant.

One of the interesting results regarding the measures of anisotropy is that the ratio of the velocity variances is z-dependent: i.e., the best-fit σ_u/u_* values—determined for a constant σ_w/u_* value—decrease with z, suggesting that σ_u^2/σ_w^2 decreases with height.

This is in contrast to *Nezu and Nakagawa* (1993) where the ratio of the σ_i^2 values for any two velocity components yields a constant value for all depths (Eqs. 7.24–7.26). A decrease in the degree of anisotropy with z is consistent with measurements obtained by *Peña et al.* (2010) in a neutral atmospheric boundary layer, where comparisons of the data with spectral model of *Mann* (1994) indicated that $\sigma_u^2/\sigma_w^2 \approx 3$ near the ground and $\sigma_u^2/\sigma_w^2 \approx 2$ at 160 m height. In comparison, the best-fit σ_u/u_* estimates for the Grand Passage data give σ_u^2/σ_w^2 values as high as 6 near the bed (Site 3, ebb), and as low as 0.7 at both mid-depth (Site 2b, ebb) and near the surface (Site 3, flood).

7.5 Conclusions

The ADCP measurements at Sites 2b and 3 have been compared to modified forms of the Kaimal and von Kármán spectra derived for diverging-beam ADCP data. Using empirical constants obtained from wind tunnel measurements (*Raupach et al.*, 1991) and $\alpha_1 = 0.5$, the Kaimal spectra better agree with the ADCP data in the near bed region. On the other hand, above mid-depth, better agreement is obtained with the von Kármán spectra, consistent with the observation that the flow is more isotropic near the surface.

The spectral densities at low frequencies are less than those predicted by the von Kármán form throughout the water column, whereas the use of a constant σ_u/u_* ratio for the Kaimal spectra yields predicted forms that overestimate the variance near the bed and underestimate the variance as z increases (Fig. 7.6). This observation, in addition to $(\sigma_u^2 - \sigma_v^2)/u_*^2$ values that decrease with z, prompted the use of a variable σ_u/u_* for the Kaimal form. The optimal values of σ_u/u_*—determined via the RMS error in the production range—decrease with height above bed except on the ebb tide at Site 2b where σ_u/u_* has a local minimum at mid-depth.

The comparisons between the measurements and the predicted forms were carried out by forcing the spectra to match at the peaks of fS_{bb}, yielding two length scale estimates related by $L_{\mathrm{K}} = 1.95 L_{\mathrm{vK}}$. For $z < 8$ m, the L_{K} values (determined from the Kaimal form) are within 25% of z, which is the expected value. However, near mid-depth and closer to the surface $L_{\mathrm{K}} < z$, due to the presence of the free surface which limits the vertical extent of the eddies. The L_{vK} values (determined from the von Kármán form) are comparable to estimates of the vertical integral length scale, L_{Iw}, determined from the along-beam autocorrelation functions. This result is surprising because, by definition, L_{vK}

is the longitudinal integral scale and expected to be given by $L_{\mathrm{vK}} \approx 2L_{Iw}$ for isotropic turbulence. In the lower half of the water column, $L_{Iw} \approx \kappa z$ (more so at Site 2b), which is a scaling for the vertical size of the eddies that is consistent with the law-of-the-wall form of the velocity profile.

The results presented in this chapter indicate that the Kaimal spectra, which allow for z-dependent anisotropy, best predict the variance at low frequencies in the Grand Passage measurements. The anisotropy—quantified by σ_u^2/σ_w^2—decreases by an order of magnitude with increasing height above bottom. This variation with z is inconsistent with open channel flows where a constant value of $\sigma_u^2/\sigma_w^2 = 3.3$ is expected (*Nezu and Nakagawa*, 1993). However, the estimates of anisotropy are comparable—at least qualitatively—to measurements made in the neutral atmospheric boundary layer by *Peña et al.* (2010), and thus, future work should include comparisons to other anisotropic spectral forms.

CHAPTER 8

CONCLUSIONS

This thesis presents ADCP and shear probe measurements acquired in Grand Passage, Nova Scotia, which is an 8×10^7 Reynolds number tidal channel. The water depth along the channel centreline ranges from 10 to 30 m, the tidal range is 5 m, and the depth-averaged flow speed reaches 2.5 m s^{-1}. The dataset consists of three separate field campaigns that included the deployment of four bottom-mounted ADCP frames and an underwater, streamlined buoy "flown" at mid-depth (a.k.a. the *Nemo* buoy). The broadband, diverging-beam ADCPs sampled at 1.5 to 1.8 Hz in 0.5-m range bins. At one of the sites, an additional second generation ADCP (i.e., AD2CP) acquired measurements along a vertical beam at 8 Hz in 12.5-cm range bins. The shear probes were mounted in the nose of the *Nemo* buoy and acquired measurements at a rate of 2048 Hz. The dataset was used to: (1) assess the capabilities and limitations of both instrumentation techniques and analysis methods for turbulence measurements in high-flow environments, (2) characterize the spatial and temporal variability in turbulence and boundary layer parameters, and (3) investigate the validity of existing theoretical and empirical relationships.

8.1 Key Findings

1) **Dissipation rates estimated from ADCP and shear probe data agree to within a factor of two.**

   Speed-bin averaged dissipation rates estimated at mid-depth from the ADCP measurements agree to within a factor of two with direct estimates obtained using shear probes mounted in the nose of the *Nemo* buoy (Chapter 4). Possible sources of bias and error in the ADCP estimates were investigated, all of which are found to be small. Thus,

the most likely cause of the factor of two discrepancy is the cross-channel separation of the instruments and the high degree of spatial variability in the passage. This finding is supported both by cross-channel transects of ϵ obtained using a vertical microstructure profiler (*McMillan et al.*, 2015) and by vertical velocity measurements recorded by the AD2CP (Chapter 4).

2) **Spectral and structure function methods yield comparable estimates of the dissipation rate when applied to broadband diverging-beam ADCP data.**

The ADCP data were used to estimate the dissipation rate at mid-depth on 5-minute timescales using a spectral method and both second- and third-order structure function methods (Chapter 5). The results indicate that the second-order structure function (SF2) method agrees with the spectral estimates to within 16% at all four sites, and the SF2 method is more robust than either the third-order method or the spectral method. The application of the SF2 method also validates the use of $C_2 = 2.0$ as the SF2 universal constant, as opposed to the value of 2.1 that has been frequently used in other studies.

3) **Doppler noise level estimates are independent of flow speed.**

The apparent Doppler noise levels, computed using the traditional SF2 method, decrease with both increasing dissipation rate and increasing flow speed. However, accurate noise levels can be obtained using a modified SF2 method that accounts for the unresolved variance due to the low-pass filtering effect associated with the finite ADCP pulse length (i.e., finite cell size). The "corrected" noise levels (i.e., estimated from the modified method) are independent of flow speed, and in agreement with the values determined from the spectral method.

4) **Dissipation rate estimates from the ADCP measurements are log-normally distributed.**

Estimates of the dissipation rate from the ADCP measurements at mid-depth are log-normally distributed (Chapter 5), consistent both with the expected distribution for small-scale (a.k.a. inner-scale) intermittency in high Reynolds number flows, and with the shear probe measurements (Chapter 4). For both measurement types, the probability density functions were computed for strong flow conditions.

5) **Streamwise advection is a significant term in the TKE balance.**

The dominant terms in the TKE equation—i.e., production ($\mathcal{P}_h$), dissipation (ϵ), and vertical diffusion of TKE (T_d)—were estimated during peak ebb and flood flows

(Chapter 6). The rates of production and dissipation are highest near the bed and close to being in balance only when the constant stress layer is sufficiently thick to be resolved in the ADCP profile. The vertical variation of the parameters is qualitatively consistent with both previous field measurements and DNS simulations of channel flow. Typically, T_d is small, and $\mathcal{P}_h$ and ϵ agree to within a factor of two throughout most of the water column, with the tendency that $\mathcal{P}_h > \epsilon$ near the bed, $\mathcal{P}_h \approx \epsilon$ at mid-depth, and $\mathcal{P}_h < \epsilon$ near the surface. The observed imbalance in $\mathcal{P}_h$ and ϵ—both locally and in a depth-averaged sense—is likely due to the streamwise advection of TKE.

6) **Mean and turbulent characteristics of the flow exhibit quantitative dependence on RMS upstream bottom roughness.**

Vertical profiles of both mean velocity and second-order turbulence parameters exhibit pronounced ebb/flood asymmetries, which are consistent with variations in the upstream bottom roughness (Chapter 6). Both the drag coefficient and the log-layer thickness are correlated with RMS bottom roughness computed over distances up to 20 water depths upstream. As the upstream roughness increases, the thickness of the log-layer increases, whereas the drag coefficient decreases. The interpretation is consistent with flow over topographic features in the atmospheric boundary layer and in laboratory flumes: the increased mixing within the wake downstream of a hill or ridge thickens the boundary layer, and hence, reduces the bottom stress compared with that obtained for a similar flow over a uniformly rough bottom.

7) **At low wave numbers—i.e., in the production range—the Kaimal spectrum provides a better fit to the data than the von Kármán spectrum.**

The velocity measurements at Sites 2b and 3 were compared to modified forms of the Kaimal and von Kármán spectra that are applicable to diverging-beam ADCP data (Chapter 7). The variance at large scales is better predicted by the Kaimal spectra than the von Kármán spectra, provided that the degree of anisotropy—quantified by σ_w^2/σ_u^2—is permitted to vary throughout the water column. This variation is in contrast to empirical models commonly used for open channel flows which give a constant σ_w^2/σ_u^2 (*Nezu and Nakagawa*, 1993). However, the Grand Passage results are qualitatively consistent with observations in neutral atmospheric boundary conditions (*Peña et al.*, 2010). The expected scaling of the Kaimal spectra with z is observed in the lower 5 to 10 m of the water column; however, near mid-depth and closer to the surface, the

length scale is smaller than z due to the constraint imposed by the free surface.

8.2 Implications

Previous field campaigns in high Reynolds number tidal channels are relatively few in number (Fig. 1.1), and have typically been limited to one or two sites within a given channel. Thus, the Grand Passage dataset—with five measurement sites separated by less than 1 km—is more comprehensive than the earlier studies. This enables several theoretical and empirical relationships to be tested. The relationships are typically used to describe turbulent flows in the atmospheric boundary layer, and hence, they are not necessarily applicable in tidal channels. In the Grand Passage dataset, the following relationships are satisfied at all sites on both the ebb and flood tides:

1) the mean velocity profile is described by the law-of-the-wall for at least $z < 5$ m,
2) an inertial subrange, where the velocity spectrum falls off at a constant rate proportional to $k^{-5/3}$, is resolved, and
3) the dissipation rate is log-normally distributed.

In contrast, the applicability of other relationships is dependent on the site and tidal phase. These include:

1) a constant stress layer, where $-\langle u'w' \rangle = u_*^2$, is not always resolved, and
2) the assumption of equilibrium turbulence (i.e., $\epsilon = \mathcal{P}_h = u_*^3/\kappa z$) is not always valid.

These results indicate that the existing empirical and theoretical relationships are not universal in Grand Passage, and possibly in other high Reynolds number tidal flows.

At all the measurement sites in Grand Passage, the turbulence characteristics are highly dependent on the upstream topography. This observation implies that obtaining high resolution bathymetric measurements would allow for better interpretation of turbulence measurements in a high Reynolds number flow. More specifically, bathymetric measurements would enable the prediction of certain flow features, such as the thickness of the log-layer and the drag coefficient. In addition, bathymetric measurements could be used to improve numerical models that simulate regional- and channel-scale flow.

Many of the existing models for simulating turbine performance implement input conditions either by representing the turbulent fluctuations as a simple percentage of the mean flow, or by specifying the spectral density based on the Kaimal or von Kármán spectra. These semi-empirical forms typically use coefficients applicable to atmospheric boundary layer flows, and length scales that ignore the upper limit on eddy size imposed by the air-water interface. The Grand Passage measurements indicate that the spectral forms should be modified to account for the conditions in a tidal channel: i.e., a z-dependent anisotropy, and a decrease in the length scale near the surface. The use of a realistic turbulent time series in a CFD model based on the Grand Passage data has recently been explored by *Leroux et al.* (2016); however, in this initial study, the turbulence was assumed to be isotropic even at the largest scales. Implementing a Kaimal spectral form with vertically varying anisotropy would be a logical next step toward realistic simulations of turbine performance in tidal flows.

8.3 Future Work

The results presented in this thesis provide an encouraging basis for future scientific studies in high Reynolds number oceanic flows. A better characterization, and subsequent understanding, of the complex dynamics of the flow could be pursued through several research avenues.

First, improved instrumentation may overcome some of the questions and uncertainties that arise out of this thesis. Because divergent-beam ADCPs were used, the assumption of horizontal homogeneity across the spread of the beams was necessary to implement many of the methods used to estimate turbulence parameters. Due to the spatial inhomogeneity in the flow, it is unlikely that this assumption is strictly valid. Several approaches to overcome this restriction are already being explored. The second generation ADCPs (i.e., AD2CPs) sample up to four times faster than the RDI Workhorse instruments, and have a vertical beam that yields a direct estimate of the vertical velocity. Measurements of w enable direct comparison to predicted forms—such as the Kaimal spectrum—and thus, provide a better basis for testing the theoretical and empirical relationships. A second instrumentation technique that does not rely on the assumption of horizontal homogeneity is a Doppler system with convergent beams, akin to a large ADV. Preliminary testing of such instruments has been performed in high Reynolds number tidal channels both in

Scotland (*Sellar et al.*, 2015) and in the Bay of Fundy (*Hay et al.*, 2015).

One of the key findings of this thesis is that the streamwise advection term in the TKE equation is significant, but it is not possible to verify this conclusion using the field measurements. However, channel scale numerical models—such as the Finite Volume Coastal Ocean Model (Appendix E) or a Detached Eddy Simulation (*Wilcox et al.*, 2017)—could provide insight into the spatial variability of the advection term. More specifically, estimates of both the mean flow speed and the TKE upstream of the measurement site could be extracted and used to compare with the local imbalance of the terms in the TKE equation.

The results of this thesis could also be extended to include additional comparisons to the properties of high Reynolds number flows. Here, only second order properties of the turbulence were investigated; however, because the dissipation rate was log-normally distributed, it is likely that higher order statistics are also in agreement with the theoretical and empirical relationships used to describe flows in the atmospheric boundary layer. These higher order statistics relate to the internal intermittency in the flow, which has not yet received much attention in tidal flows.

APPENDIX A

COORDINATE SYSTEMS

A.1 RDI Workhorse ADCP

The instrument coordinates (x_I, y_I, z_I) are pictured in Fig. A.1. The coordinate system is right handed and—importantly—the x_I and z_I directions are reversed in comparison to the default convention used by RD Instruments (*Gordon*, 1996). In the pictured configuration, the beam velocities, v_i, can be expressed as

$$v_1 = - u_I \sin\vartheta - w_I \cos\vartheta + e_1, \tag{A.1}$$

$$v_2 = u_I \sin\vartheta - w_I \cos\vartheta + e_2, \tag{A.2}$$

$$v_3 = - v_I \sin\vartheta - w_I \cos\vartheta + e_3, \tag{A.3}$$

$$v_4 = v_I \sin\vartheta - w_I \cos\vartheta + e_4, \tag{A.4}$$

where u_I, v_I and w_I are the velocity components in instrument coordinates and e_i is an error associated with Doppler noise.

A frame dependent coordinate system was also defined such that $+x_F$ was directed along the beam pair that was best aligned with the flood tide direction. The y_F and z_F directions then defined a right handed coordinate system with z_F normal to the frame base and directed upward (i.e. $z_F = z_I$). The frame coordinates at each site are labelled in Fig. 3.6 and the relationships between the frame coordinates and the instrument coordinates are summarized in Table A.1.

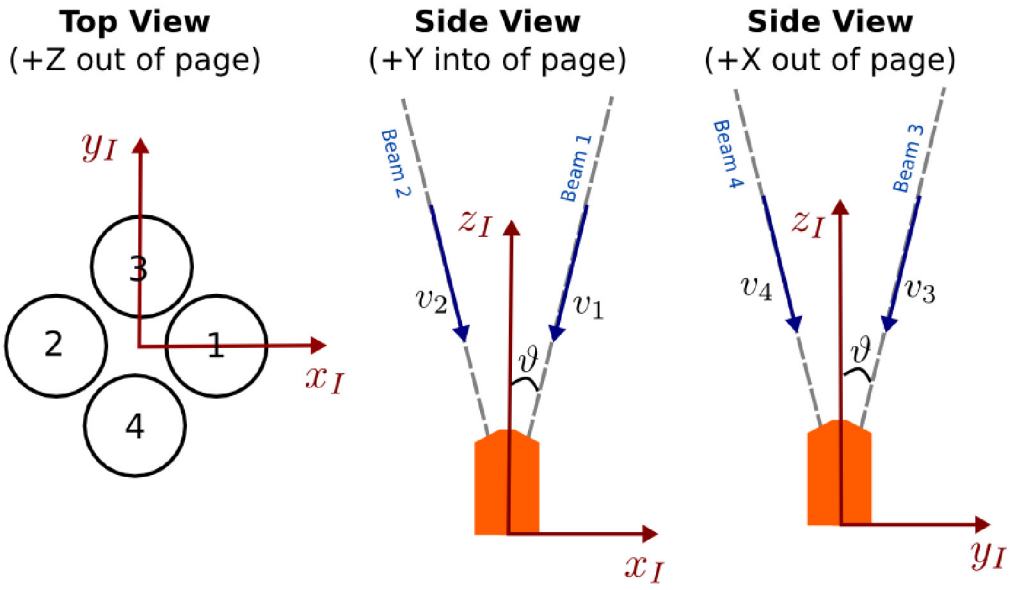

Figure A.1: Graphical representation of the instrument coordinate system (x_I,y_I,z_I). The circled numbers correspond to the transducer faces. For the RDI Workhorse instruments the angle of the transducer beams to the z_I axis is $\vartheta = 20°$.

Table A.1: Relationship between the axes of the frame coordinates (x_F,y_F,z_F) and instrument coordinates (x_I,y_I,z_I).

Site	x_F	y_F	z_F
1	$-y_I$	x_I	z_I
2a	x_I	y_I	z_I
2b	$-y_I$	x_I	z_I
3	x_I	y_I	z_I

APPENDIX B

ADCP QUALITY CONTROL

B.1 Pressure, Temperature and Attitude

The ancillary data is presented below for each of the ADCP sites. The included scalars are the pressure (P), temperature (T), heading (θ_H), pitch (θ_P) and roll (θ_R). Time periods excluded from the analysis are highlighted in red and one-day intervals for which time series are shown throughout the thesis are highlighted in yellow.

B.1.1 Site 1

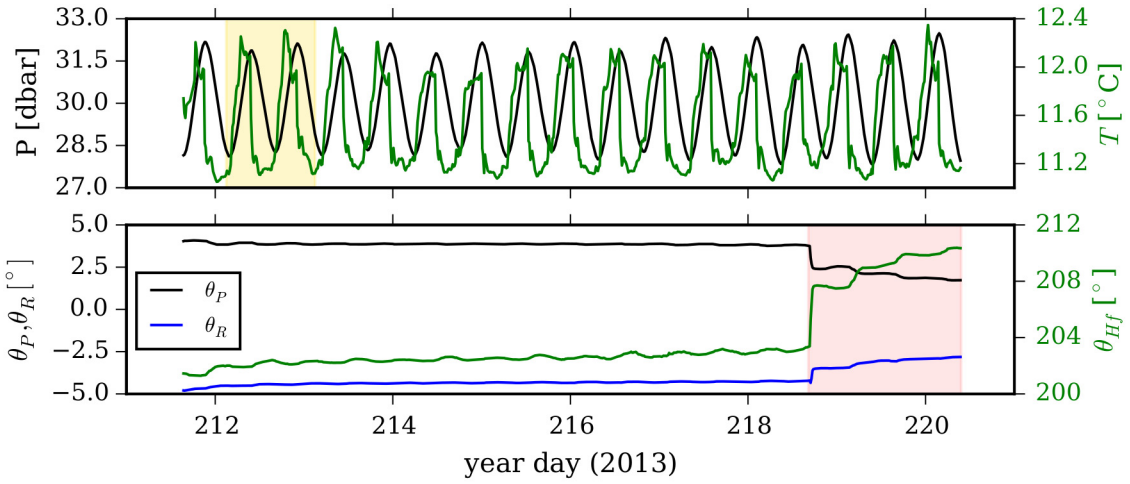

Figure B.1: Pressure, temperature and attitude parameters at Site 1. The red region highlights a time period that was rejected from analysis due to frame movement. The yellow region corresponds to the interval shown in the time series throughout the thesis.

B.1.2 Site 2a

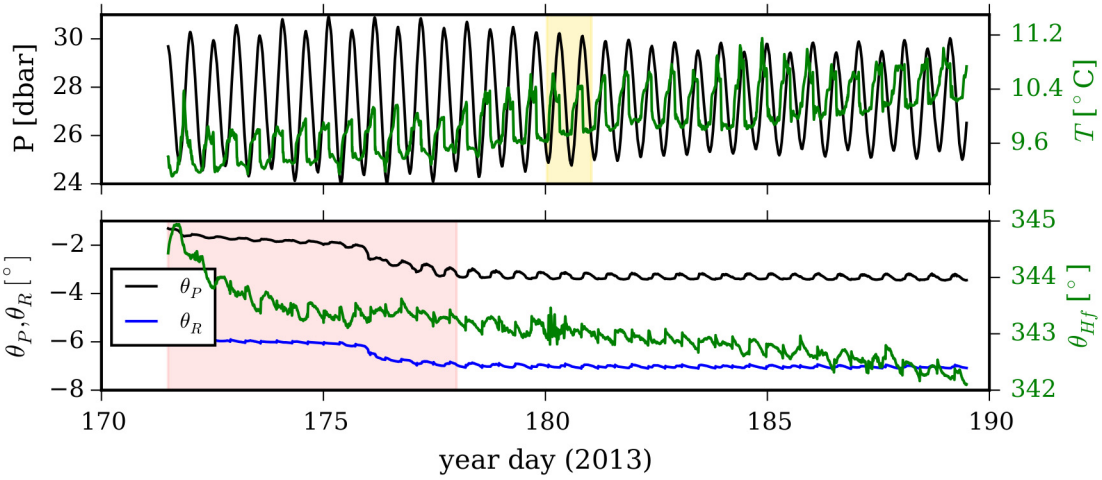

Figure B.2: Pressure, temperature and attitude parameters at Site 2a. The red region highlights a time period that was rejected from analysis due to frame movement. The yellow region corresponds to the interval shown in the time series throughout the thesis.

B.1.3 Site 2b

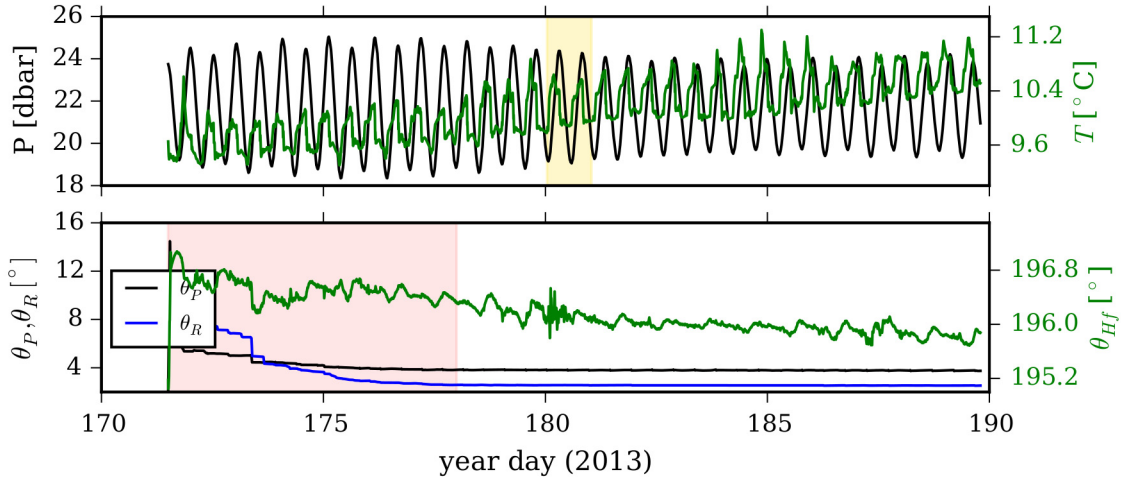

Figure B.3: Pressure, temperature and attitude parameters at Site 2b. The red region highlights a time period that was rejected from analysis due to frame movement. The yellow region corresponds to the interval shown in the time series throughout the thesis.

B.1.4 Site 3

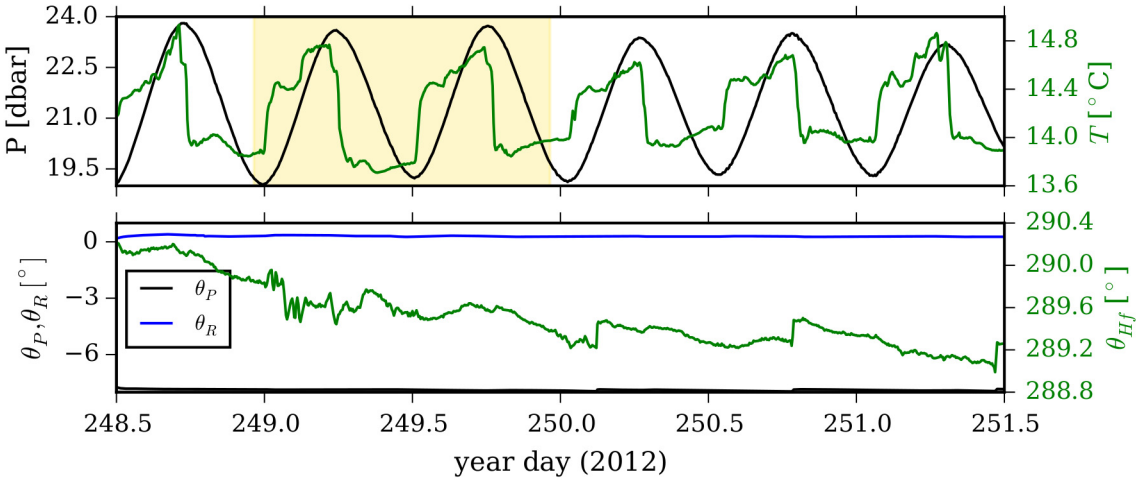

Figure B.4: Pressure, temperature and attitude parameters at Site 3. The yellow region corresponds to the interval shown in the time series throughout the thesis.

B.2 Backscatter Amplitude and Correlation

The mean correlation and backscatter amplitude of the ADCP measurements were computed for each 7-minute burst (Site 1) and 5-minute ensemble (Sites 2a, 2b, 3). The averages were used to qualitatively assess the data. At all sites, the mean correlations for all four beams were typically within 95% of the level expected (128 counts) for high-quality velocity estimates (*Gordon*, 1996), which indicates that there was sufficient signal-to-noise ratio to generate high-fidelity ADCP data. The backscatter amplitude decreased with height above bed, as expected, due to transmission losses; however, the signal was always strong enough to permit high fidelity measurements. The variation of the backscatter amplitude and correlation as a function of flow speed at 10 m above bottom is plotted in Fig. B.5.

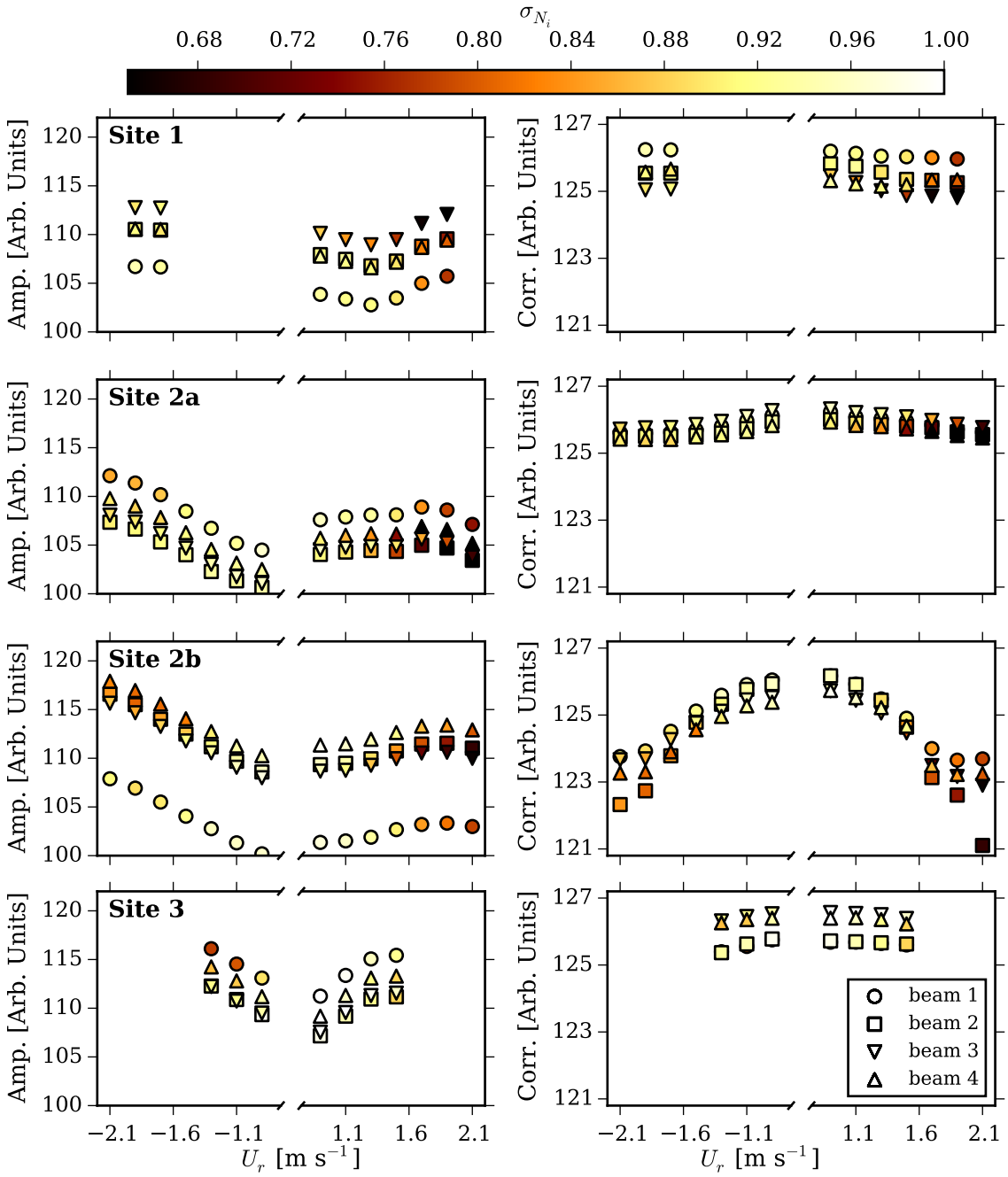

Figure B.5: Speed-bin averaged backscatter amplitude (left panels) and correlation (right panels) as a function of flow speed (negative speeds correspond to ebb tides) at $z = 10$ m. The colours correspond to the normalized Doppler noise standard deviations, σ_{N_i} (Chapter 5). Marker shapes represent beam numbers as given in the legend.

APPENDIX C

WAVES

Surface wave occurrences were identified by first computing averaged velocity spectra for the near-surface measurements. Along-beam velocity spectra were computed in 10-minute intervals with an approximate resolution of 0.01 Hz and averaged over a time-varying 5 m region where the top bin was at 85% of the total depth. The spectra were further averaged amongst the four beams and the average noise level was subtracted.

The resulting spectra were then analyzed for the presence of a peak in a wave band interval of $f \in [0.1, 0.25]$ Hz. The variance within the wave band, σ^2_{wb}, was computed and compared to the total variance up to the upper limit of the wave band, σ^2_{spec}: i.e. within $f \in [0, 0.25]$ Hz. Large variance ratios, i.e. $\sigma^2_{wb}/\sigma^2_{spec}$, indicate the presence of surface waves, however, the actual amplitude and direction of the waves could not be determined.

The specification of a cutoff threshold for $\sigma^2_{wb}/\sigma^2_{spec}$ above which waves were present was not trivial. In the absence of waves, the variance ratio changed with both flow speed and turbulence level and, like the turbulence itself, the ratio was highly intermittent. Thus, a qualitative analysis of the spectra was used to identify a site-dependent threshold above which there was consistently a peak in the wave band. The threshold therefore only identified the presence of the largest waves. Smaller waves, especially in high turbulence conditions, were observed visually in the spectra but did not contribute sufficiently to the total variance to exceed the threshold. The increased variance associated with these smaller waves did not typically penetrate to depths greater than 10 m.

In the following sections, the wind, current and wave conditions are summarized for each of the ADCP deployment sites. The wind data was obtained from hourly measurements at the Environment Canada meteorological station at the North Point lighthouse on Brier

Island (Fig. 3.3, pink marker). At all locations, the waves were predominantly present when the current direction opposed the wind direction, leading to wave height amplification.

C.1 Site 1

A threshold of $\sigma^2_{wb}/\sigma^2_{spec} = 0.6$ was used for the variance ratio at Site 1. This resulted in wave occurrences only on the ebb tide when the winds were blowing towards the northeast, i.e. in opposition to the current direction. Peaks in the wave band were observed for wind speeds ranging from 5 km h^{-1} to 20 km h^{-1}. The largest variance ratio occurred on year day 216 when the wind speed and direction were 17 km h^{-1} and 40°, respectively.

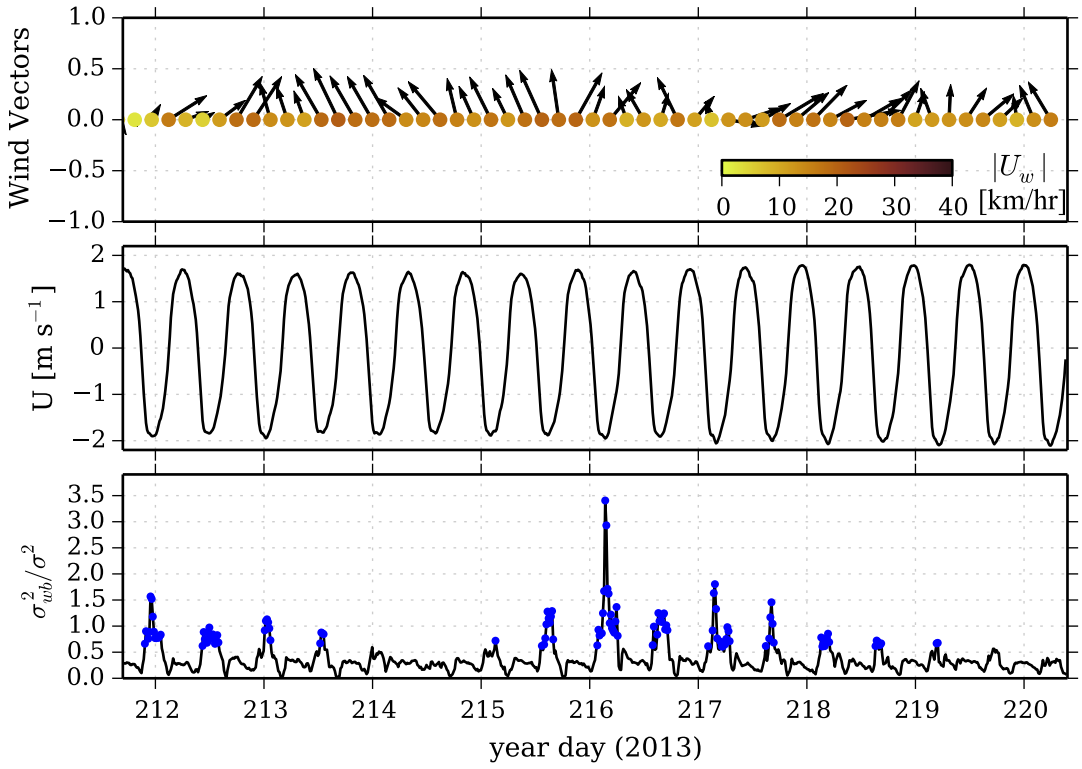

Figure C.1: Timeseries of the wind vectors (top panel), surface current speed (middle panel) and variance ratio (bottom panel) at Site 1. The colours in the top panel indicate wind speed. The markers in the bottom panel correspond to instances on the ebb tide when the variance ratio exceeded 0.6.

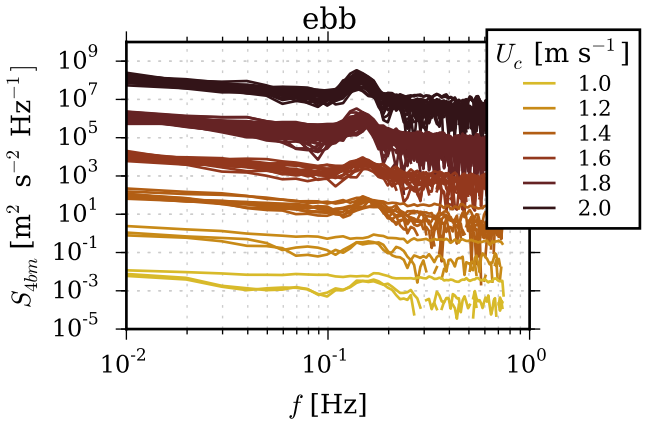

Figure C.2: Averaged along-beam velocity spectra for intervals when the variance ratio exceeded 0.6 at Site 1. Line colours correspond to speed-bin intervals of 0.2 m s^{-1} as identified in the legend. Spectra for each of the speed bins have been shifted vertically.

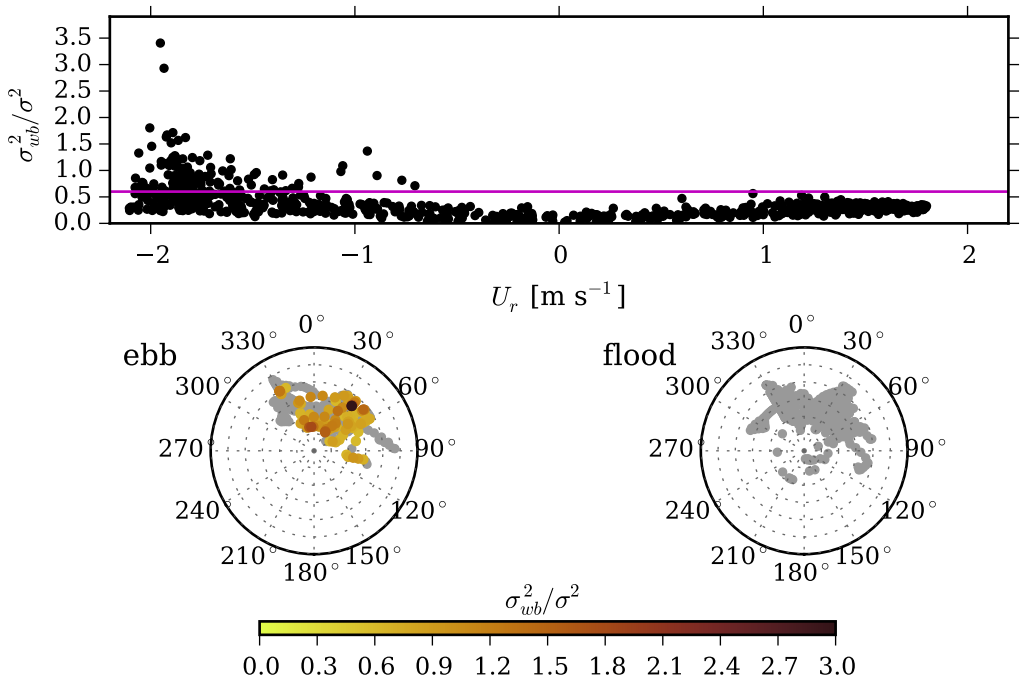

Figure C.3: The variance ratio as a function of flow speed (top panel) at Site 1. The magenta line indicates the cutoff threshold of 0.6. The compass plots show the wind conditions during flood and ebb tides. The radial lines are in 5 km h^{-1} intervals and the outermost circle corresponds to a wind speed of 30 km h^{-1}. The grey markers correspond to all the measurements during the deployment interval, whereas the coloured markers indicate the magnitude of the variance ratio during intervals when the threshold was exceeded.

C.2 Sites 2a and 2b

A threshold of $\sigma^2_{wb}/\sigma^2_{spec} = 0.7$ was used for the variance ratio at Sites 2a and 2b. This resulted in wave occurrences on most ebb tides when the winds were blowing towards the northwest, i.e. in opposition to the current direction. Waves were also present on the flood tides near days 178 and 184 (Site 2b only). Peaks in the wave band were observed for all wind speeds. The largest variance ratio occurred on ebb tides (days 180.4 and 180.9 at Sites 2b and 2a respectively). At both times the wind speed exceeded 30 km h^{-1} and was oriented towards the northwest.

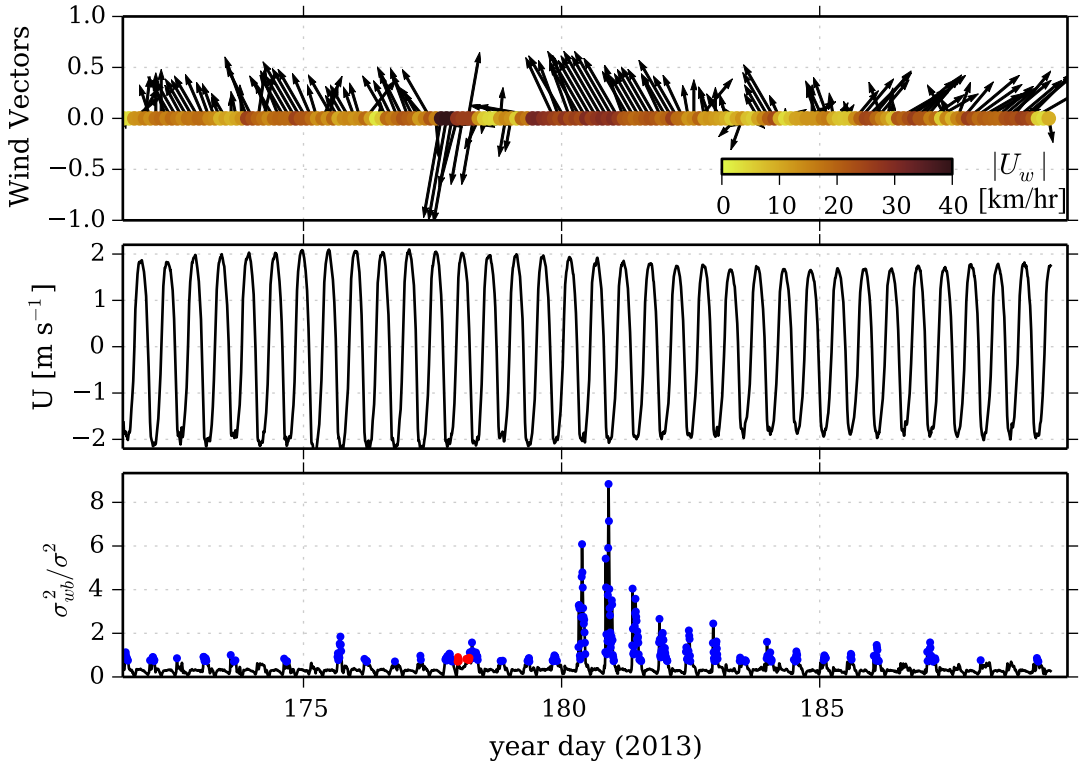

Figure C.4: Timeseries of the wind vectors (top panel), surface current speed (middle panel) and variance ratio (bottom panel) at Site 2a. The colours in the top panel indicate wind speed. The markers in the bottom panel correspond to instances on the flood (red) and ebb (blue) tides when the variance ratio exceeded 0.7.

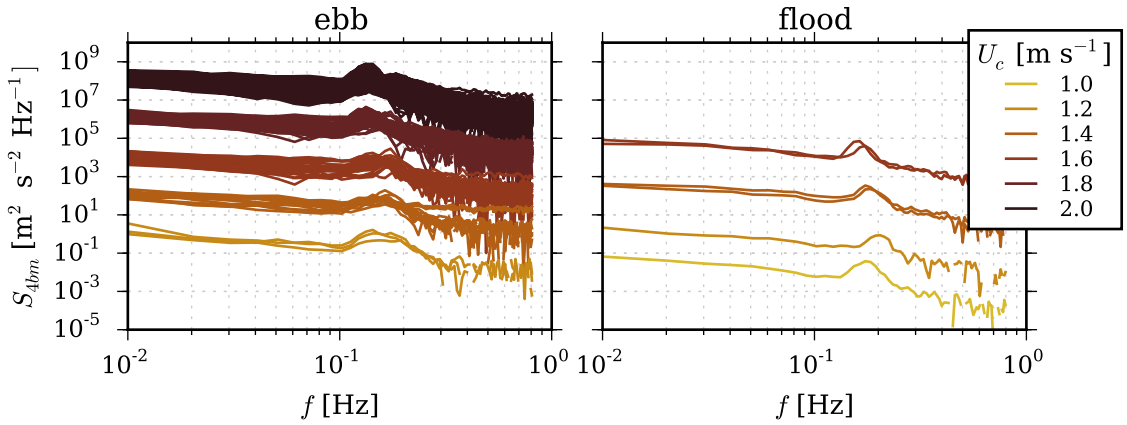

Figure C.5: Averaged along-beam velocity spectra for intervals when the variance ratio exceeded 0.7 at Site 2a. Line colours correspond to speed-bin intervals of 0.2 m s^{-1} as identified in the legend. Spectra for each of the speed bins have been shifted vertically.

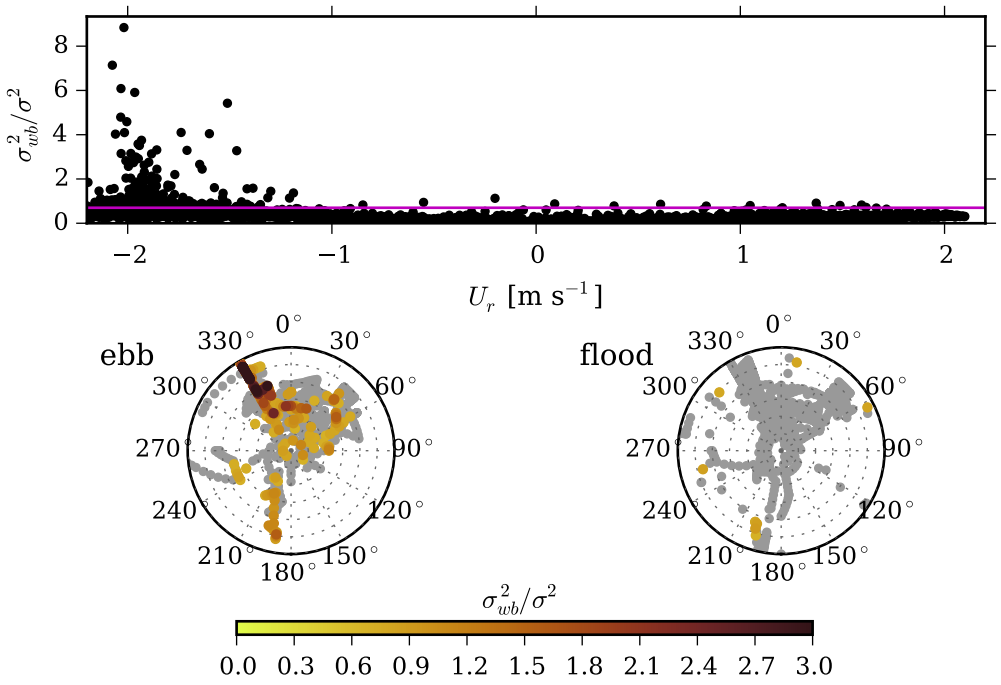

Figure C.6: The variance ratio as a function of flow speed (top panel) at Site 2a. The magenta line indicates the cutoff threshold of 0.7 The compass plots show the wind conditions during flood and ebb tides. The grey markers correspond to all the measurements during the deployment interval, whereas the coloured markers indicate the magnitude of the variance ratio during intervals when the threshold was exceeded.

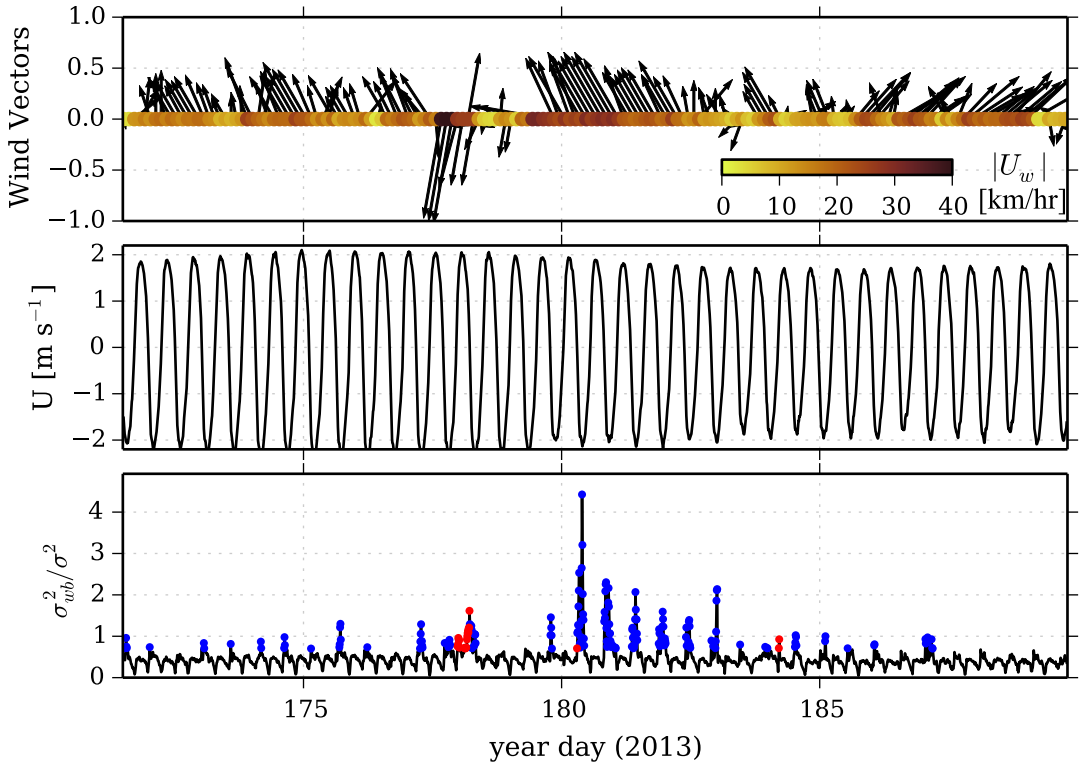

Figure C.7: Timeseries of the wind vectors (top panel), surface current speed (middle panel) and variance ratio (bottom panel) at Site 2b. The colours in the top panel indicate wind speed. The markers in the bottom panel correspond to instances on the flood (red) and ebb (blue) tides when the variance ratio exceeded 0.7.

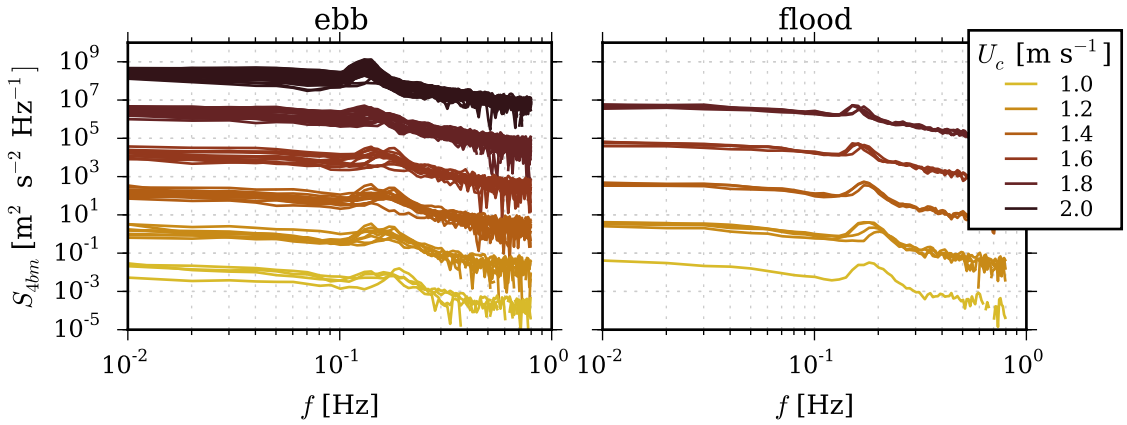

Figure C.8: Averaged along-beam velocity spectra for intervals when the variance ratio exceeded 0.7 at Site 2b. Line colours correspond to speed-bin intervals of 0.2 m s^{-1} as identified in the legend. Spectra for each of the speed bins have been shifted vertically.

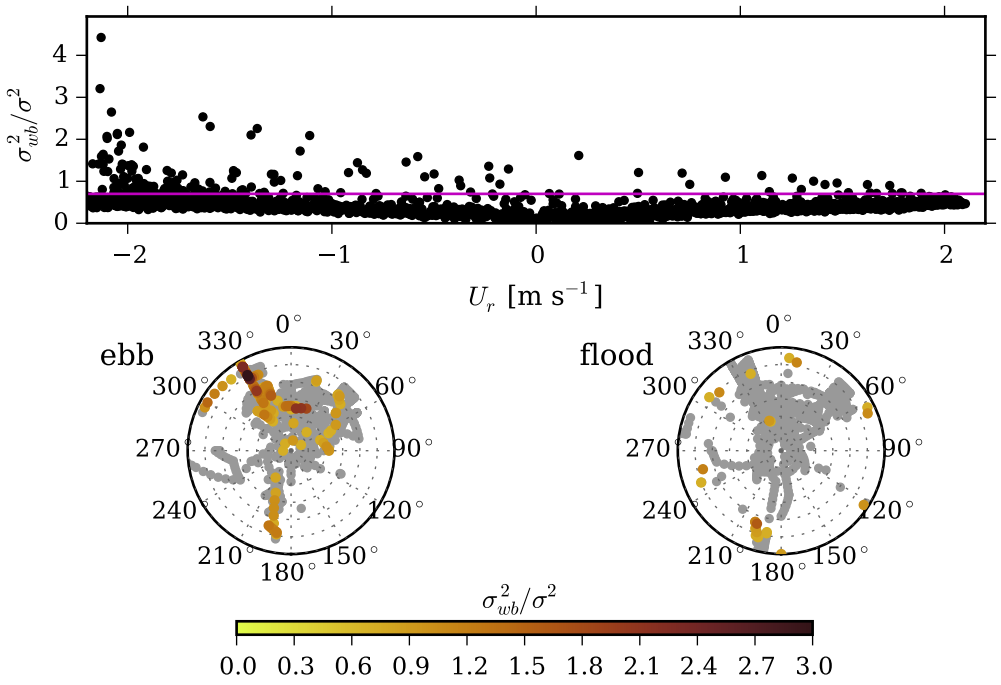

Figure C.9: The variance ratio as a function of flow speed (top panel) at Site 2b. The magenta line indicates the cutoff threshold of 0.7. The compass plots show the wind conditions during flood and ebb tides. The grey markers correspond to all the measurements during the deployment interval, whereas the coloured markers indicate the magnitude of the variance ratio during intervals when the threshold was exceeded.

C.3 Site 3

A threshold of $\sigma^2_{wb}/\sigma^2_{spec} = 0.5$ was used for the variance ratio at Site 3. This resulted in wave occurrences during only two intervals. The first occurred on day 249.8 as the tide transitioned from flood to ebb and the winds were oriented towards the north-northeast. High variances were also observed on the subsequent flood tide when the winds were towards east-south-east and thus obliquely opposed to the northward flowing current.

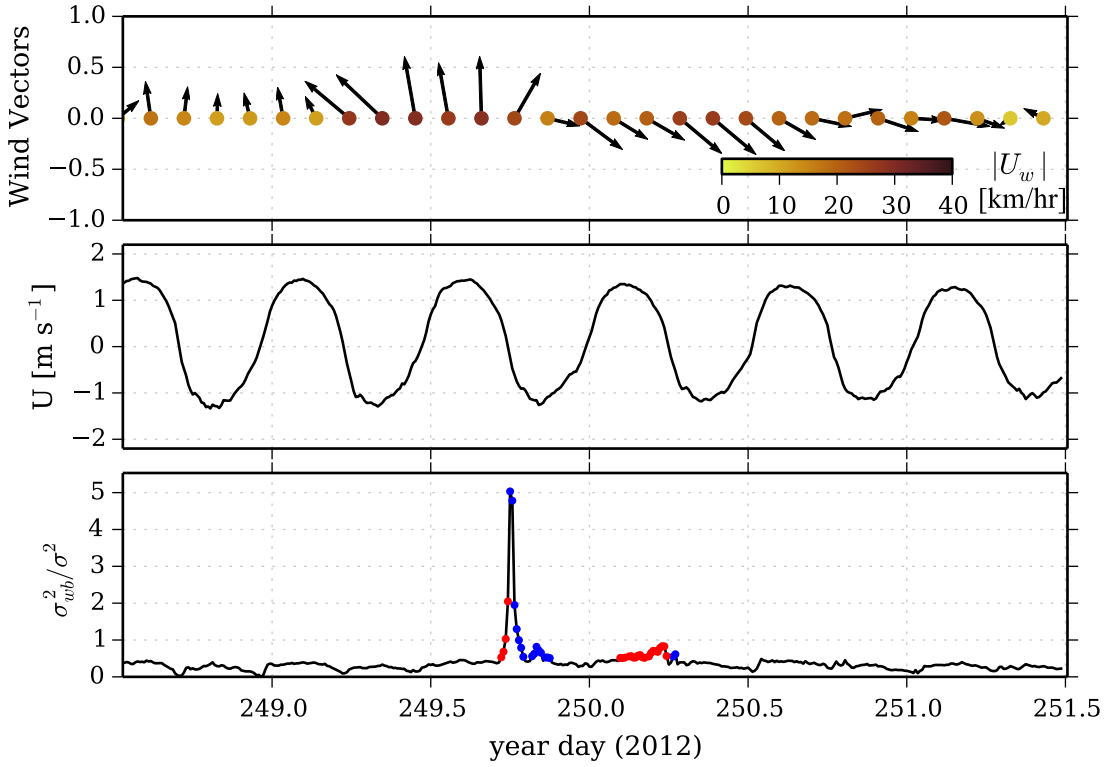

Figure C.10: Timeseries of the wind vectors (top panel), surface current speed (middle panel) and variance ratio (bottom panel) at Site 3. The colours in the top panel indicate wind speed. The markers in the bottom panel correspond to instances on the flood (red) and ebb (blue) tides when the variance ratio exceeded 0.5.

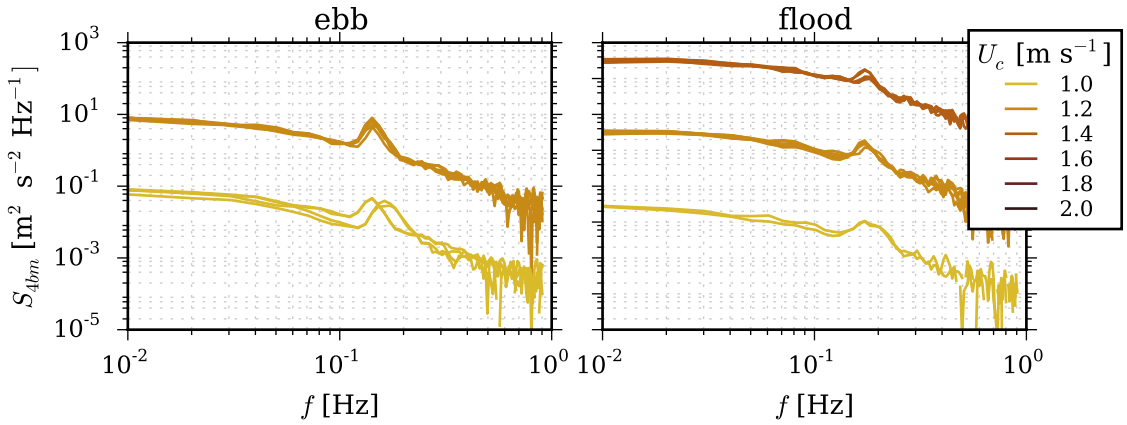

Figure C.11: Averaged along-beam velocity spectra for intervals when the variance ratio exceeded 0.5 at Site 3. Line colours correspond to speed-bin intervals of 0.2 m s^{-1} as identified in the legend. Spectra for each of the speed bins have been shifted vertically.

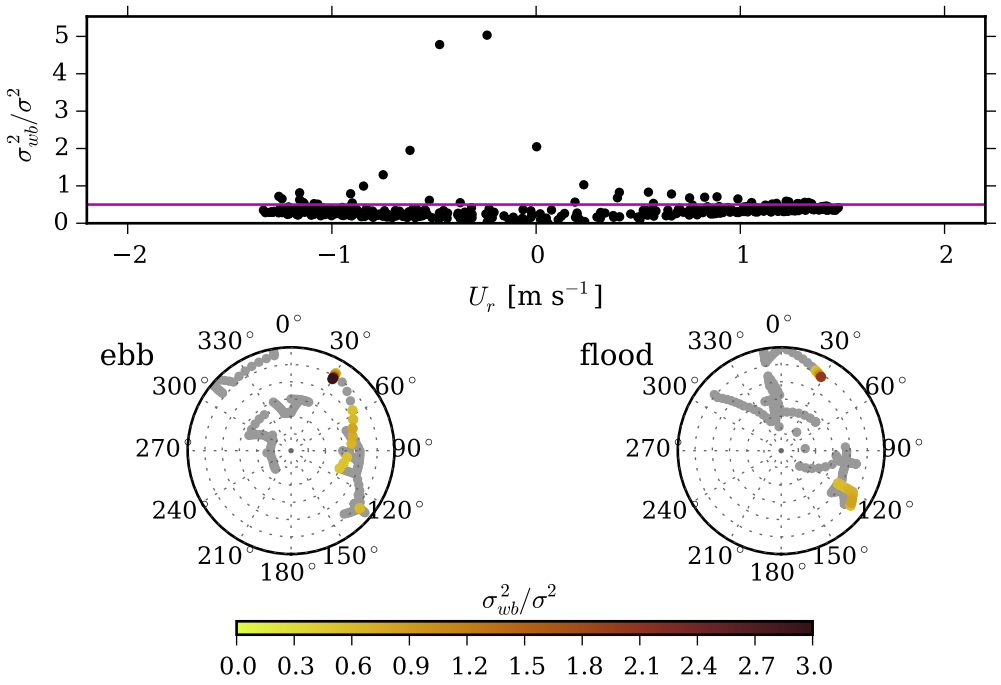

Figure C.12: The variance ratio as a function of flow speed (top panel) at Site 3. The magenta line indicates the cutoff threshold of 0.5. The compass plots show the wind conditions during flood and ebb tides. The grey markers correspond to all the measurements during the deployment interval, whereas the coloured markers indicate the magnitude of the variance ratio during intervals when the threshold was exceeded.

APPENDIX D

DOPPLER NOISE LEVELS

The Doppler noise levels were estimated from the velocity spectra of the along-beam ADCP measurements. For each ensemble (7-minutes at Site 1, 5-minutes otherwise), along-beam spectral densities, $\widehat{S}_{ii}(f)$ were computed for each vertical bin using Hanning-windowed intervals of 20 points (approximately 11-13 s) with 50% overlap. This resulted in spectra with a frequency resolution of approximately 0.075 Hz and up to 100 degrees of freedom (*Nuttall*, 1971). For each depth and beam, the velocity spectra for the lowest flow speeds ($|U_c| < 0.2$ m s^{-1}) were averaged together and the mean spectral level from $f \in [0.5 f_N, f_N]$ was computed, yielding an estimate of N_i (Fig. D.1). The corresponding standard deviations—given by $\sigma_{e_i} = (N_i f_N)^{1/2}$—are plotted in Fig. D.2. The Doppler noise estimates are nearly independent of beam and depth and within 10% of the expected value of 4.6×10^{-2} m s^{-1}.

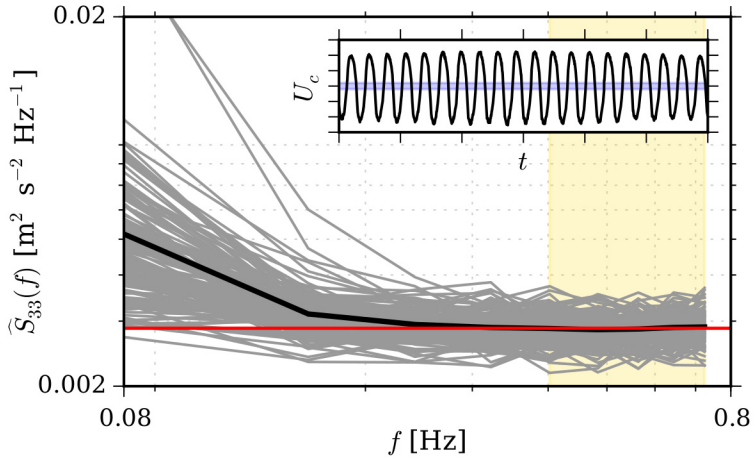

Figure D.1: Along-beam velocity spectra for $|U_c| < 0.2$ m s^{-1} at $z = 9.61$ m at Site 2b. The spectra for each ensemble are shown in grey and the mean is plotted in black. The frequency range over which the noise level was computed is highlighted in yellow and the noise level is represented by the horizontal red line. The range of flow speeds satisfying $|U_c| < 0.2$ m s^{-1} is highlighted in blue in the inset.

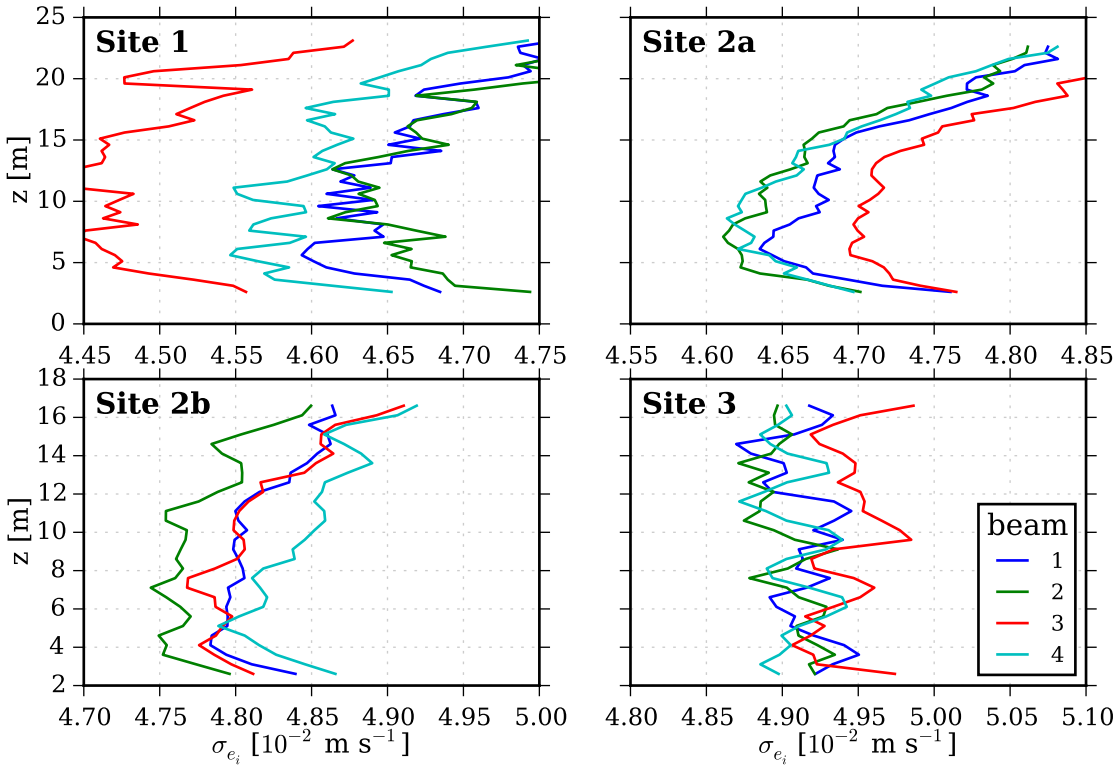

Figure D.2: Vertical profiles of Doppler noise standard deviations, σ_{e_i}, determined from the spectra at slack water. Note: The x-axes limits are site dependent.

APPENDIX E

FINITE VOLUME COMMUNITY OCEAN MODEL (FVCOM)

The Finite Volume Community Ocean Model (FVCOM) is an unstructured-grid, free surface, three dimensional ocean circulation model (*Chen et al.*, 2006). The model uses the modified Mellor and Yamada level 2.5 (MY-2.5) and Smagorinsky turbulent closure schemes as the default for vertical and horizontal mixing and a terrain-following vertical coordinate to follow bottom topography.

The original model grid was obtained from David Greenberg and Jason Chaffrey at the Bedford Institute of Oceanography and contained the entire Bay of Fundy and Gulf of Maine regions (Fig. E.1, left). The model was validated by *Karsten et al.* (2008) by comparing measurements of surface elevation at multiple sites throughout the Bay of Fundy. The model grid has since been adapted to have high resolution within Grand Passage (Fig. E.1, right), where the average side length of an element is 15 m (*O'Flaherty-Sproul*, 2013).

The simulation of tidal flow in Grand Passage was performed using the hydrostatic version of FVCOM. The model was forced using five tidal constituents (M2, N2, S2, K1, and O1), which were specified at the open boundaries located beyond the continental shelf. The constituents were predicted using Webtide, which is a program developed by Fisheries and Oceans Canada (*Dupont et al.*, 2005). A uniform drag coefficient of 2.5×10^{-3} was used throughout the domain. For the model results presented in this thesis (Fig. 3.2, Section 6.4.3), the simulations were three dimensional with 10 vertical layers. The tidal forcing was applied for June 20-27th, 2013, i.e. the first week that the ADCPs at Site 2a and 2b were deployed.

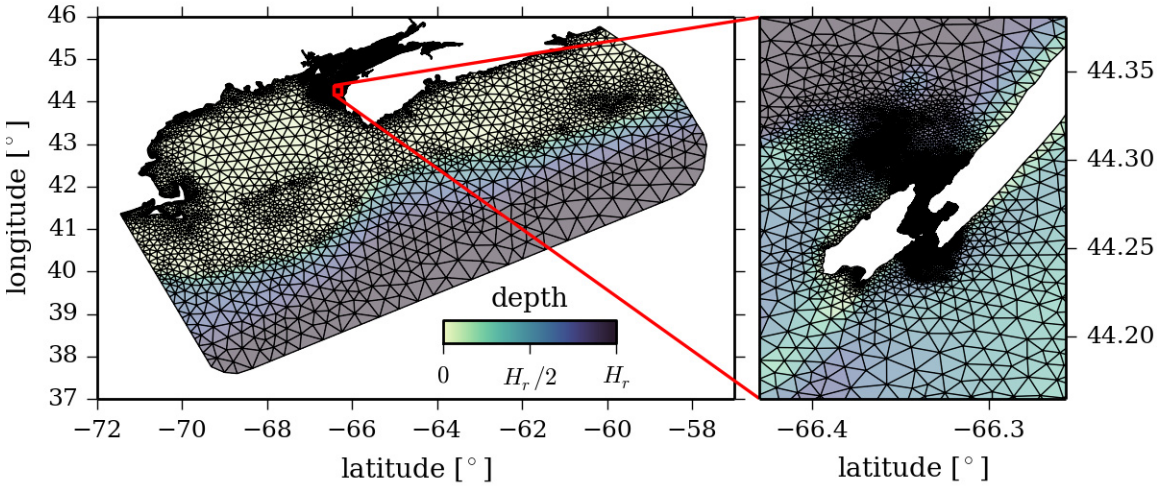

Figure E.1: The full numerical grid used for FVCOM simulations (left) and the Grand Passage region (right). The colours correspond to the water depth; the reference values, H_r, are 4 km and 100 m in the left and right panels, respectively.

APPENDIX F

COPYRIGHT PERMISSIONS

Gmail Justine McMillan <mcmillanjustine@gmail.com>

Copyright Permissions for Thesis

Perriello, Rebecca <rperriello@ametsoc.org> Wed, Jun 28, 2017 at 4:11 PM
To: justine.mcmillan@dal.ca
Cc: permissions <permissions@ametsoc.org>

Dear Justine,

Thank you for your email. This signed message constitutes permission to use the material requested in your email below.

You may use the content in your upcoming publication with the following conditions:

+ please include the complete bibliographic citation of the original source for each, and
+ please include the following statement with that citation for each: ©American Meteorological Society. Used with permission.

Thank you for your request and if you need any further information, please get in touch with me.

Best regards,

Rebecca Perriello
Permissions
American Meteorological Society
permissions@ametsoc.org | ametsoc.org

---------- Forwarded message ----------
From: **Justine McMillan** < justine.mcmillan@dal.ca>
Date: Fri, Jun 23, 2017 at 11:56 AM
Subject: Copyright Permissions for Thesis
To: copyrights@ametsoc.org

Hi,

I have two papers published in the Journal of Atmospheric and Oceanic Technology (see below). I have included some of the content from the papers in my thesis.

What sort of permission is needed from you to ensure that I am not infringing on the copyright agreements? I've attached a standard letter that may or may not be needed, depending on your policies.

Cheers,

Justine

___
Papers:
1) McMillan, J. M., A. E. Hay, R. G. Lueck, and F. Wolk, Rates of dissipation of turbulent kinetic energy in a high Reynolds number tidal channel, J. Atmos. Oceanic Technol., 33, 817–837, 2016.

2) McMillan, J. M., and A. E. Hay, Spectral and structure function estimates of turbulence dissipation rates in a high-flow tidal channel using broadband ADCPs, J. Atmos. Oceanic Technol., 34, 5–20, 2017.

--

_____
Justine McMillan
Department of Oceanography
Room 5678
Dalhousie University
Halifax, NS Canada B3H 4R2

BIBLIOGRAPHY

Alfonsi, G., S. Ciliberti, M. Mancini, and L. Primavera, Direct numerical simulation of turbulent channel flow on high-performance GPU computing system, *Computation*, *4*, 19, 2016.

Batchelor, G. K., *The Theory of Homogeneous Turbulence*, Cambridge University Press, Cambridge, 1953.

Blackmore, T., and W. M. J. Batten, Influence of turbulence on the wake of a marine current turbine simulator, *Proc. Roy. Soc. A*, *470*, 1–17, 2014.

Blunden, L. S., and A. S. Bahaj, Tidal energy resource assessment for tidal stream generators, *Proc. Inst. Mech. Eng., Part A*, *221*, 137–146, 2007.

Borrell, G., J. A. Sillero, and J. Jiménez, A code for direct numerical simulation of turbulent boundary layers at high Reynolds numbers in BG/P supercomputers, *Comput. Fluids*, *80*, 37–43, 2013.

Briggs, D. A., J. H. Ferziger, J. R. Koseff, and S. G. Monismith, Turbulent mixing in a shear-free stably stratified two-layer fluid, *J. Fluid Mech.*, *354*, 175–208, 1998.

Brumley, B. H., R. G. Cabrera, K. L. Deines, and E. A. Terray, Performance of a broad-band acoustic Doppler current profiler, *IEEE J. Oceanic Eng.*, *16*, 402–407, 1991.

Burton, T., N. Jenkins, D. Sharpe, and E. Bossanyi, *Wind Energy Handbook*, 2nd ed., John Wiley & Sons Ltd, United Kingdom, 2011.

Chamorro, L. P., C. Hill, S. Morton, C. Ellis, R. E. A. Arndt, and F. Sotiropoulos, On the interaction between a turbulent open channel flow and an axial-flow turbine, *J. Fluid Mech.*, *716*, 658–670, 2013.

Chen, C., R. C. Beardsley, , and G. Cowles, An unstructured grid, finite-volume coastal ocean model (FVCOM) system, *Oceanogr.*, *19*, 78–89, 2006.

Cheng, W., and R. Samtaney, Power-law versus log-law in wall-bounded turbulence: A large-eddy simulation perspective, *Phys. Fluids*, *26*, 011703, 2014.

Collignon, A. G., and M. T. Stacey, Turbulence Dynamics at the Shoal–Channel Interface in a Partially Stratified Estuary, *J. Phys. Oceanogr.*, *43*, 970–989, 2013.

Diedrich, F. W., and J. A. Drischler, Effect of spanwise variations in gust intensity of the lift due to atmospheric turbulence, *NACA Technical Note 3920*, 1957, [Available online at https://ntrs.nasa.gov/search.jsp?R=19930084862].

Dupont, F., C. G. Hannah, and D. Greenberg, Modelling the sea level in the upper Bay of Fundy, *Atmos.-Ocean*, *43*, 33–47, 2005.

Fer, I., and M. B. Paskyabi, Autonomous ocean turbulence measurements using shear probes on a moored instrument, *J. Atmos. Oceanic Technol.*, *31*, 474–490, 2014.

Gargett, A. E., Observing turbulence with a modified acoustic Doppler current profiler, *J. Atmos. Oceanic Technol.*, *11*, 1592 – 1610, 1994.

Goodman, L., E. R. Levine, and R. G. Lueck, On measuring the terms of the turbulent kinetic energy budget from an AUV, *J. Atmos. Oceanic Technol.*, *23*, 977–990, 2006.

Gordon, L., Acoustic Doppler current profiler: Principles of operation a practical primer, *RD Instruments Tech. Rep. P/N 951-6069-00*, 1996.

Grant, H. L., R. W. Stewart, and A. Moilliet, Turbulence spectra from a tidal channel, *J. Fluid Mech.*, *12*, 241–268, 1962.

Greene, A. D., P. J. Hendricks, and M. C. Gregg, Using an ADCP to estimate turbulent kinetic energy dissipation rate in sheltered coastal waters, *J. Atmos. Oceanic Technol.*, *32*, 318–333, 2015.

Gunawan, B., V. S. Neary, and J. Colby, Tidal energy site resource assessment in the East River tidal strait, near Roosevelt Island, New York, New York, *Renewable Energy*, *71*, 509–517, 2014.

Hay, A. E., J. M. McMillan, R. Cheel, and D. J. Schillinger, Turbulence and drag in a high reynolds number tidal passage targetted for in-stream tidal power, in *Proc. Oceans 2013*, p. 10 pp., Institute of Electrical and Electronics Engineers (IEEE), San Diego, CA, 2013.

Hay, A. E., L. Zedel, S. Nylund, R. Craig, and J. Culina, The Vectron: A pulse coherent acoustic Doppler system for remote turbulence resolving velocity measurements, in *Proc. IEEE/OES/CMTC Eleventh Current, Waves and Turbulence Measurement Conf.*, p. 7, St. Petersburg, FL, 2015.

Jabbari, A., L. Boegman, and U. Piomelli, Evaluation of the inertial dissipation method within boundary layers using numerical simulations, *Geophys. Res. Lett.*, *42*, 1504–1511, 2015.

Jonkman, B. J., TurbSim User's Guide: Version 1.50, *NREL Tech. Rep. TP-500-46198*, 2009, [Available online at http://www.nrel.gov/docs/fy09osti/46198.pdf].

Kaimal, J. C., and J. J. Finnigan, *Atmospheric Boundary Layer Flows*, Oxford University Press, New York, 1994.

Kaimal, J. C., J. C. Wyngaard, Y. Izumi, and O. R. Coté, Spectral Characteristics of Surface-Layer Turbulence, *Q. J. R. Meteorol. Soc.*, *98*, 563–589, 1972.

Karsten, R. H., J. M. McMillan, M. J. Lickley, and R. D. Haynes, Assessment of tidal current energy in the Minas Passage, Bay of Fundy, *Proc. Inst. Mech. Eng., Part A*, *222*, 493–507, 2008.

Kim, J., P. Moin, and R. Moser, Turbulence statistics in fully developed channel flow at low Reynolds number, *J. Fuid Mech.*, *177*, 133–166, 1987.

Klebanoff, P. S., Characteristics of turbulence in a boundary layer with zero pressure gradient, *NACA Annual report No. 1247*, 1955.

Kolmogorov, A. N., The local structure of turbulence in incompressible viscous fluid for very large Reynolds numbers, *Dokl. Akad. Nauk SSSR*, *30*, 299–301, 1941a, reprinted in Proc. R. Soc. London A 434, 9–13 (1991).

Kolmogorov, A. N., Dissipation of Energy in the Locally Isotropic Turbulence, *Dokl. Akad. Nauk SSSR*, *32*, 19–21, 1941b, reprinted in Proc. R. Soc. London A 434, 15–17 (1991).

Kolmogorov, A. N., A refinement of previous hypotheses concerning the local structure of turbulence in a viscous incompressible fluid at high Reynolds number, *J. Fluid Mech.*, *13*, 82–85, 1962.

Korotenko, K., A. Sentchev, F. G. Schmitt, and N. Jouanneau, Variability of turbulent quantities in the tidal bottom boundary layer: Case study in the eastern English Channel, *Cont. Shelf Res.*, *58*, 21–31, 2013.

Kundu, P. K., and I. M. Cohen, *Fluid Mechanics*, 2nd ed., Academic Press, San Diego, California, 2002.

Lanckriet, T., and J. A. Puleo, Near-bed turbulence dissipation measurements in the inner surf and swash zone, *J. Geophys. Res. Oceans*, *118*, 6634–6647, 2013.

Laufer, J., The structure of turbulence in fully developed pipe flow, *NACA No. 1174*, 1954.

Leroux, T., N. Osbourne, J. M. McMillan, D. Groulx, and A. E. Hay, Numerical modelling of a tidal turbine behaviour under realistic unsteady tidal flow, in *Proc. of Asian Wave and Tidal Energy Conference*, p. 10, Marina Bay Sands, Singapore, 2016.

Lesieur, M., *Turbulence in Fluids*, 2nd ed., Kluwer Academic Publishers, 1990.

Lien, R.-C., and T. B. Sanford, Spectral characteristics of velocity and vorticity fluxes in an unstratified turbulent boundary layer, *J. Geophys. Res.*, *105*, 8659–8672, 2000.

Lohrmann, A., B. Hackett, and L. P. Røed, High resolution measurements of turbulence, velocity and stress using a pulse-to-pulse coherent sonar, *J. Atmos. Oceanic Technol.*, *7*, 19–37, 1990.

Lorke, A., Boundary mixing in the thermocline of a large lake, *J. Geophys. Res.*, *112*, C09019, 2007.

Lorke, A., and A. Wüest, Application of coherent ADCP for turbulence measurements in the bottom boundary layer, *J. Atmos. Oceanic Technol.*, *22*, 1821–1828, 2005.

Lu, Y., and R. Lueck, Using a broadband ADCP in a tidal channel. Part II: Turbulence, *J. Atmos. Oceanic Technol.*, *16*, 1568–1579, 1999.

Lu, Y., R. G. Lueck, and D. Huang, Turbulence characteristics in a tidal channel, *J. Phys. Oceanogr.*, *30*, 855–867, 2000.

Lucas, N. S., J. H. Simpson, T. P. Rippeth, and C. P. Old, Measuring turbulent dissipation using a tethered ADCP, *J. Atmos. Oceanic Technol.*, *31*, 1826–1837, 2014.

Lueck, R., F. Wolk, J. Hancyck, and K. Black, Hub-height time series measurements of velocity and dissipation of turbulence kinetic energy in a tidal channel, in *Proc. Current, Waves and Turbulence Measurement Workshop (CWTM), 2015 IEEE/OES Eleventh*, Institute of Electrical and Electronics Engineers (IEEE), St. Petersburg, FL, 2015.

Lueck, R. G., Calculating the rate of dissipation of turbulent kinetic energy, *RSI Tech. Note TN-028*, 2013, [Available online at http://www.rocklandscientific.com/Support/TechnicalNotes/tabid/68/Default.aspx].

Lueck, R. G., F. Wolk, and H. Yamazaki, Oceanic velocity microstructure measurements in the 20th century, *J. Oceanogr.*, *58*, 153–174, 2002.

Lueck, R. G., F. Wolk, and K. Black, Measuring tidal channel turbulence with a vertical microstructure profiler (VMP), *RSI Tech. Note TN-026*, 2013, [Available online at http://www.rocklandscientific.com/Support/TechnicalNotes/tabid/68/Default.aspx].

Macoun, P., and R. G. Lueck, Modeling the spatial response of the airfoil shear probe using different sized probes, *J. Atmos. Oceanic Technol.*, *21*, 284–297, 2004.

Malinka, C. E., Acoustic detection ranges and baseline ambient noise measurements for a marine mammal monitoring system at a proposed in-stream tidal turbine site: Grand Passage, Nova Scotia, B.Sc. thesis, Dalhousie University, 2013.

Mann, J., The spatial structure of neutral atmospheric surface-layer turbulence, *J. Fluid Mech.*, *273*, 141–168, 1994.

Mann, J., Wind field simulation, *Probab. Eng. Mech.*, *13*, 269–282, 1998.

McCaffrey, K., B. Fox-Kemper, P. E. Hamlington, and J. Thomson, Characterization of turbulence anisotropy, coherence, and intermittency at a prospective tidal energy site: Observational data analysis, *Renewable Energy*, *76*, 441–453, 2015.

McCann, G. N., Tidal current turbine fatigue loading sensitivity to waves and turbulence – a parametric study, in *Proc. of European Wave and Tidal Energy Conference 2013*, p. 10 pp., Aalborg, Denmark, 2007.

McMillan, J. M., and A. E. Hay, Spectral and structure function estimates of turbulence dissipation rates in a high-flow tidal channel using broadband ADCPs, *J. Atmos. Oceanic Technol.*, *34*, 5–20, 2017.

McMillan, J. M., A. E. Hay, R. H. Karsten, G. Trowse, D. Schillinger, and M. O'Flaherty-Sproul, Comprehensive tidal energy resource assessment in the lower Bay of Fundy, Canada, in *Proc. of European Wave and Tidal Energy Conference 2013*, p. 10 pp., Aalborg, Denmark, 2013.

McMillan, J. M., A. E. Hay, R. G. Lueck, and F. Wolk, An assessment of the dissipation rates at a tidal energy site using a VMP and an ADCP, in *Proc. of European Wave and Tidal Energy Conference 2015*, p. 8 pp., Nantes, France, 2015.

McMillan, J. M., A. E. Hay, R. G. Lueck, and F. Wolk, Rates of dissipation of turbulent kinetic energy in a high Reynolds number tidal channel, *J. Atmos. Oceanic Technol.*, *33*, 817–837, 2016.

Milne, I. A., R. N. Sharma, R. G. J. Flay, and S. Bickerton, Characteristics of the turbulence in the flow at a tidal stream power site, *Philos. Trans. Roy. Soc., A*, *371*, 1–14, 2013.

Mohrholz, V., H. Prandke, and H. U. Lass, Estimation of TKE dissipation rates in dense bottom plumes using a Pulse Coherent Acoustic Doppler Profiler (PC-ADP) – Structure function approach, *J. Mar. Syst.*, *70*, 217–239, 2008.

Monin, A. S., and A. M. Yaglom, *Statistical Fluid Mechanics: Mechanics of Turbulence (Volume 2)*, The MIT Press, Cambridge, 1975.

Morales, A., M. Wächter, and J. Peinke, Characterization of wind turbulence by higher-order statistics, *Wind Energy*, *406*, 391–406, 2012.

Morfiadakis, E. E., G. L. Glinou, and M. J. Koulouvari, The suitability of the von Karman spectrum for the structure of turbulence in a complex terrain wind farm, *J. of Wind Eng. Ind. Aero.*, *62*, 237–257, 1996.

Moriarty, P. J., W. E. Holley, and S. Butterfield, Effect of turbulence variation on extreme loads prediction for wind turbines, *J. Sol. Energy Eng.*, *124*, 387–395, 2002.

Moser, R. D., J. Kim, and N. N. Mansour, Direct numerical simulation of turbulent channel flow up to Re_τ= 590, *J. Fuid Mech.*, *11*, 943–945, 1999.

Moum, J., and T. Rippeth, Do observations adequately resolve the natural variability of oceanic turbulence?, *J. Mar. Syst.*, *77*, 409–417, 2009.

Mycek, P., B. Gaurier, G. Germain, G. Pinon, and E. Rivoalen, Experimental study of the turbulence intensity effects on marine current turbines behaviour. Part I: One single turbine, *Renewable Energy*, *66*, 729–746, 2014.

Nasmyth, P. W., Oceanic turbulence, Ph.D. thesis, University of British Columbia, 1970, [Available online at https://circle.ubc.ca/handle/2429/34947].

Nezu, I., and H. Nakagawa, *Turbulence in Open Channel Flows*, A. A. Balkema, Rotterdam, Netherlands, 1993.

Nuttall, A. H., Spectral estimation by means of overlapped Fast Fourier Transform processing of windowed data, *NUSC Tech. Rep. No. 4169*, 1971, [Available online at http://oai.dtic.mil/oai/oai?verb=getRecord&metadataPrefix=html&identifier=AD0739315].

Obukhov, A., On the energy distribution in the spectrum of a turbulent flow, *Dokl. Akad. Nauk SSSR*, *32*, 19–21, 1941.

Obukhov, A. M., Some specific features of atmospheric turbulence, *J. Geophys. Res.*, *67*, 3011–3014, 1962.

O'Flaherty-Sproul, M., New high and low resolution numerical models of the tidal currents through the Digby Neck passages, Master's thesis, Acadia University, 2013.

Örlü, R., T. Fiorini, A. Segalini, G. Bellani, A. Talamelli, and P. H. Alfredsson, Reynolds stress scaling in pipe flow turbulence—first results from ciclope, *Philos. Trans. Roy. Soc., A*, *375*, 2017.

Osalusi, E., J. Side, and R. Harris, Reynolds stress and turbulence estimates in bottom boundary layer of Fall of Warness, *Int. Commun. Heat Mass Transfer*, *36*, 412–421, 2009.

Osborn, T. R., Vertical profiling of velocity microstructure, *J. Phys. Oceanogr.*, *4*, 109–115, 1974.

Paparoditis, E., Frequency domain bootstrap for time series, 2002.

Peña, A., S.-E. Gryning, and J. Mann, On the length-scale of the wind profile, *Q. J. R. Meteorol. Soc.*, *136*, 2119–2131, 2010.

Petersen, E. L., N. G. Mortensen, L. Landberg, J. Højstrup, and H. P. Frank, Wind power meteorology. Part I: climate and turbulence, *Wind Eng.*, *1*, 25–45, 1998.

Plueddemann, A. J., Observation of the upper ocean using a multi-beam doppler sonar, Ph.D. thesis, Scripps Institution of Oceanography, 1987, [Available online at http://oai.dtic.mil/oai/oai?verb=getRecord&metadataPrefix=html&identifier=ADA188896].

Pond, S., R. W. Stewart, and R. W. Burling, Turbulence spectra in the wind over waves, *J. Atmos. Sci.*, *20*, 319–324, 1963.

Pope, S. B., *Turbulent Flows*, Cambridge University Press, 2000.

Raupach, M. R., R. A. Antonia, and S. Rajagopalan, Rough wall turbulent boundary layers, *Appl. Mech. Rev.*, *44*, 1–25, 1991.

Richardson, L. F., *Weather Prediction by Numerical Process*, Cambridge University Press, Cambridge, 1922.

Rippeth, T. P., E. Williams, and J. H. Simpson, Reynolds stress and turbulent energy production in a tidal channel, *J. Phys. Oceanogr.*, *32*, 1242–1251, 2002.

Rippeth, T. P., J. H. Simpson, E. Williams, and M. E. Inall, Measurement of the rates of production and dissipation of turbulent kinetic energy in an energetic tidal flow: Red Wharf Bay revisited, *J. Phys. Oceanogr.*, *33*, 1889–1901, 2003.

Ruddick, B., A. Anis, and K. Thompson, Maximum likelihood spectral fitting: The Batchelor spectrum, *J. Atmos. Oceanic Technol.*, *17*, 1541–1555, 2000.

Saddoughi, S. G., and V. Veeravalli, Local isotropy in turbulent boundary layers at high Reynolds number, *J. Fluid Mech.*, *268*, 333–372, 1994.

Sauvageot, H., *Radar Meteorology*, Artech House, Norwood, MA, 1992.

Sellar, B., S. Harding, and M. Richmond, High-resolution velocimetry in energetic tidal currents using a convergent-beam acoustic Doppler profiler, *Meas. Sci. Technol.*, *25*, 85801, 2015.

Simpson, J. H., P. J. Wiles, and B. J. Lincoln, Internal seiche modes and bottom boundary-layer dissipation in a temperate lake from acoustic measurements, *Limnol. Oceanogr.*, *56*, 1893–1906, 2011.

Simpson, J. H., N. S. Lucas, B. Powell, and S. C. Maberly, Dissipation and mixing during the onset of stratification in a temperate lake, Windermere, *Limnol. Oceanogr.*, *60*, 29–41, 2015.

Sreenivasan, K. R., On the universality of the Kolmogorov constant, *Phys. Fluids*, *7*, 2778–2784, 1995.

Stacey, M. T., Estimation of diffusive transport of turbulent kinetic energy from acoustic Doppler current profiler data, *J. Atmos. Oceanic Technol.*, *20*, 927–935, 2003.

Stacey, M. T., S. G. Monismith, and J. R. Burau, Measurements of Reynolds stress profiles in unstratified tidal flow, *J. Geophys. Res.*, *104*, 10933–10949, 1999.

Stewart, R. W., Turbulence, National Committee for Fluid Mechanics Films, 1969, available online (Nov. 22, 2016) at http://web.mit.edu/hml/ncfmf.html.

Stewart, R. W., J. R. Wilson, and R. W. Burling, Some statistical properties of small scale turbulence in an atmospheric boundary layer, *J. Fluid Mech.*, *41*, 141–152, 1970.

Talamelli, A., G. Bellani, and A. Rossetti, *The "Long Pipe" in CICLoPE: A Design for Detailed Turbulence Measurements*, pp. 127–131, Springer International Publishing, Cham, 2014.

Talke, S. A., A. R. Horner-Devine, C. C. Chickadel, and A. T. Jessup, Turbulent kinetic energy and coherent structures in a tidal river, *J. Geophys. Res. Oceans*, *118*, 6965–6981, 2013.

Taylor, G. I., Statistical theory of turbulence, *Proc. R. Soc. A*, *151*, 421–444, 1935.

Tennekes, H., and J. L. Lumley, *A First Course in Turbulence*, The MIT Press, Cambridge, MA, 1972.

Thomson, J., Wave breaking dissipation observed with "SWIFT" drifters, *J. Atmos. Oceanic Technol.*, *29*, 1866–1882, 2012.

Thomson, J., B. Polagye, V. Durgesh, and M. C. Richmond, Measurements of turbulence at two tidal energy sites in Puget Sound, WA, *IEEE J. Oceanic Eng.*, *37*, 363–374, 2012.

Thomson, J., L. F. Kilcher, and S. Harding, Multi-scale coherent turbulence at tidal energy sites, in *Proc. 5th Intl. Conf. Ocean Energy*, p. 6 pp., Halifax, Canada, 2014.

Townsend, A. A., *The Structure of Turbulent Shear Flow*, 2nd ed., Cambridge University Press, Cambridge, UK, 1976.

Van Atta, C. W., and R. A. Antonia, Reynolds number dependence of skewness and flatness factors of turbulent velocity derivatives, *Phys. Fluids*, *23*, 252–257, 1980.

Van Atta, C. W., and W. Y. Chen, Structure functions of turbulence in the atmospheric boundary layer over the ocean, *J. Fluid Mech.*, *44*, 145–159, 1970.

Vermeulen, B., A. J. F. Hoitink, and M. G. Sassi, Coupled ADCPs can yield complete Reynolds stress tensor profiles in geophysical surface flows, *Geophys. Res. Lett.*, *38*, L06406, 2011.

von Kármán, T., Progress in the statistical theory of turbulence, *Proc. Natl. Acad. Sci. U. S. A.*, *34*, 530–539, 1948.

von Kármán, T., and L. Howarth, On the statistical theory of isotropic turbulence, *Proc. Roy. Soc. A*, *164*, 192–215, 1938.

Wächter, M., H. Heißelmann, M. Hölling, A. Morales, P. Milan, T. Mücke, J. Peinke, N. Reinke, and P. Rinn, The turbulent nature of the atmospheric boundary layer and its impact on the wind energy conversion process, *J. Turbul.*, *13*, 1–21, 2012.

Walter, R. K., N. J. Nidzieko, and S. G. Monismith, Similarity scaling of turbulence spectra and cospectra in a shallow tidal flow, *J. Geophys. Res. Oceans*, *116*, C10019, 2011.

Whipple, A. C., and R. A. Luettich, A comparison of acoustic turbulence profiling techniques in the presence of waves, *Ocean Dyn.*, *59*, 719–729, 2009.

Wilcox, K. W., J. T. Zhang, I. M. McLeod, A. G. Gerber, T. Jeans, J. McMillan, A. Hay, R. Karsten, and J. Culina, Simulation of device-scale unsteady turbulent flow in the Fundy tidal region, *Submitted to Ocean Eng.*, p. 13, 2017.

Wiles, P. J., J. H. Simpson, and T. P. Rippeth, A novel technique for measuring mixing using acoustic Doppler current profilers (ADCPs), in *Proc. of the IEEE/OES Eighth Working Conference on Current Measurement Technology*, pp. 9–13, 2005.

Wiles, P. J., T. P. Rippeth, J. H. Simpson, and P. J. Hendricks, A novel technique for measuring the rate of turbulent dissipation in the marine environment, *Geophys. Res. Lett.*, *33*, L21608, 2006.

Wolk, F., H. Yamazaki, L. Seuront, and R. G. Lueck, A new free-fall profiler for measuring bio-physical microstructure, *J. Atmos. Oceanic Technol.*, *19*, 780–793, 2002.

Wyngaard, J. C., and O. R. Cote, The budgets of turbulent kinetic energy and temperature variance in the atmospheric surface layer, *J. Atmos. Sci.*, *28*, 190–201, 1971.

Yaglom, A. M., Similarity laws for constant-pressure and pressure-gradient turbulent wall flows, *Annu. Rev. Fluid Mech.*, *11*, 505–540, 1979.